

**DESIGN AND DEVELOPMENT OF HOLOGRAPHIC  
OPTICAL TWEEZERS AND STUDIES ON COLLOIDAL  
SYSTEMS**

*By*

**DEEPAK KUMAR GUPTA**

**PHYS 02 2010 04 022**

**Indira Gandhi Centre for Atomic Research, Kalpakkam**

*A thesis submitted to the  
Board of Studies in Physical Sciences*

*In partial fulfillment of requirements  
for the Degree of*

**DOCTOR OF PHILOSOPHY**

*of*

**HOMI BHABHA NATIONAL INSTITUTE**



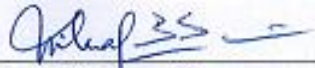
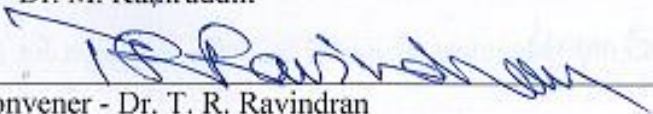
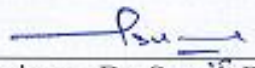
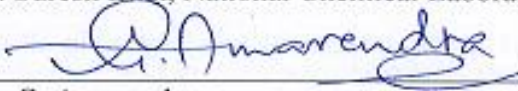
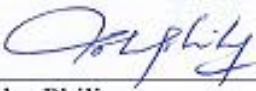
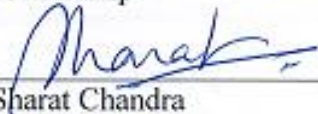
**November 2017**



# Homi Bhabha National Institute<sup>1</sup>

## Recommendations of the Viva Voce Committee

As members of the Viva Voce Committee, we certify that we have read the dissertation prepared by Deepak Kumar Gupta entitled "Design and Development of Holographic Optical Tweezers and Studies on Colloidal Systems" and recommend that it may be accepted as fulfilling the thesis requirement for the award of Degree of Doctor of Philosophy.

 Chairman - Dr. M. Kamruddin	Date: 21/1/19
 Guide / Convener - Dr. T. R. Ravindran	Date: 21/1/2019
 Examiner - Dr. Suresh Bhat, National Chemical Laboratory, Pune	Date: 21/1/19
 Member 1 - Dr. G. Amarendra	Date: Jan 21, 2019
 Member 2- Dr. John Philip	Date: 21.01.19
 Member 3- Dr. Sharat Chandra	Date: 21/01/19

Final approval and acceptance of this thesis is contingent upon the candidate's submission of the final copies of the thesis to HBNI.

I hereby certify that I have read this thesis prepared under my direction and recommend that it may be accepted as fulfilling the thesis requirement.

Date: 21.1.2019

Place: Kalpakkam

  
<Signature>

Guide

<sup>1</sup> This page is to be included only for final submission after successful completion of viva voce.

## STATEMENT BY AUTHOR

This dissertation has been submitted in partial fulfillment of requirements for an advanced degree at Homi Bhabha National Institute (HBNI) and is deposited in the Library to be made available to borrowers under rules of the HBNI.

Brief quotations from this dissertation are allowable without special permission, provided that accurate acknowledgement of source is made. Requests for permission for extended quotation from or reproduction of this manuscript in whole or in part may be granted by the Competent Authority of HBNI when in his or her judgment the proposed use of the material is in the interests of scholarship. In all other instances, however, permission must be obtained from the author.

*Deepak Kumar Gupta*

Deepak Kumar Gupta

## DECLARATION

I hereby declare that the investigations presented in this thesis have been carried out by me. The work is original and has not been submitted earlier as a whole or in part for a degree / diploma at this or any other Institution / University.

*Deepak Kumar Gupta*

Deepak Kumar Gupta

## List of Publications

### Journal

1. “Temperature-driven volume phase transition of a single stimuli-responsive microgel particle using optical tweezers”, **Deepak K. Gupta**, D. Karthickeyan, B. V. R. Tata and T. R. Ravindran, *Colloid Polym. Sci.*, **2016**, 294, 1901-1908.
2. “Optimization of a spatial light modulator driven by digital video interface graphics to generate holographic optical traps”, **Deepak K. Gupta**, B. V. R. Tata and T. R. Ravindran, *Appl. Opt.*, **2018**, 57, 8374-8384.
3. “Effect of entanglements on temperature response of gel immobilized microgel photonic crystals”, , R. G. Joshi, D. Karthickeyan, **Deepak K. Gupta** and B. V. R. Tata, *Colloids Surfaces A Physicochem. Eng. Asp.* **2018**, 558, 600–607.
4. “Crystalline arrays of submicron-sized particles through colloidal route”, B. V. R. Tata, R. G. Joshi, **D. K. Gupta**, J. Brijitta, and B. Raj, *Curr. Sci.*, **2012**, 103, 1175-1184.
5. \* “Identification of Volume Phase Transition of a Single Microgel Particle using Optical Tweezers”, D. Karthickeyan, **Deepak K. Gupta** and B. V. R. Tata, *J. Opt.*, **2016**, 18, 105401-105407.
6. \* “Optical and rheological studies on weak gel-sol transition in aqueous solutions of poly(N-isopropylacrylamide)-block-polystyrene”, S. Sanjeevi Prasath, J. Brijitta, B. V. R. Tata, R. G. Joshi, K. Chennakesavulu and **D. K. Gupta**, *Express Polym. Lett.*, **2017**, 11, 589-599.

\* Papers not included in this thesis.

## Published Conference Proceedings

- 1 “Setting up of Holographic Optical Tweezer Arrays”, **Deepak K. Gupta**, B. V. R. Tata and T. R. Ravindran, *AIP. Conf. Proc.*, **2017**, 1832, 060028 (1-3).
- 2 “Disorder in Stimuli-responsive Microgel Photonic Crystals: A Confocal Microscopic Study”, **Deepak K. Gupta**, B. V. R. Tata, J. Brijitta and R. G. Joshi, *AIP. Conf. Proc.*, **2011**, 1391, 266-268.
- 3 “A Technique to Calibrate Spatial Light Modulator for Varying Phase Response over its Spatial Regions”, **Deepak K. Gupta**, B. V. R. Tata and T. R. Ravindran, *AIP. Conf. Proc.*, **2018**, 953, 140112 (1-3).

## Conferences

- 1 “A Technique to Calibrate Spatial Light Modulator for Varying Phase Response over its Spatial Regions”, **Deepak K. Gupta**, B. V. R. Tata and T. R. Ravindran, 2nd International Conference on Condensed Matter & Applied Physics, 24-25th Nov. 2017, Bikaner.
- 2 “Setting up of Holographic Optical Tweezer Arrays”, **Deepak K. Gupta**, B. V. R. Tata and T. R. Ravindran, DAE SSPS 2016, 26<sup>th</sup> -30<sup>th</sup> December, 2016, Bhubaneswar (**Won the Best Poster Award**).
- 3 “Design and development of Holographic Optical tweezer arrays”, **Deepak K. Gupta**, D. Karthickeyan and B. V. R. Tata, 2<sup>ND</sup> Soft Matter- Young Investigators Meet (SMYIM ) 2014, 18<sup>th</sup>-20<sup>th</sup> December, 2014, Pondicherry.
- 4 “Holographic Optical Tweezers as a tool for trapping and characterizing Mesoscopic Objects in a Solvent”, **Deepak K. Gupta** and B. V. R. Tata, Theme meeting on Novel and Innovative measurements in Non-Destructive Evaluation (NIM-NDE), 23<sup>rd</sup>-24<sup>th</sup> February, 2012, Anupuram, Tamilnadu.

- 5 “Influence of Disorder on the Diffraction of Thermo-responsive Nanogel Crystals”, **Deepak K. Gupta**, B. V. R. Tata, J. Brijitta and R. G. Joshi, India-Brazil-South Africa (IBSA) Nanotechnology School on Advanced Materials, 22<sup>nd</sup> -26<sup>th</sup>, February 2010, Mahabalipuram, India.
- 6 “Optical tweezers experiment on pH responsive microgel particles”, D. Karthickeyan, **Deepak K. Gupta** and B. V. R. Tata, NLS-23, S. V. University, 3<sup>rd</sup> -6<sup>th</sup>, December 2014, Tirupathi.

*Deepak Kumar Gupta*

Deepak Kumar Gupta

*I dedicate this thesis to  
my Mother  
and everyone who have brought me to this day*

## ACKNOWLEDGEMENTS

First and foremost, I express my heartfelt gratitude to my thesis supervisor Dr. T. R. Ravindran for his patient, invaluable guidance, active support and concern during my Ph.D. tenure. I thank Dr. B .V. R. Tata for introducing me to the field of Holographic Optical Tweezers and pursue my research career in this field. I express my deepest appreciation for his inputs and comments. I sincerely thank my doctoral committee members Dr. M. Kamruddin, Dr. G. Amarendra, Dr. John Philip, and Dr. Sharat Chandra for sharing their valuable time, insightful comments and encouragement during my Ph.D. tenure. I also thank Dr. N. V. Chandrasekhar for his invaluable support in all the ways during my research career.

I extend my sincere thanks to Dr. David G. Grier, New York University and Dr. Raktim Das Gupta, RRCAT, Indore, for useful technical discussions and suggestions in setting up the Holographic Optical Tweezers set-up. I also thank Dr. S. Sivakumar for clearing my doubts related to optics, Dr. K. Gururaj in programming and Dr. Sharat Chandra for providing me all kind of technical help and discussions for improving my work. A special thanks to Dr. Soumee Chakraborty for going through my thesis in detail and corrections. I also thank my colleague Dr. R. G. Joshi, for technical discussions and corrections in the thesis. I thank all my lab mates, Section mates and all those who have directly or indirectly supported me through my research career.

Last but not the least, I thank all my family members, who have selflessly become the part of my journey and given me support and encouragement. Especially to my son *Reyansh*, who has been a driving force, by seeing whose smile makes me forget all pains, disturbances and motivating me to work with focus. Thank you all for your encouragements!

# CONTENTS

	<b>Page No.</b>
<b>SYNOPSIS</b>	<b>xiii</b>
<b>LIST OF FIGURES</b>	<b>xxvi</b>
<b>LIST OF TABLES</b>	<b>xxxv</b>
<b>CHAPTER 1</b>	<b>1</b>
INTRODUCTION	1
1.1 Optical Tweezers	3
1.1.1 Optical Tweezers: The Early Experiments	3
1.2 Multiple Optical Traps and Holographic Optical Tweezers (HOTs)	11
1.2.1 Static Beam Shaping	12
1.2.2 Dynamic Beam Shaping	13
1.2.2.1 Holographic Optical Tweezers (HOTs)	15
1.3 Applications of State-of-the-Art Optical Manipulation	19
1.4 Colloidal Systems	21
1.4.1 Hard Sphere Colloidal Systems	23
1.4.2 Charge-Stabilized Colloidal Systems	25
1.4.3 Stimuli-Responsive Microgel Systems	27
1.4.3.1 Thermo-responsive behavior of PNIPAM based Microgels	28
1.4.3.2 Internal Structure of PNIPAM Microgels	29
1.4.3.3 Phase behavior of Neutral and Ionic Microgels	31
1.4.3.4 Structure of PNIPAM and PNIPAM-based Microgel Crystals	35
1.5 Motivation for the Thesis	36
1.6 Key Findings of the Thesis	43
<b>CHAPTER 2</b>	<b>47</b>
DEVELOPMENT OF OPTICAL TWEEZERS	47
2.1 Introduction	47
2.2 Physics of Optical Trapping	48
2.2.1 Rayleigh regime ( $d \ll \lambda$ )	49
2.2.2 Ray (Geometrical) optics regime ( $d \gg \lambda$ )	50
2.2.2.1 Scattering and Gradient Forces	54
2.2.3 Intermediate regime ( $d \sim \lambda$ )	58
2.3 Factors affecting the optical trap efficiency	58
(i) Numerical Aperture	58
(ii) Size of the microsphere	59
(iii) Depth of trapping position	59
(iv) Laser beam Polarization	59
(v) Ratio of Beam radius to the Aperture radius	60
2.4 Optical Tweezers Set-up	60

2.4.1 Design Considerations	61
(a) Trapping Laser	61
(b) Microscope and Objective	62
(c) Laser Beam Coupling to Objective Back Aperture	62
(d) Steerable optical traps	66
2.4.2 Sample Preparation and optical trapping	67
2.4.3 Environmental isolation	68
2.5 Data acquisition and calibration of optical tweezers	68
2.5.1 Digital video microscopy	68
2.5.2 Calibration of the optical trap	69
2.5.2.1 Optical potential analysis	69
2.5.2.2 Equipartition method	71
2.6 Generation of ring pattern of trapped particles with optical tweezer	75
2.7 Conclusion	76
<b>CHAPTER 3</b>	<b>77</b>
DEVELOPMENT OF HOLOGRAPHIC OPTICAL TWEEZERS	77
3.1 Introduction	77
3.2 HOTs set-up	82
3.3 Calibration of the SLM	88
3.3.1 Optimization of Graphics Card settings	88
3.3.2 Phase characterization and compensation of phase nonlinearity	92
3.3.2.1 Characterization of Phase modulation	92
3.3.2.2 Phase Compensation	95
3.3.3 Calibration of the SLM for SVPR	98
3.4 Generation of holographic optical traps	102
3.4.1 Propagation of Field from SLM plane to the trapping plane	102
3.4.2 Hologram Construction	106
3.4.3 Algorithm to generate holographic optical traps	108
(i) Random Mask Encoding (RM)	108
(ii) Superposition of Prisms and Lenses (S)	108
(iii) Random Superposition (SR)	109
(iv) Direct Search (DS)	110
(v) Gerchberg-Saxton (GS) Algorithm	110
(vi) Generalized Adaptive Additive (GAA) Algorithm	111
(vii) Weighted Gerchberg Saxton (WGS) Algorithm	112
3.4.4 Numerical Propagation	115
3.5 Array of traps	117
3.6 Determination of Laser Beam Profile over SLM	122
3.7 Conclusion	124
<b>CHAPTER 4</b>	<b>127</b>
TEMPERATURE DRIVEN VOLUME PHASE TRANSITION OF A SINGLE STIMULI RESPONSIVE MICROGEL PARTICLE USING OPTICAL TWEEZERS	127

4.1 Introduction	127
4.2 Experimental Details	130
4.2.1 Synthesis and Characterization of PNIPAM-co-Aac Microgel Particles	130
4.2.2 Characterization of Size and Size Polydispersity	131
4.2.3 Heating Stage suitable for Microscopy and Sample Preparation	134
4.2.4 Optical Trapping Experiment	136
4.2.5 Determination of Optical Trap Stiffness	137
4.3 Results and Discussion	138
4.3.1 Identification of VPTT using DLS	138
4.3.2 Identification of VPTT of single microgel particle using optical tweezers	138
4.4 Conclusions	143
<b>CHAPTER 5</b>	<b>145</b>
DISORDER IN STIMULI RESPONSIVE MICROGEL PHOTONIC CRYSTALS	145
5.1 Introduction	145
5.2 Experimental Details	149
5.2.1 Synthesis of PNIPAM-co-Aac microgel particles	149
5.2.2 Sample Preparation	150
5.2.3 Confocal Laser Scanning Microscopy	151
5.3 Results and Discussion	153
5.3.1 Calculation of Pair Correlation	153
5.3.2 Calculation of Structure Factor	155
5.3.3 Influence of Osmotic Pressure on SPD	157
5.4 Conclusion	158
<b>CHAPTER 6</b>	<b>161</b>
EFFECT OF ENTANGLEMENTS ON TEMPERATURE RESPONSE OF GEL IMMOBILIZED MICROGEL PHOTONIC CRYSTALS	161
6.1 Introduction	161
6.2 Materials and Methods	164
6.2.1 Preparation of PNIPAM-co-Aac Microgel Particles	164
6.2.2 Immobilization of PNIPAM-co-Aac Microgel Crystal in PAAm Hydrogel	165
6.2.3 3D Dynamic Light Scattering analysis of gel-immobilized samples	166
6.3 Results and Discussion	170
6.3.1 Identification of VPT of PNIPAM-co-Aac Microgel Particles	170
6.3.2 Evidence for Entanglements of Polymer Chains between Microgel and Hydrogel	171
6.3.3 Consequences of Entanglements on Structural Ordering of Gel- Immobilized Microgel Crystal using UV-vis Spectroscopy	176
6.4 Conclusion	183
<b>CHAPTER 7</b>	<b>185</b>
SUMMARY AND FUTURE OUTLOOK	185

7.1 Summary and Conclusions	185
7.2 Future Outlook	192
REFERENCES	194

## SYNOPSIS

Colloidal systems are heterogeneous assemblies where small particles of one type of material (~10 nm-10  $\mu$ m) are dispersed in a continuous matrix of another type of material. Specifically, when solid particles are dispersed in a liquid medium these are referred to as *colloidal suspensions*. There is a special class of colloidal systems known as stimuli-responsive microgel suspensions that exhibit an important property: they respond to external stimuli and exhibit a rich phase behavior. The system of interest in this thesis, poly N-isopropylacrylamide (PNIPAM) microgel particles are temperature sensitive: they change their size with respect to temperature and undergo a volume phase transition (VPT) from swollen to a de-swollen state characterized by a volume phase transition temperature (VPTT) [1]. This transition is reversible. PNIPAM when co-polymerized with acrylic acid group forms PNIPAM-co-Aac microgel particles which respond to pH in addition to temperature [2]. Dense suspensions of these microgels exhibit liquid-like, crystalline and glassy structures similar to those of atomic systems, thus serving as model condensed matter systems. Furthermore, since they are stimuli-responsive and change their volume in response to various stimuli, which results in a change in other physical parameters, both associated at single particle level, and at macroscopic level. This renders them as an ideal system to understand physical phenomena crucial to science and technology [3].

To understand the macroscopic mechanics of microgel particles in suspension, it is an essential prerequisite to first understand the mechanics of individual single microgel particle [3]. For example, applications of microgels in site-specific drug delivery, optical sensors, bio-sensing, smart coatings, environmental remediation and many other applications [4–7] require a good understanding of the response to various stimuli at the single particle level. However, the measurement of properties of sub-

micron sized mesoscopic particles is a challenging problem. The forces involved in these measurements are of the order of pico-Newtons (pN) for particles suspended in a liquid solvent. Even though there are a few reports of measurements to probe single particle physics using atomic force microscopy (AFM) on the microgels of PNIPAM, they are difficult to carry out for many other microgels systems [8,9]. This is where the technique of optical tweezers [10] stands unique, and the ease with which it can probe forces of  $\sim$  pN is remarkable. A detailed introduction to optical manipulation techniques and colloidal systems is discussed in Chapter 1 of the thesis. Using optical tweezers, one can not only measure the forces but can visually observe their real-time dynamics, since they can be easily integrated with the microscopy systems. With this motivation, an optical tweezers set-up capable of trapping sub-microscopic particles stably in three dimensions was developed. The details of building the optical tweezers set-up, the principles of its operation, the physics of trapping in various regimes and calibration of the optical trap are described in **Chapter 2**. Optical tweezers involve trapping of a single or multiple particles in a single, tightly focused laser beam. However, many applications require the study of interaction between multiple particles in which independent trapping and manipulation of multiple particles at different locations in two or three dimensions becomes essential. This is accomplished by the use of a spatial light modulator (SLM) in the optical manipulation system using the technique of digital holography known as holographic optical tweezers (HOTs). With this motivation to create an array of traps, manipulate multiple particles and to study the interaction between the different trapped particles, we have designed and developed a HOTs set-up. The details of its construction and operation are discussed in **Chapter 3**. The development of optical tweezers, its extension to a HOTs system and its optimization to generate highly efficient, uniform optical traps form the first

theme of this thesis. The developed optical manipulation system has been employed to study the VPT in PNIPAM-co-Aac microgels at the single particle level. The details of these investigations are presented in **Chapter 4**. In addition, the crystals of these microgels have been studied for their disorder (in particular second type disorder) under osmotic compression, and the results are discussed in **Chapter 5**. Since the practical use of these stimuli-responsive systems needs them to be in portable immobilized form, these microgels were immobilized in a hydrogel matrix and were studied for presence of entanglements. These immobilized crystals were also studied for their order and disorder. The details of these investigations are presented in **Chapter 6**. These studies on PNIPAM using the developed optical manipulation systems and other light scattering techniques forms the second theme of this thesis. This thesis is organized into seven chapters and contents of each chapter are summarized below.

### **Chapter 1 – Introduction**

Chapter 1 is an introduction to the field of optical manipulation, with its history of different stages of development. A major leap through in optical manipulation occurred with the invention of single-beam gradient trap, the *optical tweezers*, and the field was further developed with HOTs for trapping multiple particles. The various applications of the optical manipulation technique have been described, starting from biology to physical sciences and in particular to colloidal systems. Subsequently, the chapter introduces colloidal systems and a particular class of PNIPAM based microgel systems that are of interest in this thesis. We also discuss in this chapter the motivation behind the various developments and research work carried out, describing the major outcomes of the thesis.

## **Chapter 2 – Development of Optical Tweezers**

The development of optical tweezers set-up along with its principle of operation is described. The principle of optical trapping in various trapping regimes: the Rayleigh regime, the ray-optics regime and intermediate regimes of trapping are discussed [11]. We also describe the various design considerations for building an optical tweezer set-up and its extension to create steerable traps in three dimensions. The various factors affecting the optical trap efficiency, viz., laser properties (laser power, polarization, and focal spot size) and the trapped object properties (size of the microsphere, relative refractive index) are discussed. Further, various calibration techniques [12,13] are discussed, and the optical traps were calibrated using the Boltzmann and equipartition methods. The trap stiffness for a trapped particle was measured as a function of laser power and found to be linear confirming the calibration to be correct. We also show the capability of the set-up to trap multiple particles in a consecutive ring pattern by focusing the laser on the top surface of the sample chamber.

## **Chapter 3 – Development of Holographic Optical Tweezers**

The design and development of a HOTS system using a phase-only reflective spatial light modulator (SLM) incorporated in the optical manipulation system is described. In general, the liquid crystal modulators suffer from non-linear phase response behavior, and it is challenging to optimize and calibrate the SLM for its phase modulation to generate efficient and uniform optical traps. In this thesis, we have presented a methodology to optimize the properties of graphics such as brightness, contrast, and gamma (the SLM used being driven by a DVI interface through graphics) by a method similar to that used for optimizing LCD televisions. A calibration function was generated for the SLM to correct for the non-linearity in the

phase response that resulted in an improvement of diffraction efficiency from the original 29% to 50% and enhanced the phase modulation depth from  $1.4 \pi$  to  $1.7 \pi$ . The SLMs, in general, may suffer from varying phase response over their spatial regions (SVPR), which can be due to non-uniform thickness of SLM or non-uniform (Gaussian) illumination. There are various methods reported to correct for SVPR [14], but these methods are time-consuming and frequent calibration with different power levels becomes tedious. We present a new technique based on diffraction to quickly calibrate the SLM for SVPR by optimizing its brightness, contrast, and gamma of different sub-sections and show traps with improved uniformity and diffraction efficiency. The diffraction efficiency improved to 55% after the incorporation of corrections for SVPR in the holograms. Uniformity in the intensity of the trap spots is found to improve from 76% to 97%, which resulted in an uniformity of 80% in the trap stiffness for the particles trapped in a circular array of eight spots. Further, the SVPR correction is found to improve the trap quality up to 6.5% as determined from spot sharpness metric calculation, resulting in a value of trap performance metric equal to 0.49. The generation of trap spots or any light distribution at the sample plane involves the creation of phase holograms, which are impressed upon the SLM to generate the desired pattern. Holograms are generated with various iterative algorithms [15], which require the input beam profile over SLM. In this thesis, we have reported a novel technique to determine the profile of the incident laser beam by using a diffraction-based set-up. We generate arrays of  $4 \times 4$  and  $5 \times 5$  optical traps, with trapped polystyrene spheres in them and provide a prescription for the trapping in arrays.

## **Chapter 4 – Temperature-driven volume phase transition of a single stimuli-responsive microgel particle using optical tweezers**

PNIPAM based microgels respond to temperature, exhibit a transition and VPT. Dynamic light scattering (DLS) is the most popular technique to identify the VPTT of these microgels, which requires concentrations of  $10^7$ – $10^8$  particles/cm<sup>3</sup> [16,17]. Polydispersity in the size of microgels makes DLS data analysis difficult. In homogeneous macrogels, the nature of VPT is shown to be of discontinuous type, whereas inhomogeneous macrogels (i.e., inhomogeneity in polymer density due to varying cross-linker concentration) are shown to exhibit a swelling-deswelling transition in a continuous manner [18]. DLS measurements on PNIPAM microgels also shows a VPT of a continuous type [1]. However, volume phase transition is the property of the polymer itself, and inhomogeneities in different microgels may in principle be different. Hence, it is required to measure the VPT on a single microgel particle. In this thesis, for the first time, we report the characterization of VPT of PNIPAM-co-Aac microgels with temperature on a single particle using an optical tweezer set-up. We studied the VPT of a single microgel by measuring its trap stiffness as a function of temperature and show it to be of a continuous type and compare it with that measured using DLS technique. The continuous nature of VPT is attributed to the presence of inhomogeneity within the microgel particle. The similar nature of VPT and VPTT as measured using optical tweezer and DLS implies the negligible effect of low size polydispersity (2%) on the VPTT and its nature, and also that the inhomogeneities in crosslinking density are of similar type among different microgels. The experimental results are validated by numerical computation of trap stiffness as a function of particle size, refractive index separately and also together.

## Chapter 5 – Disorder in Stimuli responsive Microgel Photonic Crystals

Dense suspensions of monodisperse thermo-sensitive PNIPAM microgel particles are known to crystallize into ordered structures, which are responsive to stimuli, known as responsive photonic crystals (RPCs). In addition to thermo sensitivity, these microgel particles (bulk modulus  $\sim$ kPa [19]) are known to undergo osmotic compression under osmotic pressure [19,20] and hence tunability in the photonic band gap and its optical properties. There are various reports of osmotic compression in dilute suspensions of PNIPAM microgels studied using DLS by the addition of a non-adsorbing polymer to the suspensions [19,20]. However, the effect of osmotic compression arising due to neighboring particles with an increase in concentration has not been investigated. Further, the colloidal suspensions of microgel systems possess various types of disorder due to shape and size polydispersity of the particles [1]. It has been demonstrated theoretically by Allard *et al.* [21] that the photonic band gap of these crystals is more sensitive to their particle size distribution than site randomness. The size and shape polydispersity in the particles forming the crystal plays an important role in determining the quality of photonic crystal [21–23]. In this thesis, we study the effect of osmotic compression of PNIPAM microgels due to increasing concentration of particles in suspension and also report for the first time that size polydispersity of microgel particles can be tuned by osmotic pressure [24]. We prepared suspensions of PNIPAM-co-Aac microgel particles with varying particle concentration by subjecting them to different osmotic pressures and characterized them for various types of disorder using confocal laser scanning microscopy (CLSM). We show that osmotic compression significantly reduced the size polydispersity (SPD) leading to the appearance of crystalline order in a highly polydisperse suspension (33% as prepared) and thereby a decrease in second type disorder. We

found that SPD of colloidal particles destroys long-range positional order, but preserves orientational order in the crystal. Experimental details and results of these experiments are presented in Chapter 5 of the thesis.

## **Chapter 6 – Effect of Entanglements on Temperature Response of Gel Immobilized Microgel Photonic Crystal**

As prepared crystals of microgel particles are in general fragile, they lose their crystalline order even under small disturbances (shear  $\sim$  a few dynes/cm<sup>2</sup>), limiting their practical use [25] that require them to be immobilized in a hydrogel matrix. The process of immobilization of these PNIPAM microgel crystals involves the preparation of microgel crystal in a pregel solution followed by polymerization to form a hydrogel. Since PNIPAM microgel particles have a porous core-shell structure [26–28], the polymerization is expected to happen both outside and inside the microgel particles. This may lead to the formation of an interpenetrating network of polymer chains between the microgel and the hydrogel [29] as shown by Song *et al.* [30] in swelling/ deswelling of PAAm hydrogel incorporated with PNIPAM-co Aac microgel particles. There are no studies of the effect of these entanglements on the dynamics of microgel particles in a hydrogel matrix and also the effect of temperature on the dynamics and photonic properties of these thermo-sensitive PNIPAM microgel crystals. In this thesis, we discuss the effect of entanglements on the dynamics of gel-immobilized PNIPAM co-Aac microgels in PAAm hydrogel with temperature using 3D DLS technique. We confirm the presence of entanglements between polymer chains of microgel and hydrogel through the study of their dynamics as a function of temperature. Further, we show the retention of crystalline order in the gel-immobilized crystals of these microgels at all temperatures across VPT using UV-visible spectroscopy. This is attributed to the entanglements between the microgel

hydrogel composite, restricting the degree of thermal vibrations and hence the crystalline order. However, there is an increase in the structural disorder with temperature induced by the collapse of microgel particle in an entangled state, causing local lattice strain. A detailed study of the effect of entanglements between the polymer chains of microgel-hydrogel composite and their effect on structure and disorder are presented in Chapter 6.

### **Chapter 7 – Summary and Future Outlook**

This chapter presents a summary of the design and development of the optical manipulation system and HOTs and the conclusions of various investigations carried out on the stimuli-responsive microgel (PNIPAM) system both at the single particle level and in its dense and immobilized suspensions for order and disorder. The significant findings from these studies are as follows:

- ✓ We have indigenously designed and developed an optical tweezer set-up capable of trapping microscopic particles stably in three dimensions. The optical traps are calibrated by measuring their stiffness by using optical potential analysis method and equipartition method and confirmed by measuring the stiffness as a function of laser power. We have trapped multiple particles using optical tweezer in a concentric ring geometry by moving the focal spot to the upper surface of the sample box.
- ✓ We have designed and developed a HOTs set-up capable of trapping multiple particles at desired locations, demonstrated its performance by trapping polystyrene particles in an array of traps, and presented a prescription for them.
- ✓ We have presented a methodology to calibrate SLMs driven by DVI interface graphics. We optimized the graphics card for parameters like brightness,

contrast and gamma for uniform resolution in addressing the gray levels throughout the available phase levels and improved efficiency. We have developed a look-up table resulting in a linear phase response of the liquid crystals of SLM.

- ✓ We have presented a simple technique for quick calibration of SLMs suffering from spatial varying phase response and showed an overall diffraction efficiency improvement from 29% to 55% and improved uniformity from 76% to 97% after optimization of SLM. The SVPR correction also improved the trap quality up to 6.5% as determined from spot sharpness metric calculation, resulting into a trap performance metric value of 0.49.
- ✓ A novel technique is presented for the determination of the laser beam profile incident over SLM as required by iterative algorithms generating the holographic optical traps.
- ✓ We present optical tweezers as a technique to characterize the VPT of stimuli-responsive microgel particles at the single particle level, enabling study of various other phenomena at single particle level.
- ✓ We have shown here for the first time that osmotic compression not only reduces the particle size but also the size polydispersity in the stimuli-responsive microgel photonic crystals of PNIPAM-co-Aac microgel particles.
- ✓ We have characterized the second type disorder and showed that with osmotic compression the disorder in these systems reduces leading to highly diffracting photonic crystals. We also showed the presence of first type disorder in these colloidal systems.

- ✓ We have provided evidence of entanglements between polymer chains of microgel particles and polymer chains of hydrogel medium in the immobilized hydrogels through the study of their dynamics as a function of temperature.
- ✓ The immobilized microgel hydrogel composites are shown to retain crystalline order above VPT and this is attributed to entanglements between the polymer chains of microgel and hydrogels, restricting the extent of thermal vibrations
- ✓ We show an increase in structural disorder with increasing temperature along with the retention of crystalline order and explain it in terms of local lattice strain induced due to the collapse of microgel particles in the entangled state.

**References:**

- [1] P.S. Mohanty, W. Richtering, *J. Phys. Chem. B* 112 (2008) 14692–14697.
- [2] M. Das, H. Zhang, E. Kumacheva, *Annu. Rev. Mater. Res.* 36 (2006) 117–142.
- [3] H.M. Wyss, J. Mattsson, T. Franke, A. Fernandez-Nieves, D.A. Weitz, in: *Microgel Suspensions*, Wiley-VCH Verlag GmbH & Co. KGaA, Weinheim, Germany, 2011, pp. 311–325.
- [4] D. Parasuraman, M.J. Serpe, *ACS Appl. Mater. Interfaces* 3 (2011) 2732–2737.
- [5] A.K. Bajpai, S.K. Shukla, S. Bhanu, S. Kankane, *Prog. Polym. Sci.* 33 (2008) 1088–1118.
- [6] Y. Gao, X. Li, M.J. Serpe, *RSC Adv.* 5 (2015) 44074–44087.
- [7] M. Wei, Y. Gao, X. Li, M.J. Serpe, *Polym. Chem.* 8 (2017) 127–143.
- [8] S.M. Hashmi, E.R. Dufresne, *Soft Matter* 5 (2009) 3682.
- [9] O. Tagit, N. Tomczak, G.J. Vancso, *Small* 4 (2008) 119–126.
- [10] A. Ashkin, J.M. Dziedzic, J.E. Bjorkholm, S. Chu, *Opt. Lett.* 11 (1986) 288.
- [11] A. Ashkin, *IEEE J. Sel. Top. Quantum Electron.* 6 (2000) 841–856.

- [12] N. Viana, M. Rocha, O. Mesquita, A. Mazolli, P.A.M. Neto, H.M. Nussenzveig, *Phys. Rev. E* 75 (2007) 21914.
- [13] N.B. Viana, A. Mazolli, P.A. Maia Neto, H.M. Nussenzveig, M.S. Rocha, O.N. Mesquita, *Appl. Phys. Lett.* 88 (2006) 131110.
- [14] D. Engström, M. Persson, J. Bengtsson, M. Goksör, *Opt. Express* 21 (2013) 16086.
- [15] J.E. Curtis, B.A. Koss, D.G. Grier, *Opt. Commun.* 207 (2002) 169–175.
- [16] Burce J. Berne, Robert Pecora, *Dynamic Light Scattering*, John Wiley & Sons, New York, 1976.
- [17] J. Brijitta, B.V.R. Tata, T. Kaliyappan, *J. Nanosci. Nanotechnol.* 9 (2009) 5323–5328.
- [18] S. Takata, K. Suzuki, T. Norisuye, M. Shibayama, *Polymer.* 43 (2002) 3101–3107.
- [19] B. Sierra-Martín, Y. Laporte, A.B. South, L.A. Lyon, A. Fernández-Nieves, *Phys. Rev. E - Stat. Nonlinear, Soft Matter Phys.* 84 (2011) 11406.
- [20] A. Fernández-Nieves, A. Fernández-Barbero, B. Vincent, F.J. de las Nieves, *J. Chem. Phys.* 119 (2003) 10383–10388.
- [21] M. Allard, E.H. Sargent, in: *Conf. Lasers Electro-Optics/International Quantum Electron. Conf. Photonic Appl. Syst. Technol.*, Optical Society of America, San Francisco, California, 2004, p. CTuDD1.
- [22] M. Allard, E.H. Sargent, E. Kumacheva, O. Kalinina, *Opt. Quantum Electron.* 34 (2002) 27–36.
- [23] M. Allard, E.H. Sargent, *Appl. Phys. Lett.* 85 (2004) 5887–5889.
- [24] D.K. Gupta, B.V.R. Tata, J. Brijitta, R.G. Joshi, in: *AIP Conf. Proc.*, 2011, pp. 266–268.

- [25] B.V.R. Tata, *Statistical Physics of Complex Fluids*, Tohoku University Press, Sendai Japan, 2007.
- [26] B.R. Saunders, *Langmuir* 20 (2004) 3925–3932.
- [27] G. Romeo, L. Imperiali, J.-W. Kim, A. Fernández-Nieves, D.A. Weitz, J. *Chem. Phys.* 136 (2012) 124905.
- [28] M. Stieger, W. Richtering, J.S. Pedersen, P. Lindner, *J. Chem. Phys.* 120 (2004) 6197–6206.
- [29] J. Museh, S. Schneider, P. Lindner, W. Richtering, *J. Phys. Chem. B* 112 (2008) 6309–6314.
- [30] W. Song, Y. Guan, Y. Zhang, X.X. Zhu, *Soft Matter* 9 (2013) 2629.

## LIST OF FIGURES

<b>Figure 1.1</b>	Schematics of a Gaussian laser beam of power 1W incident upon a 100% reflecting mirror of mass 1 kg and a microscopic particle of mass 1picogram, showing the orders of acceleration produced in them due to radiation pressure as per the back of the envelope calculation done by Arthur Ashkin in late 1969 [7]. The radiation pressure has a negligible effect on the macroscopic object mirror ( $a = 10^{-9}g$ ), whereas the effects on the microscopic particle are observable, producing an acceleration of the order of ( $a = 10^{+6}g$ ) due to radiation pressure.....	5
<b>Figure 1.2</b>	Schematics of the geometry of the apparatus as used by Arthur Ashkin in his first experiment in 1969 [7], which demonstrated the acceleration and trapping of micron-sized particles using the radiation pressure from a CW laser. A TEM <sub>00</sub> mode laser is weakly focused using a lens into the volume of a glass chamber of thickness t. The latex spheres either of sizes (0.59, 1.31 and 2.68 $\mu\text{m}$ diameter) suspended in water are pulled into the beam and pushed forward until they are stuck to the front wall. Particles are being guided by light and observed through a microscope M. ....	6
<b>Figure 1.3</b>	Schematics of the geometry of the apparatus used by Arthur Ashkin to create the first stable optical potential well using two counter-propagating Gaussian laser beams [7]. Note the position of the stable equilibrium point and the beam waists of the two laser beams symmetric to the equilibrium point. Any deflection of the particle from the equilibrium point induces a restoring force to bring back the particle into the optical potential well, by the scattering forces of the counter-propagating laser beams along the beam axis and by the gradient force transverse to the beam axis. Observation is done with a microscope M situated down to the transverse direction. ....	7
<b>Figure 1.4</b>	(a) Schematics of the levitation apparatus used by Arthur Ashkin [9,12]. Particle is shaken loose by setting up an acoustic vibration with the piezoelectric ceramic cylinder (PC) to break the van der Waals attraction between the particle and the plate supporting it. A focused laser beam directed vertically upwards levitates the particle from the surface of the glass plate to a position above beam focus in air/vacuum balanced by gravity. (b) Schematic of the optically levitated liquid drops arranged in order of size, the largest closest to the beam focus and the smallest at a farther distance [11]......	9
<b>Figure 1.5</b>	Schematics of the first ‘Optical tweezers’- the <i>single-beam gradient optical trap</i> apparatus used by Arthur Ashkin [28]. A tightly focused Gaussian laser beam ( $\lambda=514.5 \text{ nm}$ ) by the use of a high numerical aperture water immersion objective directed vertically downwards to trap various Mie and Rayleigh particles suspended in water medium, by the	

	use of gradient force of the single laser beam. The trapped particles are viewed from the side by the microscope M.....	11
<b>Figure 1.6</b>	Phase diagram of monodisperse hard sphere colloidal suspensions.....	24
<b>Figure 1.7</b>	(a)Variation of hydrodynamic radius, $R_h$ of PNIPAM-co-Aac microgel particles with temperature T, (b) Schematics diagram of the chemical structure changes occurring across the volume phase transition for PNIPAM-co-Aac microgel, (c) Photograph of PNIPAM-co-Aac microgel suspension before and after VPT and schematic of individual PNIPAM-co-Aac microgel showing the transition from swollen (hydrophilic) to de-swollen (hydrophobic) state and vice-versa. ....	28
<b>Figure 1.8</b>	(a) Schematic of the core-shell structure of PNIPAM microgel particle in the swollen state, with a core of radius $R_c$ and shell of thickness $\rho$ , $R_h$ is the hydrodynamic radius. (b) Radial polymer density profiles of PNIPAM microgel at various temperatures as measured using SANS, showing the increase of core thickness with increase in temperature, $R$ indicating the distance where the core density is half of its value. (Adapted from Stieger et al. [193]) .....	30
<b>Figure 1.9</b>	Phase diagram of aqueous PNIPAM microgel dispersion determined from turbidity measurements (symbols) and thermodynamic perturbation theory with empirical temperature correction (lines), adapted from [189]. Inset shows the phase diagram predicted without any empirical temperature correction.....	33
<b>Figure 1.10</b>	Phase diagram of ionic microgels with diameter $\sigma = 100$ nm, adapted from [200]. The crosses denote the calculated phase boundaries; lines connecting them are guide to the eye. The inset shows a high-density, high-charge region of the phase diagram in detail. ....	34
<b>Figure 1.11</b>	(a) Micrograph showing an ABC type stacking obtained by overlaying three consecutive layers of PNIPAM microgel crystal obtained using CLSM. The micrograph shows an FCC structure (layer A-red, layer B-green, layer C-blue), (b) $g(r)$ calculated for the structure in (a) shown as dark solid circle being compared with $g(r)$ calculated for an ideal FCC structure, shown as lines. The experimental $g(r)$ and the simulated one match very closely confirming the crystal structure to be FCC. (Adapted from Brijitta et al. [204]) .....	35
<b>Figure 2.1</b>	Schematics of a Gaussian laser beam focused using a high numerical aperture (N.A) objective to create a diffraction-limited spot at the trapping plane capable of trapping microscopic particles stably in three dimensions. $F_{scatt}$ pushes the particle away from the focus in the direction of the incident laser beam, and $F_{grad}$ pulls the particle towards the region of high intensity, i.e., towards the focal spot.....	48

<b>Figure 2.2</b>	Illustration showing the trapping mechanism for a spherical particle laterally shifted away from the focus of the Gaussian beam in the ray optics regime by considering the incident focused beam as a bunch of rays. The mechanism of trapping explained by considering two of the rays one high intense and the other low intense ray suffering the change in momentum per second due to refraction and a net force pulling the particle towards the focus of the laser beam.....	51
<b>Figure 2.3</b>	Illustration showing the trapping mechanism for a spherical particle (a) with particle centers below the focus and (b) with particle center above the focus of the tightly focused Gaussian beam in the ray optics regime. The mechanism of trapping explained by considering two of the refracting rays suffering the change in momentum per second due to refraction and a net force pulling the particle towards the focus of the laser beam.....	53
<b>Figure 2.4</b>	Geometry of the scattering of a single incident ray of power $P$ on a dielectric sphere visualized in the plane of incidence with reflected ray and an infinite set of refracted rays, considered while calculating the forces in ray optics regime. Here $i$ is the angle of incidence and $r$ is the angle of refraction.....	54
<b>Figure 2.5</b>	Photograph of the home-built optical tweezers set-up, built around a commercial inverted microscope OLYMPUS IX 81. M, M0,M1, M2 are (>99%) reflecting mirrors, LE and LC are the beam expander lenses. ....	60
<b>Figure 2.6</b>	Schematics of the optical layout of the optical manipulation system. The lenses LE and LC expand the laser beam to a diameter equal to the ratio of their focal lengths. The expanded laser beam is reflected off two steering mirrors (M1) and (M2) and coupled to the microscope objective (O) through a dichroic mirror (DM) to produce tightly focused diffraction limited spot at the sample plane (SP). The trapped particles are imaged by a CCD detector placed at the trinocular port of the microscope.....	64
<b>Figure 2.7</b>	Schematics of the steering mirrors M1 and M2 steering the laser beam. (a) and (b) describing the procedure of beam alignment, (a) Mirror M1 rotated to centre the beam and pass through pinhole P1, (b) Mirror M2 rotated to centre the beam and pass through pinhole P2, giving a laser beam propagating in a given direction, (c) Mirrors M1 and M2 rotated by same angle in either clockwise or anticlockwise direction shift the laser beam laterally. The schematic shows the steering in a plane, the mirrors being kinematic, the laser beam can be steered all over the perpendicular plane of beam propagation. Dashed blue ray shows the original direction, and the dark blue solid ray shows the shifted laser beam direction parallel to the original direction by rotation of the steering mirrors clockwise by the same angle. ....	65

<b>Figure 2.8</b>	(a) Schematic of the steerable optical tweezer set-up with two lenses L1 and L2 in the fixed trap set-up shown in Fig. 2.6, (b) Photograph of the sample prepared between the glass slide and the coverslip using a spacer and (c) an image of a 1.2 $\mu\text{m}$ diameter polystyrene sphere trapped. ....66	
<b>Figure 2.9</b>	Schematic of the position distribution of a trapped particle and the potential obtained using Eq. (2.16).....70	
<b>Figure 2.10</b>	(a), (b) and(c) Images of the trapped polystyrene sphere of diameter 1.2 $\mu\text{m}$ trapped with laser powers 1.4mW, 5.4mW, and 44mW respectively. (d), (e) and (f) shows the scattering plot of the positions of the trapped spheres recorded up to 10000 frames for the particles trapped with different laser powers as in (a), (b) and (c). (g),(h) and (i) shows the respective histogram of position distributions of the particle under the optical trap and (j),(k) and (l) shows the optical potential landscape calculated using Eq. (2.16) and fitted with a 5th order polynomial. ....72	
<b>Figure 2.11</b>	(a) Optical trapping potential for a trapped polystyrene sphere of diameter 1.2 $\mu\text{m}$ at various laser powers showing the increase in the depth and the shrinking of the potential well towards the trap center, and (b) variation the trap stiffness as a function of laser power fitted to a straight line. ....74	
<b>Figure 2.12</b>	(a) Image of the focused optical spot being moved upwards at the lower surface of the upper glass slide, showing a ring pattern at the interface, and (b) Polystyrene spheres of diameter 600nm trapped in the concentric ring pattern created using a single laser focus. ....75	
<b>Figure 3.1</b>	(a) Photograph of SLM with the active area zoomed showing pixelated nature of SLM, (b) Schematic of the side view of SLM showing the parallel aligned nematic liquid crystals sandwiched between the pixelated back electrode and the front transparent glass plate, (c) Schematic of the orientation of liquid crystal molecules within the cylindrical volume of single pixel without any applied field, and (d) with applied field showing effective birefringence.....83	
<b>Figure 3.2</b>	Schematics of the HOTs setup. Polarization optics consisting of a polarizer and a half-wave plate controls the polarization and its orientation. M1, M2, M3, M4, M5, and M6 are (>99%) reflecting mirrors for the laser ( $\lambda = 1064 \text{ nm}$ ). Beam expansion optics expand the laser beam to fill the active area of the SLM. Lenses L1 and L2 in 4f configuration image the SLM at the back focal plane of the microscope objective (MO). SF is the spatial filter (a pinhole) for filtering the various orders of the diffracted beam.....85	
<b>Figure 3.3</b>	Photograph of the HOTs set-up. ....86	
<b>Figure 3.4</b>	(a) Schematic of the Experimental setup based on diffraction to measure the first-order diffracted power at the Fourier plane of the SLM using a	

power meter with binary holograms (with 50% duty cycle): (i) a zero gray level imposed on SLM required for brightness optimization, and (ii) a series of binary diffraction gratings ( 50% duty cycle) with varying gray levels from 0 to 65,535 imposed on SLM for gamma optimization of the graphics card respectively. (b) Plot of normalized first-order diffracted power versus the brightness levels set in the graphics card, showing a minimum at 97% of brightness level. (c) Plot of normalized first-order diffracted power measured at the Fourier plane of SLM as a function of gamma of graphics card, with a hologram (shown as inset) representing a linear binary diffraction grating with one of the phase levels having a gray value 32,768 and other 0. ....91

**Figure 3.5** (a) Plot of normalized power measured at the first-order diffracted beam versus gray level: (i) using a linear-lut, shown as magenta circles fitted piece-wise with a ninth-order polynomial (fit is shown as blue lines), and (ii) using a system-lut provided by the supplier. (b) Plot of extracted phase modulation curve from the normalized power measured using linear-lut as a function of addressed gray values. The right-hand-side axis shows the equivalent phase levels in units of the converted gray level.....93

**Figure 3.6** (a) Plot of the phase compensation profile (termed dkg2-lut), showing the gray level out used for addressing of the SLM for each of the input gray values, required for having a linear phase response. (b) Plot of measured phase modulation curve as a function of gray level (i) using system-lut (shown in red circles) and (ii) using the generated phase compensation profile, i.e. dkg2-lut (blue circles) and a linear fit to the measured data (shown as a black line as a fit to the measured data) showing the corrected phase response behavior.....96

**Figure 3.7** Diffraction spots recorded by a camera by displaying a blazed grating over the SLM (a) by using system-lut and (b) by using the generated phase compensation profile, i.e., dkg2-lut showing the improvement in first-order diffraction efficiency. ....98

**Figure 3.8** (a) Typical hologram divided into 64 subsections with the  $i$ th subsection with a blazed grating and the other subsections being kept blank. (b) Set of holograms with varying brightness level to be displayed in the  $i$ th subsection, and the hologram, marked with the red boundary, with given brightness/contrast level producing maximum intensity at the first-order diffracted beam as an example. (c) Set of holograms with varying gamma levels for the hologram with optimized brightness/contrast marked with a red boundary in (b) to be displayed in the  $i$ th subsection, and the hologram with the red boundary showing a typical hologram with given gamma level producing maximum intensity at the first-order diffracted beam. ....99

**Figure 3.9** (a) Typical blazed hologram displayed on the SLM to produce a first-order diffracted spot at the Fourier plane of the SLM. (b) A table with 64

- subsections, each subsection being divided into three compartments. The two top parameters represent the optimized brightness/contrast level, with parameters in the range [0.0-0.9, 0.1-1.0], and the bottom one represents the optimized gamma level, ranging 0.1 onward, for each of the subsections. These parameters are the corrections for the SVPR. (c) Typical blazed hologram calculated by WGS algorithm, while taking into account the correction for the SVPR. ....101
- Figure 3.10** (a) Simplified schematic of the HOTs set up of Fig. 3.2 describing the propagation of field from the SLM plane to the trapping plane. SLM being imaged by L1 and L2 at the back aperture of the microscope objective and the Fourier plane of SLM being imaged by L2 and microscope objective at the imaging plane making a simple Fourier transform relationship between the SLM plane and the focal plane (Imaging plane) of the microscope objective. ....104
- Figure 3.11** Schematics representation of the geometry of the effective Fourier field propagation from the SLM plane to the trapping site  $(x_m, y_m, z_m)$  relative to the center of the Fourier plane. ....106
- Figure 3.12** Flow chart describing the modified (WGS) algorithm. An estimate of kinoform is taken from a random superposition (SR) algorithm with the amplitude as the profile of laser over the SLM as an initial field. The field is propagated from the SLM plane to the trapping plane. A new field is constructed using the obtained phase and amplitude with the weighted combination of target amplitude and obtained amplitude (taking into account weighting of diffraction effects due to SLM pixelation). The field is propagated back to the SLM plane, and the amplitude is replaced with the amplitude of the laser while keeping the phase the same. The field is again propagated to the trapping plane. The iteration is repeated until an optimized phase is obtained. Finally, the hologram is corrected for the SVPR. ....113
- Figure 3.13** Schematic of numerical propagation to improve resolution at the trapping plane by zero padding pixels around SLM pixels. ....116
- Figure 3.14** (a) 4×4 array of spots without uniformity correction showing a decrease in intensity as we move away from the zeroth order, (b) 4×4 array of spots with uniformity correction showing equal intensity at the trap spots (except for the effects of ghost order on the uniformity). ....117
- Figure 3.15** (a) Circular array of eight trap spots around the strong central zeroth order with a radius of 100 pixels corresponding to 12.8  $\mu\text{m}$ , generated using WGS algorithm with the system-lut, showing non-uniform intensities among the trap spots. (b) Circular array of eight traps around a weak zeroth order with a radius of 100 pixels generated using same WGS algorithm with the developed LUT, dkg2-lut, in place, showing fairly uniform intensities among the trap spots with higher diffraction efficiency. (c) Polystyrene spheres of diameter 1.2  $\mu\text{m}$  trapped in the

	array shifted 1 $\mu\text{m}$ above the focal plane, generated using an optimized hologram with SVPR correction and using dkg2-lut. (d) Variation of uniformity with number of traps.....	119
<b>Figure 3.16</b>	(a) Intensity plot of a typical trap spot (a) before SVPR correction and (b) after SVPR correction.....	120
<b>Figure 3.17</b>	(a) Scatter plot of particle positions in a given trap spot (a) without SVPR correction and (b) with SVPR correction. ....	121
<b>Figure 3.18</b>	(a) Typical hologram generated by the WGS algorithm incorporated with correction for SVPR to generate 4 $\times$ 4 optical traps. (b) Polystyrene spheres of diameter 1.2 $\mu\text{m}$ suspended in water trapped in a 4 $\times$ 4 array.....	122
<b>Figure 3.19</b>	(a) Table showing the maximum power (mW) diffracted off each of the sub-sections (8 $\times$ 8 pixels) of SLM, with each sub-section displayed by a blazed grating, (b) Calculated Laser profile of the beam over SLM fitted to a Gaussian function centered at (210, 253)th pixel. ....	123
<b>Figure 4.1</b>	(a) Photograph of sample cell containing the sample with the heating element showing the manganin wire coil and PT100 sensor on the surface of coverslip mounted on the universal stage of microscope. (b) Schematic of the sample cell containing the sample in a well between the standard glass slide and cover slip separated by a thin spacer with the heating element made on teflon sheet having hole for illumination and a PT100 sensor at bottom for measurement of temperature.....	134
<b>Figure 4.2</b>	(a) Calibration set-up for calibrating the PT100 sensor using a standard heater and ETS-D5 sensor. (b) Plot of temperature versus resistance curve showing the temperature corresponding to the resistance measured using a PT100 sensor and being fitted to a straight line. ....	136
<b>Figure 4.3</b>	(a) Hydrodynamic radius, $R_h$ , of PNIPAM-co-Aac microgel particles versus temperature measured using DLS. Inset shows the schematics of a microgel particle in swollen and deswollen state, i.e., before and after VPTT (34 $^\circ\text{C}$ ). (b) Plot of lateral trap stiffness, $\kappa$ measured on a single microgel particle as a function of temperature using optical tweezers showing VPTT at 34 $^\circ\text{C}$ . Inset shows the image of trapped microgel particle before and after VPTT showing an increase in contrast after VPTT. Continuous lines are guide to the eye.....	139
<b>Figure 4.4</b>	(a) Computed lateral trap stiffness as a function of temperature considering only the effect of variation of refractive index with temperature keeping size of the particle fixed.(b) Computed lateral traps stiffness as a function of temperature considering only the effect of variation of size of the particle with temperature keeping refractive index fixed.(c) computed lateral trap stiffness as a function of temperature taking into account variation of both parameters, the refractive index and the size of microgel particle. Continuous lines are guide to the eye. ....	142

<b>Figure 5.1</b>	Schematic of the ultra-filtration set-up (Millipore stirred cells equipped with ultrafiltration membrane) for osmotically compressing the microgels to different concentration.....	150
<b>Figure 5.2</b>	Photographs of (a) un-crystallized ( $n_p: 1.2 \times 10^{13} \text{ cm}^{-3}$ ) and (b) crystallized ( $n_p: 5.7 \times 10^{13} \text{ cm}^{-3}$ ) samples at room temperature (25° C). .....	151
<b>Figure 5.3</b>	Schematics of a confocal laser scanning microscope, showing its capability of optical slicing and hence z-sectioning for imaging in depth by the use of a variable pinhole along with XY scanning. ....	152
<b>Figure 5.4</b>	CLSM images of single crystalline domains in sample S1 (a) and sample S2 (b). Corresponding $g(r)$ 's are shown in (c) and (d) respectively. $g(r)$ 's for respective ideal lattices are shown in bottom panels. ....	154
<b>Figure 5.5</b>	Schematic of the influence of osmotic pressure on PNIPAM-co-Aac microgel particles showing the shrinking of microgels to smaller sizes with osmotic compression. ....	154
<b>Figure 5.6</b>	Structure factor $S(q)$ for the single crystalline domain in sample S1 (a) and sample S2 (b). Radial profiles of $S(q)$ averaged over three different directions as marked in Fig.(a) and (b) for sample S1 (c) and sample S2 (d). ....	155
<b>Figure 5.7</b>	Exponential fit of area under the $S(q)$ peaks of Fig. 5 as a function of diffraction order $q/q_{10}$ for single crystalline domains of sample S1, S2. The relative full width at half maximum peak widths $\delta q/q_{10}$ of the $S(q)$ peaks as a function of the diffraction order $q/q_{10}$ for the single crystalline domains of sample S1, S2 and the reference lattice. ....	156
<b>Figure 5.8</b>	Images of the PNIPAM particles recorded using CLSM: (a) before osmotic compression and (b) after osmotic compression.....	158
<b>Figure 5.9</b>	Particle size distribution for the dilute (uncompressed) and the crystallized (compressed) samples of S3 fitted to Gaussian.....	158
<b>Figure 6.1</b>	(a) Ray diagram showing scattering geometry of 3D light scattering setup, (b) Schematic diagram of the cross-correlation light scattering setup.....	168
<b>Figure 6.2</b>	(a) Photograph showing iridescence from PNIPAM-co-Aac microgel crystal in a container at 22 °C. b) Variation of hydrodynamic diameter, $d$ of PNIPAM-co-Aac microgel particle with temperature at pH ~ 3.4.....	170
<b>Figure 6.3</b>	$f(q,t)$ for PAAm hydrogel at different temperatures (a) without and (b) with PNIPAM-co-Aac microgel particles incorporated. (c) Decay rate, $\Gamma$ and (d) $f(q,\infty)$ of PAAm hydrogel with and without microgels, as a function of temperature. Inset in (d) is temperature dependence of $\langle \delta^2 \rangle$ of microgels in the hydrogel. Error bars are obtained from the average of	

three measurements. (e) time dependence of  $\Gamma$  and  $f(q, \infty)$  for microgel-hydrogel composite and (f) time dependence of microgel size in aqueous suspension, at different temperatures in the vicinity of VPT. Continuous lines are guide to the eyes.....175

**Figure 6.4** (a) UV-vis transmission spectra from gel immobilized microgel crystal at different temperatures showing Bragg diffraction dip. Temperature dependence of position (b) and minimum (c) of the diffraction dip in transmission spectra. (d) time dependence of Bragg diffraction (gel size) for immobilized microgel crystal at 40 °C.....177

**Figure 6.5** (a) Variation of width,  $W$  of the diffraction dip across the VPT. Continuous line is guide to the eye. Schematic representation of gel-immobilized microgel crystal having entanglements of polymer chains between microgel (blue) and hydrogel (red) showing (b) unstrained hydrogel network below VPT and (c) strained hydrogel network above VPT. ....182

## LIST OF TABLES

<b>Table 2.1</b>	Lateral trap stiffness as a function of laser power for a trapped polystyrene particle of diameter $1.2\mu\text{m}$ as measured using optical potential analysis method and equipartition method. ....	73
------------------	--	----



### INTRODUCTION

---

Light *can exert force*, a consequence of which is its ability to hold and manipulate microscopic objects has triggered the rise of a new era in the scientific world. The phenomenon, that light exerts force, immediately makes us think of it carrying momentum. Light consists of photons, *the quantum of light* and each photon carries momentum as stated by quantum mechanics. Light can transfer momentum to illuminated objects, the result of which is radiation pressure, was predicted by James Clerk Maxwell in his famous theory of electromagnetism, even prior to the existence of quantum mechanics [1]. The existence of such pressure in the context of thermodynamics was also predicted by Bartoli, known as *Maxwell-Bartoli force* [2]. However, the ability of light to exert force was recognized much before as hypothesized by Kepler (1619), while explaining the deflection of comet tails by the sunlight, and subsequently studied by Euler (1746). There were even two independent attempts by P.N. Lebedev (1901) [3] and by E. F. Nichols and G. F. Hull (1903) [4,5], who performed experiments and demonstrated the existence of radiation pressure, much before the discovery of laser. However, their measurements were hindered by thermal effects, but qualitatively proved the effect of light's momentum, *the radiation pressure*. Furthermore, light can exert torque too, as was demonstrated in 1936 by Beth in his experiment of the interaction of circularly polarized light with a birefringent quartz plate [6].

Light is one of the most important tools for researchers. Through the development of microscopy techniques, the full potential of light has been exploited. With the use of light applied to various microscopic techniques, it has been possible

to explore the miniature world of objects and living organisms from nanometers to microns level. The evolved techniques such as bright field microscopy, dark field, phase contrast and fluorescence microscopy have enabled great insight into the various phenomena at microscopic and sub-microscopic level. Furthermore, with the advent of laser- *a coherent source of light*, there took place a major leap-through in the light technologies and remarkable experimental capability providing deep insights into various physical phenomena. The discovery of laser has not only allowed us to see the objects, but now we can hold, manipulate, reposition, cut, ablate and selectively stimulate them, through the rise of a new technology known as *optical manipulation*. Optical manipulation has led to the discovery of many new phenomena, deep understanding of processes at a length scale, which was not possible by the use of other existing technologies. There is a continuous push to further advance this technique and the various areas in which it can be exploited.

In this thesis, development of the state of the art technique of optical manipulation tool and its extension to a more advanced set-up are discussed. Applications to a class of colloidal systems to understand certain phenomena at single particle level have been exploited along with their study of various structural and dynamical properties with other light based techniques. This forms the major theme of this thesis.

In the forthcoming section, we discuss the tool, which has extended the capability of light to a different level, i.e., to hold and manipulate microscopic objects, the *optical tweezers*.

## 1.1 Optical Tweezers

The pioneering work for the development of the technique of optical tweezers was carried out by Arthur Ashkin. In recent years, this technique has become an indispensable tool for innumerable studies across various disciplines of science. Ashkin first demonstrated the acceleration and trapping of micron-sized particles using radiation pressure and by the use of multiple laser beams. The technique took an upswing after he established the trapping of microscopic particles using a single laser beam, by the use of its gradient force achieved by tight focusing of the laser, known as “single beam gradient force optical trap” named as optical tweezers. The ability of optical tweezers to stably hold and manipulate microscopic objects with nanometer precision with temporal resolution down to microseconds, measuring forces of the order of pN, makes it an impressive tool for scientists to probe microscopic phenomena taking place at time, length and force scales inaccessible by conventional techniques. In addition to the sensitivity, the non-destructive nature of this probe makes it an ideal tool for biologists to study living cells like bacterial cells, human red blood cells, other living biological cells, and molecules. In the next section, we discuss the historical development and evolution of the optical manipulation, which is essential for a clear understanding of the subject and forms the starting point of the thesis.

### 1.1.1 Optical Tweezers: The Early Experiments

In 1969, Arthur Ashkin contrived a new era of research in the field of science, i.e., *optical manipulation* with a “back of the envelope” calculation of the acceleration produced by the radiation pressure of light [7]. He calculated the force experienced by a 100% reflecting mirror of mass 1 kg by the radiation pressure of a continuous wave

## Introduction

CW argon laser light of wavelength 514.5 nm, power 1 W and compared it with that incident on a lossless microscopic particle of mass of the order of picograms and density as that of water. According to the wave-particle duality concept of quantum mechanics [8], light can be considered both either as waves or as particles. The fundamental particles of which light is composed of are known as *photons*, and each photon carries a linear momentum determined by the wavelength  $\lambda$  of light as

$$p = \frac{h}{\lambda}, \quad (1.1)$$

where  $p$  is the linear momentum of each photon pointing in the direction of propagation of light and  $h$  is the Planck's constant,  $h = 6.626 \times 10^{-34}$  Js. Suppose a laser of power  $P$  strikes a 100% reflecting mirror of mass  $m$ . Then, the number of photons striking the mirror per sec is,

$$\frac{dN}{dt} = \frac{P}{pc}, \quad (1.2)$$

where  $E = pc$ , is the energy per photon. The total change in momentum per second suffered by the light upon reflection from the mirror is given by

$$\frac{dp}{dt} = \left( \frac{dN}{dt} \right) \times 2p, \quad (1.3)$$

This change in momentum of light, in turn, accelerates the mirror with acceleration,

$$a = \frac{1}{m} \frac{dp}{dt} = \frac{1}{m} \times \left( \frac{dN}{dt} \right) \times 2p = \frac{1}{m} \times \frac{2P}{c}, \quad (1.4)$$

For a laser of power 1 W incident on a mirror of mass 1 kg, the acceleration produced is of the order of  $10^{-9}$   $g$ ,  $g$  being the acceleration due to gravity. Thus the radiation pressure due to laser has a negligible effect on the mirror, and hence it can be

neglected while dealing with the macroscopic objects. If the same laser of power 1 W is incident upon a microscopic particle of mass of the order of picograms (assumed to be a 100% reflecting and having density similar to that of water), then the acceleration produced due to the radiation pressure is of the order of  $10^6 g$ , which is enough to accelerate the particle, leading to observable effects.

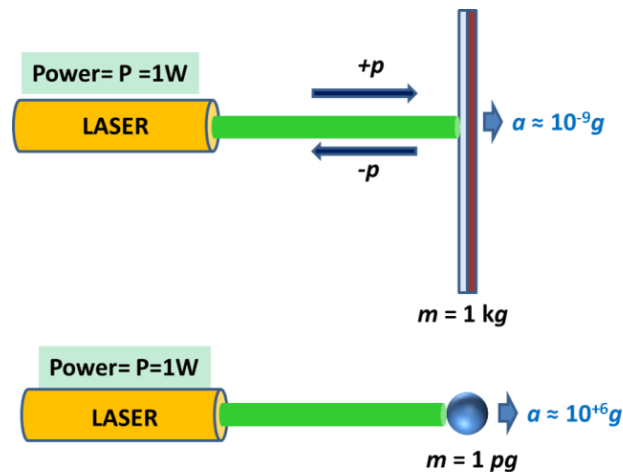


**Figure 1.1** Schematics of a Gaussian laser beam of power 1W incident upon a 100% reflecting mirror of mass 1 kg and a microscopic particle of mass 1picogram, showing the orders of acceleration produced in them due to radiation pressure as per the back of the envelope calculation done by Arthur Ashkin in late 1969 [7]. The radiation pressure has a negligible effect on the macroscopic object mirror ( $a = 10^{-9}g$ ), whereas the effects on the microscopic particle are observable, producing an acceleration of the order of ( $a = 10^{+6}g$ ) due to radiation pressure.

This enormous effect of radiation pressure on microscopic particles, the outcome of his “back of the envelope calculation,” [7] motivated Ashkin to perform the first-ever experiment with radiation to study its effect on the microscopic world. He showed the acceleration and trapping of transparent latex spheres suspended in water using a weakly focused Gaussian laser beam of few milliwatts power. He observed, as anticipated, the particle motion in the direction of laser beam propagation, the force responsible for it termed as *the scattering force*. Also, to his surprise, he discovered another type of force, which pulled the particles from the low

intense region of the beam to the high intense region on the beam axis, named as *the gradient force*. Once these particles were drawn to the beam axis, they were accelerated forward in the direction of light and got collected on the front chamber of the wall and remained trapped in the laser beam. The particles performed random Brownian motion when the laser was turned off and drawn back to the beam axis once the laser was turned on again. Particles were being guided by the laser light. This force was found to pull the particles with higher refractive index (compared to the surrounding medium) into the high intense region, whereas it pushed out particles having a relatively low refractive index (such as air bubbles) away from the beam axis, as they were accelerated along the direction of beam propagation.

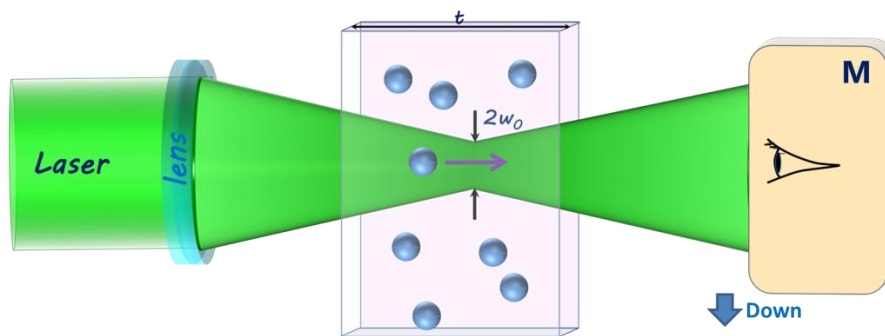


**Figure 1.2** Schematics of the geometry of the apparatus as used by Arthur Ashkin in his first experiment in 1969 [7], which demonstrated the acceleration and trapping of micron-sized particles using the radiation pressure from a CW laser. A  $TEM_{00}$  mode laser is weakly focused using a lens into the volume of a glass chamber of thickness  $t$ . The latex spheres either of sizes (0.59, 1.31 and 2.68  $\mu\text{m}$  diameter) suspended in water are pulled into the beam and pushed forward until they are stuck to the front wall. Particles are being guided by light and observed through a microscope M.

Fig. 1.2 shows a schematic of a typical apparatus used by Ashkin [7] when he observed for the first time the acceleration and trapping of microscopic particles using radiation pressure. The particles used were transparent latex spheres of the size of the order of microns suspended in water in a glass chamber. A  $TEM_{00}$  mode CW argon laser focused nearly to the size of the order of the size of latex spheres was propagated

horizontally to accelerate and trap the particles. As shown in Fig. 1.2, the particle near to the focus gets pulled into the high intense region of the beam and is accelerated forward until it reached the front wall of the chamber.

After the discovery of the acceleration of microscopic particles by radiation pressure, Ashkin performed another experiment [7] using two counter-propagating TEM<sub>00</sub> Gaussian laser beams, with their respective beam waists at a position shown in Fig. 1.3. This configuration created a stable optical trap in which the particles were confined through a combination of scattering force and the gradient force. The particles drifting near either of the beam focus were pulled in and accelerated to a stable equilibrium point, equidistant from either of the beam waist (Fig. 1.3). Any displacement of the particle from this symmetry point induces a restoring force, and the particle is pulled back to its equilibrium position, the “optical potential well.”

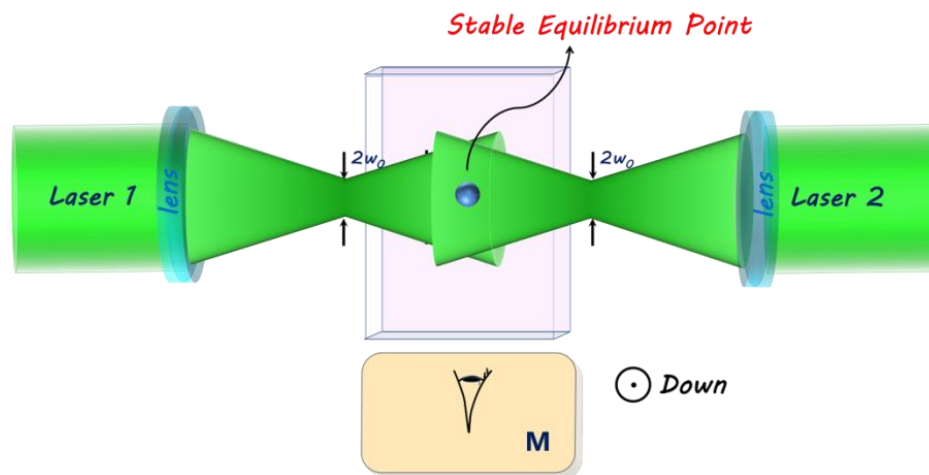


**Figure 1.3** Schematics of the geometry of the apparatus used by Arthur Ashkin to create the first stable optical potential well using two counter-propagating Gaussian laser beams [7]. Note the position of the stable equilibrium point and the beam waists of the two laser beams symmetric to the equilibrium point. Any deflection of the particle from the equilibrium point induces a restoring force to bring back the particle into the optical potential well, by the scattering forces of the counter-propagating laser beams along the beam axis and by the gradient force transverse to the beam axis. Observation is done with a microscope M situated down to the transverse direction.

In 1971, a subsequent advancement in the field of optical trapping was made by the demonstration of optical levitation in air by the use of radiation pressure and the effect of gravity [9]. Arthur Ashkin used a vertically directed focused laser beam to levitate glass spheres from the surface of a glass plate and hold it stably at a point much above the beam waist. The glass sphere is held at equilibrium by the balance between the scattering force and the glass sphere's weight as shown in Fig. 1.4(a). Once levitated, the object can be easily manipulated by simply moving the beam in a horizontal plane and by moving the lens in the z-direction and can also be positioned on the top surface of the chamber. In the period 1971 to 1980, Ashkin published a series of papers on his work based on optical levitation of particles. The levitation of another class of particles, in particular, hollow glass spheres was demonstrated by the use of a  $TEM_{01}$  mode (doughnut mode) of the laser beam [10]. The use of  $TEM_{01}$  mode of the laser beam having a central hollow region allows for stable trapping since these hollow spheres behave like air bubbles which are being pushed from the high intense region of the light to the low intense central region leading to a stable trap configuration. The optical levitation technique was also used for levitation and optical sorting of liquid drops [11]. The levitated drops arrange themselves in order of their increasing size, the bigger ones remain close to the beam focus, and the lighter ones remain at a farther distance (Fig. 1.4(b)), the farther drops being arranged in a position of the optical field modified by the drops located below them, i.e., near the focus. The optical levitation of particles was also demonstrated in high-vacuum regime [12] and was feedback-stabilized to damp oscillations of levitated particles due to random fluctuations of the beam [13].

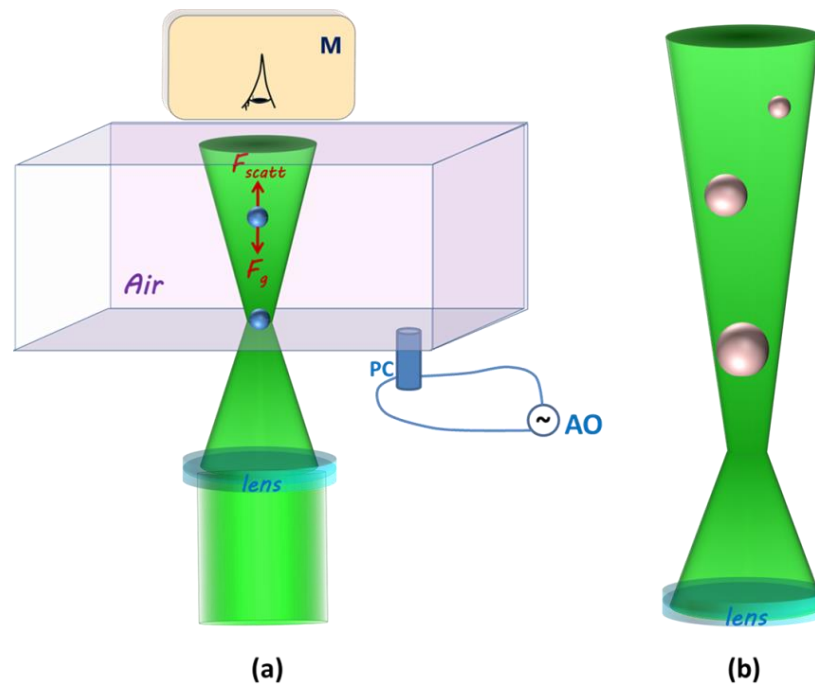


**Figure 1.4** (a) Schematics of the levitation apparatus used by Arthur Ashkin [9,12]. Particle is shaken loose by setting up an acoustic vibration with the piezoelectric ceramic cylinder (PC) to break the van der Waals attraction between the particle and the plate supporting it. A focused laser beam directed vertically upwards levitates the particle from the surface of the glass plate to a position above beam focus in air/vacuum balanced by gravity. (b) Schematic of the optically levitated liquid drops arranged in order of size, the largest closest to the beam focus and the smallest at a farther distance [11].

With the aid of the optical levitation technique, one can combine two or more levitated particles to form non-spherical compound particles such as spheroids, spherical doublets, triplets, quadruplets, etc. and carry out light scattering experiments on them as test particles [14–18]. The principle of optical trapping and manipulation was even demonstrated for the case of neutral atoms by the use of resonance radiation pressure forces [19,20]. This led to the beginning of a new field called *atom optics*, atoms being guided by light in a way similar to the manipulation of microscopic particles by the gradient force of laser [21–26]. This discovery led to the extension of optical trapping regime from microscopic world to a dimension of few angstroms, the

atomic world and this earned Steven Chu, jointly with Claude Cohen-Tannoudji and William D. Phillips, the Nobel prize in physics in the year 1997.

All of the above experiments starting from the first by Ashkin, i.e., acceleration and trapping of microscopic particles [7], used a balancing force acting in the opposite direction, such as (i) holding the particle against the chamber wall, or (ii) by the use of a counter-propagating beam for balancing the scattering force [7], or (iii) by the use of gravity against the scattering force as in case of optical levitation to stably hold the particle in three dimensions [9,11,12]. Further, the applications requiring manipulations required one or more laser beams making the system somewhat complicated [11–13,16,17,27]. It was when Ashkin realized that the gradient force alone could be utilized for stable trapping the microscopic particles. In the year 1986, Arthur Ashkin along with his co-workers [28], showed the use of a single laser beam to stably trap and manipulate microscopic particles in three dimensions without the aid of any other extra balancing forces, known as the *single beam gradient optical trap* or *optical tweezers*. The optical tweezers possess the capability of holding microscopic particles in three dimensions stable by the use of a tightly focused laser beam achieved by a high numerical aperture (N.A.) objective. The tight focusing enables trapping of the particle both in the plane transverse to beam propagation and in the axial direction, leading to a stable trap in three-dimensions.

Fig. 1.5 shows the apparatus used by Ashkin *et al.* [28], using which he demonstrated the first optical trapping using a single laser beam without the aid of any other balancing forces. A Gaussian laser beam TEM<sub>00</sub> mode ( $\lambda=514.5\text{nm}$ ) directed vertically downwards tightly focused using a high N.A. water immersion objective

traps nearby particles by the use of gradient force of the laser. The tight focusing maximizes the gradient force, responsible for pulling the particles into the beam focus compared to the scattering force, which pushes the particles away from the beam focus, and hence a stable optical trap using a single laser beam.

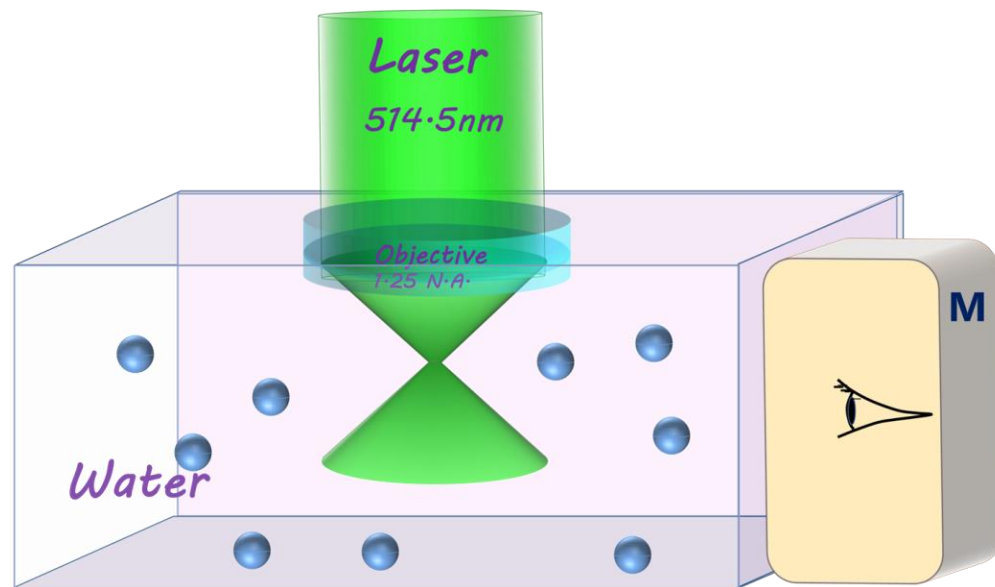


**Figure 1.5** Schematics of the first ‘Optical tweezers’- the *single-beam gradient optical trap* apparatus used by Arthur Ashkin [28]. A tightly focused Gaussian laser beam ( $\lambda=514.5$  nm) by the use of a high numerical aperture water immersion objective directed vertically downwards to trap various Mie and Rayleigh particles suspended in water medium, by the use of gradient force of the single laser beam. The trapped particles are viewed from the side by the microscope M.

## 1.2 Multiple Optical Traps and Holographic Optical Tweezers (HOTs)

Optical tweezers involve the creation of a single beam trap. The lateral and axial displacements of the trap are controlled by the use of multiple steering mirrors and lenses [29,30]. However, many applications like probing of higher-dimensional structures in more than one direction, the study of certain complex mesoscopic systems, required simultaneous control over a multitude of particles, positioning them in three-dimensional spaces at desired locations. In the context of optical trapping and

manipulation, to create multiple beams out of a single beam is accomplished by the use of beam shaping techniques, which can be roughly grouped into three categories, viz., (i) complex modulation, (ii) amplitude-only modulation and (iii) phase-only modulation. Out of these, the devices based on complex modulation modulate both phase and amplitude but are complicated in case of requirement of time-varying beam shaping. Amplitude modulation devices are of low efficiency; they work by physical removal of sections of the beam [31]. The devices working by phase modulation only are more efficient compared to the other two and are readily available in the market [32]. Focusing on the beam shaping by phase-only modulation techniques, they can be classified into two categories; (i) static methods and (ii) dynamic methods.

### 1.2.1 Static Beam Shaping

Static methods of light modulation use optical components like prisms, lenses, mirrors, gratings, etc. that alter the beam shape in a way they are static; they cannot be changed in real time and hence are limited to specific kind of applications. Static methods also include the diffractive optical elements (DOEs), which are either amplitude or phase mask objects, which can produce an array of spots or any pattern of light in the far field depending upon the complexity of the optical elements. The first use of diffractive optical elements to produce multiple trapping spots was first demonstrated by Fournier *et al.* by the use of a two-dimensional crystal of monodisperse polystyrene spheres as a diffractive element [33]. One early use of diffractive optical elements to generate multiple beams was by Dufrense and Grier, termed as *the hexadeca tweezer* [34]. Apart from multi-beam generation, DOEs also found active applications in the microfluidic optical sorting of particles [35], in creating a different configuration of colloidal arrangements like linear chains, crystal

lattices, etc. [36]. Another approach to creating a static array of traps was by using an array of semiconductor lasers, like the generation of multiple beams by a vertical-cavity surface-emitting laser (VCSELs) array [37]. The individual trapping sites can be switched on or off by turning on-off the lasers, and even the possibility of modulating the individual trapping beam shape was demonstrated by the use of VCSELs emitting Laguerre-Gaussian laser mode [38].

### 1.2.2 Dynamic Beam Shaping

Dynamic beam shaping methods are versatile; they have the advantage of changing the beam shapes in real time. This allows the experimenter to manipulate the trapped structures quickly in real time and allows to study the various physical phenomena. Dynamic beam shaping is employed in two ways, either a single beam is scanned continuously and shared between the desired locations, or a single beam is split in different directions simultaneously. The first method includes optical devices like rapid scanning mirrors, deformable mirrors and acousto-optic deflectors (AODs) or electro-optic deflectors (EODs).

The rapid scanning beam method for creating multiple beams from a single beam involves the scanning of the single laser beam with a refresh rate much higher than the resonant frequency of the particle under the optical trap. The single laser beam is time-shared between different trapping sites and allows simultaneous trapping of particles at the desired locations [39–44]. In general, a particle under an optical trap behaves like a damped harmonic oscillator being acted upon by the restoring force created by the tightly focused laser beam and damped by the frictional forces experienced in the suspending medium. The resonance frequency of a typical trapped particle in a liquid medium range from 100 Hz to 1 kHz, overdamped by an order of

magnitude due to fluid friction. The scanning mirrors used for producing multiple beams are generally galvanometer or piezo-electric driven mirrors, which scan at quite high speeds of frequency  $\sim 2$  to  $10$  kHz. The speed with which a single laser beam can be switched between different spots limits the number of traps that can be created, i.e., approximately nearly ten numbers and they do suffer from wobble and jitter stability problems [45]. However, they offer an advantage of negligible power loss and large beam deflection angles compared to other techniques. The scanning laser optical trapping technique allows even for the trapping of particles having a refractive index less than the medium in which it is suspended [46,47].

Another method of creating multiple trapping sites using a single laser beam is by diffracting the laser using acousto-optic modulators. The modulators create acoustic waves along the length of a suitable crystal by the use of a piezoelectric element, which upon reflection from other surface form standing waves, resulting in the formation of Bragg gratings of a certain period, which diffracts the incident laser beam into different directions. The angular deflection of the beam is controlled by changing the frequency of the piezo-electric element, which in turn alters the periodicity of the Bragg grating causing different angular deflection. These modulators allow for time-sharing of the diffracted beam with speeds of  $\sim 20$  kHz, enabling the creation of more number of traps compared to those by techniques based on scanning mirrors. However, one of the disadvantages of these modulators is that their diffraction efficiency varies with angles over its acoustic bandwidth, resulting in power variation between traps at different angles. Electro-optic deflectors (EODs) operate at frequencies of  $100$  MHz, which facilitates the switching of the diffracted laser beam between different positions with MHz frequency, approximately three orders of magnitude faster than that of scanning mirrors [45]. This allows for the

creation of hundreds of trapping sites, which can be positioned independently [48]. EODs also have higher optical transmission of ~80% and diffraction efficiency at higher angles with better precision as compared to that of acousto-optic deflectors (AODs) having a transmission of ~65% and a slightly less diffraction efficiency [45,49].

The scanning mirrors and modulators can introduce angular deflection of the beam, which results in the lateral displacement of the spots in the focal plane of the lens, but they lack the capability to displace traps in the axial direction. The deformable mirrors consist of small segments of mirrors each controlled by an actuator, which modulates the phase of the incoming wavefront [50]. The deformable mirrors can change the divergence of the laser beam, resulting in axial displacement of the trap spots [51]. The ranges of axial displacement of traps are limited to few microns due to their limited dynamic range but have the high mechanical bandwidth, which enables fast modulation of the trap. Even these deformable mirrors can change the simple Gaussian laser beam into many complex beam shapes, such as Laguerre-Gaussian, Bessel, or Matthieu, etc. [50], and are also useful in beam aberration correction in optical tweezers [52].

### **1.2.2.1 Holographic Optical Tweezers (HOTs)**

The second class of dynamic beam shaping involves the splitting of a single beam into multiple beams in different directions simultaneously, instead of scanning a single beam into multiple spots as discussed above. The splitting of a single beam into multiple beams makes use of a dynamic diffraction device; liquid crystal-based spatial light modulator (LCOS SLM) in combination with the technique of digital holography. SLMs offer an advantage of diffracting beams in many directions

simultaneously along with the possibility of axial displacement of the optical trap without the aid of any other optical element. The very first successful use of SLMs in creating multiple traps was demonstrated by Hayasaki *et al.* [53] and Reicherter *et al.* [54]. The extension of the use of SLMs in displacing traps in axial direction along with lateral displacements was demonstrated by Liesener *et al.* [55]. SLMs work at a relatively low speed of around 60 to 120 Hz compared to other methods of dynamic beam shaping. SLMs based on ferroelectric liquid crystals operate at high speeds of  $\sim$ kHz, but have only a binary phase response, and hence have a poor diffraction efficiency [56].

Commercially available phase-only SLMs possess diffraction efficiency around 50% compared to previously used miniature liquid crystal displays. Although having a diffraction efficiency and refresh rate much lower compared the other methods of dynamically shaping the beam, HOTs have become more versatile devices due to two reasons. Along with the capability of displacing traps laterally and axially, the beam shapes of the individual trap types can be modified. For example, they can convert a Gaussian beam into a Laguerre- Gaussian, as demonstrated first by Curtis *et al.* [57]. This established holographic optical tweezers as an important tool across the various fields of sciences. In addition to generating trap spots in three dimensions and controlling their shape, SLMs can be used to correct for aberrations in an optical manipulation system [52,58–61]. SLMs itself may introduce aberrations such as astigmatism and spherical aberration in the system, but they can be corrected by modifying the phase holograms displayed on the SLM [62]. With the use of SLMs in HOTs, typically working with video resolution, the trap spots can be manipulated to several tens of microns in lateral dimension as well as along axial direction [63], and the traps can be placed with nanometer precision [64,65].

The key to the generation of multiple traps using the diffractive characteristics of SLM is the generation of phase-only holograms, which needs to be displayed over the SLM. The holograms displayed over SLM modulate the refractive indices of the liquid crystals over its spatial regions, which in turn modulate the incident wave's phase, amplitude or both. In holographic optical tweezers, SLMs are used in phase-only modulation configuration, which gives rise to maximum diffraction efficiency. Simple phase-only holograms or the so-called kinoforms to displace the trap spots in the lateral direction and axial direction are blazed gratings and Fresnel lenses [55]. In general, to generate multiple trap spots in different configurations and beam shapes in three dimensions, various optimized iterative algorithms such as Gerchberg-Saxton algorithm (GS) [66–68], Generalized Adaptive Additive (GAA) [69], direct binary search (DBS) [68,70], random mask encoding [71], Quadrant kinoform approach [72] and their various modified versions are used. To improve the diffraction efficiency and uniformity among the generated trap spots, various optimizations and modifications in the algorithms have been developed [69,73–79]. Further, with the advent of multi-core processing technologies and improvement in computation fast generation and control of holographic optical traps in real time have been demonstrated [80,81], new interactive interfaces for controlling the traps like joystick/hand-driven interfaces, haptic feedback control have been explored [82–85].

The optimized algorithms for the generation of phase holograms to create holographic optical traps, as described above, ideally produces traps with 99% uniformity and high diffraction efficiency, but practically the quality of traps in the experiment depends on the phase levels realized by the SLM. The SLMs consisting of liquid crystal molecules (parallel nematic or twisted nematic) suffer from the non-linear phase response behavior, and the surfaces of SLMs could also be non-flat. Such

non-ideal conditions cause degradation of the quality of traps in terms of their uniformity and diffraction efficiency. There are various calibration methods based on interferometric approach and diffraction-based methods reported in the literature to correct for the phase response behavior of these liquid crystals based SLMs [86–94]. SLMs can also suffer from varying phase response across its spatial regions [95,96], either due to surface non-flatness or non-uniform illumination due to use of Gaussian beams, which leads to non-uniformity and low diffraction efficiency in the generated trap spots. There are few reports in which methods to compensate for spatially varying phase response have been described [95,96]. They involve characterizing the SLM for each of its small sub-sections for phase modulation and fitting them to a higher order polynomial. Such methods are strenuous when the SLMs have to be calibrated for various incident power levels as required for certain experiments.

We discuss in Chapter 2 the development of optical tweezers and its extension to a holographic optical tweezer system by using a SLM to generate multiple optical traps in Chapter 3. Design strategies are discussed in Chapter 3, where we also discuss a unique calibration procedure of the SLM driven by digital video interface (DVI) through a graphics card to compensate for the linear phase response behavior. A novel technique to quickly calibrate the SLM for spatially varying phase response, along with a method to determine the actual beam profile required as an input to algorithms, generating traps will be discussed. This development of optical tweezer system along with its extension to a HOTs system with various optimization work for SLM to generate uniform optical traps with improved diffraction efficiency forms the first theme of this thesis. Having discussed the design and development strategies, we will now discuss the applications of the optical manipulation systems to various disciplines of science, especially to colloidal systems which are of our main interest.

### 1.3 Applications of State-of-the-Art Optical Manipulation

The invention of the optical tweezers “*the single-beam gradient optical trap*” in 1986, has opened up a new era in the field of science. Biologists were the first to exploit the usefulness of the technique. In 1987, Ashkin showed the trapping of viruses and bacterial cells using a green laser [97] and subsequently by an infrared (IR) laser [98,99] in order to avoid cell damage caused by the high flux of laser light ( $10^7$  W/cm<sup>2</sup>) [100]. This opened up a new area of research in biological experiments for the use of optical tweezers with the advent of IR laser for optical trapping. They could not only trap and manipulate single cells [101,102] but also they could manipulate cell organelles within the cell and measure the force of cell organelle transport within the cell by the use of IR laser beam [103]. Optical tweezers along with a counter-propagating trap in microfluidic systems act as *optical stretcher* [104–106], being able to cause mechanical extension of cells, characterizing the bulk stiffness of the cells [106]. Optical tweezers have enabled measurements of mechanical properties of biological cells such as red blood cells [107,108], study the mechanics of cell membranes [109–111]. Mechanical properties of protein molecules, DNA, lipid membranes have been studied, and individual biomolecules rotated (optical spanners) and manipulated [112–117]. The capability of HOTs to create a multitude of optical spots along with ease of having beam shapes other than Gaussian have been used for separation of living cells and study of the interaction between individual cells, arranging them in desired 3D structures [118–120]. The technique of optical manipulation has revolutionized the field of biological science by its capability of probing at single molecule level and it remains as one of the most important single molecule techniques.

Apart from applications in biology, optical trapping and manipulation technique finds applications in the field of physical sciences and other interdisciplinary fields. Even Ashkin, in his first optical tweezer paper [28], demonstrated optical trapping and manipulation of dielectric particles. Later, trapping of metallic particles by Svoboda and Block [121], nano rods by Pelton *et al.* [122] were also demonstrated, opening up its application in the area of plasmonics and nano photonics [123,124]. The use of scanning beam technique to create templates of two-dimensional arrays of particles in a polymerization matrix for seeding of three-dimensional structures was also demonstrated [43,125,126]. Holographic optical tweezers enable trapping two particles at the same lateral coordinates displaced by a certain distance in the axial direction and hence offer the ability to create flexible optical patterns [127]. This enabled creation of complex three dimensional crystalline [68] and quasi-crystalline structures [128], hydrodynamic interactions measurement between colloidal spheres [129], study of particle interactions in complicated geometries [130], optical binding [131,132], colloidal transport [133–136], optical sorting [118] and anomalous effects in colloidal systems [137]. The capability of HOTs in creating different beam shapes allowed the study of translation-rotation coupling between particles arising from hydrodynamic interactions [138–140]. The capability of tweezers to hold and measure the forces of the order of pico-newtons has allowed investigations in many areas of soft matter such as micro-rheology using OTs [141–145], mechanical properties of polymers [146], accumulation of molecules [147], colloidal and liquid crystal interactions [148–150]. One of the most important applications of tweezers to colloidal systems is its ability to measure Casimir forces, arising due to concentration fluctuations between two nearby surfaces separated by a binary liquid [151]. The advantage of the optical manipulation system is that it can be

combined with many other characterization techniques to probe trapped particles.

Optical trapping and manipulation find applications in the field of colloidal physics as discussed above. In particular, there is a class of colloidal systems that are stimuli-responsive [152], i.e., respond to various stimuli like temperature, pressure, ionic strength and pH. They are known as *responsive colloidal systems*. The power of optical manipulation to exploit this class of systems has not been effectively utilized. The study of these systems at single particle level using optical manipulation technique and their structures for order and disorder using other light scattering techniques forms the second theme of this thesis. Having discussed the capabilities and applications of optical tweezers especially to the class of colloidal systems, we shall briefly introduce colloidal systems in the next section and discuss the importance of studying them.

#### **1.4 Colloidal Systems**

Colloidal systems are heterogeneous systems where small particles of one type of material ranging in dimensions 10 nm to 10  $\mu\text{m}$  are dispersed in a continuous matrix of another material. They can be solid particles dispersed in a liquid medium, referred to as *colloidal suspensions*, liquid in liquid, known as *colloidal emulsions* or gas in liquid, *aerosols*. The systems of interest in this thesis are colloidal suspensions of some mesoscopic particles dispersed in a medium, i.e., water. The mesoscopic particles sizes are large enough that the medium in which they are dispersed can be regarded as continuous and homogeneous, and they are small enough to perform Brownian motion due to scattering by thermal fluctuations of the solvent molecules. Colloidal suspensions are technologically important. They find many applications such as in inks, paints, coatings and many more. The dispersed particles in the

colloidal suspensions flow like a fluid, and the particles can be prepared with perfect precisions of polydispersity down to 3% or less [153]. The inter-particle interactions in colloids can be tuned precisely from strongly repulsive to strongly attractive or different magnitudes of attractive and repulsive forces could be designed to be present in the colloid. The range of interaction can be varied from a few nanometres to distances larger than the particle's size. In general, the colloidal particles dispersed in a solvent possess only intrinsic kinetic stability; they tend to aggregate when they come closer than a distance of the order of a nanometer or less, due to van der Waals attraction. This process is called flocculation. This aggregation can be prevented either by coating particles with a thin layer of polymer, called steric stabilization or by adding charges on the surface of these particles, called the electrostatic stabilization. By tuning the surface charge on these particles, their diameter, and the concentration, the inter-particle interactions in these systems can be tuned. The ability to precisely control of the particle sizes and the inter-particle interactions makes them an ideal system to study different types of phase behaviors.

Colloidal particles themselves possess rich phase behavior, which makes the study of colloidal suspensions interesting. Under suitable conditions, monodisperse suspensions of colloidal particles exhibit structural ordering similar to that observed in atomic systems, particularly liquid-like, crystalline, gas-like and glassy structures, of course with larger inter-particle separations [154–156]. The time scales of dynamics in these systems range from micro-seconds to several seconds, giving easy access to study the structure and dynamics in various phases. Due to the difference of ~three orders of magnitude of sizes between the colloidal particles and atomic systems, the typical number densities of these systems are  $\sim 10^{13}$  particles/cm<sup>3</sup> and  $\sim 10^{23}$  particles/cm<sup>3</sup>, respectively for colloidal systems and atomic systems. This

striking difference in the number densities is reflected in the elastic constants of these systems: typical values of elastic constant in colloidal systems  $\sim 10$  dynes/cm<sup>2</sup> compared to that of atomic systems  $\sim 10^{12}$  dynes/cm<sup>2</sup> [155,157]. Colloidal systems are soft and fragile. The molar latent heat of melting and molar elastic constants of colloidal crystals matches closely to that of atomic systems [157]. The scaling of magnitudes of different physical properties with particle concentrations implies that the interaction energy in colloidal systems is of the same order as in atomic systems. Hence, the phase behavior of colloidal systems is similar to that of atomic systems. Further, due to scaled up sizes of colloidal particles, even if they are not visible to the naked eye, they can be easily imaged with microscopy techniques, which gives a clear advantage to study the dynamics of these systems in both space and time. This allows probing dynamics and phase behavior of the system at the single particle level, which is not possible, in general, in atomic systems. All these combinations of properties makes colloidal systems as model condensed matter systems to understand fundamental phenomena in condensed matter like crystal nucleation and growth [158–161], glass transitions [162,163], various types of disorder [164,165], and dynamics [159]. In addition, ordered structures of these colloidal suspensions known as colloidal crystals find high tech applications in Bragg filters [166], sensors [167–169], optical switches [170], template for the development of novel materials, display devices, photonic crystals [171], etc.

#### 1.4.1 Hard Sphere Colloidal Systems

Hard sphere colloidal suspensions are the simplest of all colloidal systems, studied for its phase behavior. The only parameter which controls the phase behavior of hard sphere colloidal suspensions is their volume fraction,  $\varphi = n_p \pi d^3 / 6$ , where  $d$  is

the diameter of the hard sphere,  $n_p$  is the particle number density. The interparticle interaction potential for hard sphere systems is expressed as,

$$U(r) = \begin{cases} 0, & \text{if } r \geq d \\ \infty, & \text{if } r < d \end{cases} \quad (1.5)$$

Hard sphere suspensions experience a steep repulsion when they come in physical contact with each other. Otherwise, they do not interact. Sterically stabilized suspensions of polymethyl-methacrylate (PMMA) particles used to study the fluid to solid and the glass transitions forms the best example of hard sphere colloidal suspensions [154,162]. Fig. 1.6 shows the phase diagram of hard sphere suspension of monodisperse colloidal particles [154].

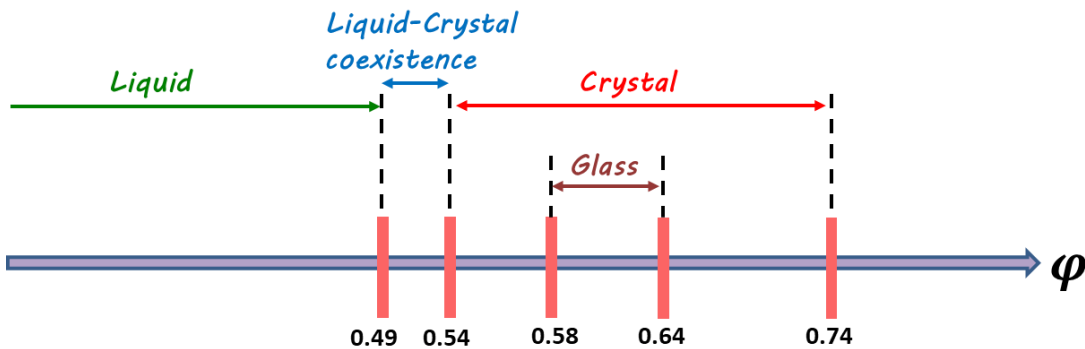


**Figure 1.6** Phase diagram of monodisperse hard sphere colloidal suspensions.

Under extreme dilute conditions, hard sphere suspensions exist in a disordered gaseous phase, and as  $\phi$  is increased, suspensions exhibit a liquid-like order. Upon increasing  $\phi$  to 0.49, they start to organize spontaneously into a crystalline order, with the co-existence of liquid and crystalline phases and form a complete crystalline phase upon reaching  $\phi=0.54$ . The hard sphere suspensions, in general, crystallize into a face-centered cubic (FCC) structure, which is the entropically driven minimum energy configuration, equilibrium structure [172–174]. However, hard sphere suspensions

also exhibit hexagonal close-packed (HCP) structure and coexist in FCC and HCP structures due to a small free energy difference (less than  $10^{-3} k_B T$  per particle,  $k_B$  is the Boltzmann constant and  $T$  is the temperature) between these two structures [172–174]. Further increase in  $\phi$  causes the particle dynamics to become slower, and the system transforms into a kinetically arrested disordered glassy phase, characterized by the hard sphere glass transition volume fraction at  $\phi=0.58$ . This glassy phase of these suspensions remains up to  $\phi=0.64$ , where the particles touch each other to form random closed packed (RCP) structures. The phase diagram shown in Fig. 1.6 is for a monodisperse hard sphere colloidal suspension. With increase in polydispersity, the volume fraction at which these particles crystallize shifts to a higher value of  $\phi$ . Hard sphere suspensions with polydispersity below 11% are found to exhibit crystalline order above which they have been found to freeze into a disordered glassy phase [163].

#### 1.4.2 Charge-Stabilized Colloidal Systems

Charged sphere colloidal suspensions are stabilized using electrostatic forces arising due to the addition of charges on the surface of the particles. They tend to crystallize into ordered structures due to the electrostatic interactions between the particles and are well described by Derjaguin-Landau-Verwey-Overbeek (DLVO) theory [155,175]. According to DLVO theory, the interaction potential between charged colloidal particles is the sum of the screened Coulomb repulsion,  $U_{er}(r)$  and van der Waals attraction  $U_{va}(r)$ , written as

$$U(r) = U_{er}(r) + U_{va}(r) \quad (1.7)$$

## Introduction

The screened coulomb repulsion term arises due to the screening of Coulomb repulsion between similarly charged particles by counter-ions and salt ions present in the suspension [176] and is expressed as

$$U_{er}(r) = \frac{e^2}{\varepsilon} \left[ \frac{Ze^{\kappa a}}{1 + \kappa a} \right] \frac{e^{-\kappa r}}{r}, \quad (1.8)$$

where,  $Ze$  is the effective charge ( $Z$  is the charge number, and  $e$  is the electronic charge) on the colloidal particle of radius  $a$ , and  $\kappa$  is the inverse Debye-screening length given by

$$\kappa^2 = \frac{4\pi e^2}{\varepsilon k_B T} (n_p Z + C_s) \quad (1.9)$$

Here  $k_B$  is the Boltzmann constant,  $T$  the temperature,  $n_p Z$  the number of counter ions and  $C_s$  is the salt concentration. The van der Waals attractive term is given as

$$U_{va}(r) = -\frac{A_H}{6} \left[ \frac{2a^2}{r^2 - 4a^2} + \frac{2a^2}{r^2} + \ln \left( \frac{r^2 - 4a^2}{r^2} \right) \right], \quad (1.10)$$

where  $A_H$  is the Hamaker constant, which sets the scale of attraction. Thus in charged colloids, parameters such as particle charge number  $Z$ , ionic strength  $C_s$ , along with volume fraction  $\varphi$ , control the phase behavior. Deionized suspensions of charged colloids exhibit crystalline order at  $\varphi$  as low as 0.005 due to long-range screened Coulomb repulsive interactions. Charged colloids show liquid-like order at low  $\varphi$  and high  $C_s$ , as the addition of salt decreases the strength and range of screened Coulombic interaction resulting in crystal melting. Upon reducing the  $C_s$ , low volume fraction ( $\varphi < 0.2$ ) suspensions crystallize into body-centered cubic (BCC) structure. With the increase in  $\varphi$ , the structure of charged colloids changes to face-centered

cubic (FCC) with BCC-FCC coexisting at intermediate  $\phi$  and  $C_s$ . At higher  $\phi$ , suspensions freeze into a glassy state, that has also been observed at low  $\phi$  upon pressure quenching [163].

### 1.4.3 Stimuli-Responsive Microgel Systems

The hard sphere and the charged sphere colloids as discussed in the previous two sub-sections consists of particles whose size and their distribution cannot be altered after their synthesis. In contrast to these suspensions, there exists a class of colloidal systems known as stimuli-responsive microgels, which are ‘soft’ and can change their shape and size in response to external stimuli such as temperature, pressure, pH, ionic strength or chemical environment. Microgels are polymer networks of cross-linked polymer chains dispersed in a liquid medium. These microgels reversibly swell and deswell in response to changes in external stimuli, and hence the phase behavior and mechanical responses of these microgels are much richer than those observed for hard sphere and charged sphere suspensions [177]. Microgels which respond to temperature and change their size, are known as thermo-responsive microgels. Among the many stimuli-responsive microgels [178], the one based on poly N-isopropyl acrylamide (PNIPAM) has received the most attention because they are thermo-responsive and undergoes swelling/deswelling with changes in temperature [179,180]. PNIPAM microgels can also be made responsive to pH by functionalizing them with acrylic acid groups (Aac), referred to as PNIPAM-co-Aac microgels [181]. PNIPAM based microgels find applications in various fields such as biological and chemical sensors, and optically active components [182–184]. The ordered structures of these PNIPAM based microgels offer tunable photonic properties and hence find applications in optical switches [170]. They are

biocompatible, and hence, are also useful in controlled drug delivery [185].

### 1.4.3.1 Thermo-responsive behavior of PNIPAM based Microgels

PNIPAM microgel particles dispersed in water show a decrease in their size with increase in temperature and undergo a transition from a swollen state to a collapsed state at around  $T \sim 34\text{ }^{\circ}\text{C}$ , which is known as volume phase transition temperature (VPTT) and the phenomenon is termed as volume phase transition (VPT) [186–188] (Fig. 1.7(a)).

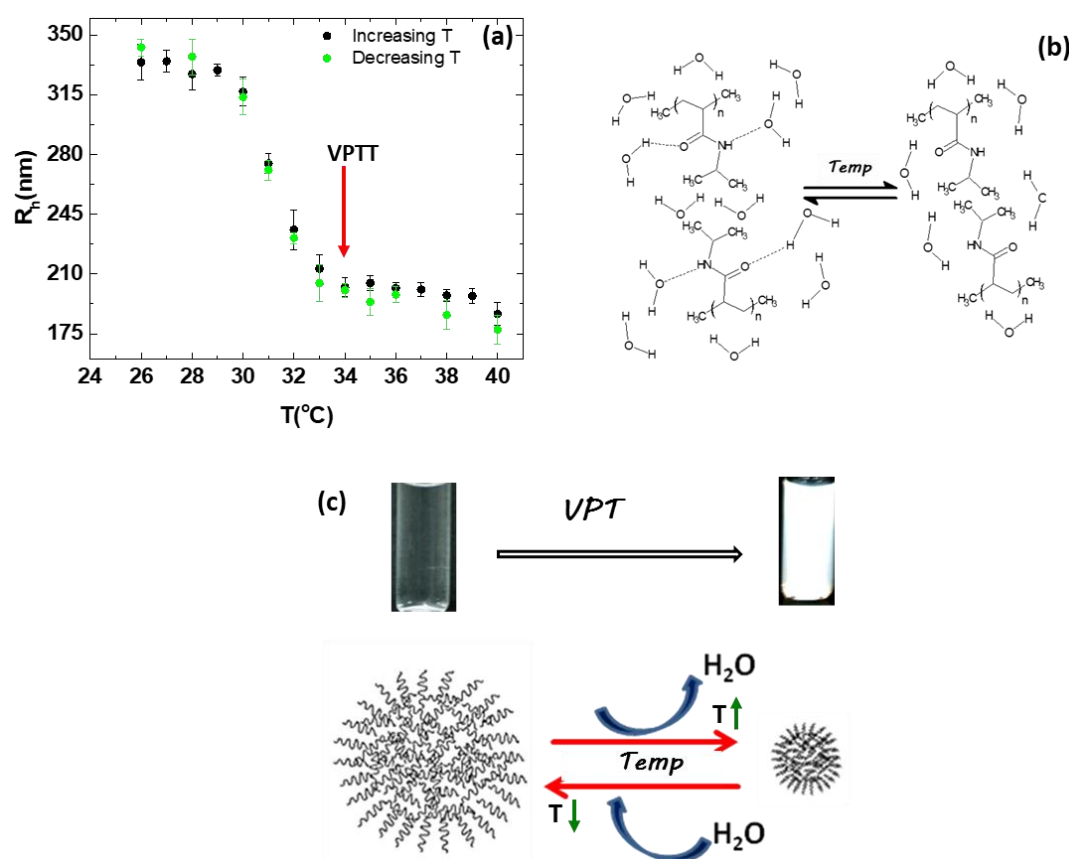


**Figure 1.7** (a) Variation of hydrodynamic radius,  $R_h$  of PNIPAM-co-Aac microgel particles with temperature  $T$ , (b) Schematics diagram of the chemical structure changes occurring across the volume phase transition for PNIPAM-co-Aac microgel, (c) Photograph of PNIPAM-co-Aac microgel suspension before and after VPT and schematic of individual PNIPAM-co-Aac microgel showing the transition from swollen (hydrophilic) to deswollen (hydrophobic) state and vice-versa.

The transition is reversible in nature. A schematic diagram of the change in the chemical structure before and after VPT is shown in Fig. 1.7 (b). Below VPT, the microgel particles are in hydrophilic state, the water molecules surrounding the polymer chains of the microgel forms hydrogen bond with the amide groups of the polymer chains. With the increase in temperature, these hydrogen bonds start breaking, and water molecules are expelled from the polymer chains, resulting in the deswelling of microgels [189,190]. In swollen state, PNIPAM microgels contain ~2 to 3% polymer and the rest is water, whereas, in the de-swollen state, these particles contain about 60% of the polymer and 40% of water [191]. The suspensions of PNIPAM microgels appear transparent (rich content of water) due to index matching with the surrounding solvent, i.e., water, and appears turbid (see Fig. 1.7(c)) upon VPT due to increase in polymer content, and hence, an increase in its refractive index.

#### **1.4.3.2 Internal Structure of PNIPAM Microgels**

PNIPAM microgel particles consist of about 2-3% cross-linked polymer chains, and the rest water [188]. The microgel particle polymer chains are cross-linked with each other either via self-cross-linking or by an external cross-linker [189], [190], to form a polymeric network type structure, which makes them soft, porous and permeable to external solvent molecules. The internal structure of a PNIPAM microgel particle was investigated using small angle neutron scattering (SANS) measurements [188], [191]. As studied by SANS, the radial polymer density profiles of the microgel particle at temperatures below VPT revealed a core-shell structure with a dense core and fuzzy shell of thickness ~20-30 nm (Fig. 1.8(a)) [192]. The polymer volume fraction at the central part of the particle is almost constant and decreases rapidly towards the periphery (Fig. 1.8(b)) [192]. The size of the microgel

as measured from SANS is less than that measured using dynamic light scattering (DLS), the hydrodynamic radius [191,192]. This is explained by the fact that the dangling polymer chains of the thin outer shell do not contribute to the scattered intensity in SANS measurement, but they do affect the microgel particle dynamics in the solvent, resulting in a higher value of radius as measured using DLS than in SANS measurements. The polymer density of the central core increases with increase in temperature, whereas the thickness of the outer shell remains unaltered [191]. The size of the core and the shell is decided by the cross-linker concentration during synthesis [193]. With the increase in cross-linker concentration, the total size of the particle decreases, but the size of the core relative to the size of the outer shell increases [193].

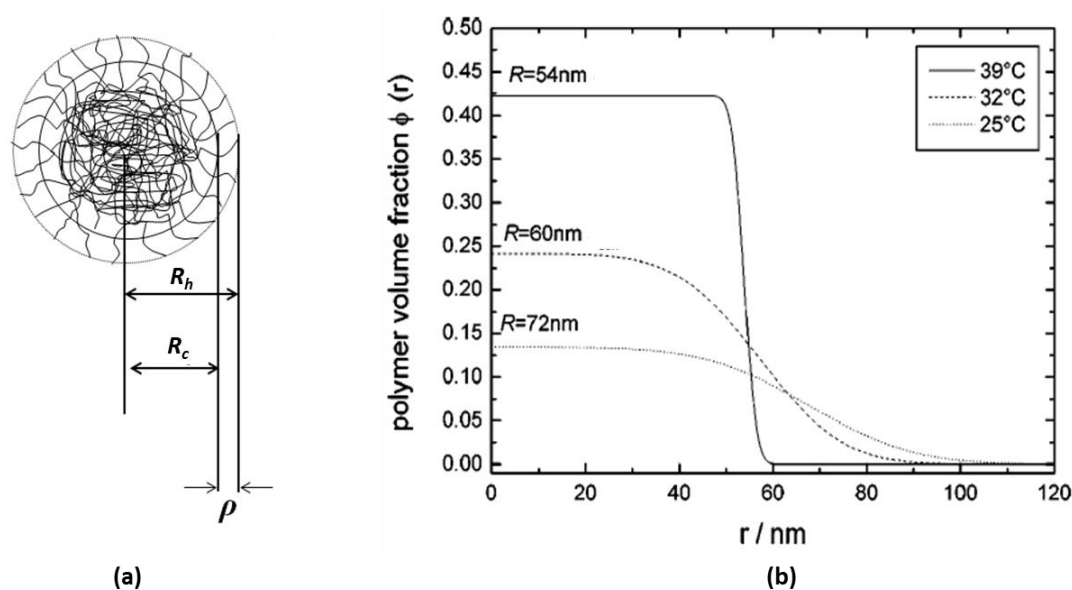


**Figure 1.8** (a) Schematic of the core-shell structure of PNIPAM microgel particle in the swollen state, with a core of radius  $R_c$  and shell of thickness  $\rho$ ,  $R_h$  is the hydrodynamic radius. (b) Radial polymer density profiles of PNIPAM microgel at various temperatures as measured using SANS, showing the increase of core thickness with increase in temperature,  $R$  indicating the distance where the core density is half of its value. (Adapted from Stieger et al. [193])

### 1.4.3.3 Phase Behavior of Neutral and Ionic Microgels

Poly N-isopropylacrylamide (PNIPAM) microgels colloidal dispersions possess a rich phase behavior compared to that of hard sphere colloidal dispersions, due to the tunability of their softness and temperature sensitiveness of the microgel size [194]. In such systems the interparticle interaction,  $U(r)$  among the microgel particles can be tuned by varying the temperature. At low temperatures (i.e.,  $T \ll VPT$ ), these microgel particles contain 97% water by weight [189]. Hence, the van der Waals force of attraction between the microgel particles is negligible due to close matching of the refractive index of microgels with the solvent (water), making the neutral microgel spheres stable in their swollen state [189]. As the temperature increases, the microgels shrink which leads to an increase in the polymer density in the individual microgels. This results in a significant increase in the van der Waals attraction between the neutral microgels, resembling that of strongly attractive colloids at higher temperatures beyond VPT.

Further, the neutral microgel suspensions of PNIPAM possess a core shell-like structure having a dense core and an external layer of polymer chains. The thickness of the external layer of polymer chains in these core-shell microgel is high enough to ensure negligible van der Waals force of attraction, making the suspension thermodynamically stable. Although an analytical form of the interparticle interaction potential is yet to be developed across the range of swelling to deswelling transition temperatures, there are several propositions predicting the interaction potential of these neutral microgels [195–197].

Wu *et al.* [196] proposed the effective interaction potential between the PNIPAM represented by a Sutherland-like function [196] and calculated the phase

diagram of neutral PNIPAM microgel suspension from turbidity measurements combined with thermodynamic perturbation theory as shown in Fig. 1.9 [196]. The phase diagram shows that the PNIPAM microgels exhibit phase transitions both above and below VPT. At low temperatures below the VPT, it exists as a liquid at low polymer concentration and transforms to a crystalline solid at high polymer concentration, resembling phase behavior of hard sphere colloids. At temperatures above VPT, it shows a phase separation, i.e., a metastable fluid-fluid equilibrium within a fluid-solid coexistence. The phase separation is driven by van der Waals attraction arising due to microgel de-swelling at high temperatures. However, Brijitta *et al.* [186] have shown experimentally that the PNIPAM microgel suspension exhibits crystallization at a much higher volume fraction compared to that of hard sphere colloids, which crystallize at volume fractions  $\sim 0.5$  to  $0.74$ . This suggests PNIPAM particles behave as soft spheres (i.e., the interparticle interaction is soft-sphere repulsive type) below VPT, as per the molecular dynamics simulations using the soft-sphere repulsive potential ( $U(r) \sim 1/r^n$ ) [198,199], which shows an increase of volume fraction at which crystallization occurs with an increase in softness. Further, Brijitta *et al.* [186] have also shown the existence of a fluid (liquid) to fluid (gas) transition below VPT of these microgels [186], without any change in the particle number density. However, there was no evidence of phase separation above VPT as predicted by Wu *et al.* [189].

The incorporation of charged groups into the neutral PNIPAM microgels leads to the formation of charged or ionic microgels with multi-responsive properties, which further respond to stimuli like pH, ionic strength in addition to temperature. Hence, they show further rich phase behavior compared to that of the neutral microgels and usual charged colloidal systems. In charged microgels, the interparticle

interaction can be tuned over a wide range by changing the Debye screening length, by changing particle concentration, charges, and the salt concentration. There are various reports predicting the phase behavior of charged microgels theoretically [200–202].

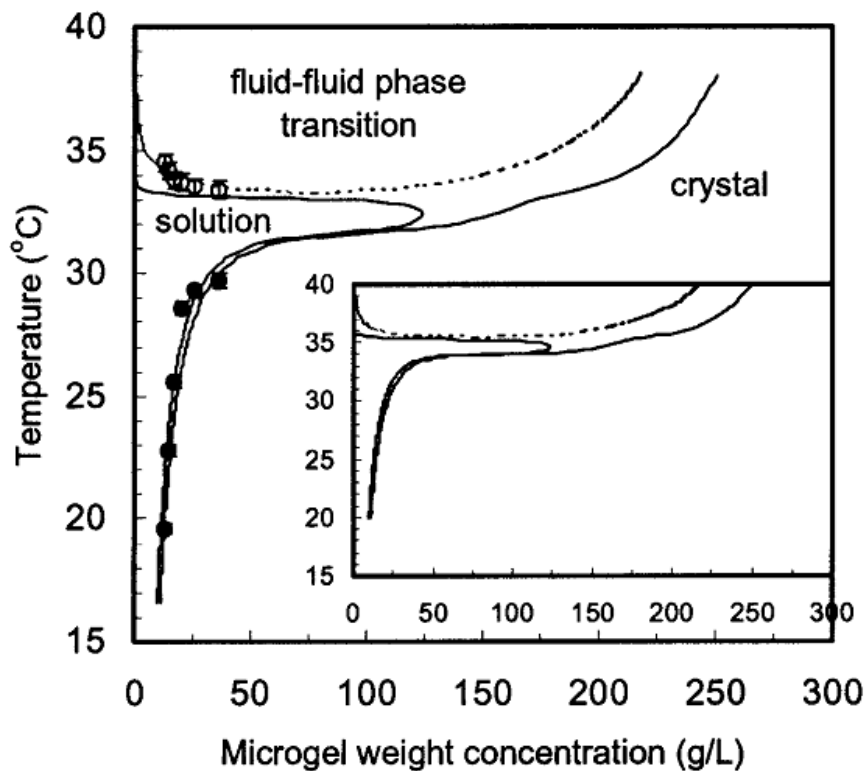


**Figure 1.9** Phase diagram of aqueous PNIPAM microgel dispersion determined from turbidity measurements (symbols) and thermodynamic perturbation theory with empirical temperature correction (lines), adapted from [189]. Inset shows the phase diagram predicted without any empirical temperature correction.

Gottwald *et al.* [200,201] predicted the phase diagram (charge vs. concentration) for ionic microgels by combining a genetic algorithm with accurate free energy calculations, as shown in Fig. 1.10. They proposed an effective interaction potential between spherical polyelectrolyte microgels to investigate the structure, thermodynamics, and the phase behavior of ionic microgel solutions. The phase diagram shows a fluid-FCC-BCC crystalline state at lower concentrations and a re-

entrant melting behavior at higher concentrations. At high concentrations and charges of microgels, hexagonal, body-centered orthogonal and trigonal crystalline structures are predicted to be stable in the phase diagram (Fig. 1.10). Experimental verification of these predictions of Gottwald *et al.* [200] for the phase behavior of ionic microgels is provided by Mohanty *et al.* [156] by studying the phase behavior of charged PNIPAM co-Aac microgels over a wide range of concentrations by using static and dynamic light scattering methods. They show that these microgel dispersions exhibit a short-range liquid order at low concentration, an FCC crystalline order at intermediate concentration and BCC-FCC coexistence at higher concentrations. However, at very high concentration, they observed a disordered state and confirmed it to be a glass, but could not prove whether the re-entrant disordered state is a liquid or glass as predicted by the theoretical simulations [200].

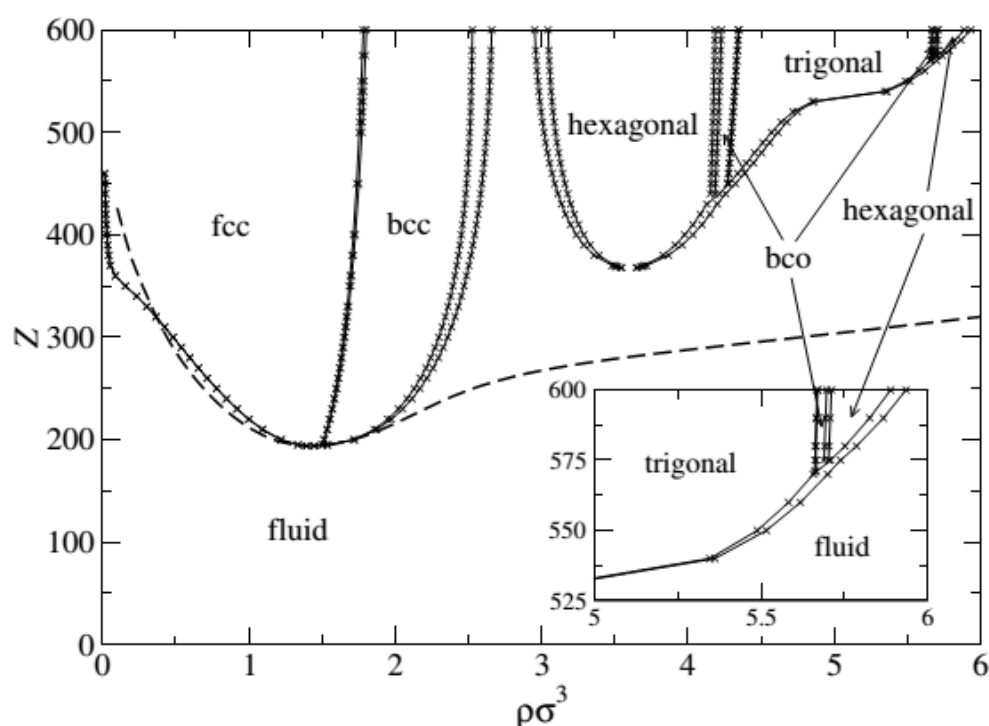


**Figure 1.10** Phase diagram of ionic microgels with diameter  $\sigma = 100$  nm, adapted from [200]. The crosses denote the calculated phase boundaries; lines connecting them are guide to the eye. The inset shows a high-density, high-charge region of the phase diagram in detail.

#### 1.4.3.4 Structure of PNIPAM and PNIPAM-based Microgel Crystals

The true inter-particle interaction potentials for PNIPAM microgel systems are still unknown, owing to the inhomogeneous structure and soft nature of PNIPAM microgels. Wu *et al.* [196] and Senff *et al.* [198] have shown that dense suspensions of monodisperse microgel particles exhibit crystalline ordering, by considering temperature-dependent interactions and soft interactions, respectively. The structure of PNIPAM microgel particle crystals investigated using scattering techniques [203] as well as confocal laser scanning microscopy CLSM [204] is found to be FCC. The crystal structure was determined by calculating the pair correlation function  $g(r)$  using the real space coordinates of the microgel particles obtained using CLSM.

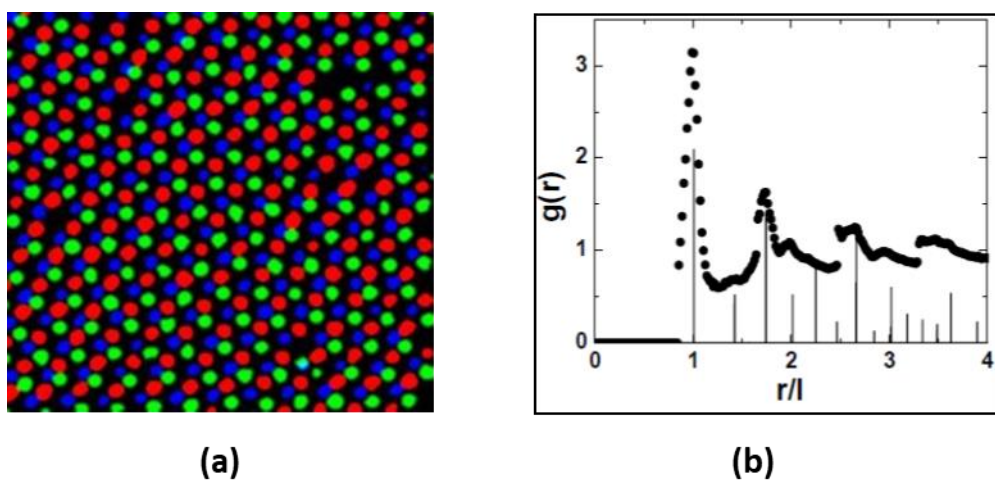


**Figure 1.11** (a) Micrograph showing an ABC type stacking obtained by overlaying three consecutive layers of PNIPAM microgel crystal obtained using CLSM. The micrograph shows an FCC structure (layer A-red, layer B-green, layer C-blue), (b)  $g(r)$  calculated for the structure in (a) shown as dark solid circle being compared with  $g(r)$  calculated for an ideal FCC structure, shown as lines. The experimental  $g(r)$  and the simulated one match very closely confirming the crystal structure to be FCC. (Adapted from Brijitta *et al.* [204])

The stacking sequence and stacking fault probability has been determined by overlaying three successive crystal layers in  $\langle 111 \rangle$  direction, which is assigned a

value 1 for ABC, BCA, and CAB stacking and zero for any other sequence. Fig. 1.11(a) shows the three successive layers overlaid showing ABC stacking in an FCC PNIPAM microgel crystal. The stacking probability of the annealed and cooled crystal was estimated to be 0.95, and the experimental  $g(r)$  was found to match with the simulated one, confirming the crystal structure to be FCC. SANS measurements also showed the crystallization of PNIPAM microgel crystals prepared with a wide range of cross-linker density, into an FCC structure.

### **1.5 Motivation for the Thesis**

Stimuli-responsive microgel suspensions feature an important phenomenon: in contrast to hard sphere suspensions, they respond to external stimuli and undergo swelling-deswelling transition and exhibit a rich phase behavior. PNIPAM microgel particles are temperature sensitive; they change their size with respect to temperature and undergo a volume phase transition (VPT) from swollen to a de-swollen state characterized by the transition temperature called VPTT [156]. The transition is reversible. PNIPAM-co-Aac microgel particles (co-polymerized with the acrylic acid group) also respond to pH in addition to temperature [177]. These microgels possess an inhomogeneous core-shell structure with a dense core and an outer loosely cross-linked thin shell ( $\sim 20\text{-}30$  nm) along with dangling polymer chains [192]. These microgels contain 2-3% polymer in their swollen state and rest water [191] and hence are closely index matched with water, making them an ideal probe for scattering techniques. Across VPT, these microgels collapse and suspensions of these microgels turn turbid. Dense suspensions of these microgel suspensions exhibit structural ordering (liquid-like, crystalline and glassy structure) similar to that of atomic systems. These microgels serve as model condensed matter system. Since, they are

stimuli-responsive and change their volume in response to various stimuli, which results in a change in the other physical parameters both associated at single particle level, and macroscopic level makes them an ideal system to understand phenomena crucial to science and technology [205].

To understand the macroscopic mechanics of microgel particles in suspension, it is essential prerequisite to first understand the mechanics of individual single microgel particle [205]. Successful interpretation of the measurements of the macroscopic behavior of the stimuli-responsive microgel systems in a meaningful way is possible only if the behavior of single microgel particle constituting the system can be experimentally accessed [205]. For example, applications of microgels, such as site-specific drug delivery, optical sensors, bio-sensing, smart coatings, environmental remediation and many other applications [178,182,206,207], require the exact understanding of the stimuli responsiveness due to various stimuli at the single particle level. The measurement of properties of sub-micron sized mesoscopic particles is a challenging problem. The forces involved in these measurements are of the order of pN (pico Newtons) for particles suspended in a liquid solvent. However, there are a few reports of measurements undertaken to probe the single particle physics using atomic force microscopy (AFM) on the microgels of PNIPAM, but they are difficult to carry out for many microgel systems [208,209]. This is where the technique of optical tweezers [28] stands out, and the ease with which it can probe the force of the order of pN is remarkable. Using optical tweezers, we can not only measure the forces but can visually observe their real-time dynamics, since they can be easily integrated with the microscopy systems. Optical tweezers is a tool that has been successfully used in various fields of research starting from biological sciences to interdisciplinary sciences [210], because of its unique ability to hold and

manipulate sub-microscopic particles in a non-invasive way and it can also be used in conjunction with various characterization tools.

With this motivation, we developed an optical tweezers set-up capable of trapping sub-microscopic particles stably in three dimensions. **Chapter 2** describes the building of basic optical tweezer set-up and the principle of its operation. The design considerations for building an optical tweezer and its extension to generate steerable optical traps are described. We have described trapping in various regimes and quantified the optical trap efficiency. The optical trap is calibrated by measuring the trap stiffness using optical potential analysis method and equipartition method. We showed the variation of trap stiffness with laser power to be linear confirming the calibration of the trap.

Optical tweezers use a tightly focused laser beam to trap and manipulate microscopic particles. In the tightly focused spot, either one or multiple particles can be trapped. However, many applications require trapping of multiple particles at different locations in two or three dimensions. To study the interaction between multiple particles, independent trapping and manipulation are needed. This is accomplished by the aid of a liquid crystal modulator called Spatial Light Modulator (SLM) along with the technique of digital holography in the optical manipulation system, called holographic optical tweezers (HOTs) [55]. With this motivation to create an array of traps and manipulate multiple particles and to study the interaction between the trapped particles and or biological cells, we have designed and developed a HOTs set-up. The details of the construction of the system and its operation are discussed in **Chapter 3** of this thesis. The success of HOTs depends on the efficient and uniform distribution of light among all the desired trapping sites. In general, these

liquid crystal modulators show a non-linear phase response [93,211], and it is a challenging task to optimize and calibrate the SLM for its phase modulation to generate efficient and uniform optical traps. There are several reports of calibration of SLM, but most of them describe SLM driven by peripheral component interconnect express (PCIe) interface [90,93,211,212]. In this thesis, we report the calibration of SLM driven by a digital video interface (DVI) through graphics for its non-linearity in the phase response behavior. We optimize the various parameters of graphics like brightness, contrast, and gamma to improve the diffraction efficiency and correct for the non-uniformity in the resolution with which the gray levels are addressed throughout the available phase levels. Further, the performance of SLM is degraded due to the varying phase response over its spatial regions (SVPR), which can be due to non-uniform thickness of SLM or can happen due to the non-uniform (Gaussian) illumination. There are various methods reported in the literature which correct for the SVPR, which are based on characterizing the SLM for its varying phase response by dividing the SLM into many subsections [95,96]. These methods are time-consuming, and frequent calibration with different power levels becomes difficult. We have demonstrated a simple technique to quickly calibrate the SLM for its SVPR by optimizing its brightness, contrast, and gamma of different subsections and show traps with improved uniformity, diffraction efficiency and trap quality. The generation of trap spots or any light distribution at the sample plane involves the creation of phase holograms, which are impressed upon the SLM to generate the desired pattern. The generation of holograms are done with various iterative algorithms [57], which require the input beam profile over SLM. In general, the input beam profile is taken as Gaussian centered at the center of SLM, which may not be true. In this thesis, we have reported a novel technique for determining the actual beam profile of the

incident laser beam by using a diffraction-based set-up [211]. Detailed methodology has been described in **Chapter 3** of this thesis.

As discussed previously, stimuli-responsive microgels change their size in response to stimuli such as temperature, pH, ionic strength, etc. In particular, PNIPAM microgels deswell with an increase in temperature leading to a collapse of size, characterized as VPTT and the process being termed as volume phase transition (VPT) [180]. In general, dynamic light scattering is the most popular technique to characterize the volume phase transition in response to various stimuli such as temperature, pH, and ionic strength [156,213]. Using DLS, one measures the variation of the microgel hydrodynamic diameter as a function of different stimuli, which requires particles of concentration  $\sim 10^7$ -  $10^8$  particles/cm<sup>3</sup> to satisfy the Gaussian distribution of the number of particles scattering light [214,215]. Size polydispersity of microgels makes DLS data analysis complex [216]. In homogeneous macrogels, the nature of VPT is shown to be of the discontinuous type, whereas inhomogeneous macrogels (i.e., inhomogeneity in polymer density due to varying cross-linker concentration) are shown to exhibit a swelling-deswelling transition in a continuous manner [217]. DLS measurements on PNIPAM microgels also shows a VPT of a continuous type [156]. Volume phase transition is the property of the polymer itself, and inhomogeneities in different microgels may in principle be different. Hence, it is required to measure the VPT on a single microgel particle. Applications like microgels in site-specific drug delivery [185] also require a clear understanding of the VPT and VPTT of individual microgel particles. In this thesis, for the first time, we report the characterization of VPT of PNIPAM-co-Aac microgels with temperature on a single particle using a home built optical tweezer set-up. We characterized the VPT of a single microgel by characterizing its trap stiffness under an optical trap as a

function of temperature and show it to be of a continuous type and compared with that measured using DLS technique [218]. The continuous nature of VPT is attributed to the presence of inhomogeneity within the microgel particle. The experimental results have been validated by numerical computation of trap stiffness as a function of particle size, and refractive index separately, and also together. The details of the experiment and the results obtained are discussed in **Chapter 4** of this thesis.

Dense suspensions of monodisperse thermo-sensitive PNIPAM microgel particles are known to crystallize into ordered structures, which are responsive to stimuli, known as responsive photonic crystals (RPCs). In addition to thermo sensitivity, these microgel particles (bulk modulus  $\sim$ kPa [219]) are known to undergo osmotic compression upon application of osmotic pressure [194,219] and hence a tunability in the photonic band gap and its optical properties. There are various reports of osmotic compression in dilute suspensions of PNIPAM microgels as studied using DLS by the addition of non-adsorbing polymer to the suspensions [194,219]. However, the effect of osmotic compression arising due to neighboring particles with an increase in concentration has not been investigated. Further, the colloidal suspensions of microgel systems possess various types of disorder due to shape and size polydispersity of the particles [156]. It has been demonstrated theoretically by Allard *et al.* [220] that the photonic band gap of these crystals is more sensitive to their particle size distribution than site randomness. The size and shape polydispersity in the particle forming the crystal plays an important role in determining the quality of photonic crystal [220–222]. In this thesis, we show the osmotic compression of the PNIPAM microgels due to increasing concentration of particles in suspension and also report for the first time that size polydispersity of microgel particles can be tuned by osmotic pressure [165]. We prepared suspensions of PNIPAM-co-Aac microgel

particles with varying particle concentration by subjecting them to different osmotic pressures and characterized them for various types of disorder using CLSM. We showed that osmotic compression significantly reduced the size polydispersity (SPD) leading to the appearance of crystalline order in a highly polydisperse suspension (33% as prepared), and thereby, a decrease in second type disorder. We found that SPD of colloidal particles destroys long-range positional order, but preserves orientational order in the crystal. Experimental details and results of the effect of osmotic compression on size and size distribution of microgels and hence disorder in the photonic crystals of the microgels are presented in **Chapter 5** of the thesis.

As prepared crystals of microgel particles are in general fragile, they lose their crystalline order even under small disturbances (shear  $\sim$ a few dynes/cm<sup>2</sup>), limiting their practical use [223]. Practical applications of these microgel crystals require them to be immobilized in a hydrogel matrix [167,224]. The gel-immobilized crystals of the microgel particles find a number of applications as optical filters [167], sensors [169,225], optical switches [226], etc. The process of immobilization of these PNIPAM microgel crystals involves the preparation of microgel crystal in a pregel solution followed by polymerization to form a hydrogel [224]. Since PNIPAM microgel particles have a porous core-shell structure [191,192,227], the polymerization is expected to happen both outside and inside the microgel particles. This may lead to the formation of an interpenetrating/entangled network of polymer chains between the microgel and the hydrogel [228] as shown by Song *et al.* [224] in swelling/ deswelling of PAAM hydrogel incorporated with PNIPAM-co Aac microgel particles. There are no studies of the effect of these entanglements on the dynamics of microgel particles in a hydrogel matrix and also the effect of temperature on the dynamics and photonic properties of these thermo-sensitive PNIPAM microgel

crystals. In this thesis, we discuss the effect of entanglements on the dynamics of gel-immobilized PNIPAM co-Aac microgels in PAAm hydrogel with temperature using 3D dynamic light scattering technique. We confirm the presence of entanglements between polymer chains of microgel and hydrogel through the study of their dynamics as a function of temperature. Further, we show the retention of crystalline order in the gel-immobilized crystals of these microgels at all temperatures across VPT using UV-visible spectroscopy. This is attributed to the entanglements between the microgel hydrogel composite, restricting the degree of thermal vibrations and hence the crystalline order. However, there is an increase in the structural disorder with temperature induced by the collapse of microgel particle in an entangled state, causing local lattice strain. A detailed study of the effect of entanglements between the polymer chains of microgel and hydrogel composite and their effect on structure and disorder are presented in **Chapter 6** of this thesis.

Finally, **Chapter 7** summarizes the work reported in this thesis and scope for future work.

## 1.6 Key Findings of the Thesis

- ✓ We have indigenously designed and developed an optical tweezer set-up capable of trapping microscopic particles stably in three dimensions. The optical traps are calibrated by measuring the trap stiffness by using two methods, (i) optical potential analysis and (ii) equipartition method. Confirmation of proper functioning of this set up is done by measuring the trap stiffness as a function of laser power and showing it to be linear. We have trapped multiple particles in ring geometry in a single optical trap.

- ✓ We have designed and developed a HOTS set-up capable of trapping multiple particles at desired locations.
- ✓ We have presented a methodology to calibrate SLMs driven by DVI interface graphics. We have developed a look up table that enabled us to obtain a linear phase response of the liquid crystals of SLM.
- ✓ We have presented a simple technique for quick calibration of SLMs suffering from spatially varying phase response (SVPR) and showed an overall diffraction efficiency improvement from 29% to 55% and improved uniformity from 76% to 97% after optimization of SLM. The SVPR correction also improved the trap quality up to 6.5%, as determined from spot sharpness metric calculation, resulting in an improved trap performance.
- ✓ A novel technique is presented for the determination of the laser beam profile incident over SLM as required by iterative algorithms generating holographic optical traps.
- ✓ We trapped polystyrene particles in an array of traps and presented a prescription for the same.
- ✓ Moreover, we have presented optical tweezers as a technique to characterize the VPT of stimuli-responsive microgel particles at the single particle level. The VPT characterized using optical tweezers are free from the effect of size polydispersity as compared to that of DLS where the analysis is affected by the size distributions. We characterized the presence of inhomogeneities at the single particle level.
- ✓ We have shown for the first time that osmotic compression not only reduces particle sizes but also the size polydispersities in the stimuli-responsive microgel photonic crystals of PNIPAM-co-Aac microgel particles.

- ✓ Thereafter, we have characterized the second type disorder and showed with osmotic compression, the disorder in these systems reduces, leading to highly diffracting photonic crystals. We also showed the presence of first-type disorder in these colloidal systems.
- ✓ Next, we have provided, the evidence of entanglements between polymer chains of microgel particles with the polymer chains of hydrogel medium in the immobilized hydrogels through a study of dynamics as a function of temperature.
- ✓ The immobilized microgel hydrogel composite are shown to retain crystalline order above VPT, and this is attributed to entanglements between the polymer chains of microgel and hydrogels, restricting the extent of thermal vibrations
- ✓ At last, we show that there is an increase in structural disorder with increasing temperature along with the retention of crystalline order. This is explained in terms of local lattice strain induced due to the collapse of microgel particles in an entangled state.



# DEVELOPMENT OF OPTICAL TWEEZERS

---

This chapter presents the physics of optical trapping and the details of an indigenously developed optical tweezers set-up, along with various calibration procedures adopted such as equipartition method, Boltzmann statistics method, etc. to calibrate the optical trap and also discusses the various factors affecting optical trap efficiency. It further demonstrates the use of a single beam spot to trap a multitude of particles in a ring pattern.

### 2.1 Introduction

Optical tweezer, a tightly focused laser beam capable of holding and manipulating microscopic objects has become an indispensable non-destructive tool since 1986 [229,230]. Due to its ability of non-invasive probing at the mesoscopic scale and manipulation capability with nanometer accuracy, it finds applications in various fields of research such as colloidal transport, organelle transport within the cells, mechanical properties of biological cells, mechanics of cell membranes, as optical spanner for rotating individual biomolecules and various studies at single particle level [117,136,145,218,231–239]. In 1970 Arthur Ashkin discovered the process of optical trapping using lasers. He demonstrated that optical forces are capable of displacing and levitating microscopic dielectric particles of masses  $\sim$  picograms in either water or air, which led to the development of the first counter-propagating optical trap [240]. Eventually, this led to the development of single-beam gradient trap, known as an optical tweezer.

## 2.2 Physics of Optical Trapping

A laser beam tightly focused using a high numerical aperture (N.A.) objective capable of holding a microscopic particle stably in three-dimensions is referred to as an optical trap. A dielectric particle near the focused beam experiences a force due to the momentum transfer of scattering photons. The forces can be split into two components: (i) a scattering force ( $F_{scatt}$ ) acting in the direction of the incident laser, which pushes the particle away from the focus of the laser (Fig. 2.1) and (ii) a gradient force ( $F_{grad}$ ) that arises due to the gradient in laser intensity and pulls the particle from a region of low intensity to a region of high intensity, i.e., towards the focus of the laser.

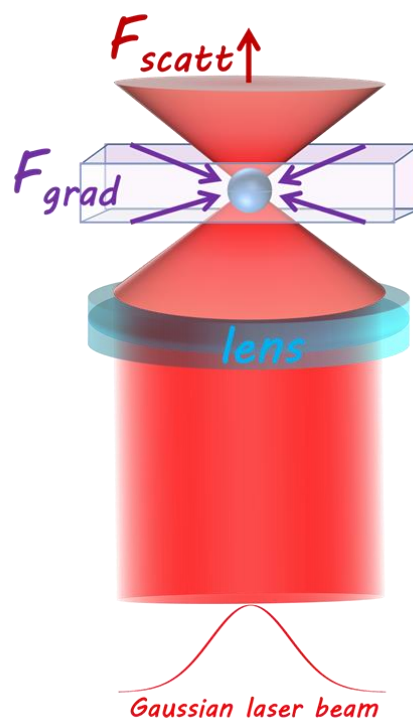


**Figure 2.1** Schematics of a Gaussian laser beam focused using a high numerical aperture (N.A.) objective to create a diffraction-limited spot at the trapping plane capable of trapping microscopic particles stably in three dimensions.  $F_{scatt}$  pushes the particle away from the focus in the direction of the incident laser beam, and  $F_{grad}$  pulls the particle towards the region of high intensity, i.e., towards the focal spot.

For stable trapping in all three dimensions, the axial gradient component of the force pulling the particle towards the focus must be greater than the scattering force pushing the particle away from the focus. This requires a tight focusing of the laser to a diffraction limited spot, which is achieved by the use of high N.A. objectives. The balance between the scattering force and the axial component of gradient force is obtained slightly below the focal point, and for small displacements, the gradient force is proportional to the displacement from the equilibrium position, i.e., the force is Hookean in nature.

The theory of optical trapping can be treated in three different regimes, depending upon the size of the microsphere to be trapped, relative to the wavelength of the light used to trap it, which is discussed in the following three sections.

### 2.2.1 Rayleigh regime ( $d \ll \lambda$ )

When particle sizes are smaller than the wavelength of light, the particles are treated as induced point dipoles immersed in the optical field that interacts with the applied field. Optical forces arise due to dipole-field interactions and can be calculated in the limit of Rayleigh approximation. There are two kinds of forces which come into play and can be readily separated into two components in this approximation: (i) a scattering force which arises due to the absorption and re-radiation of light by the induced dipole [241,242], which is given by

$$F_{scatt} = \frac{I_0}{c} \frac{128\pi^5 R^6}{3\lambda_0^4} \left( \frac{m^2 - 1}{m^2 + 2} \right)^2 n_m \quad (2.1)$$

where  $I_0$  is the incident intensity of the laser and  $R$  is the radius of the particle trapped,  $c$  is the speed of light,  $n_m$  is the refractive index of the medium in which the particle is

suspended, and  $m$  is the relative refractive index defined as the ratio of the refractive index of particle to the refractive index of the medium, i.e.,  $m=n_p/n_m$ . (ii) a force arising due to intensity gradients known as the gradient force,  $F_{grad}$ , is directed towards the beam focus and is given by [243]

$$F_{grad} = -\frac{n_m}{2}\alpha\nabla E^2 = -\frac{n_m^3 R^3}{2}\left(\frac{m^2-1}{m^2+2}\right)^2\nabla E^2 \quad (2.2)$$

where  $\alpha$  is the particle's polarizability, and  $E$  is the incident electric field. These two forces act in opposite directions. In order to achieve a stable optical trap, the ratio of the gradient force to the scattering force must be greater than unity. Increasing the laser power increases the scattering force, whereas a gradient in intensity is achieved by using high N.A. objectives, which focuses the light into a tight focal spot, and hence leads to an increase in the gradient force required for stable optical trapping. It may also be noted that, in the Rayleigh regime, the scattering force,  $F_{scatt}$  is proportional to  $R^6$ , whereas the gradient force  $F_{grad}$ , is proportional to  $R^3$ , implying that  $F_{scatt}$  decreases faster than  $F_{grad}$  as the size of the microsphere to be trapped decreases.

### 2.2.2 Ray (Geometrical) optics regime ( $d \gg \lambda$ )

When the diameter of the scattering object to be trapped is much larger than the wavelength of the light used for trapping, the scattering becomes independent of the wavelength, and hence in this regime, the diffraction effects can be neglected [244]. In this case, light propagation can be considered as a bunch of individual rays, each having characteristics of a plane wave with their respective intensities, direction, and polarization, propagating in a given medium.

A qualitative description of optical trapping in geometrical optics limit is illustrated in Fig. 2.2 and Fig. 2.3 below. Consider a dielectric particle of refractive index  $n_2$  suspended in a medium of a lower refractive index  $n_1$  than the particle, near a tightly focused Gaussian laser beam, created by a high N.A. lens (Fig. 2.2). Let the particle be laterally shifted by a certain distance from the axis of the beam propagation direction. In the ray optics limit, let us assume the incident Gaussian laser beam as a bunch of rays with their intensity maximum at the central optical axis, and

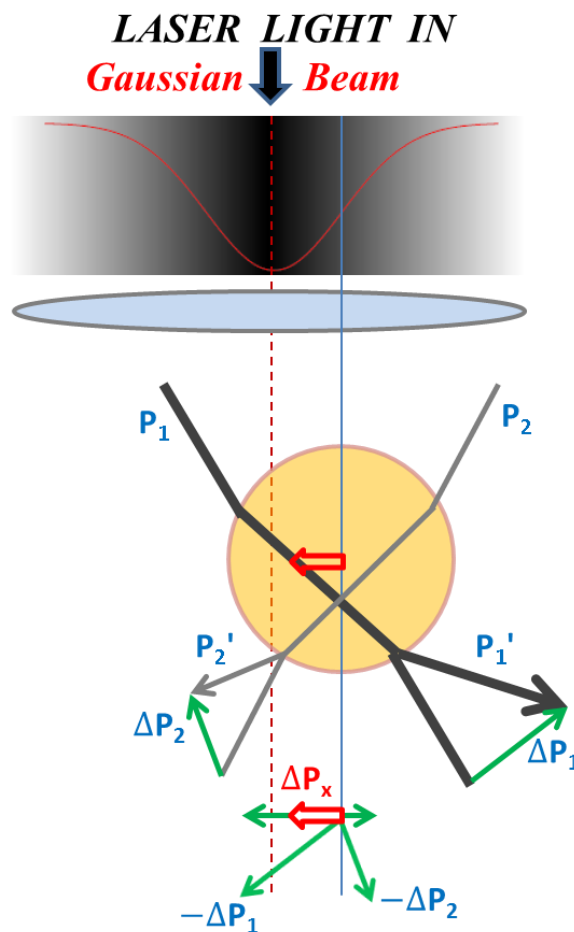


**Figure 2.2** Illustration showing the trapping mechanism for a spherical particle laterally shifted away from the focus of the Gaussian beam in the ray optics regime by considering the incident focused beam as a bunch of rays. The mechanism of trapping explained by considering two of the rays one high intense and the other low intense ray suffering the change in momentum per second due to refraction and a net force pulling the particle towards the focus of the laser beam.

decreasing in a Gaussian fashion away from the optic axis. Out of all these rays, consider two rays 1 and 2 passing through the sphere, with their corresponding momenta per second  $P_1$  and  $P_2$  (Fig. 2.2), one ray from near the axis, shown as bold thicker ray, and the other slightly away from the axis, shown as a thinner ray, representing their corresponding intensities. As these rays pass through the sphere of high refractive index, they get refracted inside and exit from the sphere by bending away from the normal to the sphere at the medium interface and suffer a change in momentum; the spherical particle, in turn, experiences a recoil, i.e., a change in momentum in the opposite direction of that suffered by the rays of light. The resultant change in momentum per second of the sphere due to refraction of these two rays is found to have a component towards the beam focus as shown in Fig. 2.2 by a red arrow pointing towards the focus of the beam on the optic axis from the center of the sphere, i.e., the particle feels a pull from a less intense region to a high intense region of the laser. This is known as the gradient force responsible for the trapping of the microscopic particles. The total force is calculated by summing the contribution due to all rays passing through the sphere. We neglect the surface reflections of the incident rays since only the refracted rays contribute to the gradient force and in the present case, we are only concerned about a qualitative picture of the optical trapping phenomenon. Similarly, Fig. 2.3 shows the case of a spherical particle with particle center displaced below and above the focus. A similar treatment shows that for a particle with its center below the beam focus (Fig. 2.3 (a)) the net force acts upwards, whereas the net force acts downwards for a particle whose center is above the beam focus (Fig. 2.3 (b)). The particle does not experience any force when its center coincides with the focus of the laser beam, which is the position of stable equilibrium and a slight arbitrary displacement of the particle induces restoring forces acting on it

to bring it back to the focal centre of the beam. The same qualitative principle of refraction of light applies for the case of trapping of arbitrary shaped objects of size much larger than the wavelength of the trapping laser [245,246].

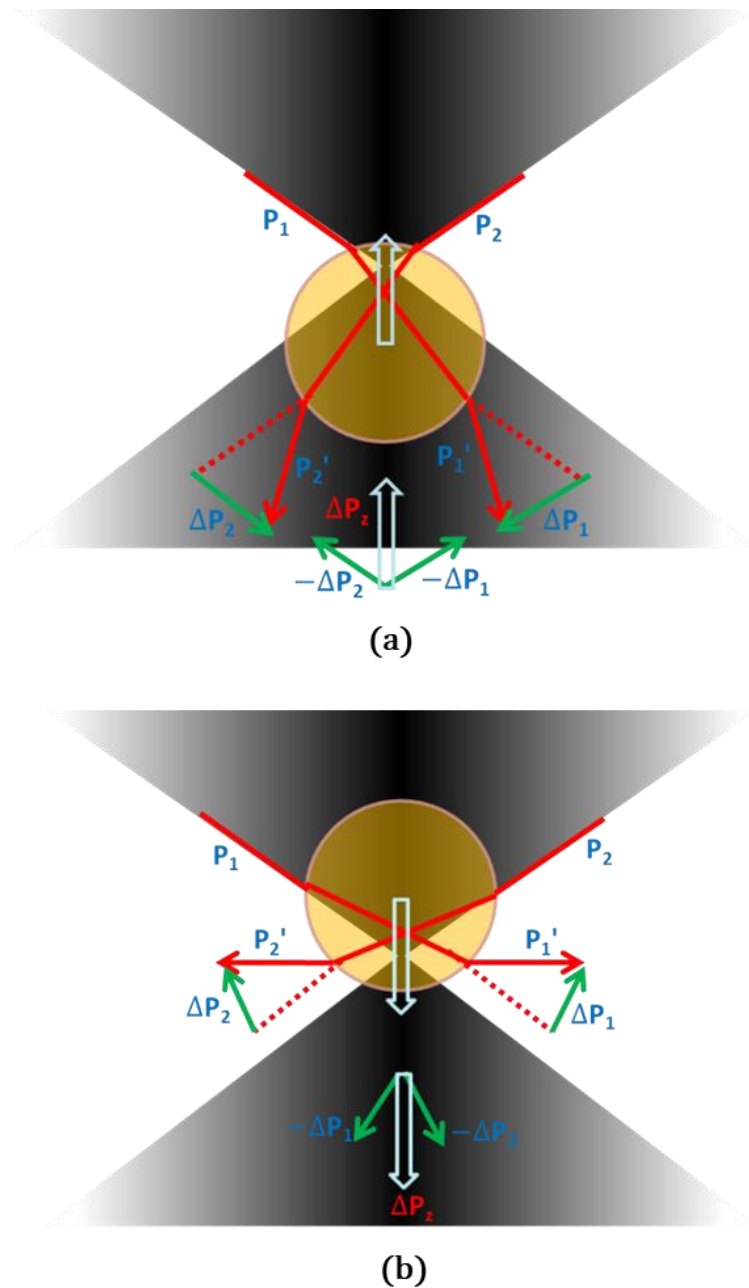


**Figure 2.3** Illustration showing the trapping mechanism for a spherical particle (a) with particle centers below the focus and (b) with particle center above the focus of the tightly focused Gaussian beam in the ray optics regime. The mechanism of trapping explained by considering two of the refracting rays suffering the change in momentum per second due to refraction and a net force pulling the particle towards the focus of the laser beam.

### 2.2.2.1 Scattering and Gradient Forces

The first quantitative description of the scattering and gradient forces in a single-beam gradient trap was given by Wright *et al.* [234] using the Gaussian mode beam propagation formula to describe a focused trapping beam. But the applicability of the model was limited to focused beams with small convergent angles of maximum 30°. The model fails to provide an accurate description for traps created using high N.A. objectives as pointed out by Ashkin *et al.* since the wave description of focused beams thus generated using high numerical aperture (N.A.) objectives are much more complex compared to the ones described by the Gaussian beam formula. A quantitative approach for high angle convergent beams used in the case of optical trapping experiments was applied to the single beam gradient trap by Ashkin [247] based on the works of Roosen [16,27] to quantify the forces responsible for optical levitation in the ray optics regime.

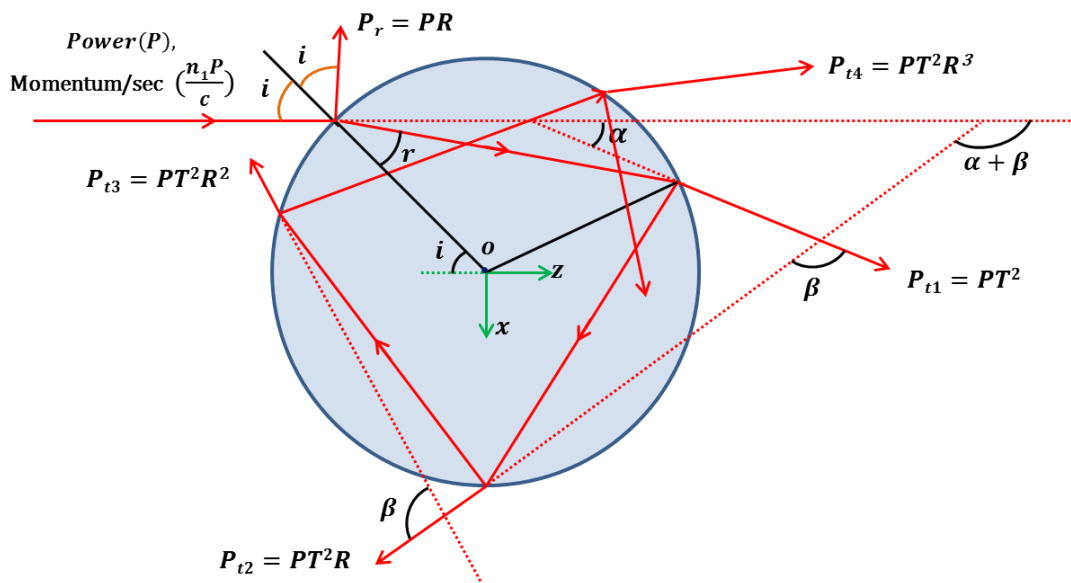


**Figure 2.4** Geometry of the scattering of a single incident ray of power  $P$  on a dielectric sphere visualized in the plane of incidence with reflected ray and an infinite set of refracted rays, considered while calculating the forces in ray optics regime. Here  $i$  is the angle of incidence and  $r$  is the angle of refraction.

The geometry used to calculate trapping forces on a spherical particle of diameter  $d \gg \lambda$  is illustrated in Fig. 2.4. Consider a single ray of power  $P$  entering the dielectric sphere at an incidence angle  $i$  with an incident momentum per second  $n_1 P/c$ ,  $n_1$  being the refractive index of the surrounding medium. A part of the incident ray gets reflected with power  $P_r = PR$ , while most of the power is transmitted with infinite number of refracted emergent rays of successively decreasing power  $P_{t1} = PT^2$ ,  $P_{t2} = PT^2R$ ,  $P_{t3} = PT^2R^2$  and so on, until all light has escaped from the dielectric sphere. The quantities  $R$  and  $T$  are the Fresnel reflection and transmission coefficients, respectively, at the surface of angle of incidence  $i$ . The total force acting on the dielectric sphere due to this single ray is given as

$$F_{tot} = \frac{n_1 P}{c} \hat{r}_i - \frac{n_1 P_r}{c} \hat{r}_r - \sum_{m=1}^{\infty} \frac{n_1 P_{t,m}}{c} \hat{r}_{t,m} \quad \text{due to a single ray} \quad (2.3)$$

where  $\hat{r}_i$ ,  $\hat{r}_r$ ,  $\hat{r}_{t,m}$  are the unit vectors in the direction of the incident ray, the reflected ray and  $m$ th emergent rays, respectively.

Eq. (2.3) expressing the total force can be split into two components, one component in the direction of the incident ray ( $\hat{r}_i$ ) called the scattering force  $F_s$  that pushes the particle away from the focal spot, i.e., in the direction of ( $\hat{r}_i$ ) and the other in a direction perpendicular to the incoming ray ( $\hat{r}_\perp$ ) as,

$$F_{tot} = F_s \hat{r}_i + F_g \hat{r}_\perp \quad (2.4)$$

Dividing the scattering force ( $F_s$ ) and ( $F_g$ ) by the quantity  $\frac{n_1 P}{c}$ , the incident momentum per second, a dimensionless parameter known as the *trapping efficiency* can be defined as,

$$\begin{aligned}
 Q_s &= \frac{c}{n_1 P} F_s, \\
 Q_g &= \frac{c}{n_1 P} F_g, \\
 \text{and } Q_{tot} &= \sqrt{Q_s^2 + Q_g^2}
 \end{aligned} \tag{2.5}$$

where  $Q_s, Q_g$  and  $Q_{tot}$  are the trapping efficiencies associated with the scattering force, gradient force and the total force respectively.

The scattered rays as in Fig. 2.4 make angles  $\pi+2i, \alpha, \alpha + \beta, \dots, \alpha + n\beta, \dots$  respectively, with the incident ray direction. The total force in the z-direction, i.e., in the direction of incident ray acting on the sphere due to scattered rays is given as [247]

$$F_z = \frac{n_1 P}{c} - \frac{n_1 P R}{c} \cos(\pi + 2i) - \sum_{n=0}^{\infty} \frac{n_1 P}{c} T^2 R^n \cos(\alpha + n\beta) \tag{2.6}$$

Similarly, in Y-direction, the force is given as,

$$F_z = 0 - \frac{n_1 P R}{c} \cos(\pi + 2i) - \sum_{n=0}^{\infty} \frac{n_1 P}{c} T^2 R^n \cos(\alpha + n\beta) \tag{2.7}$$

Eq. (2.6) and (2.7) can be rewritten as [16,247],

$$F_s = \frac{n_1 P}{c} \left\{ 1 + R \cos 2i - \frac{T^2 [\cos(2i - 2r) + R \cos 2i]}{1 + R^2 + 2R \cos 2r} \right\} \tag{2.8}$$

$$F_g = \frac{n_1 P}{c} \left\{ R \sin 2i - \frac{T^2 [\sin(2i - 2r) + R \sin 2i]}{1 + R^2 + 2R \cos 2r} \right\} \tag{2.9}$$

Eqs. (2.8) and (2.9) give the exact expression for the scattering and gradient force component for a single incident ray. To calculate the total force, the contribution

due to each of the rays depending upon the shape of the trapping beam used for generating single beam gradient trap has to be added vectorially. Further, the forces are polarization dependent through  $R$  and  $T$  for rays polarized parallel and perpendicular to the plane of incidence. The gradient force is conservative in nature since it can be expressed solely as a function of the radial distance from the ray to the particle. It also implies that the gradient force for an arbitrary collection of rays corresponding to different beam profile is also conservative. On the other hand, the scattering force is not conservative.

The magnitude of the total force  $F_t$  is given by,

$$\begin{aligned} F_t &= \sqrt{F_s^2 + F_g^2} \\ &= Q \frac{n_1 P}{c} \end{aligned} \quad (2.10)$$

The dimensionless parameter trapping efficiency  $Q$  gives an idea of the maximum radiation pressure which can be derived from a ray of momentum per second  $\frac{n_1 P}{c}$ , with a maximum value of 2 in the case of a ray reflected off a mirror. It is found that the  $Q$  corresponding to gradient force  $Q_g$  grows much faster than the  $Q$  associated with the scattering force,  $Q_s$  with an increase of the angle of incidence, implying maximum trapping efficiencies for rays incident at higher angles. Hence, highly convergent laser beams produced using high N.A. objectives produce large number of rays incident at higher angles and hence increase the trap stability. It is also interesting to note that these  $Q_s$  are independent of the particle size in the ray optics regime.

### 2.2.3 Intermediate regime ( $d \sim \lambda$ )

When the particle size is comparable to the wavelength of light used for trapping, optical forces are calculated using the Mie theory [248]. Using a simplified Mie theory [249,250], the gradient force in the plane  $z=0$  is given by [250]

$$F_{grad}(r) = \alpha I_0 \omega^2 A(\varepsilon) e^{-\left(\frac{r^2}{2\omega^2}\right)} \left[ \sinh\left(a_c \frac{r}{\omega}\right) \right] \quad (2.11)$$

where  $\alpha = \frac{\varepsilon_p}{\varepsilon_m} - 1$ ,  $\varepsilon_p$  is the dielectric constant of the particle and  $\varepsilon_m$  is the dielectric

constant of the medium in which particle is dispersed.

$$A(\varepsilon) = 4\pi \varepsilon \operatorname{erf}\left(\frac{a_c}{\sqrt{2}}\right) \operatorname{erf}\left(\frac{a_c}{\varepsilon\sqrt{2}}\right) e^{-\frac{a_c^2}{2}} \quad \text{with } a_c = \frac{r_0}{\omega} \left(\frac{\pi}{6}\right)^{1/3} \quad (2.12)$$

where the Gaussian laser beam is approximated as

$$I = I_0 \exp\left(-\frac{r^2}{2\omega^2} - \frac{z^2}{2\omega^2 \varepsilon^2}\right) \quad (2.13)$$

where  $\omega$  is the radius of the beam waist,  $r$  and  $z$  are cylindrical coordinates and  $\varepsilon$  is the eccentricity of the focal volume in the axial direction.

## 2.3 Factors affecting the optical trap efficiency

The different factors affecting the trap stiffness are as follows:

### (i) Numerical Aperture

High numerical aperture objectives tightly focus the laser beam into a diffraction-limited spot. Trapping efficiency is a measure of the amount of radiation

pressure, which can be extracted from a ray of momentum per second  $\frac{n_1 P}{c}$ . With the increase in N.A., higher angle rays are brought to the trap focus, which in turn increase the gradient force and hence, the trapping efficiency associated with the gradient force leading to a stable trap.

### (ii) Size of the microsphere

From Eq. (2.1) and (2.2), it is clear that with increase of particle size the scattering force and the gradient force increases, and hence the associated optical trap efficiency also increases up to the Rayleigh limit, after which  $Q$  becomes a constant independent of the particle size, as discussed in the ray optics regime of trapping [251].

### (iii) Depth of trapping position

The trap efficiencies decrease steadily as a function of depth, and eventually, after a certain distance, the particle can no longer be trapped. The decrease in  $Q$  is due to the increase in the spherical aberration as we move into the sample, due the use of high N.A. objectives. This is overcome by the using immersion oil of a different refractive index to reduce the mismatch between the objective and the coverslip [252].

### (iv) Laser beam Polarization

Polarization of the laser beam plays an important role in determining the  $Q$  in the direction of polarization and perpendicular to it. It is found that moving the particle in the direction perpendicular to the laser beam polarization results in a force of up to 20% lower compared to that of motion parallel to the polarization direction [232]. The difference in the lateral trap stiffness in the two orthogonal directions, one

along the polarization and the other perpendicular to it, depends on the size of the microsphere trapped [253]. This problem is avoided by converting the beam into a circularly polarized beam.

(v) **Ratio of Beam radius to the Aperture radius**

The optical trapping force is directly dependent on the laser power used. The power of the laser beam at the trapping plane decreases as the radius of the beam entering the objective back aperture increases, leading to a low stiffness. However, at the same time, beam radius of very small size increases the scattering force more compared to the gradient force, leading to a decrease in  $Q$ . Hence the laser beam should slightly overfill the objective back aperture, i.e., by 1.2 times the diameter of the objective back aperture.

## 2.4 Optical Tweezers Set-up

We have designed and developed an optical tweezers set-up for trapping experiments, by coupling an Nd-YAG fiber coupled laser (wavelength 1064 nm, TEM<sub>00</sub>) to an

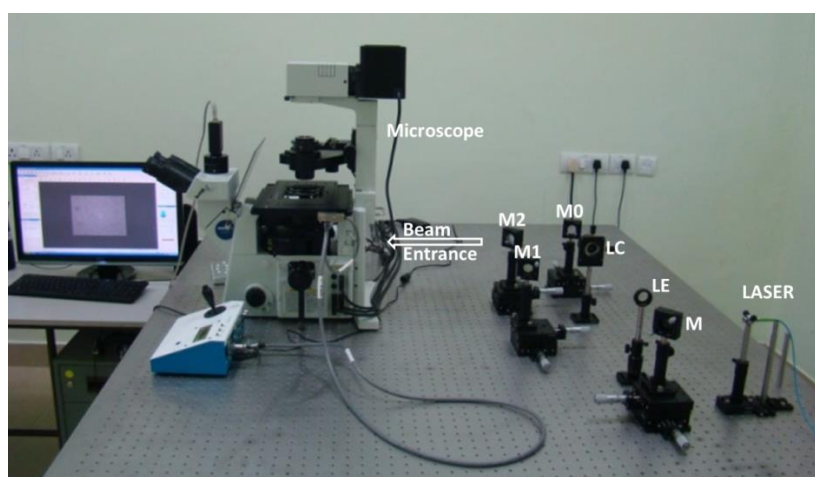


**Figure 2.5** Photograph of the home-built optical tweezers set-up, built around a commercial inverted microscope OLYMPUS IX 81. M, M0, M1, M2 are (>99%) reflecting mirrors, LE and LC are the beam expander lenses.

inverted microscope (OLYMPUS IX81) through a set of optical components as shown in Fig. 2.5.

### **2.4.1 Design Considerations**

#### **(a) Trapping Laser**

The trapping laser is an Nd-YAG fiber coupled laser from Manlight (France) with an output power of 10 W, delivering a linearly polarized, single mode output (typically TEM<sub>00</sub> Gaussian mode) at 1064 nm.

Typically, the power required at the trapping plane for stably trapping sub-microscopic objects are of the order of a few milliwatts, hence a laser with an output power of about 10 to 100 mW is sufficient to generate an optical trap, considering the losses caused during propagation through various optical components and the microscope objective. The choice of the high power is made keeping in mind the extension of the optical manipulation system into a holographic optical tweezer system, which employs a spatial light modulator and other optical components causing more losses compared to the optical tweezers.

The fiber coupled delivery of the laser helps in isolating the laser and the immediate region of the optical trap from the noise and the heat produced by the laser power supply. The choice of 1064 nm laser wavelength is made in order to avoid potential photo damage to biological cells to be used in trapping experiments and to minimize the absorption by the typically aqueous medium in which the samples are dispersed to prevent local heating [254,255].

The mirrors used in this set-up to reflect the laser beam are all dielectric mirrors with an appropriate coating to reflect  $> 99\%$  of the incident light. All lenses are achromatic doublets with antireflection coating for 1064nm.

### **(b) Microscope and Objective**

The microscope used in this set-up is an inverted bright field optical microscope from OLYMPUS (IX 81). A high N.A. oil immersion objective 100X (N.A. 1.4) is used to focus the input laser light to a diffraction-limited spot. The transmittance of the objective for 1064 nm is  $\sim 40$  to 45%. The high numerical aperture of this lens entails bending of wide-angle rays to improve the trap efficiency. The input laser is directed towards the objective by an 850 short-pass dichroic mirror inside the turret of the microscope, which reflects the trapping beam towards the microscope objective and allows simultaneous imaging by allowing the white light used for imaging towards the CCD detector. The CCD camera (Basler Scout, scA 640-120fm) used for imaging of the trapped particles is mounted on the trinocular port of the microscope, capable of imaging at a frame speed of 100fps. The microscope is equipped with a motorized sample stage (ASI Imaging) to mount samples for trapping experiments. The motorized stage allows movement of the sample in steps of 100 nm. This allows in bringing the required object to be trapped near the focused trapping spot and relative movement of the trapped object with respect to its surroundings as if required.

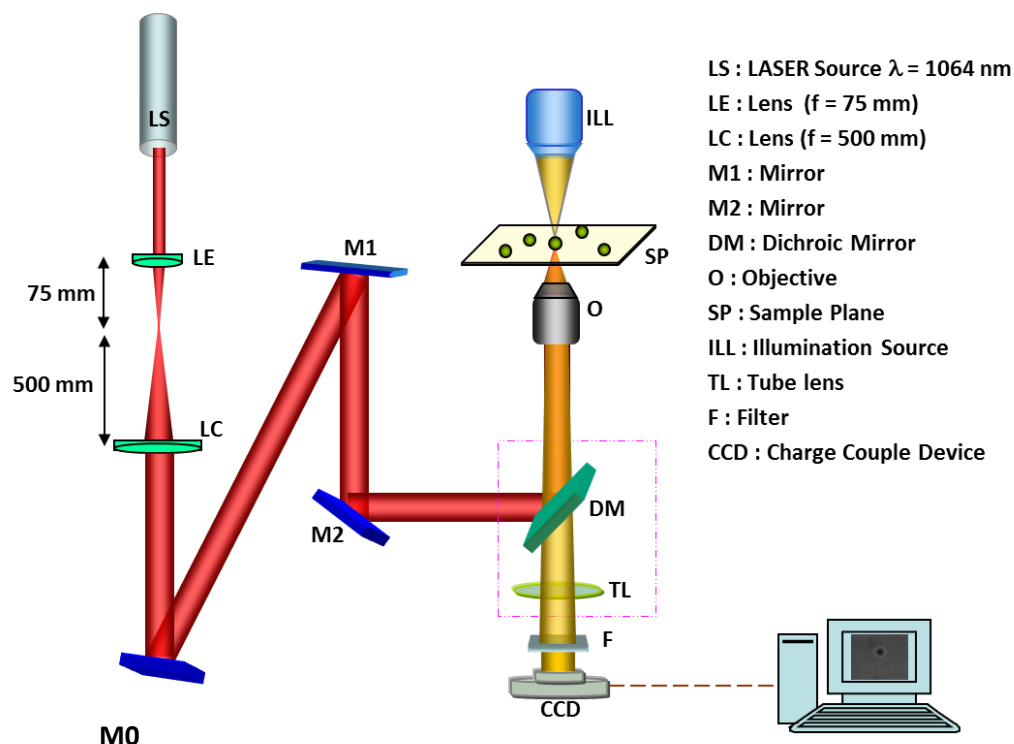
### **(c) Laser Beam Coupling to Objective Back Aperture**

Fig. 2.6 shows the schematics of the optical layout of our optical tweezers set-up. The design considerations in obtaining a stable optical trap at the trapping plane are as follows. First, the laser beam is expanded by a pair of lenses LE and LC in 4f

configuration to slightly overfill the back aperture of a high N.A. ( $\sim 1.4$ ) 100X objective to produce a tightly focused beam at the focal plane capable of trapping submicron- to micron-sized colloidal particles in three dimensions. The laser beam is first aligned with the center of the mirror M0. Then LE is placed on the optical path and aligned in the XY plane perpendicular to the direction of propagation to ensure the laser beam is still centered with the center of the mirror M0. In the next step LC is kept at a distance equal to sum of the focal lengths of LE and LC and aligned in a similar way in the transverse plane so as to ensure we have a beam expanded by a factor equal to the ratio of the focal lengths of LC and LE, and aligned with the center of the M0. The expanded laser beam is reflected off two mirrors M1 and M2 and then coupled to the back port of the microscope. M1, and M2 are steering mirrors required for centering and tweezing of focused light in the trapping plane. These mirrors allow for aligning the laser beam at the back port of the microscope objective by shifting them laterally in XY plane (Objective back aperture plane), without adding any angle of incidence at the input of the back aperture. This enables the creation of an aberration-free diffraction limited spot, which can be translated in the sample plane (required for beam tweezing) by maintaining the beam profile throughout the sample plane. The working of the steering mirrors is explained in Fig. 2.7. Figs. 2.7 (a) and 2.7 (b) describe the procedure of aligning the beam to center in a given direction. Two pinholes P1 and P2 are used for this purpose. First M1 is rotated to align the laser pass through P1 placed close to M2, then M2 is rotated in order to center the beam that passes through P2 kept at a larger distance from P1. This procedure allows for aligning the beam center in a given direction in line with P1 and P2.

As shown in Fig. 2.7 (c) the two mirrors M1 and M2 rotated by the same angle  $\theta$  in a clockwise direction shift the laser beam laterally parallel to the original

direction of the laser beam. Similarly, the rotation of these mirrors anticlockwise by the same angle will shift the laser beam parallelly downward.



**Figure 2.6** Schematics of the optical layout of the optical manipulation system. The lenses LE and LC expand the laser beam to a diameter equal to the ratio of their focal lengths. The expanded laser beam is reflected off two steering mirrors (M1) and (M2) and coupled to the microscope objective (O) through a dichroic mirror (DM) to produce tightly focused diffraction limited spot at the sample plane (SP). The trapped particles are imaged by a CCD detector placed at the trinocular port of the microscope.

The steering procedure is shown in a plane, but since the mirrors used are kinematic mirrors the steering can be done in any direction parallel to the original direction. These kinematic mirrors are equipped with micrometer screws to rotate them. The precision with which the focused laser beam can be shifted depends on the least count of these micrometer screws and the distance between the steering mirrors. However, a higher resolution can be obtained in a holographic optical tweezers (HOTs) set-up, which will be discussed in the next chapter. Using the above two methodologies (Fig. 2.7) of centering the beam in a given direction and shifting the

beam laterally in a plane perpendicular to the laser beam propagation, we have aligned and centred the laser beam (the Gaussian profile) at the back focal plane of the microscope objective to ensure an aberration-free diffraction limited focused spot at the focal plane.

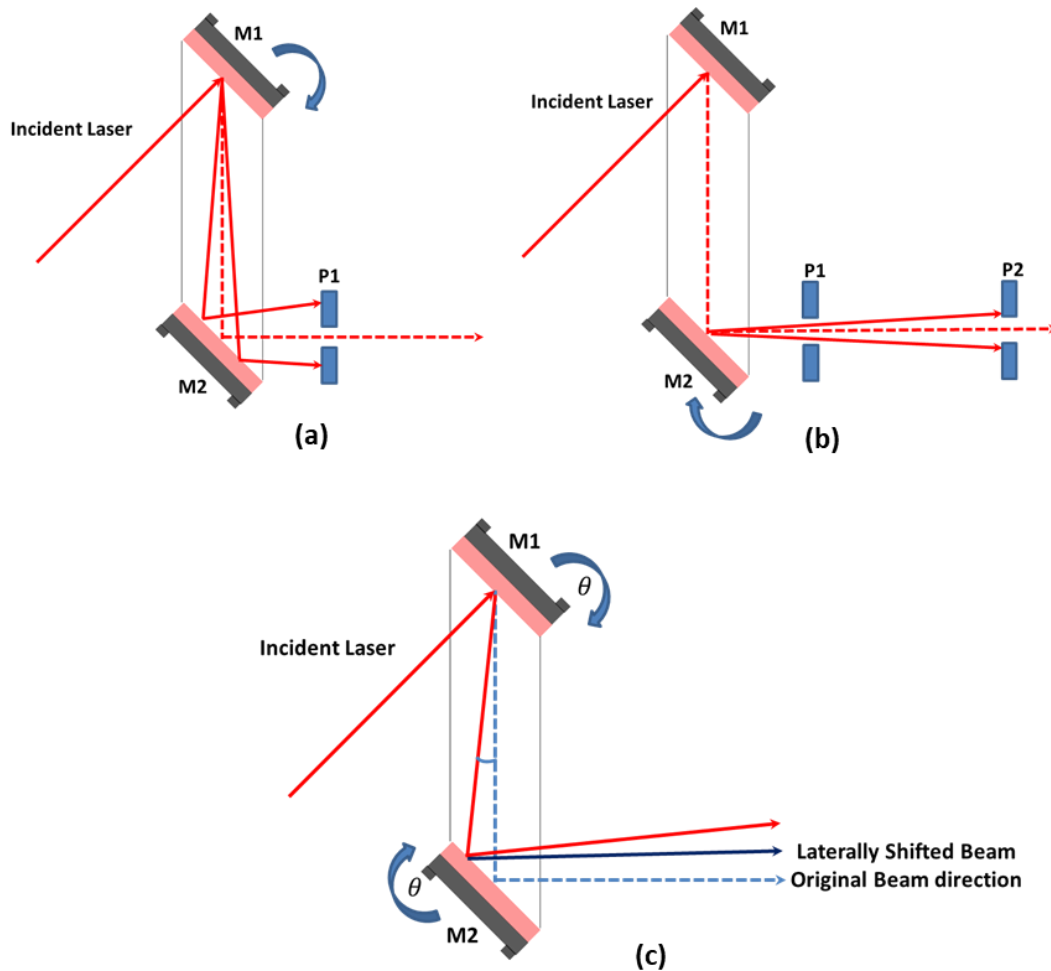


**Figure 2.7** Schematics of the steering mirrors M1 and M2 steering the laser beam. (a) and (b) describing the procedure of beam alignment, (a) Mirror M1 rotated to centre the beam and pass through pinhole P1, (b) Mirror M2 rotated to centre the beam and pass through pinhole P2, giving a laser beam propagating in a given direction, (c) Mirrors M1 and M2 rotated by same angle in either clockwise or anticlockwise direction shift the laser beam laterally. The schematic shows the steering in a plane, the mirrors being kinematic, the laser beam can be steered all over the perpendicular plane of beam propagation. Dashed blue ray shows the original direction, and the dark blue solid ray shows the shifted laser beam direction parallel to the original direction by rotation of the steering mirrors clockwise by the same angle.

The coupled laser beam is reflected off the 850 short-pass dichroic mirror and slightly overfills the back focal plane of the high numerical aperture objective. This produces a diffraction-limited spot at the focal plane capable of trapping microscopic particles stably in three dimensions.

#### (d) Steerable optical traps

The spot produced by the above procedure is a fixed spot at the focal plane. To trap particles in the given spot, the stage on which the sample is mounted needs to be moved to bring the particle under consideration to be trapped near the focal spot. The trapped particle can be moved with respect to surroundings only by moving the sample stage. However, in order to move the trap spot over the field of view, with the same optical power and profile, we have developed a steerable optical tweezers set-up (Fig. 2.8 (a)).

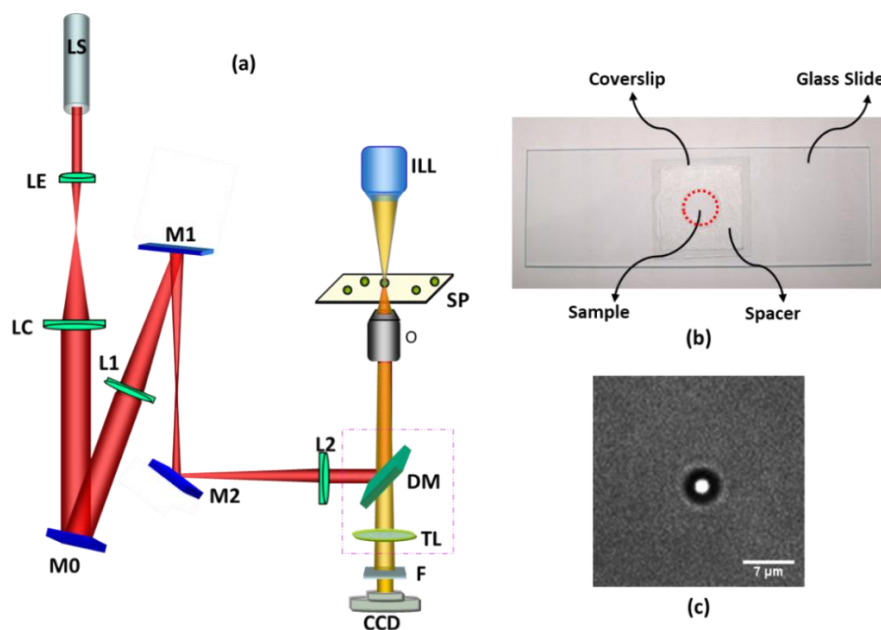


**Figure 2.8** (a) Schematic of the steerable optical tweezer set-up with two lenses L1 and L2 in the fixed trap set-up shown in Fig. 2.6, (b) Photograph of the sample prepared between the glass slide and the coverslip using a spacer and (c) an image of a 1.2  $\mu\text{m}$  diameter polystyrene sphere trapped.

Two lenses L1 and L2 are incorporated, one between M0 and M1 and the other between M1 and M2. They are separated by a distance equal to the sum of their focal lengths. M0 is kept at a distance equal to one focal length distance from L1 and L2 is separated by a distance equal to its focal length from the objective aperture. This arrangement images M0 to the back focal plane of the objective. Hence M0 becomes a conjugate plane to the back aperture of the objective, and thereby any tilting of M0 allows for the steering of beam in the focal plane without altering the beam profile and the power behind the objective back aperture. Hence, the beam can be steered in the trapping plane by tilting M0 and hence the XY motion of the trapped object. Translation in the z-direction is carried out by shifting any one of the lens L1 and L2 along the optical path, leading to either a converging or diverging beam, which allows for the motion of the trapped particle in the z-direction.

#### **2.4.2 Sample Preparation and optical trapping**

Fig. 2.8 (b) shows a photograph of the sample prepared for the optical trapping experiment. This sample containing the particles in a suspension is placed between a standard glass slide and an imaging coverslip of 100  $\mu\text{m}$  thickness, separated by an imaging spacer (SS1X9: 9mm dia.  $\times$  0.12mm depth) from SIGMA-ALDRICH. The imaging spacer sandwiched between the coverslip and glass slide creates a cylindrical volume of  $\sim 8 \mu\text{l}$  with a circular cross-section of 9 mm diameter available for trapping and imaging experiments. The suspension is placed inside this volume and mounted on the motorized stage. The microscope objective produces a tightly focused diffraction-limited spot at the focal plane. The trap is created at a distance of 20  $\mu\text{m}$  above the top surface of the coverslip by moving the objective. All trapping experiments are done at this height in order to avoid any coverslip effect. Fig. 2.8 (c)

shows a polystyrene particle of diameter 1.2  $\mu\text{m}$  trapped using this set-up. The minimum power required to stably trap the polystyrene sphere was found to be 1.2 mW at the trapping plane. The power at the trapping plane was estimated by considering 40% transmission of the objective at 1064 nm, by measuring the power at the back focal plane of the 100X objective using a laser power meter (Maestro, Gentec-EO, Germany).

### **2.4.3 Environmental isolation**

The different factors affecting the sensitivity, stability, and signal to noise ratio in the optical trapping experiments are temperature fluctuation, acoustic noise, mechanical vibrations, and air convection. To isolate optical trapping experiments from these factors, the optical tweezers set-up is built on active vibration isolation table from Thorlabs, which pneumatically isolates the set-up from external vibrations. Experiments are performed at a constant temperature in a closed environment to avoid any air drift, etc.

## **2.5 Data acquisition and calibration of optical tweezers**

### **2.5.1 Digital video microscopy**

To measure the forces exerted by the optical tweezers which range from tens of femto-newtons to hundreds of pico-newtons, it is necessary to track the motion of the trapped particle and measure the corresponding potential well. The motion of the trapped object is imaged using a Basler Scout (scA-640-120fm) monochrome CCD camera at a speed of 100fps. The field of view of the camera is 649 $\times$ 494 pixels. The CCD camera is calibrated by imaging a standard TEM grid (M/s. PELCO, US, 500 mesh grids) and one pixel corresponds to a distance of 0.12282  $\mu\text{m}$  in the trapping

plane. The exposure time of the camera is chosen to be 16  $\mu\text{s}$  for acquisition. This is two orders of magnitude less than the characteristic time scale of the relaxation of the trapped particle, which ensures an unbiased measurement of the position distribution of the trapped particle as a function of time [256]. The acquired video is cropped to a smaller size containing only a small region around the trapped particle, typically an area of 100 $\times$ 100 pixels. The videos were processed using image processing software (image J and Leica Qwin). The coordinates of the particles were extracted by an advanced particle detection technique using intensity profiles of the particle image as Gaussian to a first approximation.

## **2.5.2 Calibration of the optical trap**

The main objective of calibration of an optical trap is to determine the trap stiffness. By measuring particle position distributions, it is possible to determine the optical potential in which the particle is trapped. There are various techniques to calibrate an optical trap using the particle trajectories within an optical trap [241,257] such as equipartition method, optical potential analysis, mean square displacement analysis, autocorrelation analysis, and power spectrum analysis. We employ two of the techniques in our work, the equipartition method and the optical potential method. Further, we check for the calibration by measuring the trap stiffness using a trapped polystyrene sphere of diameter 1.2  $\mu\text{m}$  at different laser powers: the trap stiffness varies linearly with laser power.

### **2.5.2.1 Optical potential analysis**

The motion of an optically trapped particle in one dimension is described by the overdamped Langevin equation as [258],

$$\frac{d}{dt}x(t) = -\frac{1}{\gamma} \frac{d}{dx}U(x) + \sqrt{\frac{2k_B T}{\gamma}} W_x(t) \quad (2.14)$$

where  $U(x)$  is the trap potential,  $\gamma$  is the particle friction coefficient and  $W_x(t)$  is the white noise.

When the particle is in thermal equilibrium with the heat bath constituted by the solvent molecules, the probability density of the 1D particle positions is given by the Maxwell-Boltzmann distribution

$$\rho(x) = \rho_0 \exp\left(-\frac{U_x}{k_B T}\right) \quad (2.15)$$

where  $\rho_0$  is the normalization constant,  $k_B$  is the Boltzmann constant.  $U_x$  can be obtained from a normalized histogram of the trapped particle positions (Fig. 2.9) and given by the expression

$$U_x = -k_B T \ln(\rho(x)) + U_0 \quad (2.16)$$

where  $U_0$  determines the potential offset that can be neglected.

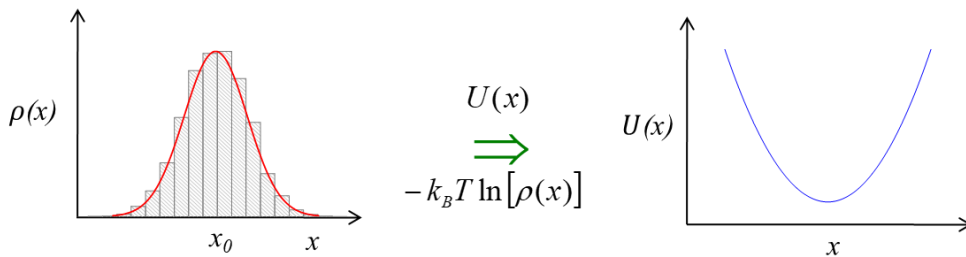


**Figure 2.9** Schematic of the position distribution of a trapped particle and the potential obtained using Eq. (2.16).

Since the trapping laser intensity has a Gaussian profile, to a first approximation the potential associated with an optical trap can be assumed to be

harmonic near the potential minima [259]. Hence, the  $U_x$  from Eq. (2.16) can be fitted to a parabola  $y = ax^2 + b$  to the data in the central region, and the trap stiffness is given by the formula

$$k_x = 2a \quad (2.17)$$

The advantage of this method is that it gives a more accurate result compared to the equipartition method to be discussed in the next section, and it also gives an idea about the shape of the potential, where it is not harmonic.

### 2.5.2.2 Equipartition method

Since the trapping laser has a Gaussian profile, the trap potential is harmonic. Then equipartition theorem can be applied to the optical trap: in equilibrium, each degree of freedom contributes  $\frac{1}{2}k_B T$  to the average energy. Trap stiffness is calculated from the mean square displacement of the particle from the trap center as

$$\frac{1}{2}k_B T = \frac{1}{2}k_x \langle (x - x_{mean})^2 \rangle \quad (2.18)$$

This method is applicable only to harmonic potentials and breaks down if the particle positions are far from the trap center where anharmonicity comes into the picture. To validate the trap calibration we trapped with different laser powers polystyrene particles of diameter 1.2  $\mu\text{m}$  suspended in water and calculated the trap stiffness. Fig. 2.10 (a), (b) and (c) show the images of trapped polystyrene spheres at 1.4 mW, 5.4 mW, and 44 mW, respectively.

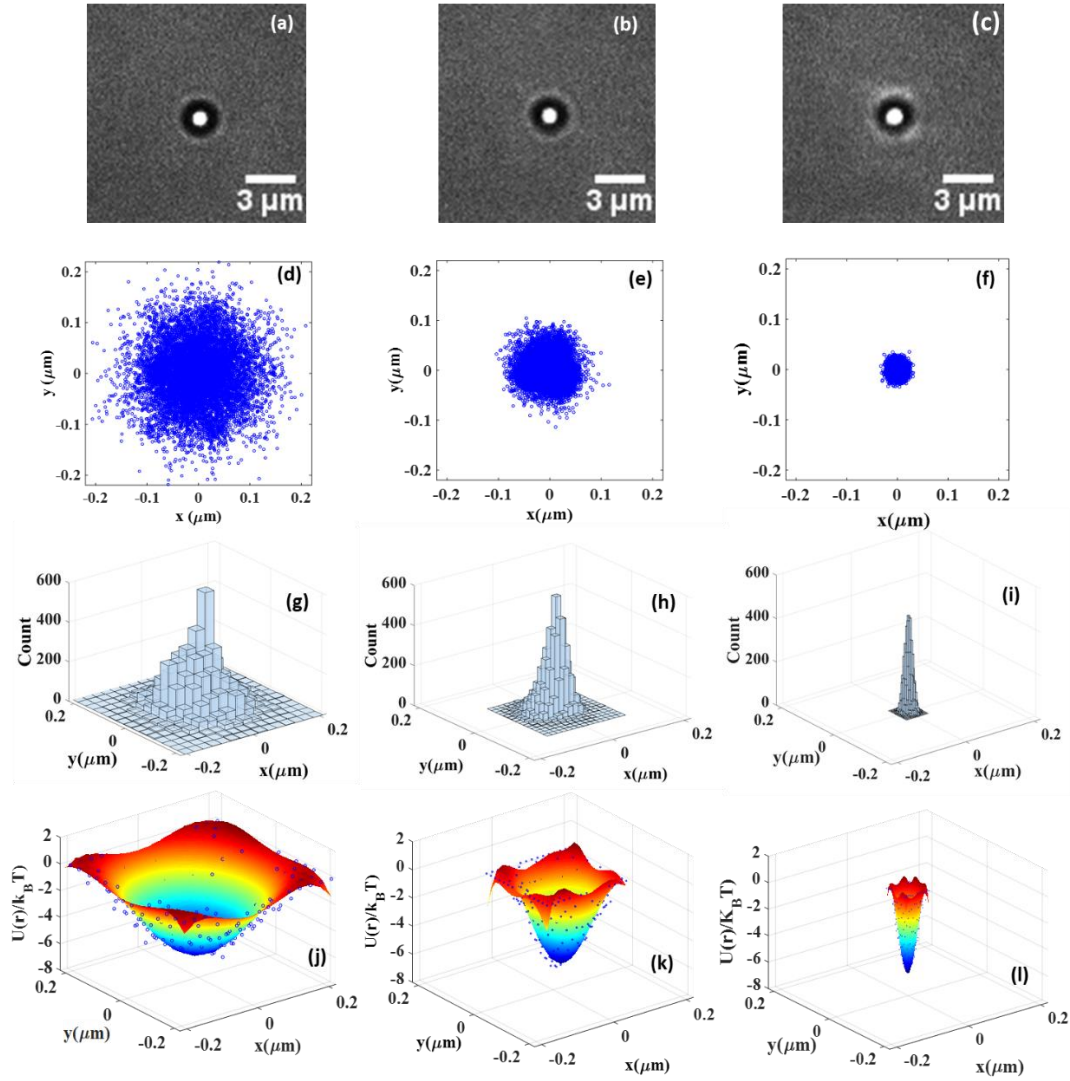


**Figure 2.10** (a), (b) and (c) Images of the trapped polystyrene sphere of diameter  $1.2 \mu\text{m}$  trapped with laser powers  $1.4\text{mW}$ ,  $5.4\text{mW}$ , and  $44\text{mW}$  respectively. (d), (e) and (f) shows the scattering plot of the positions of the trapped spheres recorded up to 10000 frames for the particles trapped with different laser powers as in (a), (b) and (c). (g), (h) and (i) shows the respective histogram of position distributions of the particle under the optical trap and (j), (k) and (l) shows the optical potential landscape calculated using Eq. (2.16) and fitted with a 5th order polynomial.

The corresponding position distributions of the trapped particle as a scatter plot and histogram of particle positions are shown in Fig. 2.10 (c), (d), (e) and (f), (g), (h) respectively. From the histogram of particle positions and the scatter plot it is clear that with an increase in laser power, the particle gets more confined near the trap center, i.e., the maximum displacement from the trap center decreases with increase in

laser power. Fig. 2.10 (j), (k) and (l) show the calculated optical potential landscape using Eq. (2.16) for the particles trapped in the order of increasing laser power fitted to a 5<sup>th</sup> order polynomial.

**Table 2.1** Lateral trap stiffness as a function of laser power for a trapped polystyrene particle of diameter 1.2 $\mu$ m as measured using optical potential analysis method and equipartition method.

Laser Power @ trapping plane (mW)	Trap stiffness ( $\mu$ N/m)	
	Equipartition Method	Optical potential analysis Method
1.9	2.01 $\pm$ 0.1	1.98 $\pm$ 0.13
3.4	3.23 $\pm$ 0.18	3.38 $\pm$ 0.19
6.3	5.26 $\pm$ 0.29	5.59 $\pm$ 0.24
7.3	6.68 $\pm$ 0.47	6.86 $\pm$ 0.34
8.9	7.44 $\pm$ 0.17	8.02 $\pm$ 0.32
9.8	8.01 $\pm$ 0.34	8.30 $\pm$ 0.67

The value of trap stiffness measured as a function of laser power by two different methods, the equipartition method, and the optical potential method, are shown in table 2.1, which shows the increase in trap stiffness with increase in laser power.

Fig. 2.11 (a) below shows the optical trapping potential landscape for the polystyrene sphere trapped at various laser powers showing the increase in the depth along with simultaneous shrinking of the potential well. A plot of the variation of the trap stiffness as a function of laser power is shown in Fig. 2.11 (b). The measured values of the trap stiffness with various laser powers could be fitted to a straight line,

i.e., the trap stiffness varies linearly with laser power, as expected. This indicates that the quality of experimental data acquired by the optical manipulation set-up is good and the trap is calibrated to its proper functioning.

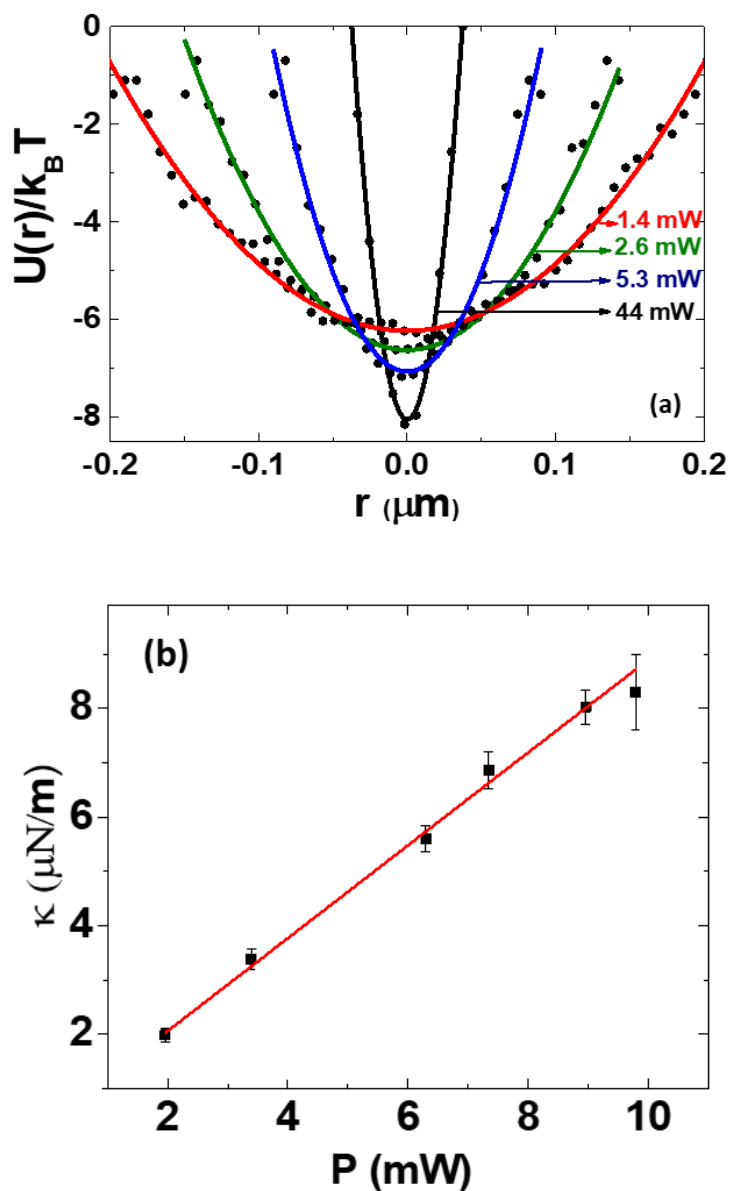


**Figure 2.11** (a) Optical trapping potential for a trapped polystyrene sphere of diameter  $1.2 \mu\text{m}$  at various laser powers showing the increase in the depth and the shrinking of the potential well towards the trap center, and (b) variation the trap stiffness as a function of laser power fitted to a straight line.

## 2.6 Generation of ring pattern of trapped particles with optical tweezer

We have trapped multiple polystyrene spheres in a single optical trap to demonstrate the multiple trapping capabilities of optical tweezers. To trap multitude of particles in a single optical trap spot, the focal spot is moved upwards towards the lower surface of the upper glass slide. Fig. 2.12(a) below shows an image of the optical trap spot at the lower surface of the glass slide, showing a ring pattern of light focused onto the glass slide.

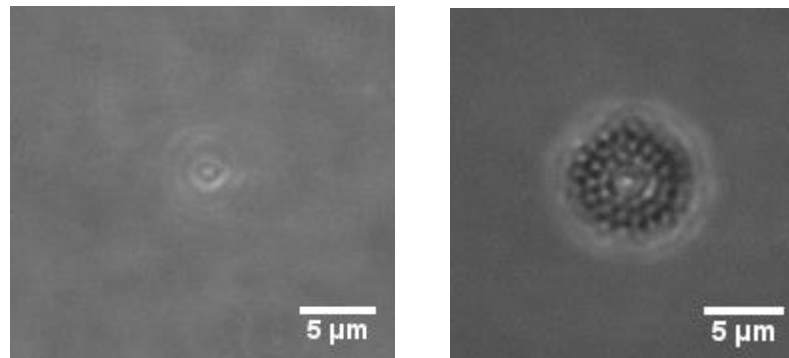


**Figure 2.12** (a) Image of the focused optical spot being moved upwards at the lower surface of the upper glass slide, showing a ring pattern at the interface, and (b) Polystyrene spheres of diameter 600nm trapped in the concentric ring pattern created using a single laser focus.

The assembly of micro-particles in ring structures is shown to be due to the smaller thickness of the chamber [260]. The polystyrene spheres get trapped in the concentric airy ring-like light fields Fig. 2.12 (b) shows a number of polystyrene spheres of diameter 600 nm trapped in a ring fashion with concentric rings around the central sphere. This shows the capability of the optical tweezer to trap a multitude of particles, which can find applications in the study of optical binding phenomena between different structures.

## **2.7 Conclusion**

We have designed and developed an optical tweezers set-up capable of trapping microscopic particles stably in three dimensions. Design considerations to build the optical tweezer and its extension to generate steerable optical traps are described. We have described the trapping in various regimes and quantified the optical trap efficiency. The optical trap is calibrated for its stiffness using optical potential analysis method and equipartition method. Further, trap stiffness as a function of laser power is measured to check the quality of the experimentally acquired data. Finally, we describe a methodology to trap a multitude of particles in a concentric ring geometry in a single beam focal spot by moving the spot towards the lower surface of the upper glass slide covering the sample.

# DEVELOPMENT OF HOLOGRAPHIC OPTICAL TWEEZERS

---

This chapter presents the details of design and development of holographic optical tweezers, optimization of the spatial light modulator (SLM) (having a phase modulation depth less than  $2\pi$ ) and different algorithms and strategies to generate uniform holographic optical traps with high diffraction efficiency.

### 3.1 Introduction

An optical tweezer is a tightly focused laser beam capable of holding and moving microscopic objects. It has become an indispensable, non-destructive tool for manipulation of different microscopic objects since 1986 [229,230]. Because of the ability of non-invasive probing at the mesoscopic scale and manipulation capability with nanometer accuracy, optical tweezers find applications in various fields of research, such as the study of particle interactions in complicated geometries, hydrodynamic interactions between colloidal spheres, optical binding, colloidal transport, optical sorting, etc. [117,130,131,134,135,218,233,235,261]. However many applications require control of a multitude of particles, like manipulating them in real time and placing them in definite positions with desired symmetry. This is where Holographic Optical Tweezers (HOTs) play an important role, allowing for the creation of multiple optical spots in real time. HOTs [34,262–264] uses the technique of beam shaping combined with digital holography accomplished by a phase-only Liquid Crystal on Silicon (LCOS) spatial light modulator (SLM). We have designed and developed a HOTs set-up around an optical tweezer set-up described in [218] by

incorporating an SLM procured from Boulder Nonlinear Systems (BNS). The HOTs setup is developed with an aim to create an array of trap spots to trap multitude sets of particles in their desired positions. The technique of HOTs requires efficient and uniform distribution of light among the desired spots, free from aberrations, to efficiently trap the particles in them. In addition, SLMs find wide application in the field of adaptive optics [265], real-time hologram display [266], wave aberration correction [61,267–269], shaping of femtosecond pulses [270], wavefront sensing [271], differential interference contrast (DIC) imaging [272], optical metrology [273,274].

Some of the above-mentioned applications require accurate control of the phase, linearity, and uniformity in the phase modulation response in the range of 0 to at least  $2\pi$ . In general, liquid-crystal-based SLMs show their inherent non-linear phase response as a function of addressed gray values, which limits their performance in some of their applications. Further, the non-uniformities in the back plane [275] or fringing field effects [276] also degrade the performance of the SLM. Suppliers of SLMs usually provide lookup tables (LUTs) for correctly addressing the phase levels. However, the phase modulation property slowly drifts with time, and, hence, these SLMs need periodic calibration for precision control of the phase, linearity, and uniformity in the phase response over the desired phase range. There exists several calibration methods, which broadly can be classified into two categories: (1) interferometric methods, such as Michelson interferometers [86], Mach-Zhender interferometers [275], Young's double slit interferometers [91], lateral shear interferometers [89], Twyman-Green interferometers [277], and (2) diffraction-based phase retrieval methods [87,90,94,211,278]. Interferometric methods, though they give accurate results, are limited by complicated alignment procedures and extreme

sensitivity to mechanical vibrations and air turbulence. Further, interferometric setups require additional optical components, making the system less cost-effective. Another difficulty with interferometric methods is that they require removal of the SLM from its working position, as it needs to be placed in one of the arms of the interferometric arrangement. The characterization method based on Young's double slit interferometry is simple compared to other interferometric techniques, but it involves illumination of the two halves of SLM with two circular beams created by two pinholes before the SLM and interfering them using a microscope objective, leading to a fringe pattern being used for characterization. The drawback of this method is that the contrast of the fringes are affected by the size and the distance between the pinholes used for making the two circular beams [93], and it allows for characterization of only that region of the SLM that is exposed to the interfering beams, not the full aperture of the SLM. On the other hand, the diffraction based-methods involve analysis of the diffracted field in the Fourier plane of SLM, SLMs encoded with certain multi-phase diffractive optical elements are relatively easy to implement in the optical manipulation system without much changes in the optical arrangement. This method of characterization based on diffraction is also insensitive to mechanical vibrations and other environmental disturbance. Furthermore, it enables characterization of the phase modulation of the SLM at the same incidence angle of the laser beam used for the experiment, the phase modulation being sensitive to angle of incidence of the laser on the SLM due to multiple reflection and interference [279].

We employed a diffraction-based technique to characterize and calibrate the SLM that is driven by a digital video interface (DVI) graphics card. In general, the SLMs are controlled either by PCIe interface or by a DVI controller interface that uses a graphics card. SLMs are normally supplied along with its calibration LUT from

the supplier to correctly address the grey levels to the desired phase value. However, SLMs driven by DVI graphics controller interface show different phase response behavior with different graphics card, and, hence, the SLM needs to be calibrated with respect to the graphics card used to drive the SLM. We present a methodology to optimize the graphics card properties and calibrate the SLM, correcting its nonlinear phase response behavior. We generate a LUT and optimize the SLM for its maximum attainable phase modulation depth and maximum diffraction efficiency.

In addition to the non-linearity in the phase response, these liquid-crystal-based modulators show different phase responses in the different spatial regions of the SLM. Xun and Cohn [86] compensated for the spatially varying phase response (SVPR) of non-flat SLMs by measuring the spatial phase for a single gray scale address voltage using phase shift interferometry technique. Oton *et al.* [88] described a multipoint phase calibration technique for phase compensation by generating a multi-LUT for precise control of the phase response, but the applicability of this method is limited to SLMs that show phase response of similar shape over different spatial regions, i.e., if the spatial non-uniformity is only due to the thickness variations across the active area of SLM. However, there are many other factors that can affect the phase response across the spatial area of an SLM, as pointed out by Zhang *et al.* [94] and Reichelt [275]. They calculated the phase compensation profile while considering the effects of spatial non-uniformity and nonlinear dynamic phase response due to the presence of imperfections in the liquid crystal layer. Apart from these factors, the performance of SLMs is affected quite extensively by factors such as non-uniform electric drive scheme, liquid crystal heating due to variation of power of the incident laser beam, and the spatial profile of the incident laser, i.e., a commonly used Gaussian beam can also lead to different phase response due to

differential heating over the spatial region of an SLM, as discussed in Ref. [95]. Engstrom *et al.* [95,96] compensated for the SVPR by characterizing the phase response of the SLM over its many subsections using diffraction-based methods [211,278] and fitting the data with a 3D polynomial to convert the desired phase to the corresponding pixel value for each SLM pixel.

The method presented by Engstrom *et al.* [95] requires a tedious characterization procedure for each subsection to generate the phase modulation curve and fitting all the measured data with a 3D polynomial. Since the phase response of these liquid crystal modulators also depends on the amount of optical power incident, causing differential liquid crystal heating over the spatial region of an SLM, it becomes complicated to generate the spatial LUT for different laser powers required by different experimental conditions. In addition, the gray level resolution for which the power can be measured at the Fourier plane of SLM is limited by the resolution of the detector. Hence for smaller subsections for which the maximum first-order diffracted power is much less compared to the full area of the SLM, the resolution of measurement drastically diminishes, resulting in an inaccurate phase modulation curve. Further, the measurement becomes relatively more inaccurate for the subsections belonging to the edges of SLM, being illuminated by the wings of the Gaussian beam. The resolution problem can be overcome by shining more power onto the SLM, but this is limited by the destruction threshold of the SLM.

All methods described above give the procedures for calibrating SLMs that are driven by a PCIe interface. There are no reports on the calibration of SLMs driven by DVI graphics cards, to the best of our knowledge. We report the calibration of an SLM driven with a DVI graphics card that is sensitive to the settings of the graphics.

Further, our method allows for addressing the gray levels with uniform resolution. In this work, we present a simple and robust method to calibrate an SLM suffering from a SVPR. This method does not require tedious characterization procedures for each subsection [95]. It is based on diffraction technique [211] and uses a blazed grating instead of a binary grating with 50% duty cycle, as described in section 5. It applies to all kind of SLMs and is particularly suitable for SLMs suffering from low first-order diffraction efficiency and having a phase modulation depth less than  $2\pi$ . The method used in this work gives more accurate results for the subsections belonging to the edges of an SLM, where the other methods are inadequate because of the limited resolution with which the diffracted power can be measured. Also, our method allows easy calibration of an SLM for different power levels.

This chapter is organized as follows. Section 3.2 describes the design and development of the HOTs set-up employing the phase-only SLM. Section 3.3 describes the calibration procedure of an SLM driven by DVI graphics. A method to calibrate the phase response due to the SVPR of the SLM is presented in section 3.3. Section 3.4 describes the methodology for uniformity correction and its implementation in the trap generating algorithm along with a prescription to trap polystyrene particles in an array of uniform optical traps. Section 3.7 summarizes the main conclusions of the work.

### **3.2 HOTs set-up**

We have designed and developed a HOTs set-up which employs a phase-only reflective SLM from Boulder Nonlinear Systems as the programmable diffraction device. The SLM consists of parallel aligned nematic liquid crystal molecules sandwiched between a pixelated back electrode and a transparent front electrode.

Each pixel can be independently controlled, allowing simultaneous and independent change in the optical properties of the LC layer corresponding to each pixel. The parallel aligned nematic liquid crystal molecules possess dielectric anisotropy. They show effective birefringence under an applied electric field and thereby retard the phase of the extraordinary component of the incident light. Our SLM consists of a set of independently controlled  $512 \times 512$  pixels allowing the phase control of the incident laser beam over all these pixels of the spatial region of SLM (Fig. 3.1).

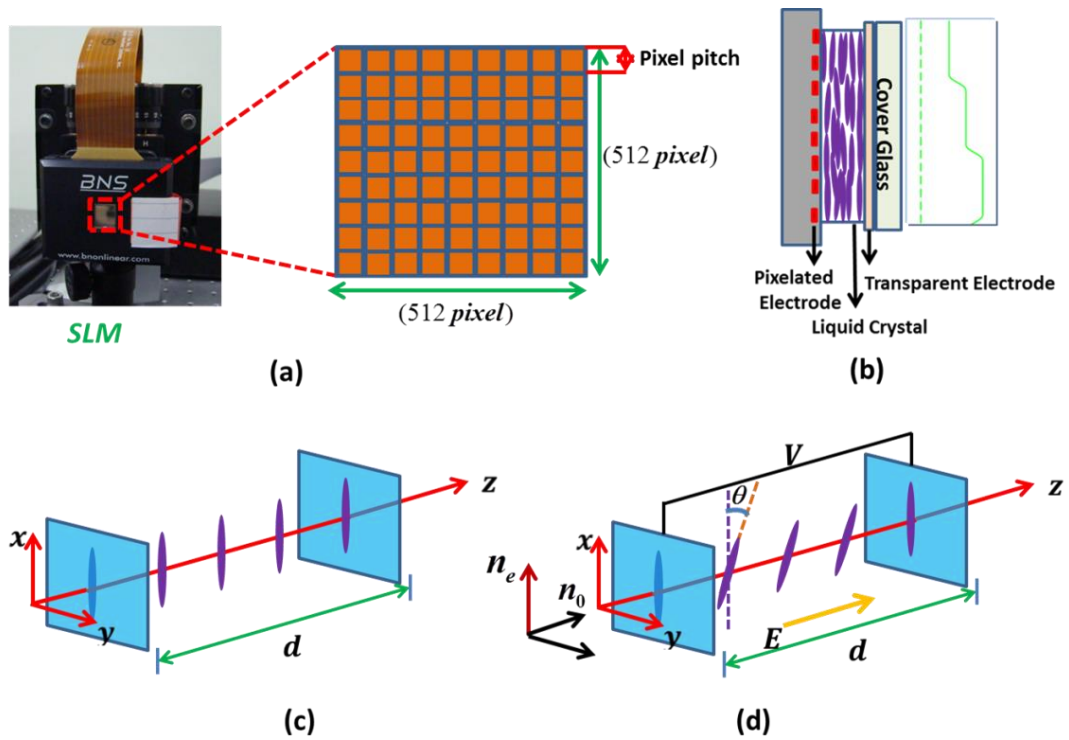


**Figure 3.1** (a) Photograph of SLM with the active area zoomed showing pixelated nature of SLM, (b) Schematic of the side view of SLM showing the parallel aligned nematic liquid crystals sandwiched between the pixelated back electrode and the front transparent glass plate, (c) Schematic of the orientation of liquid crystal molecules within the cylindrical volume of single pixel without any applied field, and (d) with applied field showing effective birefringence.

The effective birefringence  $\Delta n$ , in these liquid crystals, is given as

$$\Delta n = n_{eff}(\theta) - n_0 \quad (3.1)$$

where

$$\frac{1}{n_{eff}^2(\theta)} = \frac{\cos^2(\theta)}{n_e^2} + \frac{\sin^2(\theta)}{n_o^2} \quad (3.2)$$

$n_e(\theta)$  is the extraordinary refractive index that varies with the orientation angle  $\theta$  of with the director axis of these liquid crystal molecules with the applied field, and  $n_o$  is the ordinary refractive index. The phase modulation experienced by the incident light in a pixel area of SLM is given by

$$\varphi = \frac{2\pi}{\lambda} [n_e(\theta) - n_o]d \quad (3.3)$$

where  $d$  is the thickness of the liquid crystal layer across each pixelated region of SLM.

Applied voltage across the electrodes of a pixel changes the orientation angle of the liquid crystal molecules in the region with respect to director, leading to a phase retardation of the incident light in that region. Hence by controlling the voltages across each of the pixels, the phase of the light can be modulated independently. The SLM employed in our HOTs setup is driven through a DVI interface providing a 16-bit pixel data to the SLM, the 16-bit operation being supported by 24-bit 512×512 images transferred through an NVIDIA graphics card (Nvidia Quadro FX 580). The graphics card setting plays a critical role in the operation of SLM as will be discussed in section 3.3.

The HOTs set-up is designed around an inverted microscope (Olympus IX81). A Nd:YAG fiber-coupled, continuous-wave TEM<sub>00</sub> laser ( $\lambda=1064$  nm) beam is coupled to the microscope through a series of optical components. The schematic of the setup is shown in Fig. 3.2. The laser beam is first passed through a set of

polarizing optics consisting of a polarizer to produce a linearly polarized beam, and then through a half-wave plate to rotate the polarization to align it parallel to the director of the SLM for maximum phase modulation. The beam is reflected off mirrors M1 and M2 and passed through beam expansion optics to fill the active area of the SLM after reflection from mirror M3. The beam expander consists of two achromatic doublet lenses in Keplerian arrangement with a pinhole at the back focal plane of the expander lens to spatially filter the light to ensure clean, Gaussian illumination on the SLM.

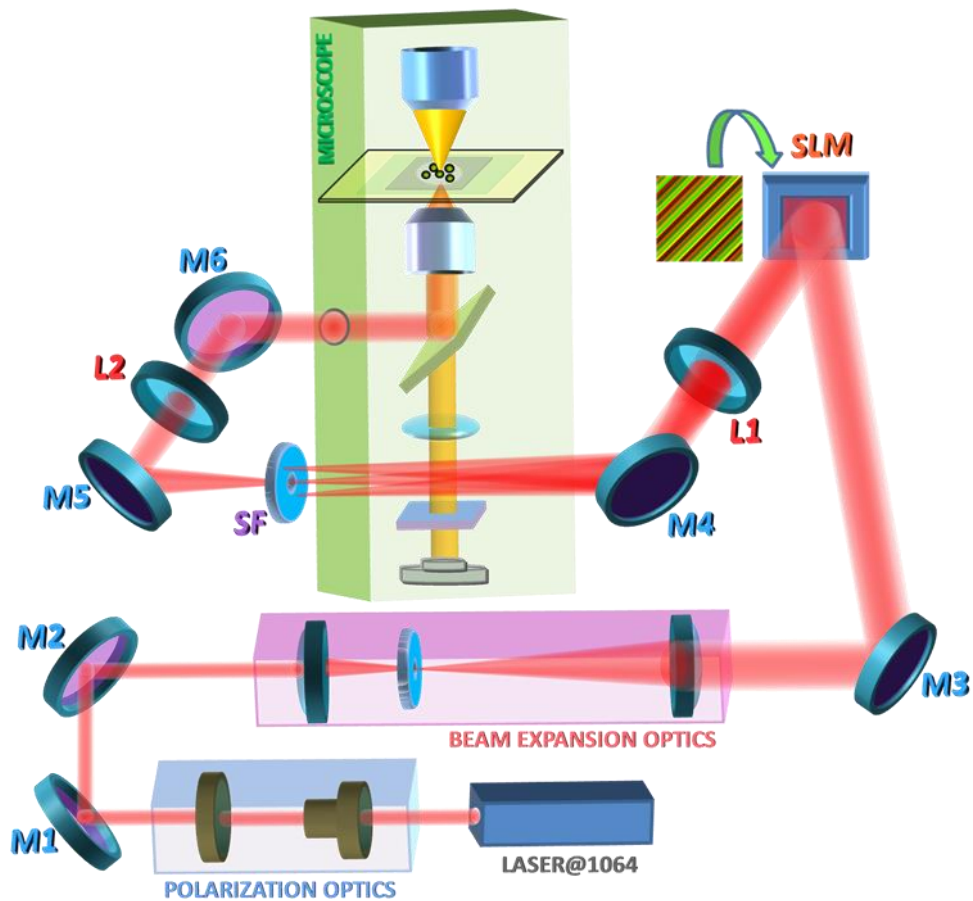


**Figure 3.2** Schematics of the HOTs setup. Polarization optics consisting of a polarizer and a half-wave plate controls the polarization and its orientation. M1, M2, M3, M4, M5, and M6 are (>99%) reflecting mirrors for the laser ( $\lambda = 1064$  nm). Beam expansion optics expand the laser beam to fill the active area of the SLM. Lenses L1 and L2 in  $4f$  configuration image the SLM at the back focal plane of the microscope objective (MO). SF is the spatial filter (a pinhole) for filtering the various orders of the diffracted beam.

The angle between the incident beam and the beam reflected off the SLM is kept around  $\sim 6^\circ$  to  $7^\circ$  to avoid pixel cross-talk that could be caused by the beam corresponding to a pixel traveling through multiple pixels. Of course, the lower the angle, the larger the minimum distance ( $d_{min}$ ) required for separating the incident and reflected beams:  $d_{min} = \varphi_{SLM} / 2 \tan \theta$  ( $\varphi_{SLM}$ , angular size of the SLM;  $\theta$ , angle between the incident and the reflected beams) [280]. In our design, we have not placed optical elements between M3 and the SLM to facilitate easy centering of the expanded beam to the active area of the SLM by steering mirror M3. There are designs reported in the literature to center the expanded beam on the active area, employing the beam expander lenses kept in the same arm, in the path of the beam incident on the SLM, i.e., between M3 and SLM. This makes aligning the expanded beam onto the center of the SLM quite cumbersome. In our design, we keep the arm containing beam expansion optics and the arm containing the incident beam on the SLM separate to eliminate this problem.

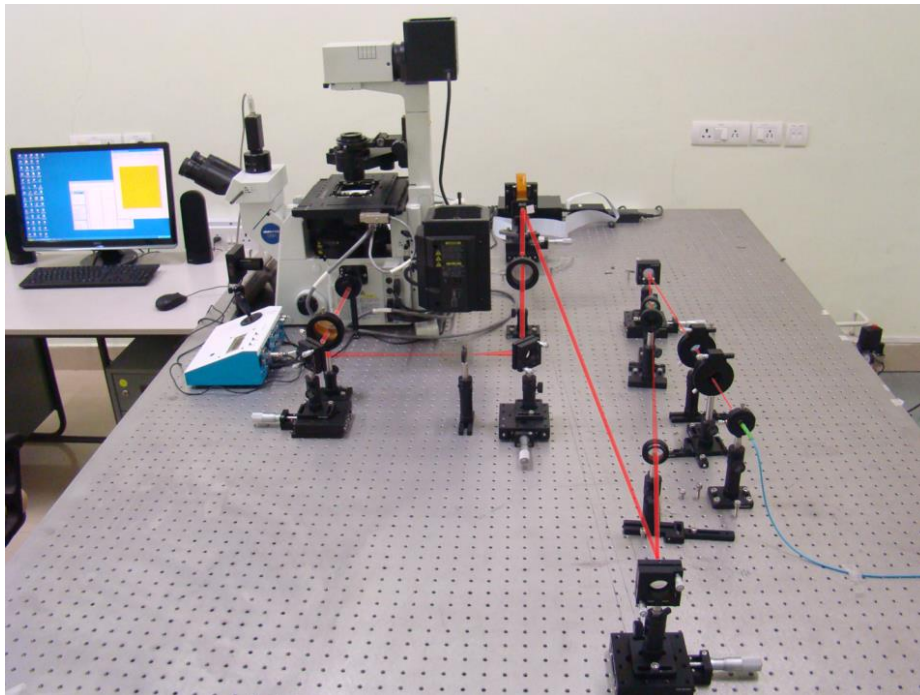


**Figure 3.3** Photograph of the HOTs set-up.

Positioning lenses L1 and L2 between the SLM and the microscope objective in a  $4f$  configuration and the SLM at a distance equal to the front focal length of the lens L1 results in a simple Fourier transform relationship between the SLM plane and the back focal plane of lens L1. Lens L2 is kept at a distance equal to its back focal length from the back aperture of the objective lens (100x, 1.4 N.A.). The objective lens in this configuration tightly focuses the laser beam into a diffraction-limited spot capable of trapping submicroscopic particles dispersed in a solvent placed at the sample plane. This optical arrangement acts like two interconnected  $4f$  imaging systems. Lenses L1 and L2 image the SLM onto the back aperture of the microscope objective (MO), and L2 and the microscope objective image the Fourier plane of the SLM onto the sample plane. In addition, this arrangement allows for the conversion of angular displacement of the diffracted beam by the SLM to lateral displacement at the sample plane, with simultaneous demagnification of the beam reflected off SLM to slightly overfill the objective back aperture by appropriate choices of focal lengths for lenses L1 and L2. Mirrors M4 and M5 steer the beam in the sample plane, and a pinhole placed at the Fourier plane of L1 enables selection of the various orders of the beam to be allowed to pass as required. The diffracted beam reflected off mirror M6 is reflected by an 850 short-pass dichroic placed inside the microscope body towards the high NA objective lens, which produces a tightly focused laser spot capable of trapping a multitude of submicroscopic particles in three dimensions. A photograph of the developed HOTs setup is shown in Fig. 3.3.

To generate multiple optical traps, there are various algorithms reported in the literature. We have used a modified version of weighted Gerchberg-Saxton (WGS) algorithm to generate an array of optical spots and random superposition (RS)

algorithm to generate the optical spots required in moving the trap spots during the course of experiment, as will be discussed in subsequent section.

### **3.3 Calibration of the SLM**

#### **3.3.1 Optimization of Graphics Card settings**

The SLM used in the HOTs set-up is driven by a DVI interface. The holograms (512×512 images) computed to produce the desired pattern at the sample plane are transferred through a graphics card to the SLM. The setting of the graphics card plays an important role in the first-order diffraction efficiency of the SLM and also in achieving uniformity in intensity among the trap spots. The parameters available with an NVIDIA graphics to be set are brightness, contrast, gamma, digital vibrance, and hue. Out of these, the important parameters that are to be optimized for good performance of SLM are brightness (B), contrast (C) and gamma (G). The effects of the other two parameters also will be discussed towards the end of this section. To optimize the graphics card settings, we employed a method similar to the one used for computer monitors given by Poynton [281]. This is implemented in our experiments by a diffraction-based method as described in Fig. 3.4(a). A sequence of holograms with two phase levels, i.e., a linear binary diffraction grating with 50% duty cycle, were imposed on the SLM, keeping one of the phase levels constant at 0 and the other stepped through a range of gray values starting from 0 to 65,535 [Fig. 3.4(a)]. A power meter was placed on the Fourier plane of the SLM after the pinhole (SF) to measure the power of various orders diffracted off the SLM when different diffractive elements are imposed over it. When brightness is set too low, it causes a large initial range of gray levels not to diffract power into the first-order, leading to loss of resolution with which the SLM can be addressed, whereas brightness set too high

causes no gray levels to display the true black level, leading to reduced first-order diffraction efficiency. To achieve a good contrast ratio in the holograms sent to the SLM through the graphics card, it is important to set the black level accurately. To optimize the brightness or black level, the contrast in the graphics card settings is set to its minimum value. Then a hologram representing a true black (i.e., a 16-bit depth image) having [0,0,0] gray values all over its 512×512 pixels is displayed on the SLM, which is shown in Fig. 3.4(a). When both gray levels from the sequence of holograms (a binary diffraction grating with 50% duty cycle) are zero, the hologram ideally becomes a blank hologram, but it can still diffract some of the laser power at the first-order spot. Although the hologram imposed over the SLM is ideally black, the hologram as realized by the SLM is not a perfect black (if the black levels are not set properly), in which case the SLM does not act like a perfect mirror and diffracts a fraction of the power to locations other than zeroth order. Hence, a change in the brightness of the graphics leads to a change in the power levels at the first-order diffraction location and the minimum in the power level is chosen to be true black. The power of the first-order diffracted beam was measured as a function of the different brightness levels of the graphics. The plot of the measured normalized first-order diffracted power versus the brightness level (%) is shown in Fig. 3.4(b). The minimum observed at a brightness level of 97%, represents the true black. Then, the contrast was set to its highest value of 100% to achieve maximum diffraction efficiency for the first-order diffracted beam.

To select a suitable gamma, experiments have been carried out using the same diffraction-based method. A sequence of holograms with two phase levels, i.e., a linear binary diffraction grating with 50% duty cycle, was displayed on the SLM, keeping one of the phase levels constant at 0 and the other being stepped through a

range of gray values starting from 0 to 65535, as shown in Fig. 3.4(a). For each displayed hologram, the power of either of the +1st or -1st-order diffracted beam was measured at the Fourier plane of the SLM. From the measured data, the location of the maxima corresponding to the phase modulation depth of  $\pi$  was identified. It was found that there was a shift in the position of the addressed gray level at which the maximum power is obtained in either of the +1st or -1st-order diffracted beam when the measurements were done at different values of gamma of the graphics card. The position of the first-order maximum (which corresponds to a phase change of  $\pi$ ) with respect to the addressed gray level plays an important role in determining the resolution at which different gray levels are addressed, corresponding to the phase values in the range 0 to  $\pi$  and in the range of  $\pi$  to  $2\pi$ , irrespective of the different nonlinearities in the phase behavior over these two regions.

To achieve uniformity in the resolution at which the gray levels are addressed over the range of 0 to  $2\pi$ , it is required to match the position of the first-order maximum with the center of the range of allowed gray values. In our case, the DVI interface driving the SLM through the graphics allows the SLM to be addressed with 16-bit holograms, allowing a range of gray values from 0 to 65,535. To shift the first-order maximum to the center ( $0.5 \times 65,535 = 32,768$ ) of these allowed gray level values, the hologram corresponding to phase level 32,768 for one of its phase levels from the sequence of holograms (linear binary diffraction gratings with 50% duty cycle) was displayed over the SLM. The hologram representing a binary diffraction grating with 50% duty cycle with one of the phase levels having a gray value 32,768 and the other having at 0 is shown as an inset in Fig. 3.4(c).

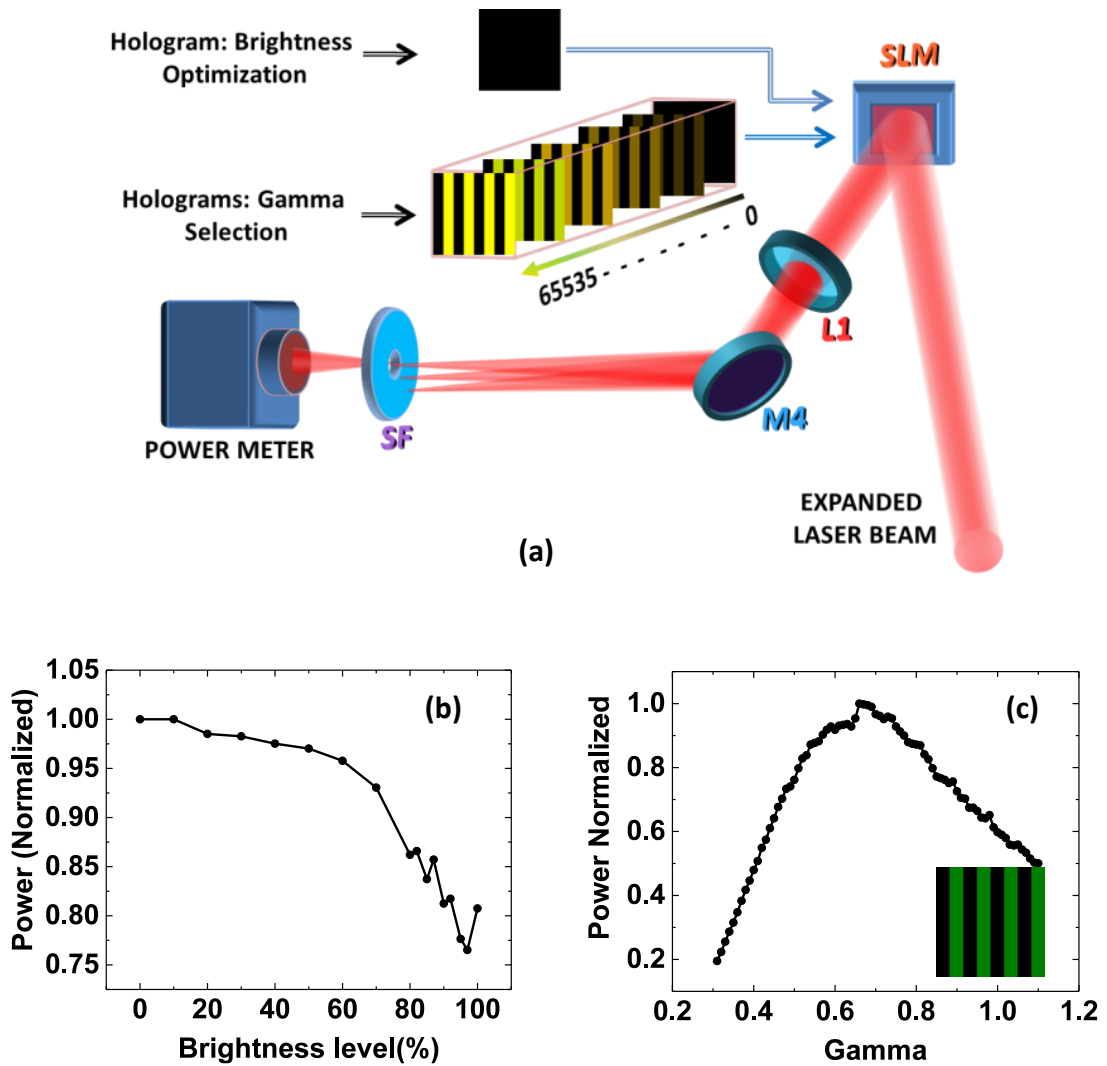


**Figure 3.4** (a) Schematic of the Experimental setup based on diffraction to measure the first-order diffracted power at the Fourier plane of the SLM using a power meter with binary holograms (with 50% duty cycle): (i) a zero gray level imposed on SLM required for brightness optimization, and (ii) a series of binary diffraction gratings (50% duty cycle) with varying gray levels from 0 to 65,535 imposed on SLM for gamma optimization of the graphics card respectively. (b) Plot of normalized first-order diffracted power versus the brightness levels set in the graphics card, showing a minimum at 97% of brightness level. (c) Plot of normalized first-order diffracted power measured at the Fourier plane of SLM as a function of gamma of graphics card, with a hologram (shown as inset) representing a linear binary diffraction grating with one of the phase levels having a gray value 32,768 and other 0.

The power of the first-order diffracted beam was measured for different values of the gamma of the graphics, and the plot is shown in Fig. 3.4(c). The value of gamma for which maximum power is obtained in the first-order diffracted beam is

identified to be 0.66. This value of gamma places the first-order maximum (corresponding to the phase value of  $\pi$ ) at the center of the available gray values, i.e., at 32,768, leading to uniformity in the resolution with which the gray levels are addressed in the range of 0 to  $\pi$  and  $\pi$  to  $2\pi$ , i.e., a symmetric phase modulation depth on either side of gray value 32,768. All measurements were done with reference to a linear LUT.

Two other parameters that affect the performance of an SLM, but not of much importance to the present context, are digital vibrance (DV) and hue (H). The values of these parameters were set to 50% and  $0^\circ$ , respectively. The digital vibrance if set below and above 50% lead to the oscillation of the power levels with respect to the addressed gray values, leading to a loss of first-order diffraction efficiency. Similarly, the hue set at any angle above  $0^\circ$  also led to decrease in first-order diffraction efficiency. The optimized graphics settings for the SLM with the NVIDIA graphics card used in our HOTs setup are B = 97%, C = 100%, G = 0.66, DV = 50%, and H =  $0^\circ$ .

### **3.3.2 Phase characterization and compensation of phase nonlinearity**

#### **3.3.2.1 Characterization of Phase modulation**

The optimization of graphics card parameters as described in the above section 3.3.1 allows improved first-order diffraction efficiency, by setting the black level properly, and uniformity in the resolution with which the gray levels are addressed in the full range of phase modulation, i.e., 0 to  $2\pi$  (by suitable adjustment of gamma). However, there exists nonlinearity in the phase response of nematic liquid crystal molecules, and its characterization helps in compensating for the nonlinear response. The same diffraction based setup shown in Fig. 3.4(a) was used for characterizing the

nonlinear phase response of the SLM. A sequence of holograms with two phase levels, one fixed at 0 and the other stepped through the range of gray levels to be characterized, i.e., 0 to 65,535, realized as linear binary diffraction gratings with 50% duty cycle with a grating period of 16 pixels are displayed over the SLM.

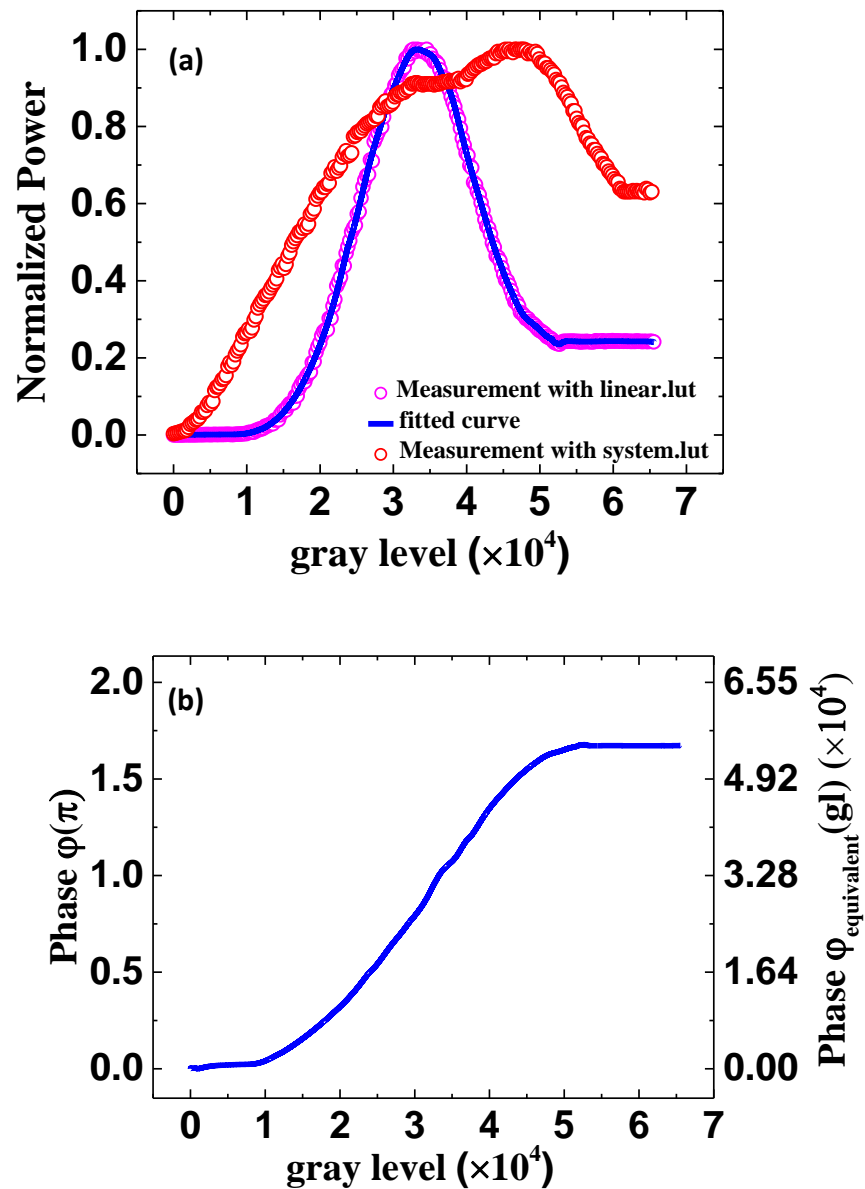


**Figure 3.5** (a) Plot of normalized power measured at the first-order diffracted beam versus gray level: (i) using a linear-lut, shown as magenta circles fitted piece-wise with a ninth-order polynomial (fit is shown as blue lines), and (ii) using a system-lut provided by the supplier. (b) Plot of extracted phase modulation curve from the normalized power measured using linear-lut as a function of addressed gray values. The right-hand-side axis shows the equivalent phase levels in units of the converted gray level.

The power of the first-order diffracted beam (either of the first order) is measured using a power meter for each of the displayed holograms in the sequence. The measurements were done with a linear LUT (named “linear-lut,” which provides a linear relationship between the input and output gray levels) in place, to characterize the true phase response of the SLM. Fig. 3.5(a) shows the plot of the normalized power of the first-order diffracted beam versus the gray levels with linear-lut, and the LUT of the supplier (henceforth called “system-lut”). The measurements with linear-lut have been carried out with the optimized graphics parameters mentioned above and compared with those measured using system-lut with default settings of the DVI. Note the outcome of the optimization, which clearly brings out the first-order maximum position to the center of the allowed gray levels, bringing uniformity in the resolution of addressed phase levels before and after the maxima corresponding to a phase of  $\pi$ . The power levels [Fig. 3.5(a)] were measured at 256 equally spaced gray levels for the range 0 to 65,535, and were fitted piecewise in different regions with a ninth-order polynomial to extract the power levels corresponding to each of the gray levels, as the fit is shown in Fig. 3.5(a), corresponding to linear-lut. The power levels shown in Fig. 3.5(a) are normalized power levels, such that the maxima corresponding to a phase level  $\pi$  correspond to a value of unity. The phase levels were extracted from the normalized power levels using the following formula

$$\varphi(gl) = \begin{cases} 2 \sin^{-1}(\sqrt{P_{norm}(gl)}) & \text{before first-order maxima} \\ 2\pi - 2 \sin^{-1}(\sqrt{P_{norm}(gl)}) & \text{beyond first-order maxima} \end{cases}, \quad (3.4)$$

where  $P_{norm}(gl)$  is the normalized power in either of the first orders ( $\pm 1$ ) corresponding to the addressed gray level ( $gl$ ).

Fig. 3.5(b) shows the extracted phase levels corresponding to different gray levels. It is clear from the phase modulation curve that the SLM used in the experiment has phase modulation capability less than  $2\pi$  and phase response is nonlinear.

### 3.3.2.2 Phase Compensation

Correction to the nonlinear phase response of the SLM requires development of a LUT that can transform the input gray level to an appropriate output gray level such that the SLM, when addressed with the transformed gray levels, results in a linear phase response of the SLM over the addressed gray levels. Towards this the following methodology has been adopted. First, the calculated phase ( $\varphi$ ) as a function of addressed gray values as shown in Fig. 3.5(b) are converted to equivalent gray levels using Eq. (3.5a) and are shown in Fig. 3.5(b) (the right side axis):

$$\varphi_{equivalent}(gl) = \text{round}\left(\frac{\varphi(\pi) \times gl(\text{max})}{2}\right) \quad (3.5a)$$

$$gl = f[\varphi_{equivalent}(gl)] \quad (3.5b)$$

where  $\varphi_{equivalent}(gl)$  is the equivalent gray level corresponding to the calculated phase in units of  $\pi$ , i.e.,  $\varphi(\pi)$ ,  $gl$  is the gray level, and  $gl(\text{max})$  is the maximum gray level with which the SLM can be addressed, i.e., 65,535 in our case.

To generate the phase compensation profile, the plotted phase modulation in units of gray level, i.e.,  $\varphi_{equivalent}(gl)$  [shown on the right-hand side axis of Fig. 3.5(b)] as a function of addressed gray levels is reversed. The addressed gray levels are plotted as a function of calculated equivalent gray levels as in Eq. (3.5b). This data is fitted piecewise in different regions with a ninth-order polynomial to extract the

equivalent gray levels corresponding to each of the addressed gray levels (i.e., for each integer values ranging from 0 to 65,535).

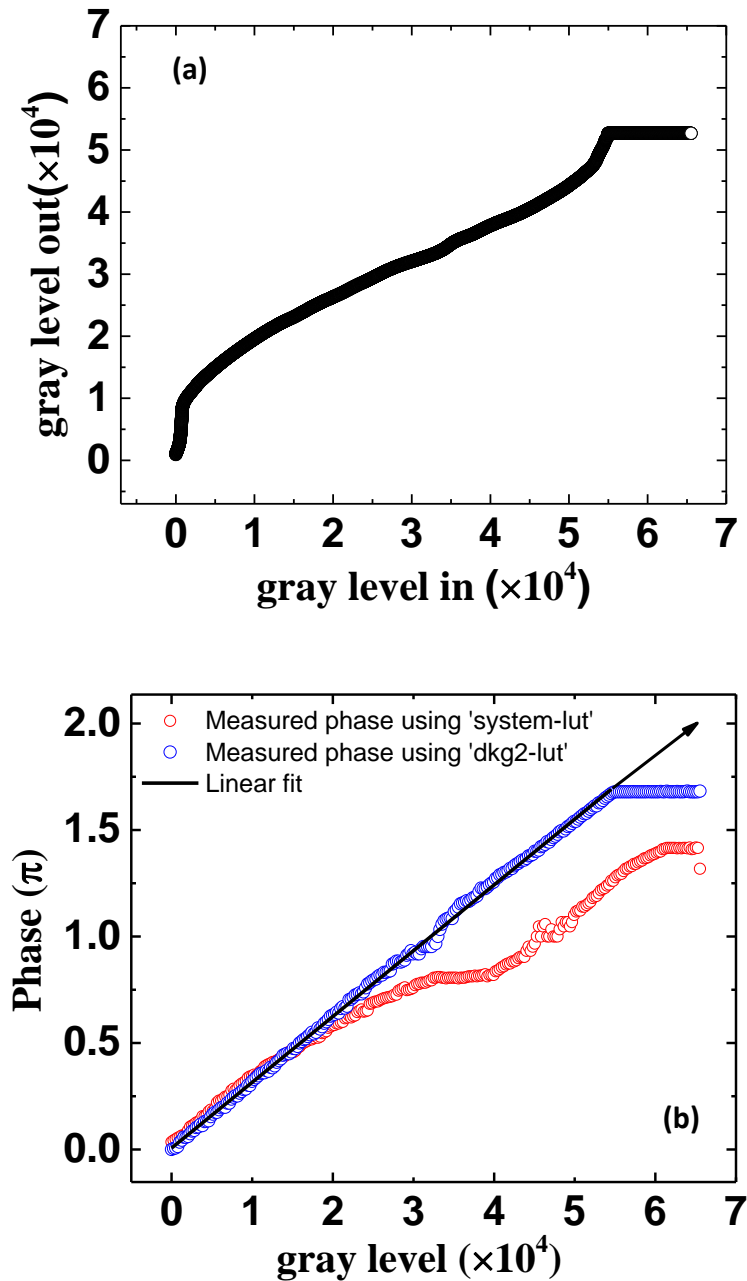


**Figure 3.6** (a) Plot of the phase compensation profile (termed dkg2-lut), showing the gray level out used for addressing of the SLM for each of the input gray values, required for having a linear phase response. (b) Plot of measured phase modulation curve as a function of gray level (i) using system-lut (shown in red circles) and (ii) using the generated phase compensation profile, i.e. dkg2-lut (blue circles) and a linear fit to the measured data (shown as a black line as a fit to the measured data) showing the corrected phase response behavior.

Since the SLM used has a limited phase modulation depth up to  $1.67\pi$  (the maximum attainable phase modulation depth for the present SLM), the gray level after which the attainable phase remains constant is assigned the same constant gray level out values. Fig. 3.6(a) shows the developed phase compensation profile (named dkg2-lut), showing a gray level out value corresponding to each of the gray level in values (i.e., input gray levels through hologram) ranging from 0 to 65,535. To test for the generated phase compensation profile, the SLM is characterized using the same diffraction-based method for both the supplier provided LUT file and the LUT generated by us. Fig. 3.6(b) shows the phase modulation curve measured for our SLM (i) using the system-lut and (ii) using the generated LUT (dkg2-lut). It is clear from Fig. 3.6(b) that the phase modulation characterized using the system-lut shows a nonlinear phase response, whereas the one using dkg2-lut shows a linear phase response; a linear fit to the phase response curve is also shown. Note that the maximum phase modulation depth also increased from  $1.4\pi$  (using system-lut) to  $1.67\pi$  (using dkg2-lut), the maximum attainable by any means for our SLM. Fig. 3.7 below shows the images of first-order diffraction spots along with the central zeroth order generated by displaying a blazed diffraction grating over the SLM (a) by using the system-lut and (b) using the phase compensation profile generated using the above-discussed methodology. It is found that the first-order diffraction efficiency (Diff. Eff.), defined by the formula,

$$\text{Diff. Eff. (1st order)} = \frac{\text{Power measured at the 1st order diffracted beam at the Fourier plane by displaying a blazed grating over SLM}}{\text{Power measured at the Fourier plane, when nothing is displayed over SLM}}, \quad (3.6)$$

is improved to 50% by using our generated phase compensation profile, dkg2-lut, as compared to the one measured using the system-lut, where the measured first-order

diffraction efficiency was only 29%. After the correction, one can note a significant decrease in intensity at the zeroth-order beam, as shown in Fig. 3.7(b). The remaining intensity in the zeroth order undiffracted beam is attributed to the limited phase modulation depth of our SLM.

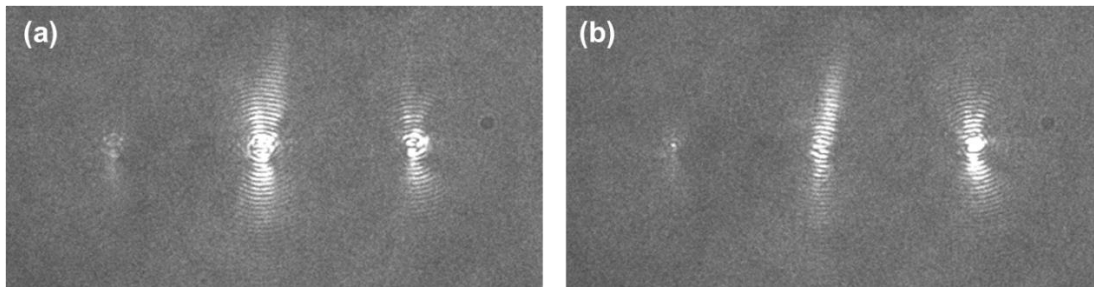


**Figure 3.7** Diffraction spots recorded by a camera by displaying a blazed grating over the SLM (a) by using system-lut and (b) by using the generated phase compensation profile, i.e., dkg2-lut showing the improvement in first-order diffraction efficiency.

### 3.3.3 Calibration of the SLM for SVPR

The above-discussed phase compensation method compensates for the nonlinearity in phase response behavior of the SLM globally. The liquid crystal SLMs are known to differ in their phase response over different spatial regions of the SLM. This may be (i) due to the varying thickness of the liquid crystal layer over the spatial region [86], and/or (ii) due to non-uniform illumination over the spatial region arising from the Gaussian profile of the incident laser, leading to differential heating in the LC layer [95]. Furthermore, experiments that require different power levels of incident laser over the SLM require frequent calibration for the SVPR. We present here a simple and robust technique for calibrating the varying phase response behavior over the spatial region of the SLM.

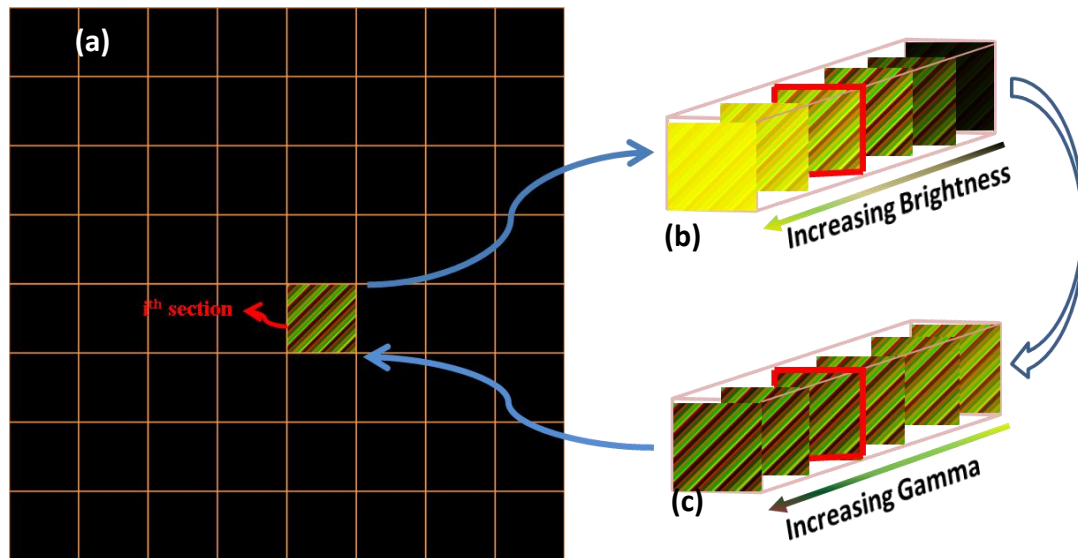


**Figure 3.8** (a) Typical hologram divided into 64 subsections with the  $i$ th subsection with a blazed grating and the other subsections being kept blank. (b) Set of holograms with varying brightness level to be displayed in the  $i$ th subsection, and the hologram, marked with the red boundary, with given brightness/contrast level producing maximum intensity at the first-order diffracted beam as an example. (c) Set of holograms with varying gamma levels for the hologram with optimized brightness/contrast marked with a red boundary in (b) to be displayed in the  $i$ th subsection, and the hologram with the red boundary showing a typical hologram with given gamma level producing maximum intensity at the first-order diffracted beam.

To characterize the local phase responses over the spatial region of the SLM, the SLM is divided into  $8 \times 8$  subsections, each consisting of  $64 \times 64$  pixels per subsection. A blazed grating is displayed on a subsection, while the rest of the sub-sections are kept blank, and the resulting power at first-order diffraction spot at the Fourier plane of SLM is measured using the diffraction set-up shown in Fig. 3.4(a). Fig. 3.8(a) shows a typical hologram with a blazed grating displayed at the  $i$ th subsection and the other subsections kept blank. The holograms for each of the subsections are generated with varying brightness/contrast levels, and the power of the first-order diffracted beam is measured for a range of brightness/contrast levels. The hologram with brightness/contrast level giving a maximum in the first-order diffracted spot is selected. Fig. 3.8(b) shows holograms (blazed gratings) with different brightness

levels imposed on the SLM to determine the brightness level that produces a diffracted beam with high intensity, and the hologram highlighted with a red boundary is a typical one that gives a maximum at the first-order diffracted spot. Then, holograms with different gamma values are generated, corresponding to the optimized brightness level and imposed on the SLM sequentially [Fig. 3.8(c)]; the corresponding power levels were measured at the first-order diffracted spot. Finally, the brightness/contrast level and the gamma value that give the maximum power at the first-order diffracted beam are identified as the optimized brightness, contrast, and gamma levels for a particular  $i$ th subsection. The procedure is repeated for each of the subsections (64 subsections in our case). Fig. 3.9(b) shows a table of optimized brightness/contrast and gamma levels for each of the 64 subsections, with each subsections divided into three compartments. The parameters in the two top compartments correspond to the optimized brightness/contrast level, and the bottom one represents the gamma level optimized for a particular subsection producing maximum intensity at the first-order diffracted spot and, hence, an improved diffraction efficiency. The two parameters characterizing brightness/contrast are in the range [0.0-0.9, 0.1-1.0], and are (i) the lower limit and (ii) upper limit of the intensity values, the interval to which the image is rescaled linearly from the input limits (i.e., lower and upper-intensity values in the input image). The intensity value [0,1] refers to a gray level value of [0,255] for an 8 bit image. The gamma level ranges from 0.1 onward, and so on. These optimized brightness/contrast and gamma levels corresponding to each subsection are incorporated in the calculation of the hologram in the WGS algorithm to generate desired patterns in the sample plane, to correct for the varying phase response over the spatial region of the SLM. Fig. 3.9(a) shows a typical hologram corresponding to a blazed grating, which produces a first-order

diffracted spot before correction for SVPR and after incorporating correction for the SVPR [Fig. 3.9(c)]. It is found that with the above correction the first-order diffraction efficiency improved from 50% to 55%.

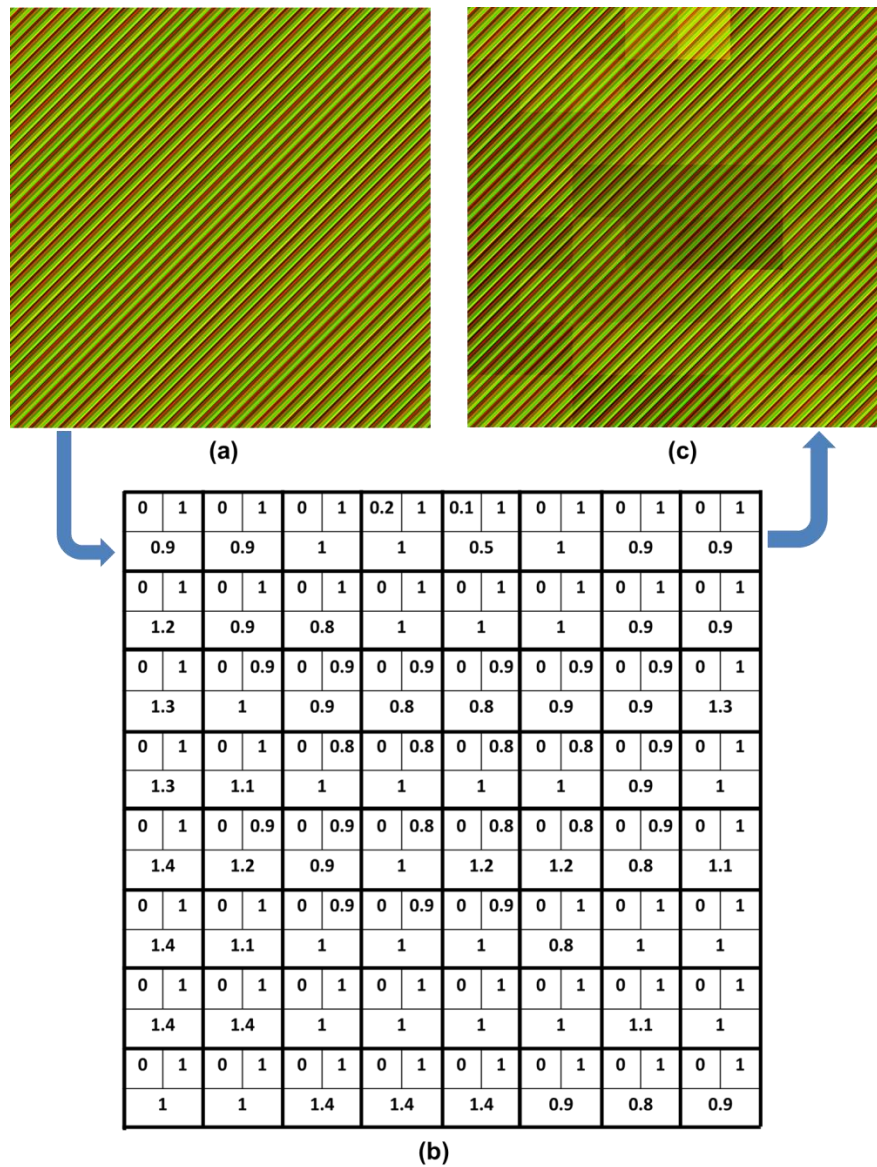


**Figure 3.9** (a) Typical blazed hologram displayed on the SLM to produce a first-order diffracted spot at the Fourier plane of the SLM. (b) A table with 64 subsections, each subsection being divided into three compartments. The two top parameters represent the optimized brightness/contrast level, with parameters in the range [0.0-0.9, 0.1-1.0], and the bottom one represents the optimized gamma level, ranging 0.1 onward, for each of the subsections. These parameters are the corrections for the SVPR. (c) Typical blazed hologram calculated by WGS algorithm, while taking into account the correction for the SVPR.

### 3.4 Generation of holographic optical traps

Holographic optical tweezers involve the creation of tightly focused multiple foci, i.e., a set of diffraction-limited spots of a laser beam at the sample plane of a microscope objective, to trap and manipulate a multitude of submicroscopic particles in three dimensions. In addition to creating a set of discrete points of light, one may require a continuous pattern of light at the sample plane as per the experimental needs. This calls for finding an optical field at the SLM plane, which on propagation to the sample plane yields the desired intensities at the intended trapping sites. This optical field on the SLM, resulting into a desired field at the trapping plane is referred as a hologram. In general, these holograms may be complex, which modulate both amplitude and phase of the incident light over the SLM. Amplitude modulation involves the physical removal of light, leading to a reduction in the efficiency of the system. Hence, we restrict ourselves to algorithms which produce phase-only modulation holograms for a desired light distribution in the trapping plane. Our SLM supports phase modulation only. The propagation of the field from the SLM plane to the trapping plane is mathematically described by scalar diffraction theory as in the following section.

#### 3.4.1 Propagation of Field from SLM plane to the trapping plane

The complex field at a point  $r(x,y,z)$  diffracted from an arbitrary aperture is given by Rayleigh-Sommerfeld diffraction integral, using scalar diffraction theory:

$$v(x, y, z) = \frac{1}{i\lambda} \iint_{\Sigma} u(\xi, \eta, 0) \frac{e^{ikr}}{r} \cos(\varphi) d\xi d\eta, \quad (3.7)$$

where  $\Sigma$  is the area of the aperture at  $z=0$ ,  $u(\xi, \eta, 0)$  is the field at the aperture,  $r$  is

the magnitude of the vector connecting the point  $(x,y,z)$  to an arbitrary point on the aperture  $(\xi,\eta,0)$  and  $\varphi$  is the angle vector  $r$  makes with the normal to the aperture.

The value of  $r$  is given by

$$r = \left[ (x - \xi)^2 + (y - \eta)^2 + z^2 \right]^{\frac{1}{2}} \quad (3.8)$$

In the paraxial approximation, when the distance of observation is much larger compared to the aperture dimension, i.e., for small  $\varphi$ ,  $r$  can be approximated by the following expression

$$\begin{aligned} r &= z \left[ 1 + \frac{(x - \xi)^2 + (y - \eta)^2}{z^2} \right]^{\frac{1}{2}} \quad (\text{Using binomial expansion}) \quad (3.9) \\ &\approx z + \frac{1}{2} \frac{(x - \xi)^2 + (y - \eta)^2}{z} \end{aligned}$$

Using this approximation for  $r$  in Eq. (3.7) for the exponential term and keeping the terms only up to the first-order for other factors, we get the Fresnel diffraction integral

$$v(x, y, z) = \frac{e^{ikz}}{i\lambda z} \iint_{-\infty}^{+\infty} u(\xi, \eta, 0) e^{\frac{ik}{2z}[(x-\xi)^2 + (y-\eta)^2]} d\xi d\eta \quad (3.10)$$

The calculation of field at the trapping plane requires the field in the plane of SLM to be numerically propagated through all the optical components of the holographic optical terrain, which may seem to be cumbersome. However, the geometry of the HOTs system as designed makes the problem of calculation of field at the trapping plane straightforward. Fig. 3.10 below shows a simplified schematic of the optical terrain between the SLM and the focal plane (Imaging plane) of the microscope objective of the HOTs set-up in Fig. 3.2.

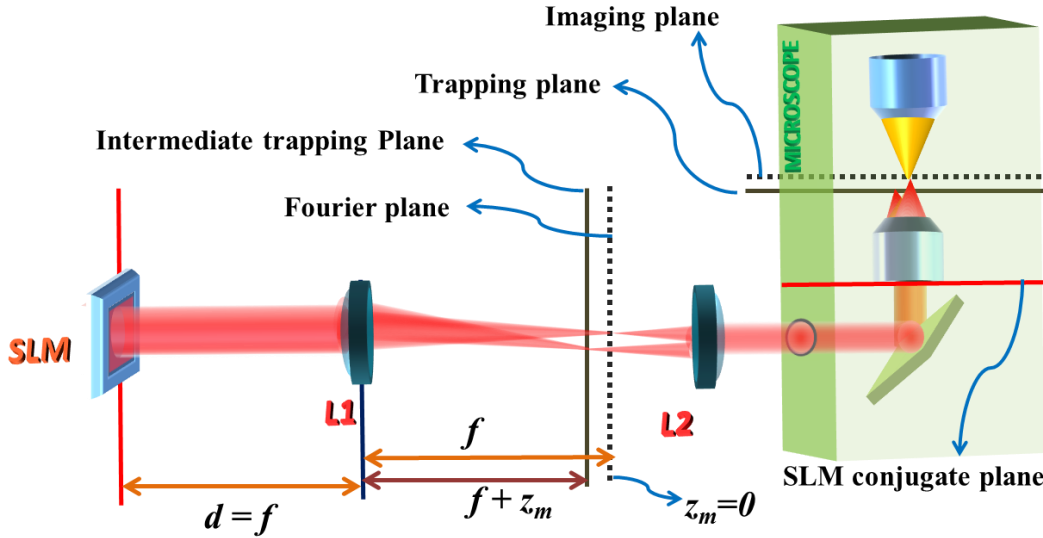


**Figure 3.10** (a) Simplified schematic of the HOTs set up of Fig. 3.2 describing the propagation of field from the SLM plane to the trapping plane. SLM being imaged by L1 and L2 at the back aperture of the microscope objective and the Fourier plane of SLM being imaged by L2 and microscope objective at the imaging plane making a simple Fourier transform relationship between the SLM plane and the focal plane (Imaging plane) of the microscope objective.

The SLM being separated from lens L1 by its focal length distance, lens L2 being separated by a distance of its focal length from the back aperture of microscope objective MO, and L1 and L2 separated by the sum of their focal lengths constitute two interconnected  $4f$ -configurations. This arrangement images the SLM on to the back aperture of MO and the Fourier plane of SLM to the focal plane (imaging plane) of MO, with a magnification factor dependent on focal lengths of the lenses. The problem now reduces to the propagation of field from the SLM plane to the rear of L1 through free space, then through L2 and finally to the location where the trap is desired shown as the intermediate trapping plane (Fig. 3.10).

The field at the rear surface (left) of L1 is given by using the Fresnel diffraction formula, (Eq. (3.10)) as

$$v(x', y', d) = \frac{e^{ikd}}{i\lambda d} \iint_{-\infty}^{+\infty} u_{SLM}(\xi, \eta) e^{\frac{ik}{2d}[(x' - \xi)^2 + (y' - \eta)^2]} d\xi d\eta \quad (3.11)$$

where  $(x', y')$  are the transverse coordinates on the plane of the lens L1,  $(\xi, \eta)$  the transverse coordinates on the SLM plane with  $u_{SLM}(\xi, \eta)$  the field at the SLM plane, and  $d$  is the distance between the SLM and L1.

The field at the right surface of L1, assuming the lens to be thin, is

$$v(x', y', f) = \frac{e^{ikd}}{i\lambda d} \iint_{-\infty}^{+\infty} u_{SLM}(\xi, \eta) e^{\frac{ik}{2d}[(x' - \xi)^2 + (y' - \eta)^2]} e^{\frac{-ik}{2f}[(x')^2 + (y')^2]} d\xi d\eta \quad (3.12)$$

Since the SLM is kept at a distance  $d=f$ , the focal length of L1, the quadratic phase factor in the intermediate coordinates  $(x', y')$  in Eq. (3.12) dies out and the above equation reduces to

$$v(x', y', f) = \frac{e^{ikf}}{i\lambda f} \iint_{-\infty}^{+\infty} u_{SLM}(\xi, \eta) e^{\frac{ik}{2f}(\xi^2 + \eta^2)} e^{\frac{-i2\pi}{\lambda f}(\xi x' + \eta y')} d\xi d\eta \quad (3.13)$$

Applying the diffraction integral in Eq. (3.10) to propagate the field from the right surface of the lens L1 to a plane at a distance,  $(f + z_m)$  and evaluating the integral over the intermediate coordinate gives an expression for the entire propagation as

$$v(x, y, z) = \frac{1}{i\lambda f} e^{i\frac{2\pi}{\lambda}(2f + z_m)} \iint_{-\infty}^{+\infty} u_{SLM}(\xi, \eta) e^{-i\frac{\pi z_m}{\lambda f^2}(x^2 + y^2)} e^{-i\frac{2\pi}{\lambda f}(\xi x + \eta y)} d\xi d\eta \quad (3.14)$$

where  $z = 2f + z_m$ . The apertures of the lenses are assumed to be of sufficient extension to transmit the light diffracted off the SLM.

### 3.4.2 Hologram Construction

The numerical propagation of the field from the SLM plane to the trapping plane needs discretization of the expression in Eq. (3.14) with sample spacing corresponding to the pixel size of the SLM. Assuming uniform illumination on SLM and restricting to Gaussian point traps for optical trapping applications, the complex field at the  $m$ th trapping site in the sample plane by summing up the contributions from all the SLM pixels ( $N=512 \times 512$ ) (Fig. 3.11) is given as [69]

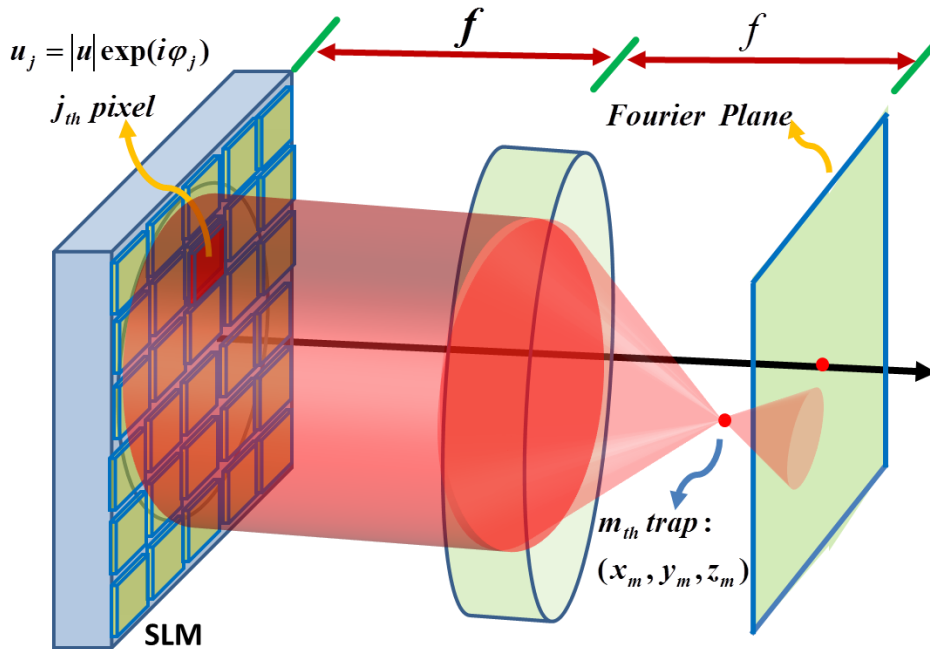


**Figure 3.11** Schematics representation of the geometry of the effective Fourier field propagation from the SLM plane to the trapping site  $(x_m, y_m, z_m)$  relative to the center of the Fourier plane.

$$v_m(x_m, y_m, z_m) = \frac{e^{i2\pi(2f+z_m)/\lambda}}{i} \frac{a^2}{\lambda f} \sum_{j=1, N} |u| e^{i(\phi_j - \Delta_j^m)} \quad (3.15)$$

where

$$\Delta_j^m = \frac{\pi z_m}{\lambda f^2} (x_j^2 + y_j^2) + \frac{2\pi}{\lambda f} (x_j x_m + y_j y_m) \quad (3.16)$$

$(x_m, y_m, z_m)$  are the coordinates of the  $m$ th trapping site relative to the Fourier plane,  $(x_j, y_j)$  are the  $j$ th pixel coordinates of the SLM,  $u_j = |u| \exp(i\varphi_j)$  the complex amplitude of the field reflected off the  $j$ th pixel of SLM and  $a^2$  is the pixel surface area of SLM (Fig. 3.11). The first term in  $\Delta_j^m$  is the lens term that is responsible for the axial displacement of the trap spot and the second term is the grating term that gives rise to the lateral displacement of trap spots. This term can also be generalized to add orbital angular momentum to the trapping beams [282]. Eq. (3.15) can be written in a more compact way by the introduction of a dimensionless variable  $V_m$  as [69]

$$V_m = \sum_{j=1, N} \frac{1}{N} e^{i(\varphi_j - \Delta_j^m)} \quad (3.17)$$

The physical significance of  $V_m$  is that the quantity  $I_m = |V_m|^2$  is a measure of the energy flux (in units of total energy flux through SLM,  $W_0 = c\epsilon_0 N |u|^2 a^2 / 2$ ) through an area  $(\lambda f)^2 / Na$  (area of the diffraction-limited spot). Also for  $z_m=0$ ,  $V_m$  is the discrete Fourier transform of  $\exp(i\varphi_j)$  at frequencies  $(x_m / \lambda f, y_m / \lambda f)$ .

The aim of different algorithms to be discussed here is to find a best choice of  $\varphi_j$ s to maximize the  $|V_m|$  on all traps for a given set of  $\Delta_j^m$ . The performance of various algorithms are quantified by three parameters, (i) efficiency ( $e$ ), (ii) uniformity ( $u$ ) and (iii) standard deviation ( $\sigma$ ) given as

$$e = \sum_m I_m, \quad u = 1 - \frac{\max[I_m] - \min[I_m]}{\max[I_m] + \min[I_m]}, \quad \sigma = 100 \sqrt{\frac{\langle (I - \langle I \rangle)^2 \rangle}{\langle I \rangle}} \quad (3.18)$$

where  $\langle \dots \rangle$  is the average over all the trap indices  $m$ . In addition to these parameters, one major effect that affects the uniformity in the holographic optical traps is the

production of ghost tweezers, which arise due to the constructive interference of higher orders of diffraction [283]. The section below describes the various types of algorithms to generate holographic optical traps.

### 3.4.3 Algorithm to generate holographic optical traps

#### (i) Random Mask Encoding (RM)

In this method, the phase shift for each of the pixels of SLM is defined to be the phase shift for any one of the traps randomly chosen from the number of traps  $M$ , and it is found through

$$\varphi_j = \Delta_j^{m_j} \quad (3.19)$$

where  $m_j$  is a number between 1 and  $M$  randomly chosen for each  $j$ , such that each trap is assigned an equal number of pixels on an average. This method of generating hologram is simple and fast. The efficiency decreases with the increase in the number of traps.

#### (ii) Superposition of Prisms and Lenses (S)

This algorithm maximizes the sum of the projections of all the  $V_m$  on a fixed axis in the complex plane. The maximization of the real part of  $\sum_m V_m$ , i.e., maximization along the real axis with respect to  $\varphi_j$  gives the phase shift as

$$\varphi_j = \arg \left[ \sum_m e^{i \Delta_j^m} \right] \quad (3.20)$$

In this algorithm, the phase of each pixel is chosen as the argument of the complex sum of separate, single trap holograms. The S algorithm is slower and has poor

uniformity than the traps produced by RM algorithm, but have higher efficiencies of an order in comparison. One of the major drawbacks of this algorithm is the production of ghost traps in case of symmetrical trap geometries.

### (iii) Random Superposition (SR)

In this case, the sum of the projections of all the  $V_m$  is maximized on randomly chosen directions in the complex plane. We seek a maximum of the real part of  $\sum_m V_m e^{-i\alpha_m}$  with respect to  $\varphi_j$  where  $\alpha_m$  are random numbers uniformly distributed in  $[0, 2\pi]$ . Phase shift is the superposition of single trap holograms with coefficients of unit modulus and a random phase, given as

$$\varphi_j = \arg \left[ \sum_m e^{i(\Delta_j^n + \alpha_m)} \right] \quad (3.21)$$

The RS algorithm results in a better performance compared to S algorithm in terms of the diffraction efficiency, though has poor uniformity. However, it produces traps with good uniformity with low symmetry geometries [69]. For symmetric trap patterns, uniformity is improved by the addition of a certain amount of spatial disorder in the trap locations [283].

All these algorithms as described above result in poor uniformities among the created trap spots. These algorithms are based on the maximization of the sum of the amplitudes of  $V_m$  with no bias towards uniformity. There are various optimization algorithms based on iterative methods which start with a guess for  $\varphi_j$ , either a random phase or the one obtained from SR, and the algorithm proceeds iteratively to obtain optimized phase shifts, to be discussed in the following sections.

**(iv) Direct Search (DS)**

This algorithm works on the basis of maximization of a gain function by a direct search. It starts with a guess for  $\varphi_j$  such as one from SR algorithm and a pixel is chosen at random and cycled through available gray levels in order to achieve a maximum in the gain function:

$$\langle I \rangle - \chi\sigma \quad (3.22)$$

with  $\chi$  parameter set to 0.5, the algorithm achieves a uniformity of  $u = 1.00$  in  $1.3 \times N$  steps of computational cost, scaling as  $M \times$  number of available gray levels and with  $e = 0.68$  [74].

**(v) Gerchberg-Saxton (GS) Algorithm**

The GS algorithm was developed by crystallographers R. W. Gerchberg and W. O. Saxton, to determine the phase of a wave with known intensity distributions in the diffraction and imaging planes [67]. In this case, to determine the optimized phase, the complex amplitude is propagated back and forth between the SLM plane and the trapping plane. In each iteration of GS algorithm, the intensity in the trapping plane is replaced with the target intensity and with the beam intensity profile of the incident laser at the SLM plane in each iteration of GS algorithm. The forward and backward propagation are performed with Fast Fourier transforms (FFT). GS algorithm can be applied to generate hologram for a continuous pattern or any discrete pattern of light in the target plane. However, in case of requirement of an array of point traps in the target plane, it becomes unnecessary to calculate the complex amplitude at points whose amplitude will be replaced to zero at the target plane before the back propagation. Further, FFT has a drawback of discretization of the trap

transverse coordinates [284]. Hence, instead of calculating the complex field at all the points using FFT, the method can be applied to calculate the field only at the desired trapping sites, a faster and more versatile implementation of GS for generation of holographic optical traps [69]. In this case the GS converges to a phase hologram by maximizing the sum of the amplitudes of  $V_m$  without projecting them onto any directions in the complex plane. The phase shift is given as

$$\varphi_j = \arg \left[ \sum_m e^{i \Delta_j^m} \frac{V_m}{|V_m|} \right] \quad (3.23)$$

$\varphi_j$  is the argument of the linear superposition of single trap holograms with coefficients of unit modulus and a phase given by the phase of  $V_m$  itself. The algorithm starts with a guess of  $\varphi_j$  that is either a random phase or a phase computed by the use of SR algorithm and then uses Eq. (3.23) in the subsequent (~10) iterations to produce an optimized phase. It acquires an efficiency and uniformity of  $e = 0.94$  and  $u = 0.60$  with around 30 iterations as described in [69].

#### (vi) Generalized Adaptive Additive (GAA) Algorithm

In this algorithm, a bias towards uniformity is introduced by seeking a maximum in the quantity like  $\prod_m |V_m|$  or equivalent quantity  $\sum_m \log |V_m|$ . The phase shift, in this case, is given as

$$\varphi_j = \arg \left[ \sum_m e^{i \Delta_j^m} \frac{V_m}{|V_m|} \left( 1 - \xi + \frac{\xi}{|V_m|} \right) \right] \quad (3.24)$$

$\xi$  is a parameter whose value determines the percentage of bias towards efficiency and uniformity. With  $\xi=0.5$ , an equal bias towards efficiency and uniformity, this

algorithm produces a uniformity  $u = 0.79$  with efficiency  $e = 0.93$  after 30 iterations [69]. It produces traps with almost the same efficiency as GS with an improved uniformity.

### (vii) Weighted Gerchberg Saxton (WGS) Algorithm

In this case, uniformity in the produced trap spots is obtained by modifying the target intensity distribution of the trapping sites at each iteration. This method introduces  $M$  extra degrees of freedom called weights  $w_m$  and maximizes the weighted sum  $\sum_m w_m |V_m|$ , with a constraint that all  $|V_m|$  are equal. The phase shift is given as

$$\varphi_j = \arg \left[ \sum_m e^{i \Delta_j^m} \frac{w_m V_m}{|V_m|} \right] \quad (3.25)$$

The iteration starts with a choice of  $\varphi_j$  either from RS or a random phase and with the starting weight, and proceeds as follows:

$$\begin{aligned} 0^{th} \text{ Step: } w_m^0 &= 1, & \varphi_j^0 &= \varphi_j^{RS} \text{ or } \varphi_j^{random}, \\ k^{th} \text{ Step: } w_m^k &= w_m^{k-1} \frac{\langle |V_m^{k-1}| \rangle}{|V_m^{k-1}|}, & \varphi_j^k &= \arg \left[ \sum_m e^{i \Delta_j^m} \frac{w_m^k V_m^{k-1}}{|V_m^{k-1}|} \right] \end{aligned} \quad (3.26)$$

In each iteration of WGS, the weight  $w_m$  is adjusted to reduce the deviations of  $|V_m|$  for all traps from the average  $\langle |V_m| \rangle$ . This algorithm produces traps with  $u = 0.99$  with efficiency  $e = 0.93$  after 30 iterations [69]. The WGS algorithm produces traps with the highest uniformity and efficiency compared to other optimization algorithms.

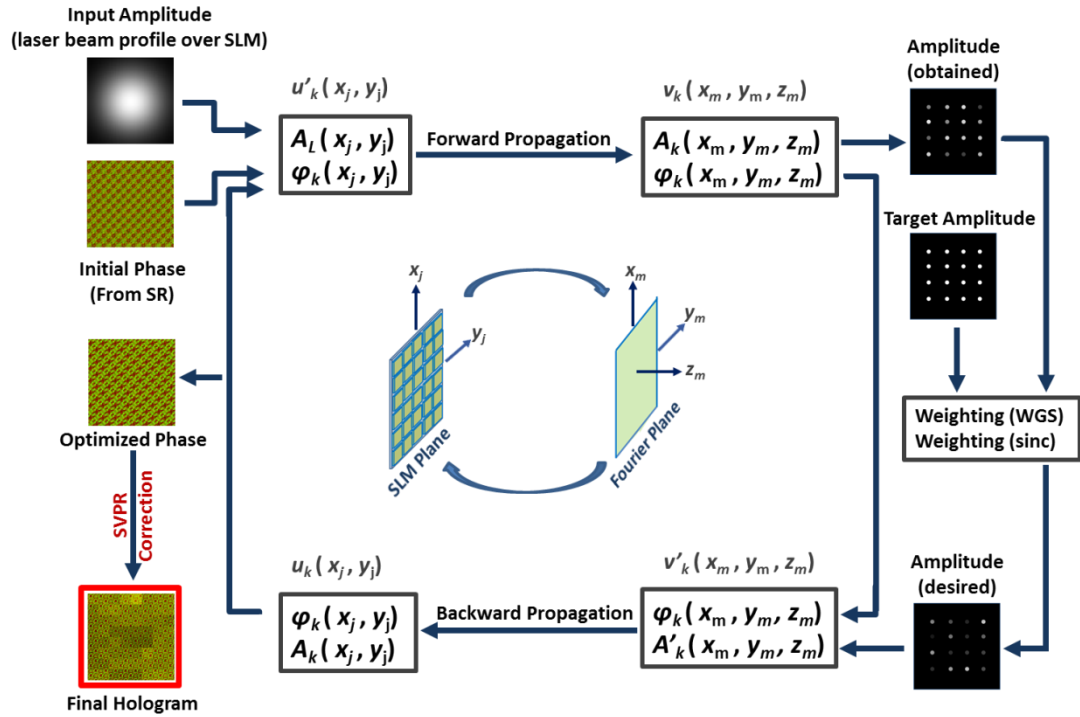


**Figure 3.12** Flow chart describing the modified (WGS) algorithm. An estimate of kinoform is taken from a random superposition (SR) algorithm with the amplitude as the profile of laser over the SLM as an initial field. The field is propagated from the SLM plane to the trapping plane. A new field is constructed using the obtained phase and amplitude with the weighted combination of target amplitude and obtained amplitude (taking into account weighting of diffraction effects due to SLM pixelation). The field is propagated back to the SLM plane, and the amplitude is replaced with the amplitude of the laser while keeping the phase the same. The field is again propagated to the trapping plane. The iteration is repeated until an optimized phase is obtained. Finally, the hologram is corrected for the SVPR.

In our work, we use the WGS algorithm to generate an array of holographic optical traps and SR algorithm to generate optical traps needed to manipulate microscopic objects during the experiment. Fig. 3.12 shows the flow chart of the WGS algorithm as implemented in our work to generate optical traps. To generate a phase modulating hologram for production of an array of focal spots in the sample plane, constraints are imposed on the amplitude of the field on either of the SLM plane and the trapping plane. The amplitude at the SLM plane is dictated by the amplitude profile of the incident laser beam over the SLM, i.e., a Gaussian profile,

and the amplitude at the trapping plane by the target amplitudes as desired by the pattern of traps. The steps to generate a hologram using the WGS algorithm as implemented in our work are as follows:

a) An initial field  $u'_k(x_j, y_j)$  is created by choosing a phase from SR algorithm  $\varphi_k(x_j, y_j)$  and amplitude  $A_L(x_j, y_j)$  as the incident laser beam profile over SLM.

b) The field is propagated from the SLM plane to the trapping plane to obtain

$$v_k(x_m, y_m, z_m) = A_k(x_m, y_m, z_m) e^{i\varphi_k(x_m, y_m, z_m)} .$$

c) At the trapping plane, the phase is kept as obtained, and the amplitude is replaced by an amplitude dictated by a combination of the obtained amplitude with the target amplitude with proper weighting as in Eq. (3.25) and weighting due to diffraction effects caused by pixelation of SLM [264].

d) The calculated field  $v'_k(x_m, y_m, z_m) = A'_k(x_m, y_m, z_m) e^{i\varphi'_k(x_m, y_m, z_m)}$  is propagated back to the SLM plane to obtain

$$u_k(x_j, y_j) = A_k(x_j, y_j) e^{i\varphi_k(x_j, y_j)} .$$

e) At the SLM plane, the amplitude  $A_k(x_j, y_j)$  is replaced with the amplitude  $A_L(x_j, y_j)$  of the laser beam to obtain

$$u'_k(x_j, y_j) = A_L(x_j, y_j) e^{i\varphi_k(x_j, y_j)} .$$

f) The steps from (b) to (e) are repeated for the number of iterations required to get the optimized phase.

g) The optimized phase is corrected for SVPR by dividing it to many subsections to get the final hologram to generate the optical traps.

### 3.4.4 Numerical Propagation

To generate a discrete set of point traps, in general, the field is propagated by numerically calculating the field only at the trap locations. To generate a continuous pattern of light in the sample plane, the numerical propagations from the SLM plane to the trapping plane back and forth are done by the use of fast Fourier transforms (FFTs). The choice of method of numerical propagation depends upon the desired pattern at the sample plane. With the use of FFT, the field can be calculated on a single plane only. By the use of the method of calculating the field at the trap locations only, traps can be generated in a 3D space near the Fourier plane, provided the Fresnel approximation is valid. If the trap spots are required in a single plane, then FFT is the most efficient method for field propagation. Further, in FFT the computation time is independent of the number of traps at the trapping plane, and hence when a large number of traps is to be generated, FFT is efficient.

In the numerical propagation of field from SLM plane to its Fourier plane, the sample spacing in the sample plane is chosen to coincide with the pixel size of SLM. The maximum displacement ( $x_{max}$ ,  $y_{max}$ ) up to which the traps can be placed is dictated by the sampling period in either direction by Nyquist criterion as

$$x_{max} = \frac{\lambda f}{2 \times spx}, \quad y_{max} = \frac{\lambda f}{2 \times spy} \quad (3.27)$$

$\lambda$  is the wavelength of the laser used for trapping,  $f$  is the distance between the SLM plane as imaged at the back aperture of the objective and its Fourier plane (trapping plane) and ( $spx$ ,  $spy$ ) are the sampling periods in x and y directions. The resolution with which the traps can be placed in the trapping plane depends on the total sampling length in the SLM plane (sampling period  $\times$  number of pixels in a given direction). In

order to place the traps with improved resolution (as required by interaction studies requiring the traps to be moved with resolution down to few nanometers such as interaction studies between bacterial cells), additional pixels were zero padded in order to increase the total sampling length in the SLM plane, which in turn causes resolution improvement as  $(\lambda f / (M + xpad) \times spx, \lambda f / (N + ypad) \times spy)$  in x and y directions respectively.  $M$  and  $N$  are number of SLM pixels, and  $xpad$  and  $ypad$  are the number of pixels with zero transmittance values in x and y directions respectively (Fig. 3.13).

Furthermore, the fields numerically computed at the SLM's Fourier plane are modulated by the Fourier transform of the field of a single pixel of SLM (SLM being pixelated in nature). Hence, the intensity in the trapping field is given by the field calculated at the trapping sites modulated by a squared sinc function, the Fourier transform of a rectangular aperture, whose minima coincides with double the maximum displacement at which a trap can be placed.

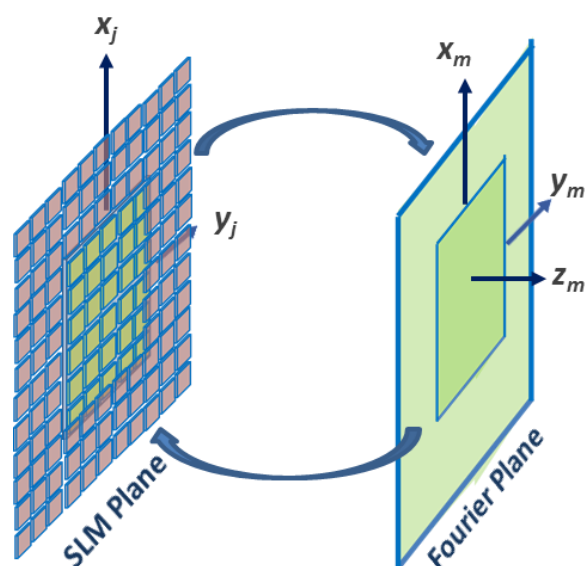


**Figure 3.13** Schematic of numerical propagation to improve resolution at the trapping plane by zero padding pixels around SLM pixels.

Fig. 3.14(a) shows a 4×4 square array of trap spots in 2D. As we move away from the zeroth order of the diffraction spot, it has been found that the intensity of the spots decreases continuously. This is attributed to the pixelated nature of SLM. The target intensities are hence weighted by an inverse of the two-dimensional squared sinc function (diffraction pattern due to a single pixel of SLM) before propagation to the SLM plane. The resulting effect after correcting for the non-uniformity due to diffraction effects due to pixelation of SLM is shown in the array of 4×4 spots in Fig. 3.14(b). The trap spots are nearly uniform in intensity except for the variation due to the interference of ghost order with the trap spots that is generated by higher order interferences. The effects of ghost order becomes more prominent in generating symmetric arrays, and are removed by introducing spatial disorder of one or two pixels in the coordinates of the trap spots.

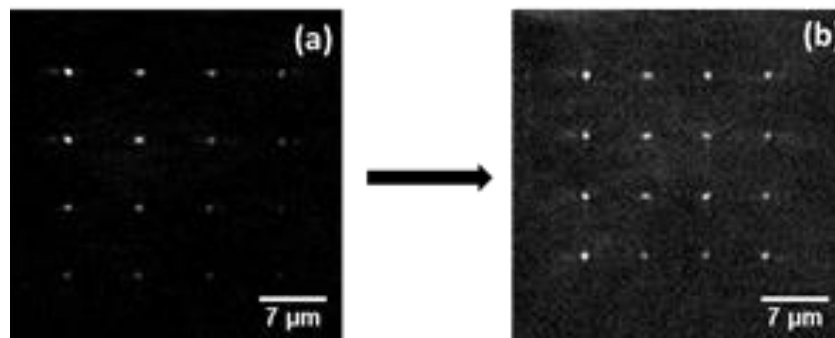


**Figure 3.14** (a) 4×4 array of spots without uniformity correction showing a decrease in intensity as we move away from the zeroth order, (b) 4×4 array of spots with uniformity correction showing equal intensity at the trap spots (except for the effects of ghost order on the uniformity).

### 3.5 Array of traps

To generate an array of traps, we use the WGS algorithm with 20 iterations (i.e., only one cycle) to generate the hologram to produce traps with theoretical uniformity (>99%). The generated hologram is displayed over SLM to produce the

desired spots at the focal plane. An array of eight focal spots (Fig. 3.15) in a circle was generated by displaying a suitable hologram on the SLM using the WGS algorithm. Fig. 3.15(a) shows the trap spots in a circle generated using system-lut. Non-uniformity in the intensities of the traps generated along with a strong zeroth-order beam are seen. Fig. 3.15(b) shows the same array of traps in a circle generated using the optimized LUT, dkg2-lut (corrected for SVPR). It is seen that the intensities of the trap spots are fairly uniform, with a less intense zeroth order, showing improved first-order diffraction efficiency. Uniformity ( $u$ ) in the intensities of the created trap spots is determined by using Eq. (3.18), with  $I_m$  representing the peak intensity of the trap spots measured from reflection measurements. Uniformity is found to be improved from 76% to 97% with the optimized LUT with correction for SVPR compared to that generated using system-lut.

Moreover, all spots in the array in the circle as shown in Fig. 3.15(a) were not able to trap the particles stably. Only a few spots were observed to trap the particles (Polystyrene, diameter 1.2  $\mu\text{m}$ ) along with a strong trapping in the zeroth-order spot, whereas all the trap spots created using the optimized hologram (Fig. 3.15(b)) were capable of trapping particles, with no trapping at the zeroth-order spot. The particles approaching the traps first get trapped at the outer boundary and do not allow the other particles to diffuse inside the circle to get trapped in the zeroth-order spot. Fig. 3.15(c) shows polystyrene spheres of diameter 1.2  $\mu\text{m}$ , suspended in water trapped in the array of eight focal spots in a circle at a distance of 10  $\mu\text{m}$  away from the coverslip. The above eight focal spots were generated using the optimized hologram with dkg2-lut and SVPR correction, shifted by a distance of  $\sim 1$   $\mu\text{m}$  from the focal plane (to avoid disturbance due to the undiffracted spot).

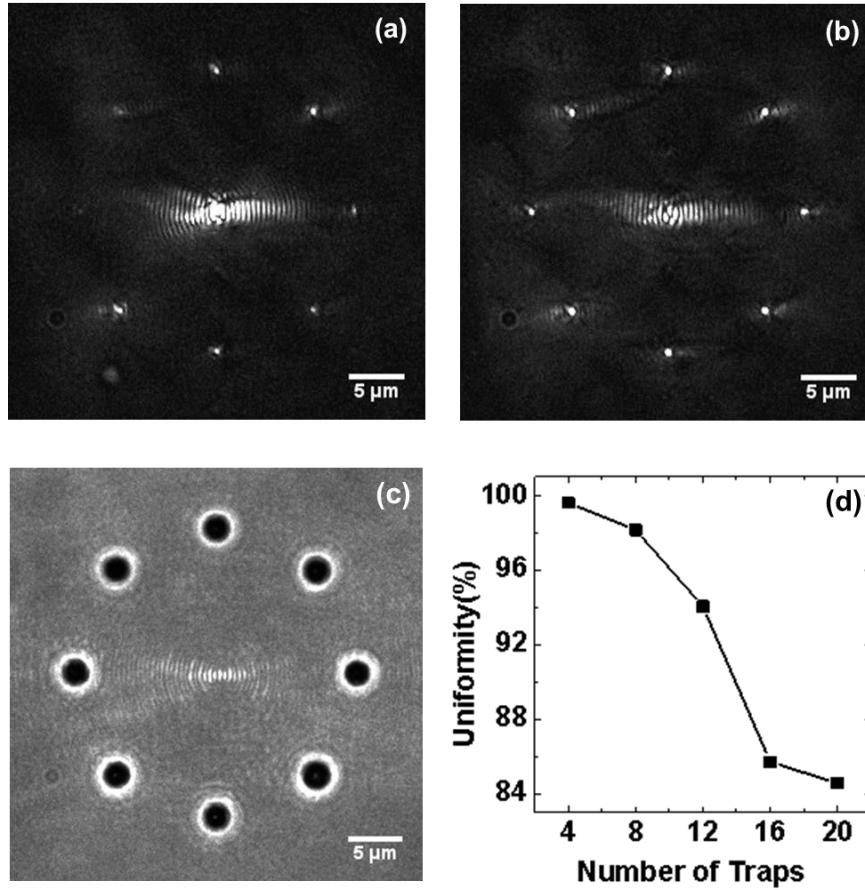


**Figure 3.15** (a) Circular array of eight trap spots around the strong central zeroth order with a radius of 100 pixels corresponding to 12.8 μm, generated using WGS algorithm with the system-lut, showing non-uniform intensities among the trap spots. (b) Circular array of eight traps around a weak zeroth order with a radius of 100 pixels generated using same WGS algorithm with the developed LUT, dkg2-lut, in place, showing fairly uniform intensities among the trap spots with higher diffraction efficiency. (c) Polystyrene spheres of diameter 1.2 μm trapped in the array shifted 1 μm above the focal plane, generated using an optimized hologram with SVPR correction and using dkg2-lut. (d) Variation of uniformity with number of traps.

The trap stiffness in all these trapping sites has been determined by recording the videos at a frame speed of 165 fps and using optical potential analysis method [218]. The average trap stiffness at all eight trapping sites is  $1.26 \pm 0.16$  μN/m. The incident laser ( $\lambda = 1064$ nm) power on the SLM was 970 mW. The uniformity in the trap stiffness is calculated by Eq. (31.8), where the peak intensities  $I_m$  were replaced by the trap stiffness  $\kappa$ . The uniformity in trap stiffness is found to be 80%, limited by

the phase modulation depth of  $1.67 \pi$  for our SLM. Further, the uniformity of the trap spots on the circle with increasing number of trap spots is calculated. It was found that the uniformity decreases [Fig. 3.15(c)] as the numbers of traps are increased.

To understand the effect of SVPR correction on trap quality, we calculated the spot sharpness metric, defined as [285]

$$M = \left( \sum_n I_n \right)^2 / \sum_n I_n^2 \quad (3.28)$$

where  $I_n$  is the intensity of the  $n$ th pixel and  $n$  is the total number of pixels in a given area. Low value of  $M$  implies a more tightly focused spot and, hence, a better trap quality.

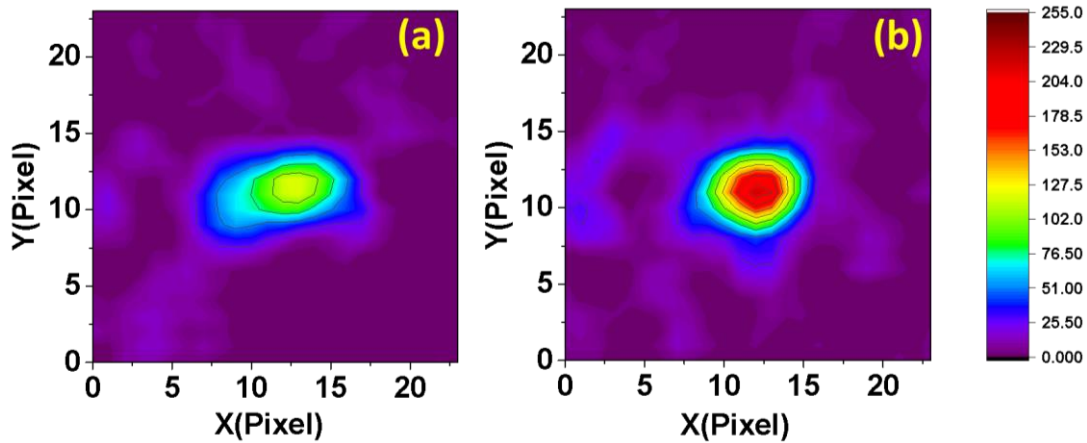


**Figure 3.16** (a) Intensity plot of a typical trap spot (a) before SVPR correction and (b) after SVPR correction.

A circle of 9 pixel diameter was chosen around each of the focal spots, with spot center coinciding with the center of the circle. The spot sharpness metric is calculated for the circular region surrounding each trap using Eq. (3.28). It is observed that the correction of SVPR leads to an improvement in trap quality up to 6.5%. Fig.

3.16 shows the intensity plot of a trap spot before and after SVPR correction, showing an improved trap quality.

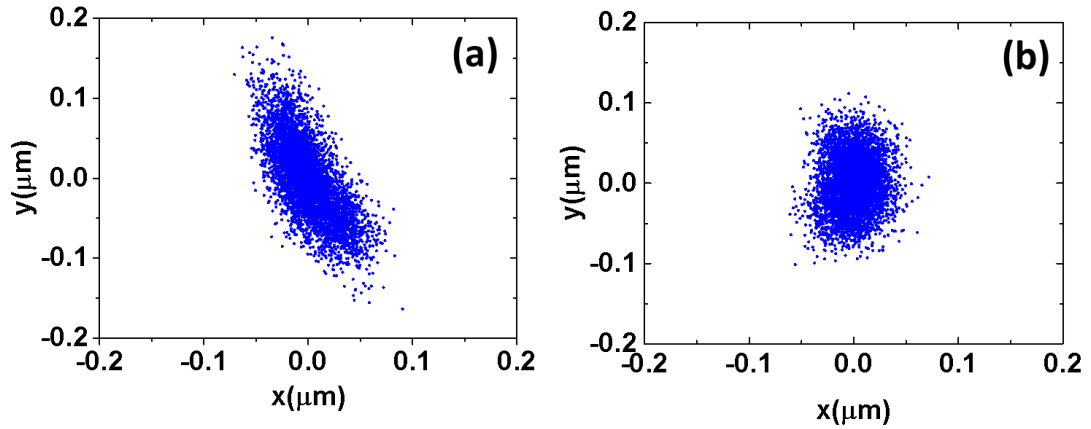


**Figure 3.17** (a) Scatter plot of particle positions in a given trap spot (a) without SVPR correction and (b) with SVPR correction.

Further, we calculated the trap performance metric ( $M_p$ ) [285], defined as the ratio of the trap stiffness before aberration correction to that after correction. A value of  $M_p=1$  corresponds to no improvement after correction,  $M_p >1$ , signifies deterioration of trap performance and  $M_p <1$  implies improved trap performance. The lower the value of  $M_p$ , better the trap performance. In our case, we found  $M_p=0.49$  for a trapped particle (diameter of  $1.2 \mu\text{m}$ ) in a given trap spot, indicating improved trap performance after SVPR correction. Fig. 3.17 shows the scatter plots of positions of a trapped particle in a given trap spot in the circular array without [Fig. 3.17(a)] and with [Fig. 3.17(b)] SVPR correction.

We also generated a square array of  $4 \times 4$  traps by using a hologram generated by using the WGS algorithm [Fig. 3.18(a)]. Polystyrene spheres of diameter  $1.2 \mu\text{m}$ , suspended in aqueous medium, were trapped in the focal spots created by imposing this hologram on the SLM [Fig. 3.18(b)]. This was implemented in two stages. First, the trap spots were generated for the central  $2 \times 2$  array by imposing a hologram, and

polystyrene particles were trapped in them. Then, a hologram to generate the 4×4 array was imposed on the SLM to create the outer boundary of the trap spots, and then the particles were trapped between them.

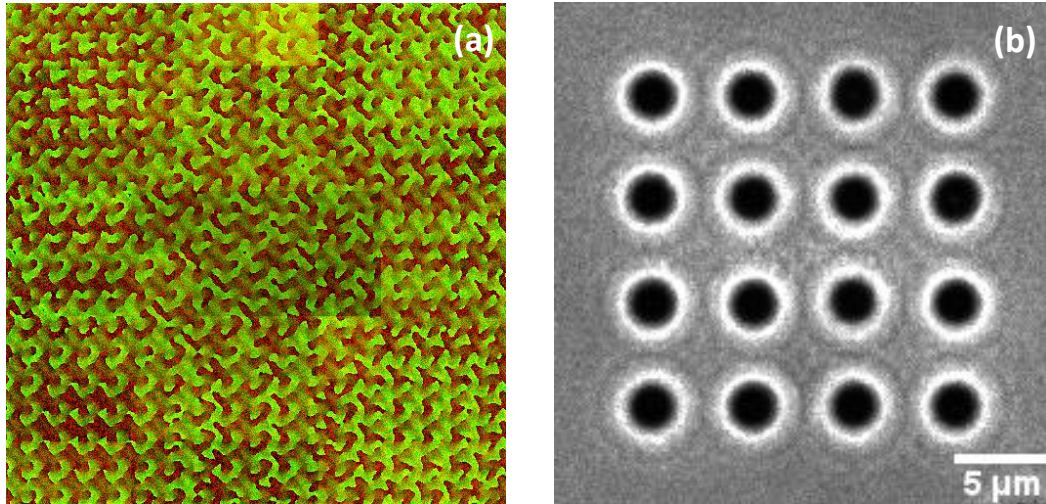


**Figure 3.18** (a) Typical hologram generated by the WGS algorithm incorporated with correction for SVPR to generate 4×4 optical traps. (b) Polystyrene spheres of diameter 1.2μm suspended in water trapped in a 4×4 array.

To increase the size of the array, a corresponding hologram to generate the outer layer of spots needs to be created. This is required since the generation of desired size of the array of traps at the first instance allows for trapping of particles only on the outer boundary. The particles cannot move to the inside of the trapping sites with particles trapped in the outer boundary. Similarly, to trap a 5×5 array, we should generate one central spot, then a 3×3 array surrounding it, and finally, a 5×5 array with particles trapped sequentially in the generated sites.

### 3.6 Determination of Laser Beam Profile over SLM

The above-discussed optimization algorithms use the beam profile of the laser as input amplitude at the SLM plane for propagation to the trapping plane. The amplitude of the field is normally a Gaussian profile for a TEM<sub>00</sub> incident laser,

assumed to be centered on the SLM. The SLMs, in general, are pixelated with pixel pitch varying from 10 to 20  $\mu\text{m}$ . It modulates the phase of the beam at each of the pixels independently. Hence matching the center of the beam, i.e., maximum of the Gaussian profile of laser to a precision of a few microns is a complex task with the physical alignment procedure of centering the maximum intensity to the central pixel of SLM. Even the non-uniform profile of the beam causes differential heating over different spatial regions of SLM, leading to a spatially varying phase response [95], affecting the efficiency and uniformity of the traps generated at the sample plane. Hence it is important to know the actual intensity profile of the laser incident on the SLM, to be given as an input to the iterative algorithms generating the holographic optical traps. We present here a novel and robust methodology to determine the actual beam profile and beam center of the incident laser beam over the SLM measured using the diffraction-based set-up [Fig. 3.4(a)].

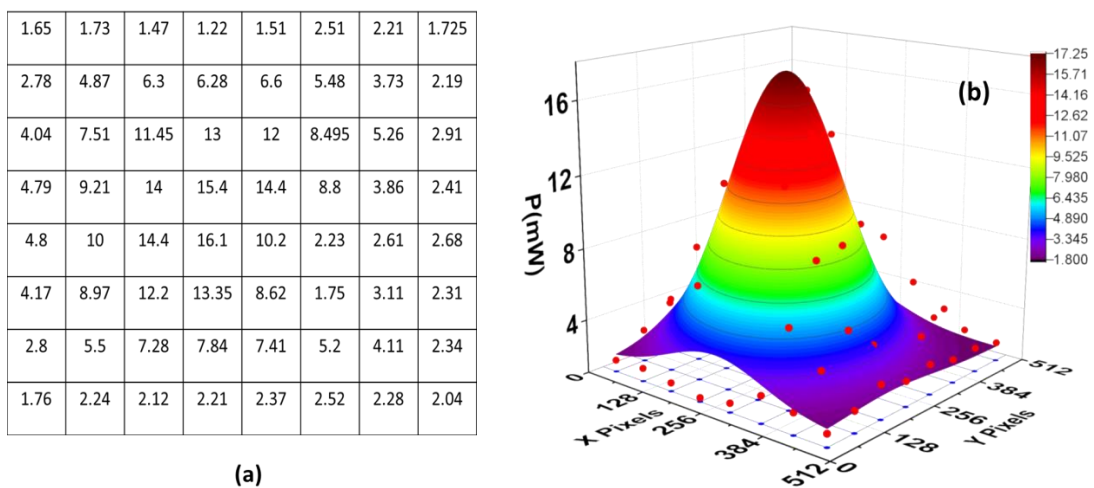


**Figure 3.19** (a) Table showing the maximum power (mW) diffracted off each of the sub-sections ( $8 \times 8$  pixels) of SLM, with each sub-section displayed by a blazed grating, (b) Calculated Laser profile of the beam over SLM fitted to a Gaussian function centered at (210, 253)th pixel.

A power meter is placed at the Fourier plane of SLM after the SF, to measure the diffracted power reflected off the SLM. We divide the SLM into  $8 \times 8$  sub-sections,

and a blazed grating is displayed over one sub-section at a time, and the other regions are kept blank as in case of SVPR correction. The maximum diffracted power with the SLM is measured at its Fourier plane for each of the sub-sections. The maximum power which can be diffracted over a region of SLM is attained after calibrating the SLM for spatially varying phase response. Fig. 3.19(a) shows an  $8 \times 8$  matrix of measured power from each of the sub-sections of SLM and Fig. 3.19(b) shows the profile of the laser beam fitted to a Gaussian function. The maximum of the Gaussian beam is found to be at the (210, 253)th pixel of SLM instead of the center corresponding to (256,256)th pixel. Hence the actual beam profile can be used as an input to the optimization algorithms to generate the holographic optical traps.

### **3.7 Conclusion**

We have designed and developed a holographic optical tweezers (HOTs) set-up using a phase-only reflective spatial light modulator (SLM) driven by a digital video interface (DVI) graphics. We presented a methodology to optimize the properties of graphics, (SLM being driven by a DVI interface through graphics) using a method similar to that used for optimizing LCD televisions. The graphics card was optimized for maximum diffraction efficiency and for addressing the gray values with uniform resolution through the range of available phase levels. A calibration function was generated for the SLM correcting for the non-linearity in the phase response that resulted in an improvement of diffraction efficiency to 50% from 29% with the calibration function from the supplier. It also enhanced the phase modulation depth from  $1.4 \pi$  to  $1.7 \pi$ , the maximum attainable by any means for our SLM. Further, a new technique based on diffraction has been presented to quickly calibrate the SLM for spatially varying phase response. We divided the SLM into  $8 \times 8$  sub-sections, and

each of these subsections were optimized for brightness, contrast, and gamma by measuring the power in the first order beam as a function of brightness, contrast, and gamma of the hologram. The optimized values were incorporated into the algorithm to generate holograms, and an improvement in diffraction efficiency of 55% from 50% was observed. Uniformity in the intensity of the traps is found to improve from 76% to 97% as observed from reflective measurements. This results in uniformity in the trap stiffness and is found to be of 80% from the particles trapped in a circular array of 8 spots. The SVPR correction is found to improve the trap quality up to 6.5% as determined by the spot sharpness metric calculation and the value of trap performance metric was found to be 0.49, showing an improved trap performance. This method presented here allows for quick calibration for spatially varying phase response (SVPR) as required for experiments performed at different laser power levels and non-uniform illumination, the phase response of the SLM being dependent on the incident power levels. We also presented a prescription to trap different particles in a square array of traps. We also reported a novel technique for determining the laser beam profile over SLM used as input for optimization algorithms to generate holographic optical traps.



# TEMPERATURE DRIVEN VOLUME PHASE TRANSITION OF A SINGLE STIMULI RESPONSIVE MICROGEL PARTICLE USING OPTICAL TWEEZERS

---

Poly (N-isopropyl acrylamide) (PNIPAM) based microgels respond to temperature and exhibits a transition from swollen to deswollen state upon variation of temperature, which is known as volume phase transition (VPT). Dynamic light scattering (DLS) is a popular technique to identify the volume phase transition temperature (VPTT) of microgel particles, which measures variation of particle size with temperature in a suspension having microgel particle concentration of  $10^7$ - $10^8$  particles/cm<sup>3</sup>. Here, we employ optical tweezers to trap a single microgel particle and identify its VPTT by measuring the lateral trap stiffness,  $\kappa$ , as a function of temperature. It is shown that near the VPTT,  $\kappa$  increases gradually upon increasing temperature, which is due to a gradual decrease in particle size with simultaneous increase in its refractive index.

### 4.1 Introduction

Stimuli-responsive microgels are micron/submicron sized polymeric gel particles, which respond to external stimuli like temperature, pressure, pH, ionic strength [156,213,286,287]. The response of microgel particles to external stimuli occurs through swelling/deswelling of microgels upon variation of the stimuli. The transition of microgel particles from swollen state to de-swollen state and vice-versa is known as volume phase transition (VPT) [156,213,286,287]. Poly N-

isopropylacrylamide (PNIPAM) microgels are one of the stimuli-responsive microgels which undergo swelling/deswelling upon variation of temperature [213], and pressure [286]. PNIPAM microgels can be made responsive to pH and ionic strength by co-polymerizing with acrylic acid [187]. Stimuli-responsive nature of microgels makes them potential candidates for many applications like site-selective and controlled drug delivery [288], solvent extraction processes [183,289]. Dense suspensions of monodisperse PNIPAM microgels are known to exhibit crystalline order making them suitable candidates for applications in optical switching, color displays, biological and chemical sensors, optically active components, responsive photonic crystals (RPCs) etc. [290–295]. In the RPCs, the external stimulus induces a change in either relative refractive indices of the constituting particles with respect to the surrounding medium or causes a change in the spatial symmetry and/or the lattice constants of the ordered crystalline arrays, leading to changes in the photonic band gap and optical properties. The stimuli-responsive property also allows to tune interparticle interactions and hence phase behavior of microgel suspensions, making them an ideal model condensed matter system [213,214]. All of the above applications depend on the property of microgel particle to swell or shrink upon change in stimuli. Hence, it is important to investigate the VPTT and its nature for PNIPAM based microgel particles with respect to various parameters like temperature, pH, ionic strength, etc. [215].

Dynamic light scattering is the most popular technique used conventionally to investigate the VPTT of microgels [156,213]. In DLS, one determines the size of the particle by carrying out experiment on sample with a particle concentration of  $\sim 10^7 - 10^8$  particles/cm<sup>3</sup> [186,214]. Such a large number of particles are required in order to satisfy the Gaussian distribution of the number of particles scattering the light [296],

which is essential to extract the electric field autocorrelation from measured intensity autocorrelation using Siegert's relation [296]. In order to identify the VPTT using DLS, one measures the microgel particle size as a function of stimulus and the collapse in the size is identified as VPTT [180]. In the case of homogeneous macrogels, the nature of VPT is shown to be discontinuous type [217], i.e., the swollen gel suddenly shrinks at the transition point. On the other hand, inhomogeneous macrogels (where inhomogeneity in polymer density arises due to inhomogeneous distribution of cross-linker) are shown to exhibit swelling/deswelling transition in a continuous manner [217]. The DLS measurements on PNIPAM microgels also show a continuous variation of microgel particle size near the VPTT [213]. But predicting the exact VPTT point and nature of VPT from DLS experiment becomes difficult due to following reasons. One is the difficulty in the analysis of DLS data due to polydispersity in size of microgels. Another is that inhomogeneities in different microgel particles may, in principle, be different. DLS measurement gives the average effect of  $10^7$ – $10^8$  particles. Thus, identification of true VPTT and its nature in PNIPAM microgels needs the measurements to be carried out on a single microgel particle. Optical tweezers is one of the tools which allow trapping of a single microscopic particle and investigation of its properties. As described in detail in chapter 2, an optical tweezers instrument consists of a tightly focused laser beam that is capable of optically trapping a microscopic particle in three-dimensions in a liquid medium [230,243]. This has become a widely used tool in physics, chemistry, and biology [233,297], because of its ability to manipulate single molecules with nanometer precision and to measure forces on these molecules with piconewton accuracy.

Optical tweezers are now routinely employed to study molecular motors at single molecule level [236,298], mechanical properties of polymers and biopolymers [238,299] and to investigate the physics of colloids and mesoscopic systems [136,235,237,300]. It is a unique non-destructive technique for exploiting single particle properties, such as measurement of refractive index [239], measurement of electrophoretic forces [145], micro-rheology using optical tweezers, etc. [301]. Here, we use an indigenously developed optical tweezers, generated using IR laser with the wavelength of 1064 nm, to trap a single PNIPAM microgel particle. The trap stiffness is measured as a function of temperature and has been used to identify the VPTT and the nature of VPT.

## **4.2 Experimental Details**

### **4.2.1 Synthesis and Characterization of PNIPAM-co-Aac Microgel Particles**

N-isopropylacrylamide (NIPAM) was purchased from Acros (Belgium), N,N'-methylene-bisacrylamide (BIS) from Fluka (Germany), acrylic acid (Aac) from LobaChem (India) and potassium persulfate (KPS) from Rankem (India) and mixed bed of ion-exchange resins (Ag501 –X8) Bio-Rad laboratories, Hercules (CA). All chemicals used for the synthesis were analytical grade reagents and were used as supplied. Dust free 0.2  $\mu\text{m}$  filtered Milli Q water was used throughout the synthesis and sample preparation. An aqueous suspension of PNIPAM microgel particles was synthesized by free radical precipitation polymerization [176].

The pregel solution was prepared by dissolving (1.4 g) NIPAM, (0.03 g) BIS, Aac (0.08 g dissolved in 10 ml of water) in 100 mL of Milli Q water taken in a three-necked flask. The acrylic acid has been chosen for copolymerization with NIPAM as it allows synthesis of large-sized microgel particles, suitable for optical microscopy

before and after VPTT under the optical trap. This reaction mixture was stirred at 400 rpm, de-aerated using argon gas to remove dissolved oxygen for 1 hour. After this, the temperature of the pregel solution was raised to 70°C and after equilibration 0.05g of KPS pre-dissolved in 10ml of water was added to the reaction flask to initiate polymerization. Polymerization was carried out at 70°C for 6 hours maintaining the argon purge. After polymerization, the suspension is cooled to room temperature and purified by dialysis against Milli Q water for two weeks to remove the unreacted monomer and other ionic impurities. The purified suspension was prepared in a pH 3.4 buffer with a concentration of  $3 \times 10^6$  particles/cm<sup>3</sup>. The particle size (hydrodynamic radius) and size polydispersity (SPD) of dilute purified PNIPAM-co-Aac suspension has been determined using dynamic light scattering (DLS) (LS Instruments, UK) technique equipped with a multi-tau correlator and a He-Ne laser (wavelength 632.8 nm) and is found to be 382.5 nm with 2% SPD at 26 °C. For the present study, PNIPAM-co-Aac microgel particles are chosen.

#### 4.2.2 Characterization of Size and Size Polydispersity

The particle size and SPD of dilute purified PNIPAM-co-Aac suspension has been determined using dynamic light scattering (DLS) technique. In a DLS experiment the intensity-intensity autocorrelation function  $g^{(2)}(q,t)$ , measured at a given scattering wave vector,  $q$  is given by

$$g^{(2)}(q,t) = \frac{\langle I(q,0) I(q,t) \rangle}{\langle I(q,0) \rangle^2} \quad (4.1)$$

$$\text{and} \quad q = \frac{4\pi\mu_m}{\lambda} \sin\left(\frac{\theta}{2}\right) \quad (4.2)$$

where  $\mu_m$  is the refractive index of the solvent,  $\theta$  is the scattering angle and  $\lambda$  is the wavelength of the incident laser light.

The normalized electric field autocorrelation function  $f(q,t)$  is related to  $g^{(2)}(q,t)$  by the Siegert-relation [302],

$$g^{(2)}(q,t) = 1 + \beta |f(q,t)|^2 \quad (4.3)$$

where  $\beta$  is the coherence factor.

For a monodisperse non-interacting dilute system,  $f(q,t)$  can be written as,

$$f(q,t) = \exp\left[\frac{-q^2 \langle r^2(t) \rangle}{6}\right] = \exp(-D_0 q^2 t) \quad (4.4)$$

where  $\langle r^2(t) \rangle$  is the mean square displacement (MSD) and is related to the free diffusion coefficient,  $D_0$  by

$$\langle r^2(t) \rangle = 6D_0 t \quad (4.5)$$

Knowing the free diffusion coefficient,  $D_0$ , the diameter,  $d$  of the particles can be obtained from Stokes-Einstein relation [302],

$$d = \frac{k_B T}{3\pi\eta D_0} \quad (4.6)$$

Here,  $k_B$ ,  $\eta$  and  $T$  are the Boltzmann constant, the solvent viscosity and the absolute temperature, respectively.

For a dilute polydisperse suspension the decay constant  $\Gamma = Dq^2$ , ( $D =$  diffusion constant) is not unique but has distribution  $G(\Gamma)$  and  $f(q,t)$  is related to  $G(\Gamma)$  by,

$$f(q,t) = \int_0^{\infty} G(\Gamma) e^{-\Gamma t} d\Gamma \tag{4.7}$$

$G(\Gamma)$  can be calculated from the Laplace inversion of  $f(q,t)$ . The mean diameter and the size polydispersity (standard deviation in diameter, mean diameter) are obtained by cumulant analysis of  $f(q,t)$  [302,303]. When the distribution is narrow and  $f(q,t)$  is close to a single exponential decay, this method of cumulant expansion is more useful. In this method,  $\ln|f(q,t)|$  is approximated by a polynomial of  $t$ , typically of the second order. The first two coefficients represent the mean and the variance of  $\Gamma$  :

$$\ln|f(q,t)| = -\langle\Gamma\rangle t + \frac{1}{2}\langle\Delta\Gamma^2\rangle t^2 - \frac{1}{3}\langle\Delta\Gamma^3\rangle t^3 + \dots \tag{4.8}$$

Where  $\Delta\Gamma = \Gamma - \langle\Gamma\rangle$  and the averages are weighted with  $G(\Gamma)$  :

$$\langle\Gamma\rangle = \int \Gamma G(t) dt, \quad \langle\Delta\Gamma^2\rangle = \int \Delta\Gamma^2 G(t) dt, \dots \tag{4.9}$$

In the absence of distribution, the second and higher-order terms disappear and  $\ln|f(q,t)|$  is a straight line. The curve fitting of the measured  $\ln|f(q,t)|$  by a polynomial gives an estimate of  $\langle\Gamma\rangle$  and  $\langle\Delta\Gamma^2\rangle$ , and hence the mean size and size polydispersity.

### 4.2.3 Heating Stage suitable for Microscopy and Sample Preparation

To study the volume phase transition (VPT) of PNIPAM microgel particles with temperature, a heating stage compatible to the microscopy study has been developed.

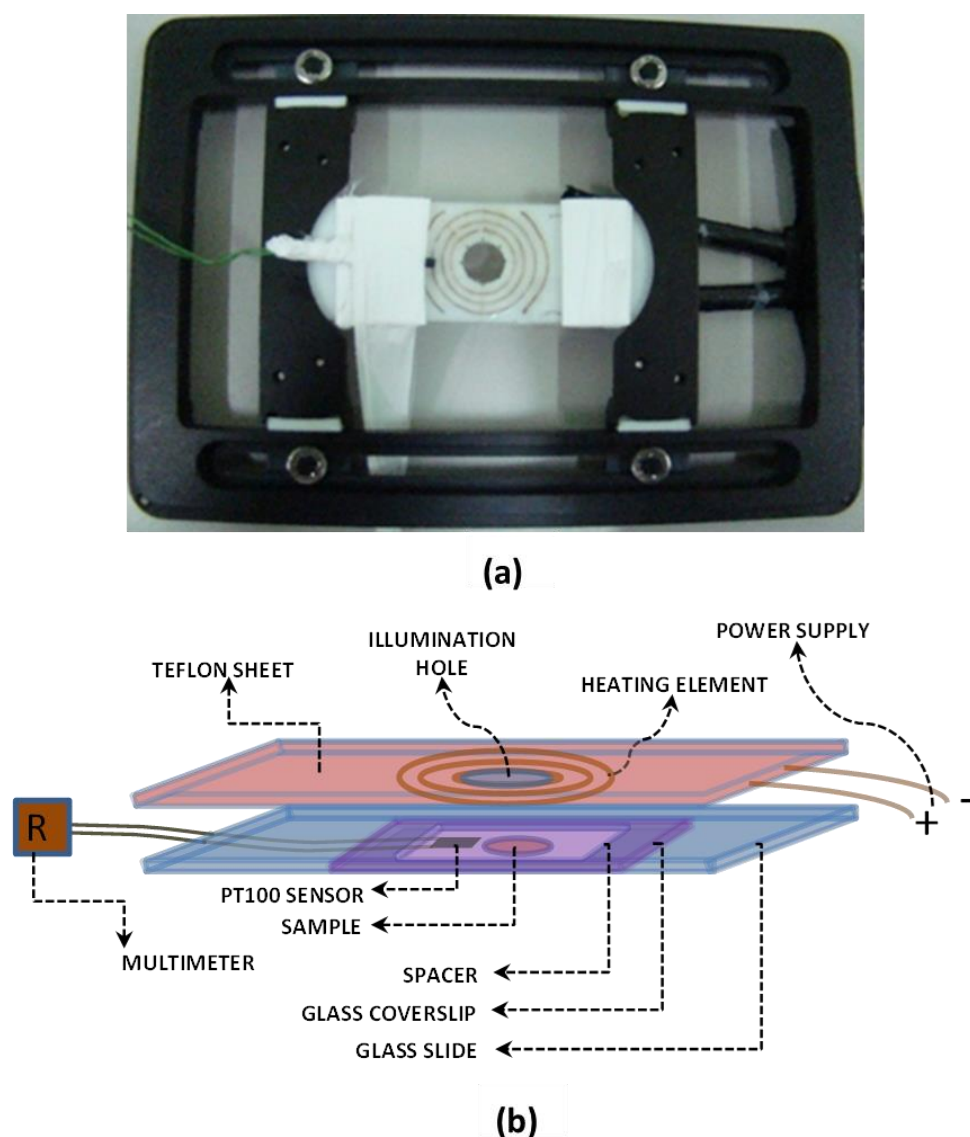


**Figure 4.1** (a) Photograph of sample cell containing the sample with the heating element showing the manganin wire coil and PT100 sensor on the surface of coverslip mounted on the universal stage of microscope. (b) Schematic of the sample cell containing the sample in a well between the standard glass slide and cover slip separated by a thin spacer with the heating element made on teflon sheet having hole for illumination and a PT100 sensor at bottom for measurement of temperature.

A Teflon sheet was cut in the shape of a standard glass slide (75mm×25mm) with a clear hole made at the center to allow the illumination light to pass for imaging of the optically trapped microgel particles. Thin concentric circular grooves were made surrounding the clear hole, and manganin wire (heating element) was fitted in the circular grooves. The resistance of the wire in the groove was measured to be 7.6  $\Omega$ . The heating element was connected to a variable power supply and was calibrated for heating from room temperature up to 50 °C. The dilute suspension of PNIPAM-co-Aac microgel particles prepared for trapping experiment was placed in the well of a thin sample cell made up of a standard glass slide and a coverslip separated by a thin imaging spacer having a circular well of 9 mm diameter and 0.12 mm depth giving a volume space of  $\sim 7.63 \mu\text{l}$  for the sample. The heating element made was placed over the sample cell on the side of glass slide for heating the sample and a PT100 sensor was glued using a conducting paste on the coverslip near the sample to measure the resistance developed due to heating of the sample (Fig. 4.1 (a)). Fig. 4.1 (b) shows the schematic of the heating arrangement on the sample cell and the measurement of resistance using PT100 sensor connected to a multimeter.

The PT100 sensor was calibrated for accurate temperature measurement using a standard heater equipped with an ETS-D5 sensor (PT1000 sensor), (IKA, Germany), which has the ability to control and measure temperature with an accuracy of  $\pm 0.1$  °C. The PT100 sensor to be calibrated was dipped in a container containing water being heated in a controlled manner by the IKA heater having an ETS-D5 sensor already dipped in to measure the temperature of the water as shown in Fig. 4.2 (a). The resistance developed at the ends of PT100 sensor was being measured as a function of temperature controlled and read by the ETS-D5 sensor of IKA heater. The temperature versus resistance curve was plotted and fitted to a straight line for

determining the slope and intercept of the curve as shown in Fig. 4.2 (b) and the PT100 sensor was calibrated. The temperature  $T$  corresponding to a measured value of resistance  $R$  is calculated as:

$$T = (\text{Measured } R \times \text{Slope}) + \text{Intercept} \quad (4.10)$$

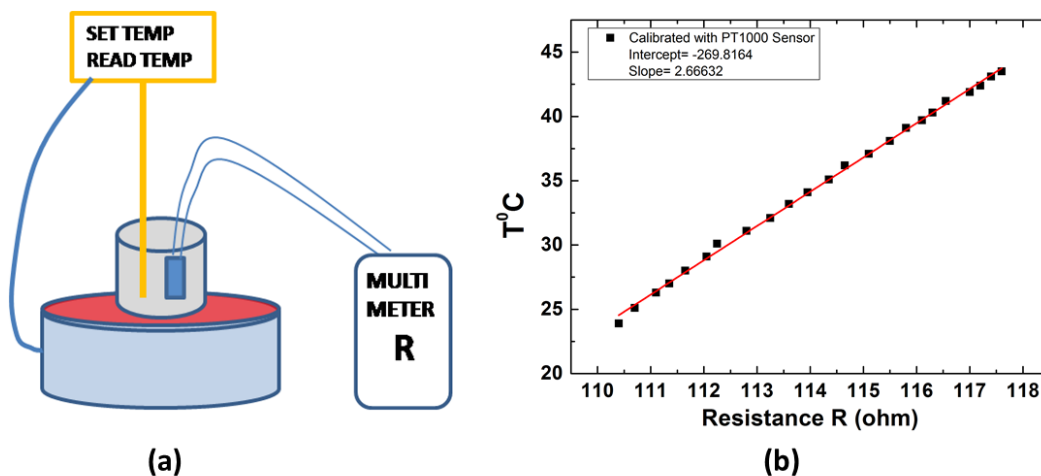


**Figure 4.2** (a) Calibration set-up for calibrating the PT100 sensor using a standard heater and ETS-D5 sensor. (b) Plot of temperature versus resistance curve showing the temperature corresponding to the resistance measured using a PT100 sensor and being fitted to a straight line.

#### 4.2.4 Optical Trapping Experiment

We performed the optical trapping experiment with the home-built optical tweezers set-up (as described in chapter 2). The PNIPAM-co-Aac microgel particles in pH 3.4 buffer placed in the thin sample cell with the heating arrangement as shown Fig. 4.1 were trapped using this optical tweezers set-up, and the videos of these trapped particles were recorded as a function of temperature. The laser power used for the trapping experiment was kept constant for all measurements and was measured to be 169 mW at the back aperture of the objective, and for all measurements, the depth

at which the particle was trapped was kept constant at 20  $\mu\text{m}$  from the upper surface of the coverslip. The videos of the trapped particles were recorded at a frame speed of 299 fps. The recorded videos were processed using Image J software and analyzed to extract the position coordinates of the trapped particle as a function of time.

#### 4.2.5 Determination of Optical Trap Stiffness

There are various methods such as equipartition method, Boltzmann statistics method and power spectrum method for the characterization of optical potential well and determinations of optical trap stiffness,  $\kappa$  [304]. We employ here a direct method based on calculating trap stiffness from the position fluctuations using a statistical approach. The method involves optical potential reconstruction using Boltzmann statistics, which can be used to determine any continuous trapping landscape by thermal agitation. The extracted coordinates of the trapped particle have been used to generate a histogram of the trapped particle positions. The normalized probability distribution function,  $P(x)$ , of the displacement of the trapped particle from the trap center is given by the expression in Eq. (4.2). The shape of the optical trapping potential has been obtained from the normalized histogram of the trapped particle positions assuming Boltzmann statistics (Eq. (4.3)). The beam used to trap the particle is a TEM<sub>00</sub> Gaussian beam which results in a harmonic trapping potential: - the optical trap potential generated has been fitted to a parabola in the central region of the potential to extract trap stiffness.

$$P(x) = \exp\left(-\frac{U(x)}{k_B T}\right) = \exp\left(-\frac{\kappa_x x^2}{2k_B T}\right) \quad (4.11)$$

$$\frac{U(x)}{k_B T} = -\ln(P(x)) \quad (4.12)$$

## 4.3 Results and Discussion

### 4.3.1 Identification of VPTT using DLS

First, the VPT of PNIPAM-co-Aac microgel particles have been identified using the conventional technique of DLS. The hydrodynamic radius,  $R_h$  of PNIPAM-co-Aac particles measured as a function of temperature by taking a non-interacting dilute suspension of these particles in pH 3.4 buffer (particle concentration  $\sim 10^7$  particles/cm<sup>3</sup>) is shown in Fig. 4.3(a). At pH 3.4, PNIPAM-co-Aac microgel remains in the protonated state, and hence a slight change in the pH of the buffer with respect to temperature does not affect the size of the microgel particles. The observed change in size is due to the change in temperature only. When the temperature is raised, the polymer chains undergo a hydrophilic to hydrophobic transition which leads to deswelling of these particles [1]. It is observed that at 34 °C, the particles undergo complete collapse which is identified as VPTT of PNIPAM-co-Aac. After 34 °C, the particle size remains constant. Variation of the microgel particle size across the VPTT is found to be continuous.

### 4.3.2 Identification of VPTT of single microgel particle using optical tweezers

After identification of VPTT using DLS on  $10^7$  particles, we move on to the characterization of VPTT of single PNIPAM-co-Aac microgel particle. Towards this, a single PNIPAM-co-Aac microgel particle is trapped using optical tweezers and lateral trap stiffness,  $\kappa$  is measured as a function of temperature using the method described in above section. Figure 4.3 (b) shows  $\kappa$  as a function of temperature. The value of  $\kappa$  increases with increase in temperature and reaches to a saturation value at 34 °C, which is identified as VPTT. After the VPTT,  $\kappa$  remains constant. The variation of  $\kappa$  in the neighborhood of VPTT is found to be continuous suggesting the

nature of VPT in microgel particle is of the continuous type, similar to that reported for macrogels synthesized at higher temperature [217]. The continuous nature of VPT in macrogels has been attributed to an inhomogeneous cross-linking density within macrogel [217].

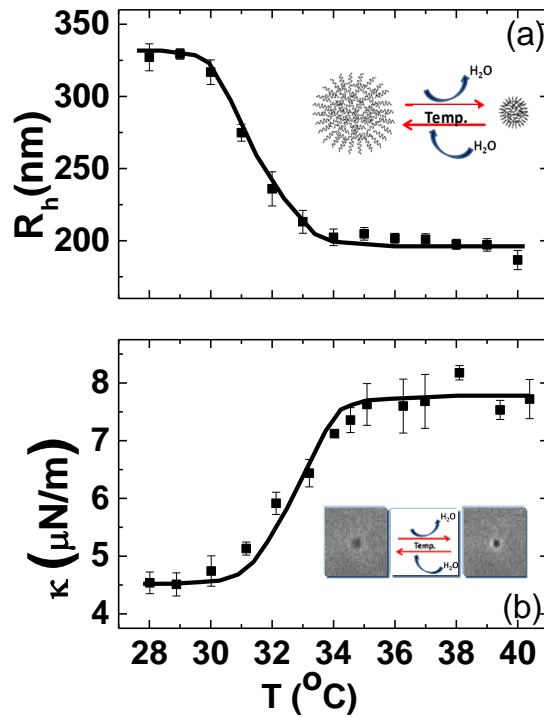


**Figure 4.3** (a) Hydrodynamic radius,  $R_h$ , of PNIPAM-co-Aac microgel particles versus temperature measured using DLS. Inset shows the schematics of a microgel particle in swollen and deswollen state, i.e., before and after VPTT ( $34^\circ\text{C}$ ). (b) Plot of lateral trap stiffness,  $\kappa$  measured on a single microgel particle as a function of temperature using optical tweezers showing VPTT at  $34^\circ\text{C}$ . Inset shows the image of trapped microgel particle before and after VPTT showing an increase in contrast after VPTT. Continuous lines are guide to the eye.

The continuous variation of trap stiffness near VPTT implies the presence of inhomogeneous cross-linking density within PNIPAM-co-Aac microgel particle. This is expected as PNIPAM-co-Aac microgel particles are synthesized at  $70^\circ\text{C}$ , which is much above the VPTT. It can be noticed from Fig. 4.3 (a) and (b) that the VPTT measured on a single particle using optical tweezers and on  $10^7$  particles using DLS is

same, i.e., 34 °C. Also, the continuous nature of VPT observed on a single microgel particle (i.e., continuous rise in trap stiffness with increase in temperature) and from average on  $10^7$  microgel particles (i.e., continuous decrease in  $R_h$  with increase in temperature) is similar. These observations imply that the low size polydispersity (2%) has a negligible effect on the VPTT and its nature when measured using DLS, and also that the inhomogeneities in crosslinking density are of similar type among different microgels. Thus, use of optical tweezers enables us to measure the VPTT on a single microgel particle unambiguously as compared to the DLS technique, which requires  $\sim 10^7$ - $10^8$  particles/cm<sup>3</sup> along with the requirement of narrow size distribution. The inset in Fig. 4.3 (b) shows the image of the trapped microgel particle before and after VPTT, showing an increase in contrast of the particle after VPTT. The lateral trap stiffness depends on the size and refractive index of the particle [305]. With the increase in temperature, size of PNIPAM of microgel particle decreases, whereas refractive index increases.

In order to understand the dependence of the lateral trap stiffness,  $\kappa$ , on temperature (hence, on size and refractive index of microgel particle), we have numerically computed  $\kappa$  using the “Optical Tweezers Computational Tool box” software developed by Nieminen *et.al.* [305] for computing the optical forces and torques for both spherical and non-spherical particles. The basic inputs to the tool box are refractive index of the sphere ( $n_p$ ), refractive index of the surrounding medium ( $n_m$ ), the particle size ( $d_h$ ), wavelength of the trapping beam ( $\lambda$ ) and the convergence angle of the trapping beam. Using above variables, the tool box computes the beam shape coefficients, T-matrix for the sphere (which relates the incident and scattered fields and depends on the properties of the particle and the wavelength of the radiation) and hence, the optical forces acting on the spherical particles. The tool box

computes the optical trapping efficiency  $Q$  which when multiplied with  $n_m P/c$  gives the optical trap stiffness in units of N/m [239,306], where  $P$  is the power measured at the trapping plane. The power at the trapping plane was estimated to be 58 mW from the power measured at the back aperture of objective (i.e., 169 mW) by considering 35% transmission of the objective at 1064 nm. The diameter ( $d_h = 2R_h$ ) measured using DLS as a function of temperature was used as an input for the size of the particle. The refractive index,  $n_p$  of the microgel particles has been determined using the following equation,

$$n_p = \frac{n_s - [n_m(1 - \varphi)]}{\varphi} \quad (4.13)$$

where ( $\varphi = \frac{\rho \pi d_h^3}{6}$ ,  $\rho$  is particle concentration) is the volume fraction of the suspension,  $n_s$  and  $n_m$  are the refractive indices of the suspension and the medium, respectively.  $n_s$  and  $n_m$  at different values of temperatures are measured using an Abbe's refractometer.

To understand the effect of the particle size and refractive index individually on lateral trap stiffness, we have computed the  $\kappa$  for the trapped microgel particle as a function of refractive index by fixing the microgel particle size to 640 nm (measured at 25 °C) and as a function of particle size by fixing the refractive index of the particle to 1.36813 (measured at 25 °C). Fig. 4.4 (a) and (b) shows the variation of lateral trap stiffness with only the particle size as a variable and with only the particle refractive index as a variable, respectively. From Fig. 4 (a), it is observed that  $\kappa$  increases with increase in temperature and reaches saturation at  $\sim 34$  °C, which results from deswelling of the microgel particle leading to an increase in the value of refractive index. After 34 °C,  $\kappa$  remains constant, as the particle size (hence, the value of

refractive index) reaches a constant value.

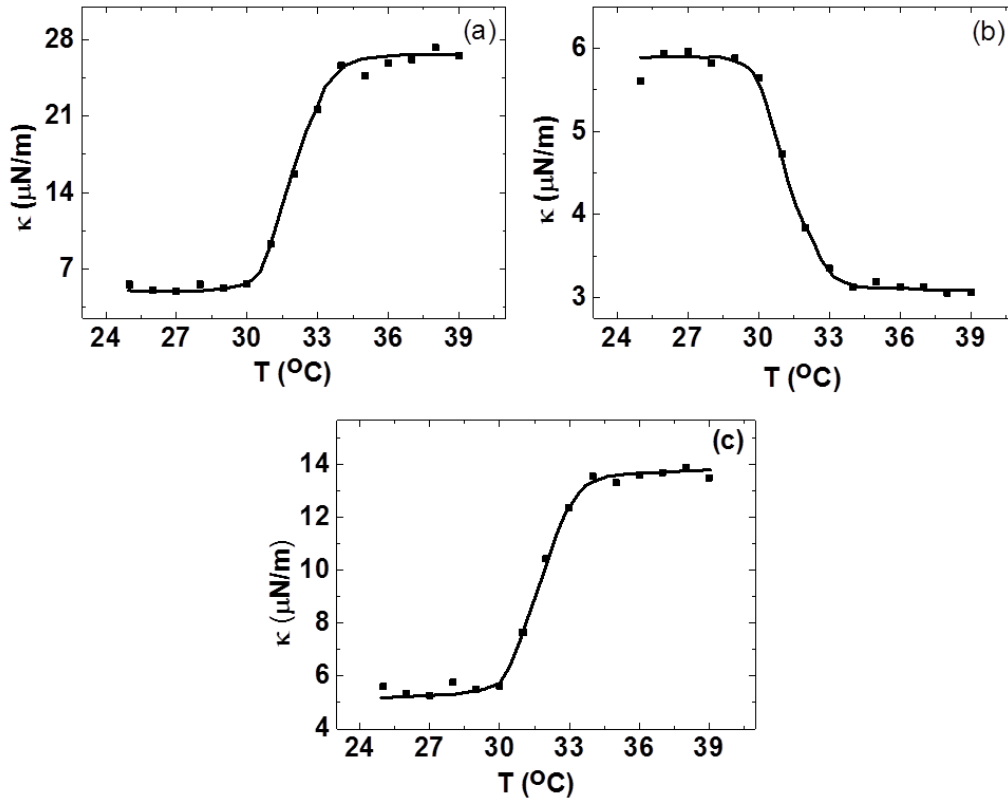


**Figure 4.4** (a) Computed lateral trap stiffness as a function of temperature considering only the effect of variation of refractive index with temperature keeping size of the particle fixed.(b) Computed lateral traps stiffness as a function of temperature considering only the effect of variation of size of the particle with temperature keeping refractive index fixed.(c) computed lateral trap stiffness as a function of temperature taking into account variation of both parameters, the refractive index and the size of microgel particle. Continuous lines are guide to the eye.

The computed lateral trap stiffness as a function of temperature, considering the particle size only as a variable parameter and refractive index fixed [Fig. 4.4 (b)] shows that  $\kappa$  decreases with a decrease in size and reaches saturation at 34  $^{\circ}\text{C}$ , after which it remains constant.

The comparison of the two computed results (Fig. 4.4 (a) and 4.4 (b)) shows that the change in refractive index at VPTT is the dominant parameter (which leads to

an increase in trap stiffness  $\sim 5$  times the value in swollen state of microgel) compared to the change in particle size (which in turn, opposes the increase in stiffness value leading to a decrease in the trap stiffness  $\sim 3$  times the value in swollen state of microgel). The deswelling of PNIPAM-co-Aac particles leads to decrease in the particle size along with a simultaneous increase in refractive index. We have computed the  $\kappa$  of the trapped microgel particle by taking into account the simultaneous variation in both the size and the refractive index of the microgel particle, which is shown in Fig. 4.4 (c). As seen from Fig. 4.4 (c),  $\kappa$  increases with increase in temperature and reaches saturation at  $\sim 34$  °C. The computed temperature dependence of trap stiffness of microgels is in qualitative agreement with experimentally measured one. The quantitative difference between the experimentally measured and computed  $\kappa$  could be due to use of approximate laser power at the focal plane, aberrations induced by the glass water interface and the use of oil immersion objective for optical trapping [307–309]. Thus, optical tweezers unambiguously characterize the VPTT of a single PNIPAM-co-Aac microgel particle.

#### **4.4 Conclusions**

We have successfully trapped single PNIPAM-co-AAc microgel particle using the home-built optical tweezers set-up. We have shown here that the VPTT of single PNIPAM-co-AAc microgels can be identified unambiguously using optical tweezers (by measuring the trap stiffness as a function temperature) as compared to the conventional DLS technique which gives an average of  $10^7$  to  $10^8$  particles. At  $\sim 34$  °C the trap stiffness reaches to a saturation value, which is identified as VPTT of a PNIPAM-co-AAc microgel particle. Variation of trap stiffness in the vicinity of VPTT is found to be continuous type indicating the continuous nature of VPT, which

is attributed to inhomogeneities present within the microgel particle. The VPTT and the nature of VPT measured on single particle using optical tweezers are found to be similar to that determined from DLS on  $10^7$  particles, suggesting a negligible effect of low (2%) size polydispersity on VPT of microgel and similar nature of inhomogeneities among the different microgels. We have also numerically computed the lateral trap stiffness as a function of temperature by keeping either the particles size or particle refractive index to be fixed. The change in refractive index is found to be a more dominant parameter which leads to a net increase in trap stiffness across the VPTT upon raising the temperature. From the calculations, taking into account both these factors (refractive index and particle size), we conclude that rise in the lateral trap stiffness upon the VPTT is due to the sudden de-swelling of these microgel particles, which leads to an increase in refractive index and decrease in particle size. We believe that the present work will motivate utilization of optical tweezers for exploring the various properties and phenomena in stimuli-responsive microgels at the single particle level.

### DISORDER IN STIMULI RESPONSIVE MICROGEL

#### PHOTONIC CRYSTALS

---

Size polydispersity induces second type disorder [310,311] in colloidal crystals of hard-spheres as well as in charged colloidal suspensions and cannot be tailored through external conditions [312,313]. We demonstrate that osmotic pressure not only reduces the particle size but also significantly reduces the size polydispersity of soft-spheres of stimuli-responsive microgels and hence second type disorder can be tailored in crystals of these soft-spheres. We employed a confocal laser scanning microscope to study the disorder in colloidal crystals formed by thermo-responsive poly (N-isopropyl acrylamide-co-acrylic acid) microgel suspensions of varying particle concentrations subjected to different magnitudes of osmotic pressure.

#### 5.1 Introduction

Photonic crystals (PCs) are a periodic arrangement of dielectric or metal-dielectric synthetic structures with lattice constants in the visible range designed to influence the propagation of electromagnetic waves in the same way as the periodic electronic potential in a semiconductor crystal influences electron motion by defining allowed and forbidden energy bands [314]. Photonic crystals are attractive optical materials for controlling and manipulating the flow of light: they can be used as waveguides for directing light along a specific path, highly reflective mirrors in laser cavities, reflective coatings on lenses, color pigments in inks and paints and many other optical applications [315–323]. Synthesis of photonic crystals can be either (i) through top-down approach which involves techniques like laser chemical vapor

deposition (LCVD) [324], layer-by-layer stacking using microelectronics fabrication technology [325,326], electrochemical etching [327], holographic lithography [328–332] or, (ii) by bottom-up approach such as self-assembly of monodisperse colloidal particles like silica ( $\text{SiO}_2$ ) or polystyrene (PS) microspheres into ordered arrays, which can be performed at ambient conditions [333–335]. The resulting photonic properties are determined by the symmetry, lattice constant of the crystal and the refractive index contrast between the colloids and the surrounding medium. Compared to photonic crystals fabricated using holographic or lithographic techniques, self-assembled photonic crystals, in particular, colloidal crystals, can be produced at much lower costs and with higher efficiencies owing to the parallel nature of the self-assembly process. There is a class of photonic materials whose properties can be tuned in response to external stimuli like temperature, pressure, and pH, known as responsive photonic crystals (RPCs). They have important applications in areas such as optical switching, color displays, biological and chemical sensors, paints and many optically active components [293,336–340]. The external stimulus effectively induces a change in the relative refractive indices of the building blocks and the surrounding medium, causing a change in the spatial symmetry and/or the lattice constants of the ordered crystalline arrays and hence the tunability of the photonic band gap and its optical properties. It is also possible to modify the building blocks of these crystalline arrays before or after the formation of crystal structures to enable responsiveness to a particular stimulus [337]. A successful example of RPCs are the crystals formed by thermosensitive poly (N-isopropyl acrylamide) (PNIPAM) microgel particles. These particles undergo a reversible volume phase transition (VPT) between a hydrated state and a dehydrated state around its lower critical solution temperature (LCST) of 32° C in water [341]. It is also found that these

particles undergo an osmotic compression under the application of osmotic pressure, the compression leading to a change in the lattice constant, and hence, tunability of the photonic band gap [342].

Colloidal systems mimic almost all phases of condensed matter. They show a rich phase behavior and exhibit structural ordering similar to that of crystalline atomic solids, liquids, gases and even glasses. Therefore, colloidal systems are analogous to atomic systems [312] and have lattice constants of the order of the wavelength of visible light [312]. Colloidal systems have an advantage over atomic systems in that they can be easily characterized in real space by simple optical microscopy techniques and their long-range order can be easily accessed by diffraction of light [312].

A perfect crystal is defined as one whose atoms are situated at perfectly positioned lattice sites [311]. However, at ambient conditions, there are no perfect crystals due to the presence of imperfections of various types [311]. Crystal imperfections often play an important role in determining the physical properties of solids like mechanical [343] and photonic properties [344] and hence characterizing the crystals for their disorder/lattice imperfections is of considerable interest and practical importance. Diffraction patterns of real crystals collected from the most refined techniques cannot be explained by the Bragg-Laue theory [311]. Hence, a method to arrive at the correct structure of a crystal by analyzing the diffraction patterns is needed. X-rays exaggerate the perfection of crystals. Imperfections are in general difficult to detect and even more difficult to measure, as these imperfections have only secondary effects in the diffraction phenomena.

Crystal imperfections are categorized into three types [311]: (i) First type disorder, arising due to thermal fluctuations of particles about the mean position, (ii)

Second type disorder, arising due to strain induced lattice deformations, where the amplitude of fluctuations increases with distance and (iii) finite size effects, arising due to abrupt loss of positional order at the boundary. The imperfections of the first type introduces fluctuations in the distances between corresponding atoms. These fluctuations in short-range order does not affect the long-range order in the crystal [311], and hence it does not have any broadening effect on the diffraction lines. However, this leads to a reduction in the intensities of the higher-order peaks in the diffraction pattern via the Debye-Waller factor [311]. The imperfections of the second type, as well as finite size effect, both have the effect of broadening the diffraction lines. They are distinguished by the fact that, in case of second type disorder, peak width of diffraction pattern increases with increasing length of the diffraction wave vector  $q$  (since it does not preserve the long-range order). On the other hand, in case of finite size, effect peak broadening is independent of the length of  $q$  [311].

Furthermore, colloidal systems possess various types of disorder due to their specific particle properties like size or shape polydispersity [345]. Theoretically, it has been demonstrated that the band gap of photonic crystals calculated from the density of states is more sensitive to size distribution in the colloidal particles than site randomness [220]. Hence polydispersity of the colloidal particles plays an important role in determining the quality of the photonic crystal [220–222]. In the case of conventionally investigated sterically stabilized (e.g., poly methylmethacrylate) or charge stabilized (e.g., silica or polystyrene) suspensions, the size of the particles and the size polydispersity (SPD) are fixed and hence disorder in the crystals of these systems cannot be tuned. However, in the case of stimuli-responsive poly N-isopropylacrylamide (PNIPAM) based nano/microgel particles, the size, as well as interparticle interactions  $U(r)$ , can be tuned as a function of various stimuli such as

temperature, pH, and ionic strength. [302]. In this chapter, we characterize disorder in self-organized stimuli-responsive microgel crystals of poly N-isopropylacrylamide-co-acrylic acid (PNIPAM-co-Aac) of varying particle concentrations subjected to different amounts of osmotic pressure by computing the diffraction pattern of these crystals using the coordinates obtained from imaging single crystalline domains of the crystal using a confocal laser scanning microscope (CLSM). Our studies show that with an increase in osmotic compression, the second type disorder decreases. We also found that SPD of the colloidal particles destroy the long-range positional order in the crystal, but preserves the orientation order.

## **5.2 Experimental Details**

### **5.2.1 Synthesis of PNIPAM-co-Aac microgel particles**

An aqueous suspension of PNIPAM microgel particles was synthesized by free radical precipitation polymerization [303,346]. All the chemicals used are as described in Sec 4.2.1 of chapter 4. The pregel solution is prepared by dissolving 124 mM NIPAM, 1.95 mM BIS, 200  $\mu$ L Aac and 1.4 mM SDS in 250 mL of Milli Q water taken in a three-necked flask. This reaction mixture is de-aerated using argon gas to remove dissolved oxygen for 1 hour. Then the temperature of the pregel solution is raised to 70° C and equilibrated for 1 hour, after which 1 mL of a pre-dissolved solution of 2.22 mM Potassium persulfate (KPS) in water is added to the reaction flask with vigorous stirring for initiation of polymerization. The polymerization is carried out at 70°C for 6 hours while maintaining the argon purge. This suspension is cooled to room temperature and purified by dialysis against Milli Q water for seven days to remove the unreacted monomer and other impurities. Later it is subjected to ultra-filtration. The purified suspensions are then kept in contact with

a mixed bed of ion exchange resins for further removal of ionic impurities. After reaching deionization equilibrium the particle size and SPD of the PNIPAM-co-Aac microgel particles were determined using dynamic light scattering (DLS) technique as described in Sec. 4.2.2 of chapter 4.

## 5.2.2 Sample Preparation

Different samples with varying particle concentration ( $n_p$ :  $1.2 - 5.7 \times 10^{13} \text{cm}^{-3}$ ) were prepared by subjecting the purified suspension to different amounts of osmotic pressure using Millipore stirred cells equipped with ultra-filtration membrane as shown in Fig.5.1. Samples with  $n_p < 2.7 \times 10^{13} \text{cm}^{-3}$  did not show iridescence for visible light and remained in the un-crystalline state even after repeated annealing; whereas upon repeated annealing of samples with  $n_p > 2.7 \times 10^{13} \text{cm}^{-3}$  showed crystallization by exhibiting iridescence for visible light.

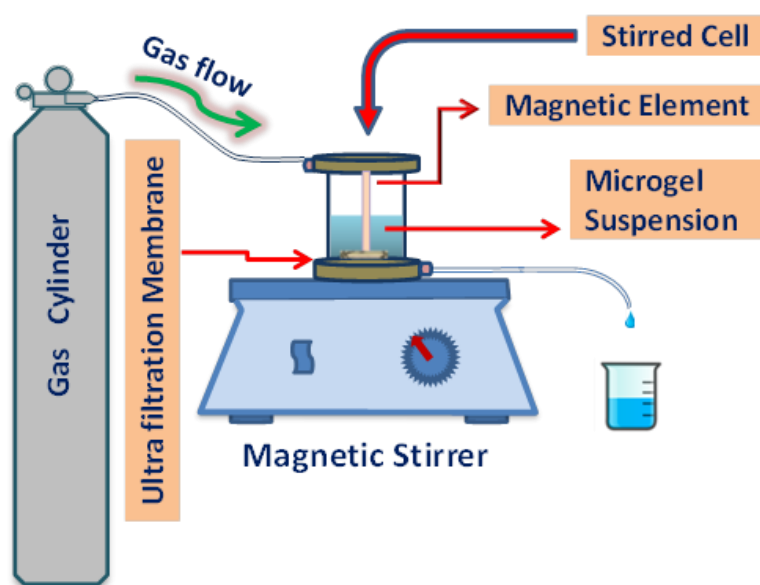


**Figure 5.1** Schematic of the ultra-filtration set-up (Millipore stirred cells equipped with ultrafiltration membrane) for osmotically compressing the microgels to different concentration.

Fig. 5.2(a) and (b) shows the photographs of un-crystallized and crystallized samples respectively. The samples were annealed by heating the samples above the volume phase transition temperature (VPTT  $\sim 34^{\circ}\text{C}$ ) of PNIPAM-co-Aac particles followed by slow cooling at a cooling rate of  $0.15^{\circ}\text{C}/\text{min}$ .

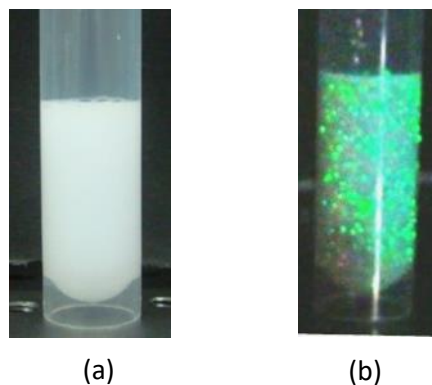


**Figure 5.2** Photographs of (a) un-crystallized ( $n_p: 1.2 \times 10^{13} \text{ cm}^{-3}$ ) and (b) crystallized ( $n_p: 5.7 \times 10^{13} \text{ cm}^{-3}$ ) samples at room temperature ( $25^{\circ}\text{C}$ ).

### 5.2.3 Confocal Laser Scanning Microscopy

Real space information of particle distribution in the dispersion can be obtained by direct observation under a microscope. A confocal laser scanning microscope (CLSM) has an improved resolving power compared to a conventional light microscope. Further, it rejects the light which does not come from the focal plane, thus enabling optical slicing of the sample. By capturing a series of optical sections at various depths in the sample, information regarding the stacking of the crystal in three dimensions can be obtained. Fig. 5.3 shows the schematics of a confocal laser scanning microscope, showing its capability of sectioning in the  $z$ -direction by removing the out of focus lights from the detector by the use of a pinhole in front of the detector.

Micrographs of PNIPAM-co-Aac microgel crystals are captured using a Leica (Germany) TCS-SP2-RS confocal microscope having a scan speed of 7.4 frames/s

equipped with a 488 nm Ar ion laser. All images are captured in the reflection geometry using a 100×, 1.3 N.A. oil-immersion objective lens and the corresponding optical slice thickness is ~ 440 nm.

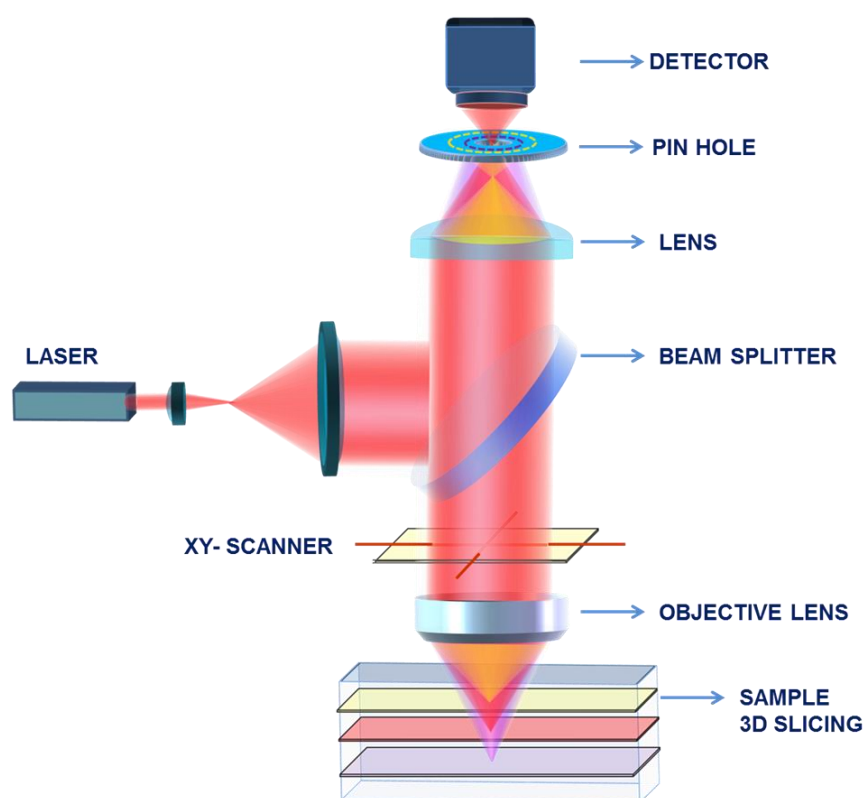


**Figure 5.3** Schematics of a confocal laser scanning microscope, showing its capability of optical slicing and hence z-sectioning for imaging in depth by the use of a variable pinhole along with XY scanning.

Crystalline samples having particle number densities  $n_p = 2.75 \times 10^{13} \text{ cm}^{-3}$  (sample S1) and  $4.75 \times 10^{13} \text{ cm}^{-3}$  (sample S2) have been investigated to characterize disorder using CLSM. Micrographs of the crystalline layers of samples S1 with  $n_p = 2.75 \times 10^{13} \text{ cm}^{-3}$ , volume fraction  $\phi = 1.81$  and sample S2 with  $n_p = 4.75 \times 10^{13} \text{ cm}^{-3}$ ,  $\phi = 3.13$  are captured in reflection geometry using a 100×, 1.3 N.A. oil-immersion objective lens and the corresponding optical slice thickness is ~ 425 nm. The values of osmotic pressures  $P$  for samples S1 and S2 are 2.8 kPa and 4.8 kPa respectively and are calculated using the equation of state of hard sphere suspensions [346]. The

(111) planes of single crystalline domains of samples S1 and S2 have been captured at a distance of 3.15  $\mu\text{m}$  and 2.47  $\mu\text{m}$  from the coverslip using CLSM, (Fig. 5.4(a) and (b)) and the corresponding  $(x,y)$  particle coordinates, as well as the SPD, are determined by image analysis using Leica Qwin software.

## 5.3 Results and Discussion

### 5.3.1 Calculation of Pair Correlation

The particle size and SPD of dilute PNIPAM-co-Aac suspension determined from DLS are found to be 501 nm and 37%, respectively, at 25°C. Figure 5.4(a) and (b) shows CLSM images of (111) planes of crystallites in samples S1 and S2 respectively. To study the 2-dimensional real space structure of the PNIPAM crystal, the 2D pair correlation function  $g(r)$  is calculated using the  $(x, y)$  particle coordinates and compared with that of an ideal hexagonal lattice.  $g(r)$  is the probability of finding a pair of particles separated by a distance  $r$ .

$$g(r) = \frac{1}{\rho} \left\langle \sum_{j \neq i} \delta(r_i - r_j - r) \right\rangle_i \quad (5.1)$$

where  $\rho$  is the average number density and the indices  $i$  and  $j$  run over all the particles. The calculated two-dimensional  $g(r)$  patterns for the crystalline layers of samples S1 and S2 showing hexagonal order is shown in Fig. 5.4 (c). The peaks in the  $g(r)$  are consistent with that of a hexagonal arrangement of particles in the layer. In  $g(r)$  the first peak corresponds to the nearest neighbor distance  $d_{nn}$ . In the case of sample S1,  $d_{nn}$  occurs at 372 nm; whereas for sample S2,  $d_{nn} = 292$  nm. Since the particles are known to form an FCC structure [347], observation of  $d_{nn} < d$  implies that particle have shrunk from 501 nm to 372 nm and 292 nm respectively in samples

S1 and S2 under osmotic compression. The peaks in the experimental  $g(r)$  are broadened and their sharpness decays with increase in 'r' suggesting the presence of disorder. The schematic of the influence of osmotic pressure on PNIPAM-co-Aac microgel particles is shown in Fig. 5.5.

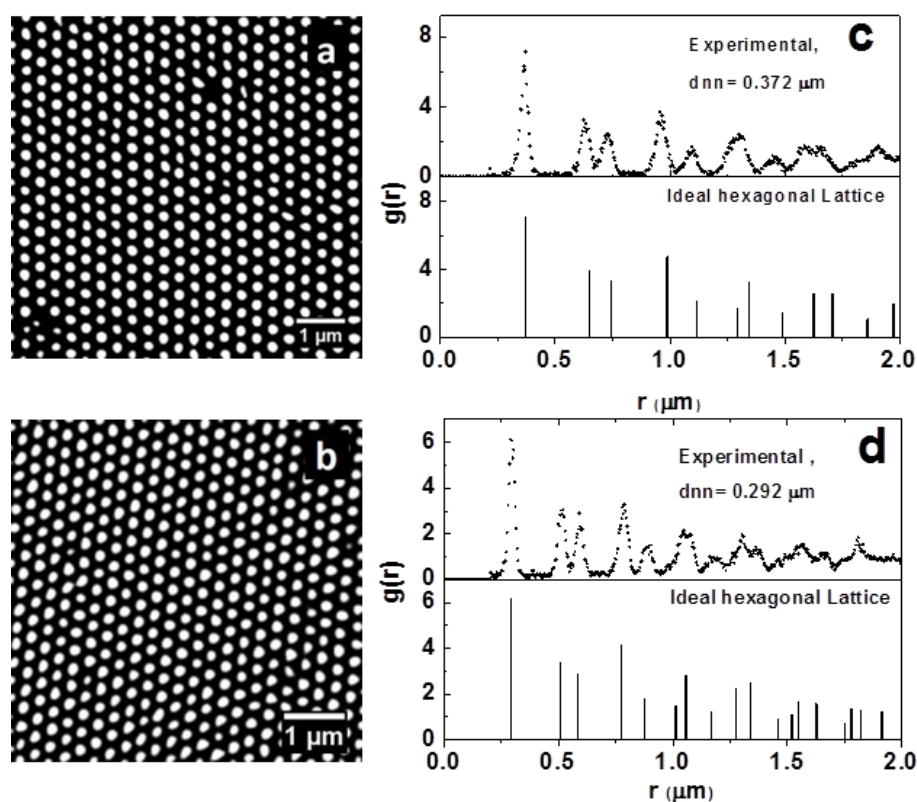


**Figure 5.4** CLSM images of single crystalline domains in sample S1 (a) and sample S2 (b). Corresponding  $g(r)$ 's are shown in (c) and (d) respectively.  $g(r)$ 's for respective ideal lattices are shown in bottom panels.

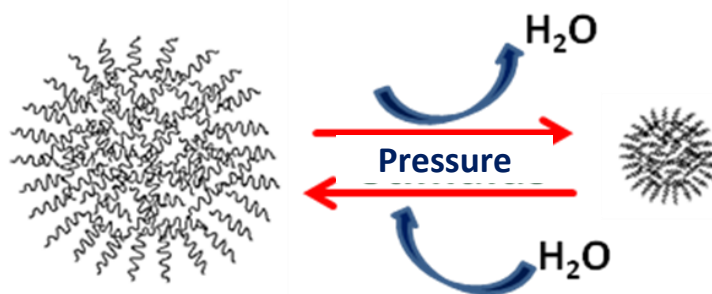


**Figure 5.5** Schematic of the influence of osmotic pressure on PNIPAM-co-Aac microgel particles showing the shrinking of microgels to smaller sizes with osmotic compression.

### 5.3.2 Calculation of Structure Factor

For characterizing the type of disorder present in samples S1 and S2 which is hidden in the details of the higher order peaks of  $g(r)$ , we calculated the 2D structure factor  $S(\mathbf{q})$  on a 2D grid of  $\mathbf{q}$  values with a sampling rate of  $\pi/L$ , where  $L$  is the image size obtained from confocal imaging [310]:

$$S(\mathbf{q}) = \frac{1}{N} \left| \sum_{n=1}^N \exp(i \mathbf{q} \cdot \mathbf{r}_n) \right|^2 \quad (5.2)$$

where  $\mathbf{r}_n$  are the position vectors of particles and  $N$  is the total number of particles.

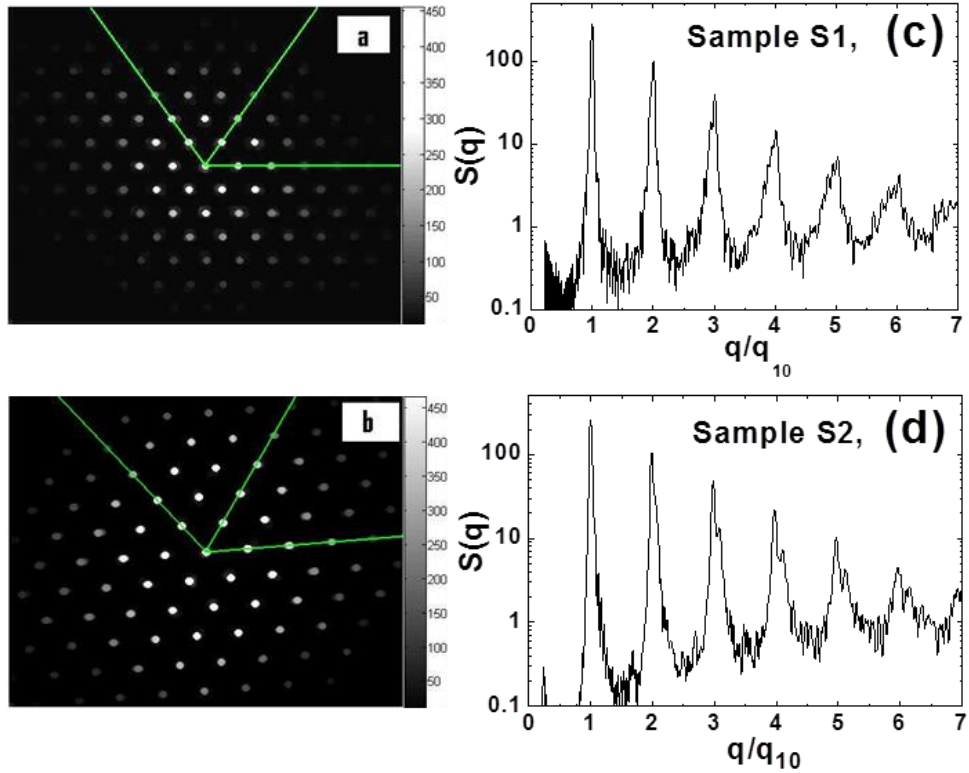


**Figure 5.6** Structure factor  $S(\mathbf{q})$  for the single crystalline domain in sample S1 (a) and sample S2 (b). Radial profiles of  $S(\mathbf{q})$  averaged over three different directions as marked in Fig.(a) and (b) for sample S1 (c) and sample S2 (d).

$S(\mathbf{q})$  calculated using Fig. 5.4(a) and (b) are shown in Fig. 5.6(a) and (b). In order to compare the difference in long-range order in the crystals of S1 and S2, we

calculated the radial profiles, which are determined by averaging  $S(q)$  over short arcs with an opening angle  $\delta\phi = 2^\circ$  and radius  $q$ . Figure 5.6(c) and (d) show the profiles averaged along three directions marked by thin lines in Fig. 5.6(a) and (b).

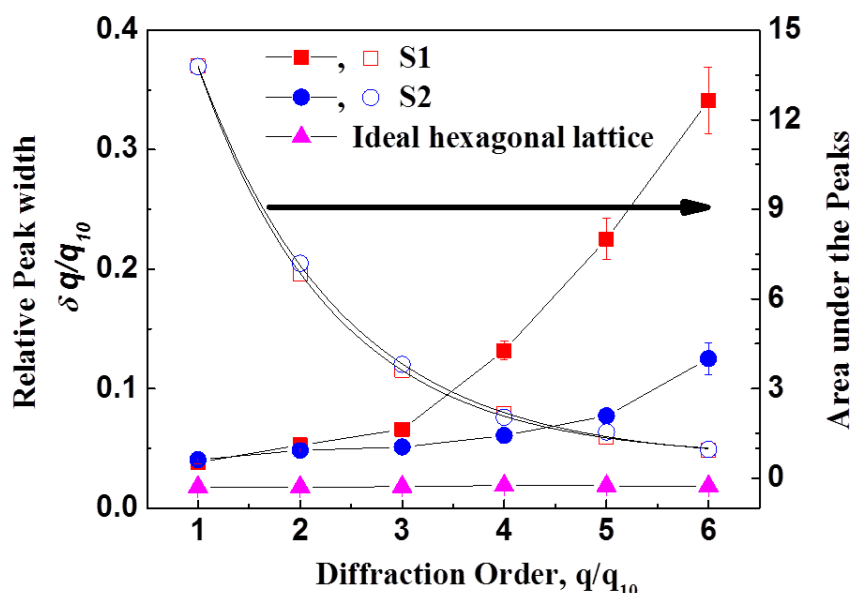


**Figure 5.7** Exponential fit of area under the  $S(q)$  peaks of Fig. 5 as a function of diffraction order  $q/q_{10}$  for single crystalline domains of sample S1, S2. The relative full width at half maximum peak widths  $\delta q/q_{10}$  of the  $S(q)$  peaks as a function of the diffraction order  $q/q_{10}$  for the single crystalline domains of sample S1, S2 and the reference lattice.

The area under the diffraction peaks is found to decrease as a function of diffraction order as shown in Fig. 5.7 (open squares and open circles), indicating the presence of first type disorder (Debye-Waller factor) as they are at the same temperature. For characterizing the presence of second type of disorder, we analyzed the radial widths of the diffraction peaks with increasing  $q$  vector. The peaks are fitted to a Lorentzian line-shape and the peak width  $\delta q$  (full-width-at-half-maximum) of the fit is analyzed for all the peaks with increasing diffraction orders. It is found that the peak width increases with increase in the diffraction order in both the samples and is shown in Fig. 5.7 (solid squares and solid circles). However, the peak width rapidly

increases with diffraction order in the case of sample S1 as compared to that of sample S2. For comparison, the width of the diffraction peaks as function of diffraction order for ideal hexagonal lattice of monodisperse particles is shown in Fig. (5.7) (triangles). For an ideal lattice, the peak width is independent of diffraction order, whereas samples S1 and S2 show monotonic increase with diffraction order. This implies the presence of second type disorder in samples S1 and S2 and arises due to SPD.

### **5.3.3 Influence of Osmotic Pressure on SPD**

Upon osmotic compression the size of the PNIPAM microgel particles have dramatically shrunk from 501 nm to 372 nm and 292 nm. These diameters are on the verge of detection limit in CLSM; hence extracting the SPD by image analysis is cumbersome. Towards addressing this issue of extracting SPD by image analysis we synthesized PNIPAM particles of large size (sample S3) by varying the monomer, crosslinker and initiator concentration. The same methodology of purification and osmotic compression has been adopted for sample S3. A very dilute suspension of sample S3 is imaged (Fig. 5.8(a)) using CLSM and image analyzed; particle size obtained is  $d=825$  nm. Upon osmotic compression the particle size significantly decreased to 488 nm. The compressed sample exhibited crystallization and the crystalline layers are imaged (Fig. 5.8(b)) using CLSM. On these images, image analysis has been carried out to obtain the SPD. Fig. 5.9 shows the particle size distribution for the dilute and the crystallized samples of S3 fitted to Gaussian. The measured value of SPD from the fit, for the dilute and the crystallized samples of S3 are 13% and 5% respectively. From this observation of decrease in SPD from 13% to 5%, we conclude that osmotic pressure not only reduces the particle size but also

significantly reduces the SPD.

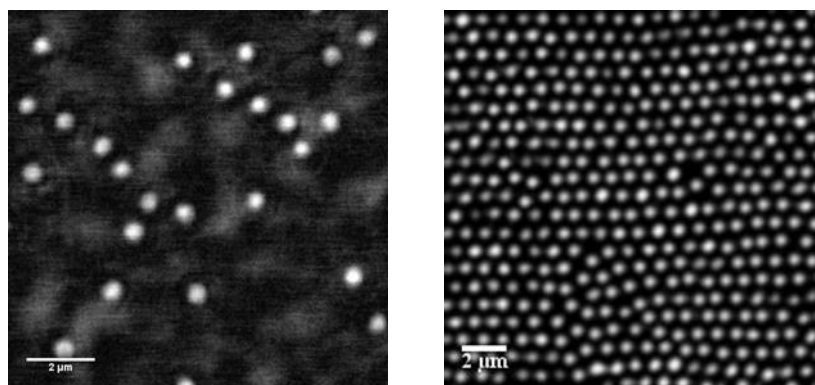


**Figure 5.8** Images of the PNIPAM particles recorded using CLSM: (a) before osmotic compression and (b) after osmotic compression.

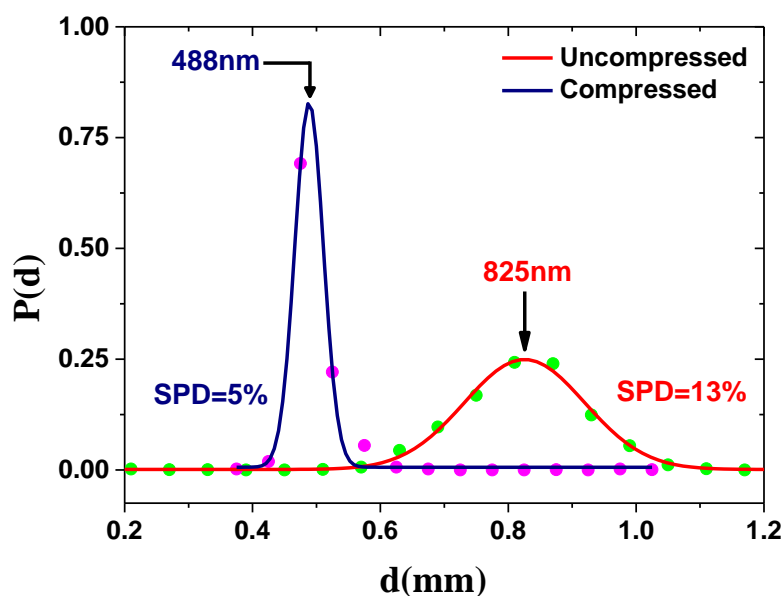


**Figure 5.9** Particle size distribution for the dilute (uncompressed) and the crystallized (compressed) samples of S3 fitted to Gaussian.

## 5.4 Conclusion

We have characterized the disorder in microgel crystals of osmotically compressed samples S1 and S2 using a confocal laser scanning microscope. These crystals are found to have first type and second type disorder. The first type disorder

is characterized by observing the exponential decay of area under the peaks of  $S(q)$  with increasing diffraction order. The second type disorder is characterized by analyzing the full width at half maximum of the peaks of  $S(q)$  as a function of diffraction order. Our analysis shows the presence of second type disorder in both crystals (Sample S1 and S2). Second type disorder is found to be more in the crystals of S1 which has a SPD of 13%. Upon compression, the second type disorder is found to decrease, due to the reduction of SPD to 7%. As synthesized PNIPAM-co-Aac particles are found to have 37% SPD. Upon osmotically compressing the suspension to a volume fraction  $> 0.74$ , the SPD is found to reduce to  $\leq 13\%$ . The increase in  $n_p$  with a simultaneous reduction in SPD is responsible for the appearance of long-range order in these samples. Present results provide the first evidence of reduction of SPD in microgel particles upon osmotic compression.



# EFFECT OF ENTANGLEMENTS ON TEMPERATURE RESPONSE OF GEL IMMOBILIZED MICROGEL PHOTONIC CRYSTALS

---

This chapter presents evidence of entanglement between polymer chains of thermo-responsive microgels with the immobilizing hydrogel by studying the temperature dependent dynamics of the microgel-hydrogel composite. The dynamics measurements show a reduction in amplitude of microgel thermal vibrations with an increase in temperature in contrast to the expected amplitude enhancement, confirming the binding between microgel and hydrogel through the entanglement of their polymer chains. The consequences of these entanglements on the temperature dependence of diffraction of immobilized microgel crystals across the volume phase transition (VPT) of microgels have been studied using UV-vis spectroscopy. Due to entanglements in immobilized microgel crystals, it is found that the crystalline order (the Bragg diffraction) is retained above VPT with a small increase in structural disorder (width of the Bragg diffraction peak). Entanglements restrict thermal motion of microgels leading to retention of crystalline order above the VPT. However, they induce local strain in the lattice due to shrinking of microgels upon VPT leading to an increase in structural disorder.

### 6.1 Introduction

Microgels are submicron sized particles of hydrogel consisting of cross-linked polymer network immersed in a solvent (water). Poly N-isopropyl acrylamide

(PNIPAM) based microgels are one of the most studied microgels, because of their responsive nature to various stimuli, such as temperature, pH, and ionic strength [183,187,188,213,348]. PNIPAM microgels respond to temperature by undergoing sudden deswelling/swelling transition (volume phase transition, VPT), upon increasing/decreasing the temperature [213,218,349]. They can be made responsive to pH by copolymerizing with co-monomers like acrylic acid [156,187]. Dense suspensions of monodisperse microgel particles exhibit crystalline order with a lattice constant of the order of the wavelength of light [204,213], which diffract wavelengths of light satisfying the Bragg's condition, making them potential candidates for applications as photonic crystals [165,350–352]. As prepared microgel crystals are fragile, *i.e.*, they lose their order to small disturbances (shear  $\sim$ a few dynes/cm<sup>2</sup>), which limits their practical use [223]. To overcome these limitations, and facilitate the use of microgel crystals for various applications, they have been immobilized either in a hydrogel matrix [167,224] or through covalent bonding between microgel particles with the addition of vinyl groups on their surface [287,353,354]. The gel immobilized microgel crystals have been shown to offer tunability of Bragg diffraction against the variation of stimuli like temperature, pH [167,224,351]. Hence, the immobilized microgel crystals are of great interest compared to those of hard/charged sphere colloidal systems [169,225] in applications as optical filters [167], sensors [169,225], optical switches [226], etc. PNIPAM microgel crystals are known to melt into liquid-like order at elevated temperature due to deswelling of microgels [213]. Thus, PNIPAM microgel crystals can be immobilized in a hydrogel matrix only at low temperatures ( $\sim$  15 °C) where microgel particles stay in swollen state and exhibit crystalline ordering. The process of gel immobilization of microgel crystal involves preparation of microgel crystal in a pregel solution and then polymerization of pregel

solution to form a hydrogel [224]. As PNIPAM based microgels have porous, core-shell structure with a dense polymeric core and a thin shell of dangling polymer chains [192,227,355], the polymerization is expected to occur outside as well as inside the microgels, leading to the formation of an interpenetrating/entangled network of polymer chains between the microgel and the hydrogel [228,356]. Studies by Song *et al.* [224] and Huang *et al.* [357] have implied the presence of such interactions between hydrogel and microgel through entanglements of polymer chains. Song *et al.* [224] have observed the swelling/ deswelling of PAAm hydrogel with temperature when incorporated with PNIPAM-co-Aac (Acrylic acid) microgel particles, whereas Huang *et al.* [357] have reported slow swelling of PNIPAM-co-Aac microgels in PAAm gel as compared to free microgels. Here, we report yet another evidence of the presence of such entanglements through dynamics study on PNIPAM-co-Aac microgel – PAAm (polyacrylamide) hydrogel composite system as a function of temperature, using 3D dynamic light scattering technique. Dynamics results show that amplitude of thermal vibrations of microgel in hydrogel matrix decreases with increase in temperature, in contrast to the expected increase, confirming the presence of entanglements/interpenetration of polymer chains between microgels and hydrogels. Further, we investigate the effect of such entanglements on the structural order of immobilized microgel crystals across VPT. Towards this, we have prepared PNIPAM-co-Aac microgel crystal and immobilized it in PAAm hydrogel matrix. The structural ordering of immobilized crystal across the VPT is characterized using UV-vis spectroscopy. The transmission spectra showed the Bragg diffraction dip, indicating the existence of crystalline order at all temperatures across the VPT. The presence of crystalline order above VPT, in spite of availability of large space around them due to a drastic decrease in their size (~ 50%) upon VPT, is due to

entanglements of polymer chains between microgel and hydrogel. Entanglements restrict the thermal vibrations of microgels within hydrogel and retain crystalline order. While the crystalline order is retained, the structural disorder (measured from the width of diffraction dip) is found to increase (though very small) upon VPT, which is explained in terms of local lattice strain induced from the collapse of microgel particles in an entangled state.

## **6.2 Materials and Methods**

### **6.2.1 Preparation of PNIPAM-co-Aac Microgel Particles**

PNIPAM-co-Aac microgel particles have been synthesized using free radical polymerization method [213]. 2.8 g of monomer (N-isopropyl acrylamide – NIPAM), 0.06 g of cross linker (N, N' methylene bisacrylamide - BIS), 0.16 g of co-monomer (Acrylic acid- Aac) and surfactant (sodium dodecyl sulfate - SDS) were dissolved in 240 mL of ultrapure deionized (Milli-Q) water. All the chemicals used in synthesis were of analytical grade and used as supplied. The filtered solution was degassed through constant Argon purging for one hour under vigorous stirring at 70 °C. Then 0.1 g of initiator (potassium persulphate – KPS) is dissolved in 10 mL of deionized water and added to the degassed solution at 70 °C. The polymerization was carried out at 70 °C for six hours, and the microgel suspension was cooled to room temperature. The synthesized suspension was dialyzed against Milli-Q water and concentrated using a stirred cell equipped with an ultrafiltration membrane. The pH of the concentrated suspension was found to be 3.4. Therefore, dilute suspensions were prepared in a buffer solution of pH of 3.4. The hydrodynamic diameter of PNIPAM-co-Aac microgel particles measured using dynamic light scattering (DLS) on dilute suspension at pH of 3.4 and 24 °C was found to be 347 nm with a polydispersity of

5.6%. The hydrodynamic diameter of the microgel particles includes the core size as well as the shell thickness. Dynamic light scattering measurements have been carried out using 3D DLS set up (LS instruments, Switzerland). The concentrated suspension, when heated to 35 °C and cooled slowly to 22 °C, exhibited iridescence, indicating crystallization. A photograph showing iridescence from PNIPAM-co-Aac microgel crystal at 22 °C in a container is shown in Fig. 6.2(a).

### **6.2.2 Immobilization of PNIPAM-co-Aac Microgel Crystal in PAAm Hydrogel**

For immobilization of PNIPAM-co-Aac microgel crystal in PAAm hydrogel, the microgel crystal was prepared in a pregel solution. The pre-gel solution consists of Acrylamide, BIS, and photoinitiator (2, 2-diethoxy acetophenone (DEAP)). Stock solutions of 5 M - acrylamide, and 0.125 M - BIS were prepared in a buffer of pH = 3.4 in order to maintain the pH as that of concentrated microgel suspension. DEAP was dissolved in DMSO (dimethyl sulfoxide) to the concentration of 10% (w/w). For the preparation of immobilized microgel crystal, 200  $\mu\text{L}$  of 5 M – acrylamide, 40  $\mu\text{L}$  of 0.125 M - BIS and 10  $\mu\text{L}$  of DEAP from stock solutions were added to 750  $\mu\text{L}$  of the concentrated suspension ( $n_p = 5.4 \times 10^{13} \text{ cm}^{-3}$ ). The suspension with pregel was then transferred to a thin quartz cell having dimensions of 10 mm  $\times$  25 mm and optical path length of 100  $\mu\text{m}$ . The sample cell was sealed with vacuum grease to avoid evaporation of water (solvent), heated to 35 °C and then cooled slowly to room temperature (22 °C) for crystallization. After crystallization, immobilization of the crystal was achieved using photopolymerization by irradiating the sample cell with UV radiation (315 nm) for about 4 hours at  $\sim$  15 °C. The immobilized crystal was then subjected to the UV-vis spectroscopic measurements using a JASCO V-650 UV-visible spectrometer.

Dilute immobilized PNIPAM-co-Aac microgel sample was prepared in a cylindrical quartz cell of 10 mm diameter by immobilizing the dilute microgel suspension ( $n_p = 2.7 \times 10^{10} \text{ cm}^{-3}$ ), by the same method used for immobilizing the crystalline sample. Dilution was done using the buffer solution of pH = 3.4 to maintain the same pH as that of the dense suspension. The pre-gel concentration in dilute suspension was maintained to be same as that used for immobilizing the crystalline sample. Dynamics measurements in this dilute immobilized microgel sample were carried out using 3D DLS set up. Upon immobilization, the sample becomes non-ergodic [358]. Therefore, during the DLS measurements, sample cell was rotated slowly (1 rotation per 20 min.) and ensemble averaged intensity-intensity correlation function was measured and used for further analysis [359].

### **6.2.3 3D Dynamic Light Scattering analysis of gel-immobilized samples**

The dynamics in gel-immobilized samples have been investigated using 3D DLS technique. It utilizes cross-correlation methods to determine intensity cross-correlation function. In case of turbid suspensions, multiple scattering affects the measured  $g^{(2)}(q, t)$ . The cross-correlation technique is helpful in removing the multiple scattering effects on  $g^{(2)}(q, t)$ , thereby giving intensity cross-correlation of singly scattered light. In 3D light scattering, two light scattering experiments are performed simultaneously using two laser beams (wave vectors  $\vec{k}_{i1}, \vec{k}_{i2}$ ) which cross each other at an angle  $\delta$  at the center of the vat and the scattered light from corresponding beams (wave vectors  $\vec{k}_{s1}, \vec{k}_{s2}$ ) are detected using two detectors (Fig. 6.1(b)). The two detectors are placed on the goniometer arm in such a way that both the detectors see the same scattering wave vector with respect to the singly scattered

light (Fig. 6.1(a)), i.e.,  $|\vec{q}| = |\vec{k}_{i1} - \vec{k}_{s1}| = |\vec{k}_{i2} - \vec{k}_{s2}|$ . The intensity cross-correlation function  $g_{12}^{(2)}(q, t)$  calculated using the scattered intensities  $I_1(q, t')$  and  $I_2(q, t' + t)$  is given as

$$g_{12}^{(2)}(q, t) = \frac{\langle I_1(q, t') I_2(q, t' + t) \rangle}{\langle I_1(q) I_2(q) \rangle} \quad (6.1)$$

The detectors detect both the singly scattered and multiply scattered light. The multiply scattered photons after scattering from many particles reach the detector with different values of  $\vec{q}$ . The intensities of light scattered at same  $\vec{q}$  are temporally correlated, whereas that for different  $\vec{q}$  is temporally uncorrelated. Upon cross-correlation of the intensity of the scattered light from the two detectors, the multiply scattered light gives rise to a constant background and only the singly scattered light contributes to the correlation function.  $f(q, t)$  obtained from  $g_{12}^{(2)}(q, t)$  using Siegert's relation is given as

$$g_{12}^{(2)}(q, t) = 1 + \beta |f(q, t)|^2 \quad (6.2)$$

where  $\beta$  is the net coherence factor given as  $\beta = \beta_m \beta_{12} \beta_c$  with  $\beta_m, \beta_{12}, \beta_c$  the coherence factor due to multiple scattering, coherence factor due to the overlap of two laser beams and the detector cross section respectively.

Upon immobilization of microgel particles into the hydrogel, samples become non-ergodic [358]. In non-ergodic systems, the time-averaged scattered intensity measured at a given scattering wave vector ( $q$ ) differs from that of ensemble-averaged intensity.

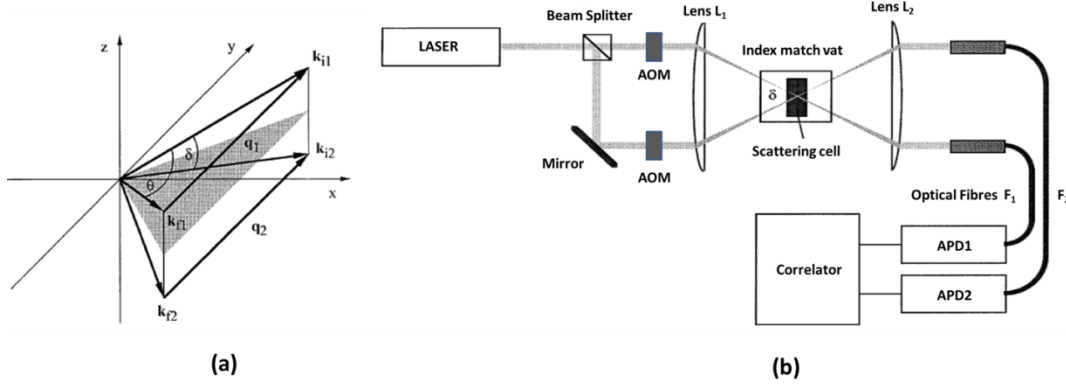


**Figure 6.1** (a) Ray diagram showing scattering geometry of 3D light scattering setup, (b) Schematic diagram of the cross-correlation light scattering setup.

In these systems, the time-averaged  $g^{(12)}(q,t)$  measured at different  $q$  values differ from each other, and the true ensemble average of  $g^{(12)}(q,t)$  is obtained by averaging the time-averaged correlation functions at different  $q$  values to obtain  $f(q,t)$ .  $f(q,t)$  for non-ergodic samples using cross-correlation scattering technique is given as [360]

$$f(q,t) = 1 + \frac{1}{\gamma} \left[ \sqrt{\left( \frac{g_{12}^{(2)}(q,t) - g_{12}^{(2)}(q,0)}{\beta^{dilute}} + 1 \right)} - 1 \right] \quad (6.3)$$

where  $\gamma = \sqrt{\langle I_1(q) \rangle_E \langle I_2(q) \rangle_E} / \langle I_1(q) \rangle_t \langle I_2(q) \rangle_t$ , subscripts  $E$  and  $t$  denote the ensemble and time-averaged intensities respectively. Subscripts 1 and 2 refer to the detectors 1 and 2 to measure the intensities for cross-correlation.  $\beta^{dilute} = \beta_{12} \beta_c$ ,  $\beta_{12}$  is the coherence factor due to the overlap of two laser beams and  $\beta_c$  is due to the finite area of the detectors. The ensemble average of the scattered intensity  $\langle I(q) \rangle_E$  is obtained by measuring the scattered intensities from different sample locations by rotating or translating the sample during the measurements and  $\langle I(q) \rangle_t$  is obtained by

measuring the time average of the scattered intensity at one location in the sample, i.e., at a single  $q$  value.

However, the above method works well only for homogeneous samples. Xue *et al.* [358] have proposed a direct method to measure the ensemble averaged intensity correlation by averaging the time-averaged intensity autocorrelations measured at different locations in the sample. It is a more direct method and works well for both homogeneous and inhomogeneous samples. The ensemble averaging is achieved by either translating or rotating the samples during the measurement. The rate of translation/rotation decides the time scales up to which the sample dynamics can be probed. In our measurements, we rotate the sample about the vertical axis at a speed of 1 rotation per 20 min. The rotation speed is decided such that the sample dynamics is completely isolated from the decay of correlation function arising due to the rotation. Our measurement directly gives the ensemble averaged intensity cross-correlation function,  $g_{12}^{(2)}(q, t)$  which is used to obtain the field correlation function  $f(q, t)$  using Siegert's relation [358] as in Eq. (6.2).  $f(q, t)$  is further analysed to study the dynamics in gel-immobilized samples.

## 6.3 Results and Discussion

### 6.3.1 Identification of VPT of PNIPAM-co-Aac Microgel Particles

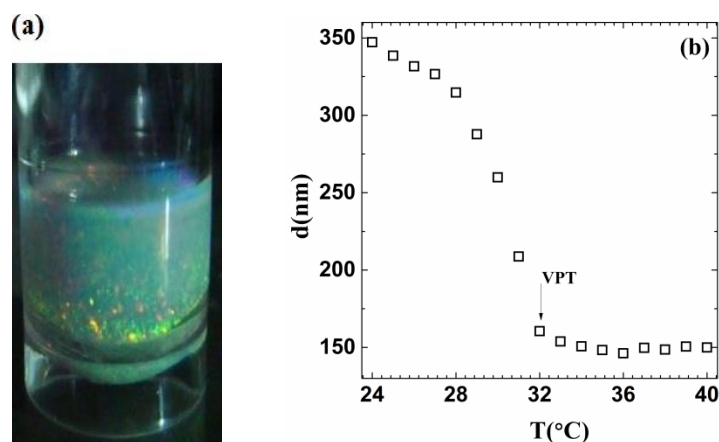


**Figure 6.2** (a) Photograph showing iridescence from PNIPAM-co-Aac microgel crystal in a container at 22 °C. b) Variation of hydrodynamic diameter,  $d$  of PNIPAM-co-Aac microgel particle with temperature at pH  $\sim$  3.4.

Temperature response of PNIPAM-co-Aac microgel particles at pH = 3.4 has been investigated by monitoring the diameter of microgel particle,  $d$  as a function of temperature. Fig. 6.2(b) shows a variation of  $d$  with temperature measured using DLS on a dilute suspension ( $n_p = 2.7 \times 10^{10} \text{ cm}^{-3}$ ). Upon increasing the temperature, the microgel diameter decreases with a sudden collapse at  $\sim 32$  °C, which is identified as volume phase transition (VPT). This transition of PNIPAM based microgels from swollen to deswollen state occurs as, the hydrophobic groups on PNIPAM favors polymer rich environment above the VPT [190]. Temperature dependent measurements were carried out around this VPTT (32 °C) of the microgels.

### 6.3.2 Evidence for Entanglements of Polymer Chains between Microgel and Hydrogel

The process of immobilization of microgels into hydrogel matrix involves the polymerization of a pre-gel solution with microgels immersed in it. As microgels are porous and core-shell structured, the polymerization of pregel solution can occur outside as well as inside the microgel, and thus may form entangled / interpenetrating network of polymer chains between microgels and hydrogel. Song *et al.* [224] have implicated the presence of such entanglements between hydrogel and microgel, from their observation of temperature dependent swelling/ deswelling of PAAm hydrogel incorporated with PNIPAM-co-Aac microgels. Here, we report another evidence of entanglements between polymer chains of microgels and immobilizing hydrogel, by investigating the dynamics in the microgel-hydrogel composite as a function of temperature. Dynamics measurements have been carried out on a dilute suspension of PNIPAM-co-Aac microgels ( $n_p = 2.7 \times 10^{10} \text{ cm}^{-3}$ ) immobilized in PAAm hydrogel matrix, across the VPT of microgels. The dilute suspension was chosen to study dynamics so that influence of inter-particle interactions between microgels [189,361] can be ignored. Dynamics measurements were carried out using 3D DLS technique [359]. At each temperature, the waiting time of 15 min was given before DLS measurement, for samples to reach to an equilibrium state. Due to non-ergodic nature of hydrogels [358], ensemble averaged intensity-intensity cross-correlation function,  $g_{12}^{(2)}(q, t)$  was measured at a given scattering wave vector,  $q$  by rotating the sample at speed of 1 rotation per 20 min. From the measured ensemble averaged intensity-intensity cross-correlation function, field correlation function  $f(q, t)$  is determined using Segert' relation,  $g_{12}^{(2)}(q, t) = 1 + |\beta_c \beta_{12} f(q, t)|^2$  with  $\beta_c$  and  $\beta_{12}$  being contribution

from detector coherence area and overlap of two laser beams used for cross-correlation. We have also measured the dynamics in PAAm hydrogel without microgel particles for reference. Fig. 6.3(a), (b) shows the  $f(q,t)$  for PAAm hydrogel without and with PNIPAM-co-Aac microgel particles at different temperatures, respectively. The second decay in correlation functions ( $\sim 0.1$  sec) is due to rotation of the sample during measurements. The rotation speed of 1 rotation per 20 min was chosen so that this second decay is well separated from initial decay of the sample. We have analyzed the correlation functions for their first decay to obtain the decay rate,  $\Gamma$  and longtime saturation limit,  $f(q,\infty)$ . In the case of hydrogel without microgel particles,  $f(q,t)$  is analyzed using gel mode plus inhomogeneity (GMPI) model [358] with the following function,

$$f(q,t) = f(q,\infty) + A \exp(-Gq^2 t / f) \quad (6.4)$$

according to which, scattering from gels consist of a dynamic part from gel modes which decay with decay rate  $\Gamma = Gq^2 / f$  and a static part from steady inhomogeneities. Here,  $A$  is the amplitude of gel modes,  $G$  is elasticity modulus of the gel and  $f$  is coefficient of friction between polymer and solvent. For all temperatures  $f(q,t)$  for hydrogel without particles is found to fit with Eq. (6.4) indicating purely diffusive modes of PAAm hydrogel. In the case of hydrogel with microgel particles, the dominant scattering comes from the microgel particles due to their dense core [192,355]. The field correlation of light scattered from the microgel-hydrogel composite can be described as [358,362],

$$f(q,t) = \exp \left[ -q^2 \langle \delta^2 \rangle \left( 1 - e^{-(\Gamma t)^\alpha} \right) \right] \quad (6.5)$$

where  $\langle \delta^2 \rangle$  is the amplitude of mean square displacement of the microgel particle within the hydrogel matrix. The exponent  $\alpha$  characterizes nature of motion of the microgel, either to be diffusive ( $\alpha = 1$ ) or deviates from diffusive ( $\alpha \neq 1$ ), hence the interaction between microgel and hydrogel matrix. The analysis of  $f(q,t)$  for hydrogel with the microgel particles using the Eq. (6.5), gives the value of  $\alpha \approx 1$  for all temperatures across the VPT, suggesting the diffusive motion of PNIPAM-co-Aac microgel particle within PAAm hydrogel matrix. It implies that either PNIPAM-co-Aac microgel particles are diffusing freely within the space confined by polymer network of PAAm hydrogel or are strongly bound to PAAm hydrogel and exhibit diffusive motion due to the gel modes.

In order to verify whether the microgels are freely diffusing or bound inside the hydrogel network, we have obtained the decay rate  $\Gamma$  and long time saturation value,  $f(q,\infty)$  for hydrogel and hydrogel-microgel composite by analyzing corresponding  $f(q,t)$ . Fig. 6.3 (c) and (d) shows  $\Gamma$  and  $f(q,\infty)$  for hydrogel without and with the microgels as a function of temperature, respectively.

For PAAm hydrogel,  $\Gamma$  increases linearly with increase in temperature as expected [358,363]. On the other hand, the temperature dependence of  $\Gamma$  for hydrogel with microgels is non-linear due to the corresponding variation of microgel size (Fig. 6.3(b)). It increases below VPT, exhibits a plateau near VPT and again increases above VPT. This suggests that the dynamics of volume phase transition in the microgel-hydrogel composite is significantly different than that for microgels in aqueous suspension. To ensure the equilibrium state of microgel-hydrogel composite, we have carried out time dependent DLS measurements at a given temperature, after equilibrium time of 15 min. Fig. 6.3 (e) shows time dependence of decay rate,  $\Gamma$  and

$f(q, \infty)$  for temperatures in the vicinity of VPT. Both the  $\Gamma$  and  $f(q, \infty)$  are constant for all the measured times, indicating the equilibrium state of samples. Time dependence of microgel size in suspension as a function of time after an equilibration time of 15 min, is shown in Fig. 6.3 (f) for comparison. The correlation functions for microgel suspension were measured at 5 min interval as they decay faster. Time independence of microgel size indicates equilibrium state. The plateau in  $\Gamma$  (Fig. 6.3 (c)) near VPT is an indication of the presence of interactions between microgel and hydrogel. Because, if microgels are freely diffusing within the hydrogel,  $\Gamma$  near VPT should increase more rapidly, as  $\Gamma$  is inversely related to microgel size [358,364] which decreases rapidly near VPT (Fig. 6.3(b)). Thus, the plateau in  $\Gamma$  indicate binding of microgel and hydrogel network. Such a binding is possible through interpenetration/entanglements between polymer chains of microgels and hydrogel, as immobilization has been carried out in swollen state of microgels (at 15 °C). As microgel particles shrink near VPT, the entanglements of polymer chains between hydrogel and microgel becomes stronger, which increases hindrance to the microgel's motion, giving rise to plateau in  $\Gamma$ .

We have also monitored the long time saturation limit,  $f(q, \infty)$  of field correlations for hydrogel without and with microgel particles, as a function of temperature across VPT (Fig. 6.3(d)).  $f(q, \infty)$  is related to the amplitude of thermal vibrations of scattering element [364].  $f(q, \infty)$  for hydrogel without microgels is constant with respect to temperature. Whereas  $f(q, \infty)$  for hydrogel with microgels increases as temperature is increased, and attains saturation after VPT.

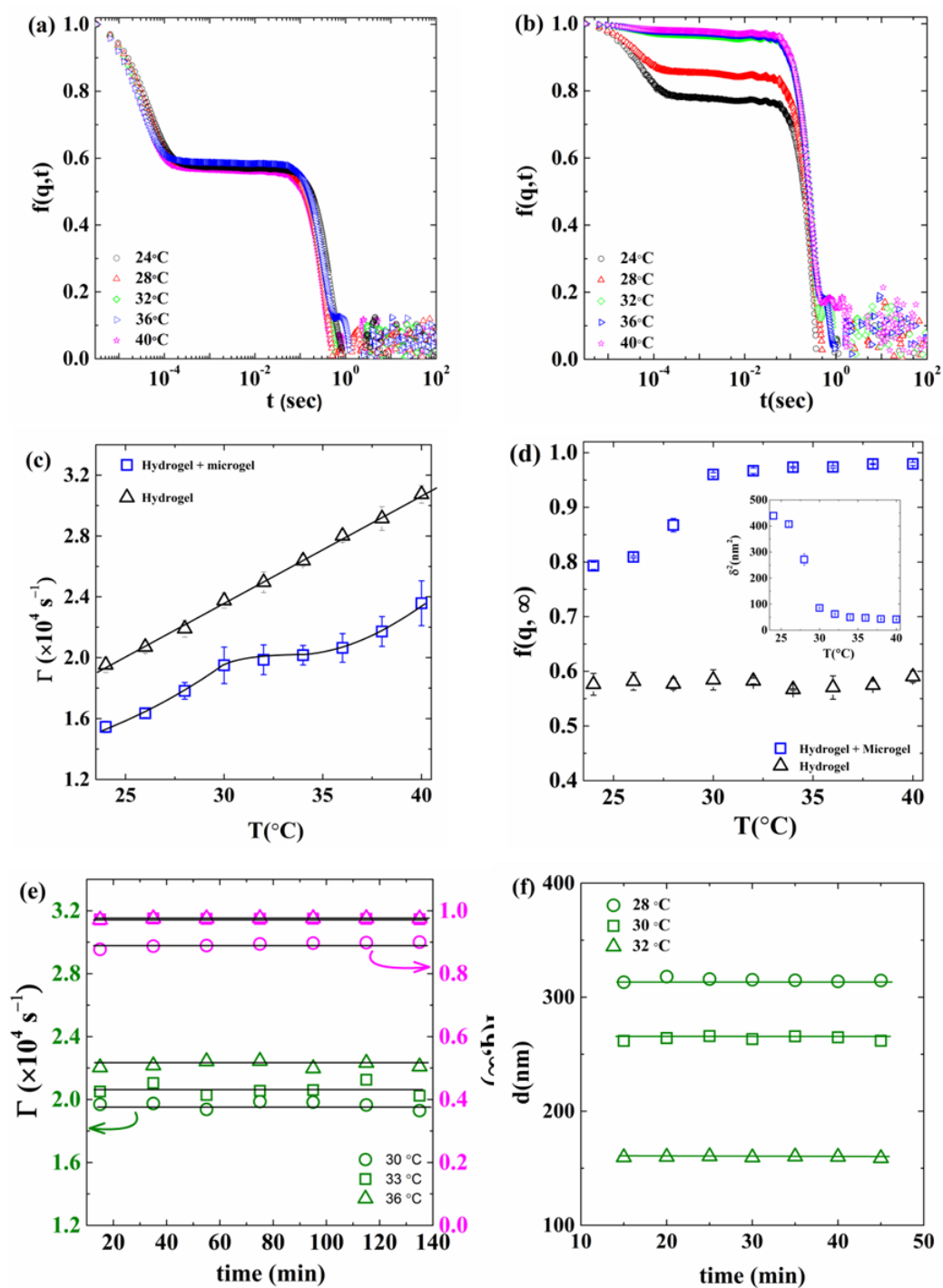


**Figure 6.3**  $f(q,t)$  for PAAm hydrogel at different temperatures (a) without and (b) with PNIPAM-co-Aac microgel particles incorporated. (c) Decay rate,  $\Gamma$  and (d)  $f(q, \infty)$  of PAAm hydrogel with and without microgels, as a function of temperature. Inset in (d) is temperature dependence of  $\langle \delta^2 \rangle$  of microgels in the hydrogel. Error bars are obtained from the average of three measurements. (e) time dependence of  $\Gamma$  and  $f(q, \infty)$  for microgel-hydrogel composite and (f) time dependence of microgel size in aqueous suspension, at different temperatures in the vicinity of VPT. Continuous lines are guide to the eyes.

The amplitude of mean square displacement,  $\langle \delta^2 \rangle$  due to thermal vibrations in hydrogel with microgels (obtained from Eq. (6.5)) is shown as an inset in Fig. 6.3(d).  $\langle \delta^2 \rangle$ , which is inversely related to  $f(q, \infty)$  [358,364], decreases as temperature is increased, and attains saturation after VPT. Again, if the microgel particles are free within the hydrogel network,  $\langle \delta^2 \rangle$  should increase as temperature is increased because shrinking creates an extra space around the microgels within the hydrogel network. However, we observe a decrease in  $\langle \delta^2 \rangle$  as temperature is increased, confirming the entanglement of polymer chains between microgel and hydrogel. As temperature increases entanglements become stronger due to the stretching of entangled polymer chains, caused due to the shrinking of microgels. This causes a reduction in  $\langle \delta^2 \rangle$  with temperature. Above VPT  $\langle \delta^2 \rangle$  saturates, as microgel size remains constant. Thus, our observations of plateau in  $\Gamma$  near VPT and decrease in  $\langle \delta^2 \rangle$  upon VPT constitute strong evidence of entanglements between polymer chains of microgels and hydrogel used for its immobilization.

### **6.3.3 Consequences of Entanglements on Structural Ordering of Gel-Immobilized Microgel Crystal using UV-vis Spectroscopy**

In the previous section, it is shown that when PNIPAM-co-Aac microgels are immobilized in PAAm hydrogel, polymer chains between the microgels and the hydrogel get entangled. We further investigate the effect of such entanglements of polymer chains between the microgels and the hydrogel on the structural ordering of the gel-immobilized microgel crystal as a function of temperature. For this purpose immobilized PNIPAM-co-Aac microgel crystal was prepared in a thin quartz cell of 100  $\mu\text{m}$  optical path length as described in experimental section.

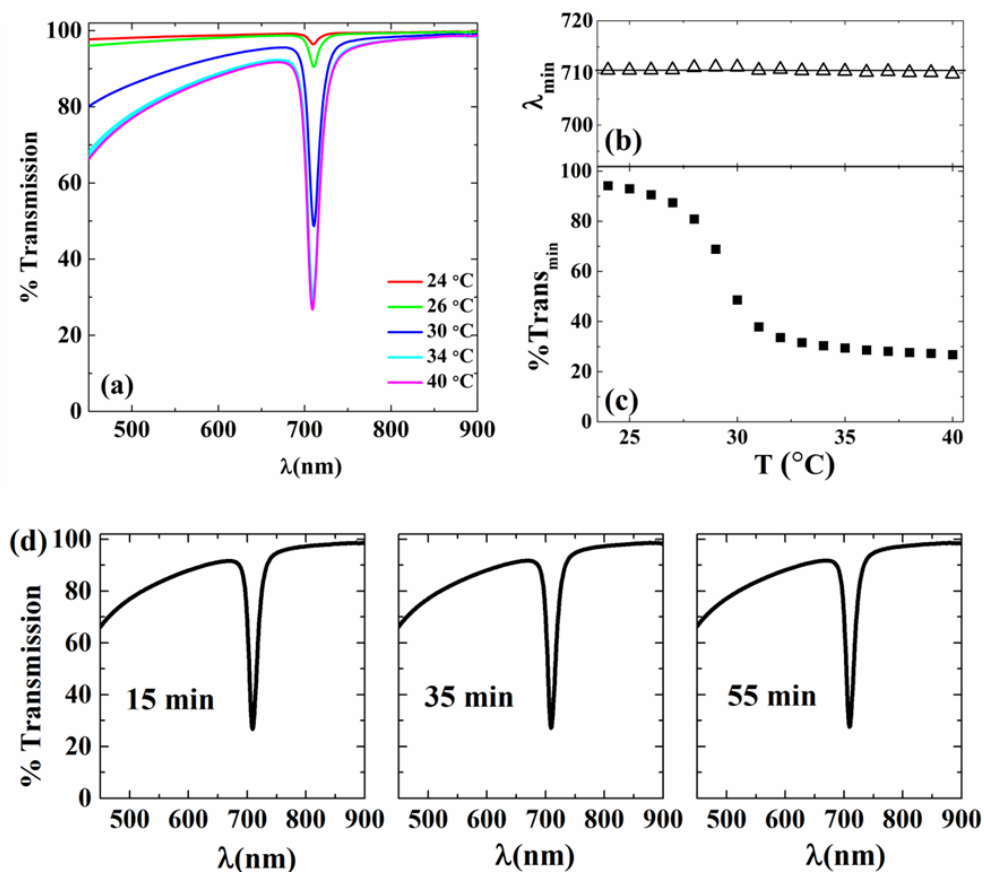


**Figure 6.4** (a) UV-vis transmission spectra from gel immobilized microgel crystal at different temperatures showing Bragg diffraction dip. Temperature dependence of position (b) and minimum (c) of the diffraction dip in transmission spectra. (d) time dependence of Bragg diffraction (gel size) for immobilized microgel crystal at 40 °C.

To investigate the temperature dependence of structural ordering in this immobilized microgel crystal, its UV-vis transmission spectra have been recorded across the VPT using a JASCO 650 spectrometer. At each temperature, samples were equilibrated for 15 min, before recording the spectra. Fig. 6.4(a) shows the UV-vis transmission spectra of the immobilized microgel crystal at different temperatures. All spectra were recorded under normal incidence. At all temperatures across the VPT, transmission spectra show a dip due to Bragg diffraction, indicating the presence of crystalline order. The diffraction dip occurs at wavelength  $\lambda_{min}$  ( $\sim 710$  nm) which satisfies the Bragg condition,

$$2\mu_s d_{hkl} \sin\theta = n' \lambda_{\min} \quad (6.6)$$

where  $d_{hkl}$  is inter-planar spacing,  $\mu_s$  is the refractive index of solvent,  $n'$  is the order of diffraction ( $n' = 1$  for the first-order) and  $\theta$  is the angle between the crystal plane and the diffracted ray which is  $90^\circ$  for normal incidence. Microgel crystals are known to grow in face-centered cubic (fcc) structure [204] with close-packed planes, having  $h,k,l <111>$ , facing parallel to the wall of the cell. Thus, the dip in the transmission spectra is due to diffraction from  $<111>$  planes of fcc structure. The number density of the fcc crystals is related to  $\lambda_{\min}$  as [364]

$$n_p = \frac{32}{3\sqrt{3}} \left( \frac{\mu_s}{\lambda_{\min}} \right)^3 \quad (6.7)$$

The  $n_p$  determined using above relation is found to be  $4.05 \times 10^{13} \text{ cm}^{-3}$  and the volume fraction ( $\phi = n_p \pi d^3 / 6$ ) at  $24^\circ \text{C}$  is found to be 0.87. This  $\phi$  of the microgel crystal at  $24^\circ \text{C}$  is higher than 0.74 (close packing of fcc) and is due to over estimation of  $\phi$  using the microgel diameter in the swollen state (347 nm). As shown in earlier studies [165,352], in dense suspensions, the microgel particle undergoes compression due to osmotic pressure from surrounding microgel particles. The near neighbor separation (327 nm) determined using  $\lambda_{\min}$  [165,352] is found to be smaller than the diameter of the microgel particle in the swollen state, providing an evidence for the compression of PNIPAM-co-Aac microgel particles. Temperature dependence of  $\lambda_{\min}$  and the minimum of the dip in transmission spectra ( $Trans_{\min}$ ) is shown in Fig. 6.4 (b) and (c) respectively, which is discussed in the latter part.

Above the VPT, microgel shrinks to a diameter of 150 nm (Fig. 6.2(b)), reducing the volume fraction of microgel particles within the hydrogel to 0.07. Thus,

the volume fraction of microgel particles in immobilized crystal changes from 0.87 at 24 °C to 0.07 above the VPT, leaving void space with the volume fraction of 0.80 within the hydrogel matrix. The hydrogel network is reported to be stable against the voids formed within the gel network due to the removal of added particles [365]. We have tested the stability of immobilized microgel crystal in a collapsed state of microgels (at 40 °C, i.e., well above VPT of microgels) by recording the Bragg diffraction as a function of time after the equilibrium time of 15 min, which is shown in Fig. 6.4(d). The wavelength of Bragg diffraction remains the same for times up to 55 min. The wavelength at which Bragg diffraction occurs is related to lattice spacing and hence to the size of the gel, suggesting that there is no change in gel size upon the collapse of microgel particles. Thus, the void space fraction of 0.80 is available for microgel particles to exhibit thermal motion. This space is good enough to destroy the crystalline order of microgels due to their thermal motion, as it happens in unimmobilized microgel crystals [364]. However, we observe here that in immobilized microgel crystal, the crystalline order is present even above the VPT. The existence of crystalline order of microgels above VPT (after 32 °C) is understandable in terms of the entanglement/interpenetration of polymer chains between microgel and hydrogel matrix. Formation of such entanglement/interpenetrating polymer network is possible as microgel crystals have been immobilized in the swollen state of microgels (at 15 °C). As discussed in the previous section, entanglements/interpenetration between polymer chains of microgel and hydrogel restricts the thermal motion of microgels and hence retains crystalline order above the VPT, in spite of the availability of large space due to shrinkage of microgels. Though the mesh size of PAAm hydrogel (~ 6nm) is much smaller than the microgel diameter, which is capable of fixing the microgels in hydrogel without

entanglements, it is only entanglements which can retain crystalline order above VPT as the hydrogel size is fixed. Thus, the presence of crystalline order and hence possible tuning of the Bragg diffraction, in immobilized PNIPAM-co-Aac microgel crystal with temperature, is due to the entanglements between polymer chains of microgel and hydrogel.

We have also measured the width of the Bragg diffraction dip as a function of temperature, which is shown in Fig. 6.4 (a). In order to estimate the width, diffraction dip was converted to reflection peak and fitted with Voigt's function [366] given as below:

$$V(x, \sigma, \gamma) = \int_{-\infty}^{+\infty} G(x', \sigma) L(x - x', \gamma) dx' \quad (6.8)$$

It is a convolution of Gaussian  $G(x', \sigma)$  and Lorentzian  $L(x - x', \gamma)$  functions. Here  $\sigma$  is standard deviation of Gaussian and  $\gamma$  is width of the Lorentzian function. Full width at half maximum of the peak is taken as total width,  $W$  of the peak. Fig. 6.5 (a) shows that at temperatures well below and above the VPT (32 °C),  $W$  shows a tendency towards saturation. However, in the vicinity of VPT, it increases rapidly. Increase in width indicates an increase in structural disorder upon VPT. S. Jia *et al.* [367] have reported such stimuli driven order-disorder transition in immobilized microgel crystals. They have doped the microgel crystal with impurity microgel and shown that the crystalline order can be tuned by changing the dopant size using glucose as stimulus. Here, we show that in an undoped immobilized PNIPAM-Aac microgel crystal, structural order is tunable with temperature. This is attributed to the entanglement of polymer chains between microgel and hydrogel. As microgel particle shrinks, the entangled polymer chains of hydrogel get strained, causing distortion

and stretching of the polymer network to which they are connected. Such strain induces structural disorder in the crystal, which is reflected in the increase of the width of diffraction dip. Schematics of immobilized microgel crystal depicting interpenetration/entanglement of polymer chains of hydrogel and microgels in unstrained condition before VPT and strained condition after VPT are shown in Fig. 6.5 (b) and (c) respectively.

Fig. 6.4(b) shows the  $\lambda_{min}$  as a function of temperature. The  $\lambda_{min}$  is found to be the same at all temperatures, suggesting that the inter-planar spacing and hence the lattice constant remains unchanged with variation in temperature. On the other hand, the minimum of the dip in transmission spectra ( $Trans_{min}$ ) is found to decrease with increase in temperature and exhibits a sudden fall at 32 °C (shown in Fig. 6.4 (c)). As interpreted by Weismann *et al.* [167] and Song *et al.* [224], the variation of transmission minimum is due to variation of refractive index of microgel particle with temperature. As particle shrinks, the polymer density of the microgel particle increases. This causes an increase in microgel refractive index and hence the scattering efficiency of particles.

Notice that the relative increase in structural disorder ( $\Delta\lambda/\lambda_{min}$ ) upon VPT is very small ( $\Delta\lambda$  is  $\sim 5$  nm in Fig. 6.5 (a) and  $\lambda_{min} \sim 710$  nm in Fig. 6.4 (a)), while there is a large increase in scattering efficiency of microgels due to increase of their refractive index [167,218]. This makes the Bragg diffraction dip in the immobilized microgel crystal more prominent above VPT as compared to that below VPT, allowing tuning of Bragg diffraction intensity of light with temperature. It must be mentioned here that our immobilized microgel crystals were prepared in a close sample cell (as discussed in experimental section), where hydrogel sticks to the walls

of the sample cell. As a result of this, the total volume of the sample remains constant across VPT ( $\lambda_{min}$  is constant in Fig. 6.3(b)). However, there is local stretching of hydrogel polymer chains, which gives rise to increase in width of the diffraction dip. On the other hand, Song *et al.* [224] have used immobilized microgel crystal detached from the sample cell, where they have observed shifting of  $\lambda_{min}$  with temperature. These observations suggest that the entanglements have a strong effect on temperature response of gel-immobilized microgel crystal, and the nature of temperature response depends on the boundary conditions imposed on the immobilized microgel crystal.

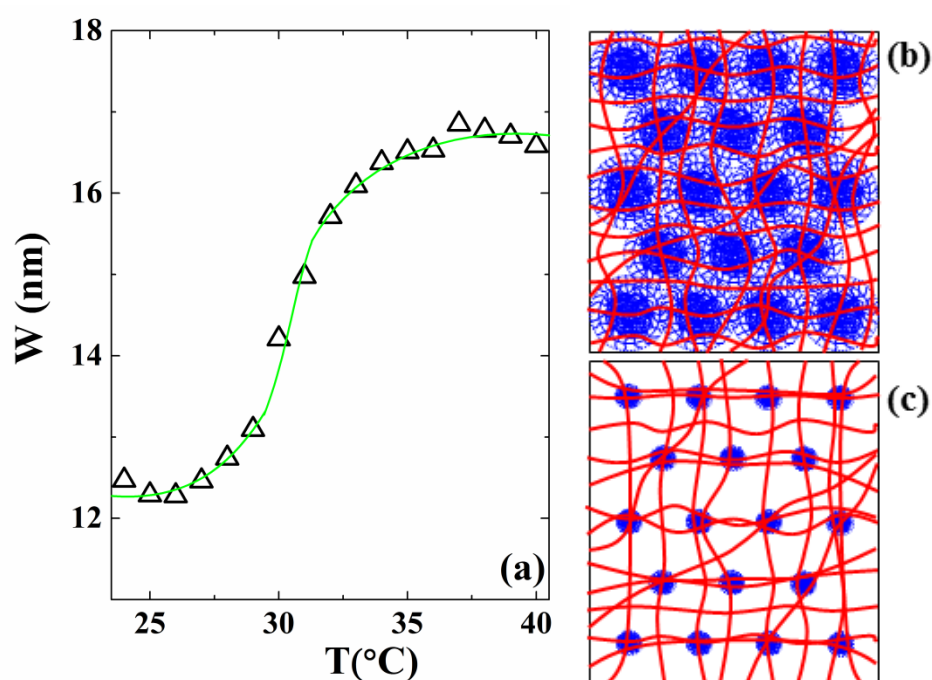


**Figure 6.5** (a) Variation of width,  $W$  of the diffraction dip across the VPT. Continuous line is guide to the eye. Schematic representation of gel-immobilized microgel crystal having entanglements of polymer chains between microgel (blue) and hydrogel (red) showing (b) unstrained hydrogel network below VPT and (c) strained hydrogel network above VPT.

In short, immobilization of microgel particles into hydrogel matrix in their swollen state leads to the formation of an interpenetrating/entangled network of polymer chains between microgel and hydrogel. These entanglements are responsible

for retaining crystalline order in the immobilized microgel crystal above VPT, with a mere increase in structural disorder. Thus entanglements make it possible to tune the intensity of Bragg peak with temperature in the immobilized microgel crystal.

#### **6.4 Conclusion**

We have synthesized monodisperse PNIPAM-co-Aac microgel particles, prepared microgel crystals and immobilized them into PAAm hydrogel matrix by photo-polymerization. UV-vis transmission spectra recorded on the immobilized microgel crystal showed a dip due to Bragg diffraction at all temperatures across VPT, indicating the presence of crystalline order. Study of dynamics in the microgel-hydrogel composite as a function temperature revealed the arrest of microgel dynamics in the deswollen state of microgels, which constitutes evidence for the entanglement between polymer chains of microgel and hydrogel. These entanglements are shown to be responsible for the existence of crystalline order of microgels above VPT under immobilized condition. While retaining the crystalline order, entanglements induce local strain causing small increase in structural disorder upon VPT. Our experiments show that binding between microgel and hydrogel plays an important role in governing the structural order of gel-immobilized microgel crystal, which is crucial for obtaining the desired optical properties for various applications. We believe that our results will motivate further investigations on microgel - hydrogel composites for their complex interactions and applications towards development of various sensors and optical devices.



### SUMMARY AND FUTURE OUTLOOK

---

---

This chapter summarizes the important new results and conclusions of the thesis followed by a discussion on possible future work.

#### 7.1 Summary and Conclusions

This thesis describes the various design and developmental aspects of an optical tweezer set up and its extension to a holographic optical tweezers (HOTs) system employing a dynamic beam shaping technique to create a multitude of spots capable of trapping and manipulating mesoscopic particles. Procedures to optimize the SLM (the heart of HOTs) to generate uniform and efficient holographic optical traps have been described. A novel technique to determine beam profile over the SLM was discussed. The contents of this thesis is broadly divided into two categories: the development of optical tweezers and its extension to a HOTs system and its optimization to generate highly efficient, uniform optical traps, form the first theme of this thesis. The developed optical manipulation system has been applied to study the volume phase transition (VPT) in a special class of colloidal systems known as stimuli-responsive microgel systems (PNIPAM-co-Aac) at the single particle level, which finds applications of utmost importance and serves as a probe for model condensed matter systems. In addition, the crystals of these microgels have been studied for their disorder (in particular, second type disorder) under osmotic compression, and our study unfolds some interesting physics in these systems. Since, the practical use of these stimuli-responsive systems requires these systems in portable immobilized form, an immobilized form of these microgels in a hydrogel

matrix has been studied. Our studies of dynamics using 3D DLS reveals the presence of entanglements, and we discuss its effects on the order and disorder in these immobilized crystals. These studies on this microgel system (PNIPAM) using our optical manipulation systems and other light scattering techniques forms the second theme of this thesis.

**Chapter 1** of this thesis is an introduction to the development of the field of optical manipulation, and its historical evolution through various experiments done by earlier researchers demonstrating radiation pressure of light. A major leap through occurred when the capability of trapping microscopic particles using a single laser beam, *the single beam gradient trap*, was discovered by Arthur Ashkin in the 1970's after the invention of lasers. This was a breakthrough in science, and it found use in various fields of research to exploit the properties of systems at a single particle level, from biology to condensed matter. Further developments in the field such as trapping multiple particles to perform various interaction studies gave birth to the technique of HOTs, through other beam shaping techniques such as the use of scanning mirrors, deformable mirrors, AODs, EODs has been described. The various applications of the state of the art optical manipulation technique have been described, in particular, in its application to colloidal systems. This chapter also introduces colloidal systems, in particular, a class known as responsive colloidal systems which change their properties with changes in various external stimuli like temperature, pressure, pH, ionic strength. **Chapter 1** discusses the motivation behind the various developments and research work carried out in the thesis, describing major outcomes of the thesis.

In **chapter 2**, the development of optical tweezers set-up along with its principle of operation is described. The principle of optical trapping in various

trapping regimes, the Rayleigh regime, ray-optic regime and intermediate regime are discussed. It also describes the various design considerations for building the optical tweezer set-up and its extension to create steerable traps in three dimensions. Further, we discuss calibration techniques and how we calibrated the optical trap by the Boltzmann method and equipartition method. The trap stiffness of a trapped particle was measured as a function of laser power and found to be linear, confirming the calibration to be correct. We also showed the capability of the set-up in trapping multiple particles in a ring geometry by placing the focus of the laser on the top surface of the sample chamber.

**Chapter 3** describes the design and development of HOTS system using a phase-only reflective spatial light modulator (SLM) incorporated in the optical manipulation system. We present a methodology to optimize the properties of graphics, (SLM being driven by a DVI interface through graphics) using a method similar to that used for optimizing LCD televisions. The graphics card was optimized for maximum diffraction efficiency and for addressing the gray values with uniform resolution through the range of available phase levels. A calibration function was generated for the SLM correcting for the non-linearity in the phase response that resulted in an improvement of diffraction efficiency to 50% from 29% with the calibration function from the supplier. It also enhanced the phase modulation depth from  $1.4 \pi$  to  $1.7 \pi$ . Further, a new technique based on diffraction has been presented to quickly calibrate the SLM for spatially varying phase response. We divided the SLM into  $8 \times 8$  sub-sections, and each of these subsections were optimized for brightness, contrast, and gamma by measuring the power in the first-order beam as a function of brightness, contrast, and gamma of the hologram. The optimized values were incorporated into the algorithm to generate holograms, and an improvement in

diffraction efficiency of 55% from 50% was observed. Uniformity in the intensity of the trap spots was found to improve from 76% to 97% as observed from reflective measurements, resulting an uniformity of 80% in the trap stiffness for particles trapped in a circular array of eight spots. The SVPR correction also improved the trap quality up to 6.5%, as calculated from spot sharpness metric and a trap performance metric of value 0.49. This method allows for quick calibration for spatially varying phase response (SVPR) as required for experiments performed at different laser power levels and non-uniform illumination, the phase response of the SLM being dependent on the incident power level. Further, using the same methodology we devised a novel technique to determine the actual beam profile of the incident laser beam over SLM, which is required as an input for algorithms to generate the holograms to be displayed over SLM.

Using the optical manipulation system, PNIPAM-co-Aac microgels have been investigated for their VPT at a single particle level as described in **chapter 4** of this thesis. We trapped a single microgel, measured its trap stiffness as a function of temperature and characterized its VPT; we compared these results to the conventional DLS technique that gives an average effect of VPT measured on  $\sim 10^7$  to  $10^8$  particles. Analysis of DLS data is affected by the polydispersity in the sizes of the particles. We found the VPT to be of continuous type and VPTT at 34 °C as observed with DLS on  $10^7$  particles, suggesting a negligible effect of low (2%) size polydispersity on VPT of microgel and similar nature of inhomogeneities among different microgels. We also computed the trap stiffness numerically as a function of temperature, the temperature change being reflected by the change in size and the refractive index of microgel with temperature. The change in refractive index played a dominant role which led to an increase in the trap stiffness compared to the size whose decrease led to a decrease in

the trap stiffness with temperature. The rise in the value of trap stiffness upon VPTT is found to be due to a sudden deswelling of the microgel, which lead to an increase in refractive index and decrease in particle size. This characterization of VPT at single particle level will motivate utilization of optical manipulation system to probe various other processes in stimuli-responsive microgel systems.

In **chapter 5**, dense suspensions of PNIPAM-co-Aac microgel suspensions subjected to osmotic compression have been investigated for their disorder. It is found that under osmotic compression the particle sizes reduce due to increasing concentration of particles in suspension, but also the size polydispersity reduces significantly, leading to the onset of crystallization in more osmotically compressed sample, compressed beyond a volume fraction of 0.74. We investigated the second type disorder in samples with different extent of osmotic compression and found that the second type disorder reduced under pressure. We also found first type disorder in this system. The increase in concentration with a simultaneous reduction in SPD is responsible for the appearance of long-range order in these osmotically compressed samples.

In **chapter 6**, PNIPAM microgels immobilized in hydrogel were investigated for the presence of entanglements. A dynamics study, using 3D DLS, revealed the presence of entanglements between the polymer chains of the microgel and the immobilizing hydrogel, and this is confirmed by the arrest of microgel dynamics in the deswollen state of microgels as a function of temperature. Investigation of the immobilized microgel crystals of these microgels showed the existence of crystalline order even after VPT, with increasing structural disorder. This has been attributed to a decrease in amplitude of the thermal motion of the microgels due to entanglements

between microgel and hydrogel polymer chains. The increase in structural disorder with an increase in temperature is due to the local strain arising from collapsed microgel in an entangled state. These results are important for the development of portable microgels for various sensors and optical devices.

The important results of this thesis work are summarized below.

- ✓ We have indigenously designed and developed an optical tweezer set-up capable of trapping microscopic particles stably in three dimensions.
- ✓ The optical traps are calibrated by measuring the trap stiffness by using optical potential analysis method and equipartition method. Confirmation was obtained by measuring the stiffness as a function of laser power that is shown to be linear.
- ✓ We have trapped multiple particles using optical tweezer in a consecutive ring geometry by moving the focal spot to the upper surface of the sample box.
- ✓ We have designed and developed a HOTS set-up capable of trapping multiple particles at desired locations.
- ✓ We have presented a methodology to calibrate SLMs driven by DVI interface graphics. We optimized the graphics for parameters like brightness, contrast, and gamma for uniform resolution in addressing the gray level throughout the available phase levels and improved efficacy.
- ✓ We have developed a look-up table resulting in a linear phase response of the liquid crystals of SLM.

- ✓ We have presented a simple technique for quick calibration of SLMs suffering from spatially varying phase response (SVPR) and showed an overall diffraction efficiency improvement from 29% to 55% and improved uniformity from 76% to 97% after optimization of SLM. The SVPR correction also improved the trap quality up to 6.5% as calculated from spot sharpness metric values along with a trap performance metric of value 0.49
- ✓ A novel technique is presented to determine the laser beam profile incident over SLM as required by iterative algorithms generating the holographic optical traps.
- ✓ We have trapped polystyrene particles in an array of traps and presented a prescription for them.
- ✓ We present optical tweezers as a technique to characterize the VPT of stimuli-responsive microgel particles at the single particle level, enabling understanding of various phenomena at a single particle level.
- ✓ We showed here for the first time that osmotic compression not only reduces the particle size but also the size polydispersity in stimuli-responsive microgel photonic crystals of PNIPAM-co-Aac microgel particles.
- ✓ We characterized the second type disorder and showed that with osmotic compression, the disorder in these systems reduces, leading to highly diffracting photonic crystals. We also showed the presence of first type disorder in these colloidal systems.

- ✓ We provide evidence of entanglement between polymer chains of microgel particles with polymer chains of hydrogel medium in immobilized hydrogels through a study of dynamics as a function of temperature.
- ✓ The immobilized microgel hydrogel composites are shown to retain crystalline order above VPT, and this is attributed to the entanglement between the polymer chains of microgel and hydrogels, restricting the extent of thermal vibrations.
- ✓ We show the increase in structural disorder with increasing temperature along with the retention of crystalline order and this is explained in terms of local lattice strain induced due to the collapse of microgel particles in an entangled state.

## **7.2 Future Outlook**

The development of optical manipulation system and its extension to HOTs opens up a new level of investigation capability to hold, manipulate and probe the underlying physics of various systems at single particle level. The scope for future work are as follows.

- ✚ To study the dynamics in the time scales of micro-seconds to milli-seconds at single particle level, in case of binary colloidal systems, a fluorescence correlation spectroscopy (FCS) set-up will be useful. Such an instrument is planned to be built around the developed HOTs set-up to trap and investigate colloidal dynamics using FCS.
- ✚ VPT study with varying cross-linker, monomer concentrations are warranted to understand the physics at single particle level.

- ✚ Using HOTs, an array of PNIPAM particles can be trapped in various configurations like hexagonal, square cages and dynamics of a single particle can be studied in this cage with their varying sizes.
- ✚ Gelation dynamics of a colloidal particle under an optical trap could be studied.
- ✚ Dynamics of immobilized PNIPAM microgels in hydrogel medium can be studied using HOTs and confocal laser scanning microscopy, to provide more insight into the nature of entanglements.

## REFERENCES

- [1] J. Maxwell, Clarendon Press. Oxford 1 (1873) 333–335.
- [2] A. Bartoli, *Nuovo Cim. Ser. 3* 15 (1884) 193–202.
- [3] P.N. Lebedev, *Ann. Phys.* 6 (1901) 433.
- [4] E.F. Nichols, G.F. Hull, *Phys. Rev. (Series I)* 13 (1901) 307–320.
- [5] E.F. Nichols, G.F. Hull, *Phys. Rev. (Series I)* 17 (1903) 26–50.
- [6] R.A. Beth, *Phys. Rev.* 50 (1936) 115–125.
- [7] A. Ashkin, *Phys. Rev. Lett.* 24 (1970) 156–159.
- [8] L. de Broglie, *Found. Phys.* 1 (1970) 5–15.
- [9] A. Ashkin, J.M. Dziedzic, *Appl. Phys. Lett.* 19 (1971) 283–285.
- [10] A. Ashkin, J.M. Dziedzic, *Appl. Phys. Lett.* 24 (1974) 586–588.
- [11] A. Ashkin, J.M. Dziedzic, *Science* 187 (1975) 1073–5.
- [12] A. Ashkin, J.M. Dziedzic, *Appl. Phys. Lett.* 28 (1976) 333–335.
- [13] A. Ashkin, J.M. Dziedzic, *Appl. Phys. Lett.* 30 (1977) 202–204.
- [14] A. Ashkin, J.M. Dziedzic, *Appl. Opt.* 19 (1980) 660.
- [15] A. Ashkin, J.M. Dziedzic, *Phys. Rev. Lett.* 38 (1977) 1351–1354.
- [16] G. Roosen, C. Imbert, *Phys. Lett. A* 59 (1976) 6–8.

- [17] A. Ashkin, J.M. Dziedzic, *Phys. Rev. Lett.* 36 (1976) 267–270.
- [18] A. Ashkin, J.M. Dziedzic, *Appl. Opt.* 20 (1981) 1803.
- [19] A. Ashkin, *Phys. Rev. Lett.* 25 (1970) 1321–1324.
- [20] A. Ashkin, *Phys. Rev. Lett.* 40 (1978) 729–732.
- [21] J.E. Bjorkholm, R.R. Freeman, A. Ashkin, D.B. Pearson, *Phys. Rev. Lett.* 41 (1978) 1361–1364.
- [22] A. Ashkin, J.P. Gordon, *Opt. Lett.* 4 (1979) 161.
- [23] J.P. Gordon, A. Ashkin, *Phys. Rev. A* 21 (1980) 1606–1617.
- [24] J.E. Bjorkholm, R.R. Freeman, A. Ashkin, D.B. Pearson, *Opt. Lett.* 5 (1980) 111.
- [25] D.B. Pearson, R.R. Freeman, J.E. Bjorkholm, A. Ashkin, *Appl. Phys. Lett.* 36 (1980) 99–101.
- [26] Chu, Bjorkholm, Ashkin, Cable, *Phys. Rev. Lett.* 57 (1986) 314–317.
- [27] G. Roosen, *Opt. Commun.* 21 (1977) 189–194.
- [28] A. Ashkin, J.M. Dziedzic, J.E. Bjorkholm, S. Chu, *Opt. Lett.* 11 (1986) 288.
- [29] A. Ashkin, *Biophys. J.* 61 (1992) 569–582.
- [30] E. Fällman, O. Axner, *Appl. Opt.* 36 (1997) 2107.
- [31] V. Arrizón, G. Méndez, D. Sánchez-de-La-Llave, *Opt. Express* 13 (2005) 7913–7927.

## References

- [32] Z. Zhang, Z. You, D. Chu, *Light Sci. Appl.* 3 (2014) e213.
- [33] J.M.R. Fournier, M.M. Burns, J.A. Golovchenko, in: *Proc. SPIE*, 1995, p. 101.
- [34] E.R. Dufresne, D.G. Grier, *Rev. Sci. Instrum.* 69 (1998) 1974–1977.
- [35] M.P. MacDonald, G.C. Spalding, K. Dholakia, *Nature* 426 (2003) 421–424.
- [36] V. Garcés-Chávez, R. Quidant, P.J. Reece, G. Badenes, L. Torner, K. Dholakia, *Phys. Rev. B* 73 (2006) 085417.
- [37] Y. Ogura, K. Kagawa, J. Tanida, *Appl. Opt.* 40 (2001) 5430–5435.
- [38] R.A. Flynn, A.L. Birkbeck, M. Gross, M. Ozkan, B. Shao, M.M. Wang, S.C. Esener, *Sensors Actuators, B Chem.* 87 (2002) 239–243.
- [39] K. Sasaki, M. Koshioka, H. Misawa, N. Kitamura, H. Masuhara, *Opt. Lett.* 16 (1991) 1463.
- [40] K. Sasaki, M. Koshioka, H. Misawa, N. Kitamura, H. Masuhara, *Jpn. J. Appl. Phys.* 30 (1991) L 907-L 909.
- [41] H. Misawa, K. Sasaki, M. Koshioka, N. Kitamura, H. Masuhara, *Appl. Phys. Lett.* 60 (1992) 310–312.
- [42] K. Visscher, G.J. Brakenhoff, J.J. Krol, *Cytometry* 14 (1993) 105–114.
- [43] C. Mio, D.W.M. Marr, *Langmuir* 15 (1999) 8565–8568.
- [44] C. Mio, T. Gong, A. Terray, D.W.M. Marr, *Rev. Sci. Instrum.* 71 (2000) 2196–2200.

- [45] K. Visscher, S.P. Gross, S.M. Block, *IEEE J. Sel. Top. Quantum Electron.* 2 (1996) 1066–1076.
- [46] K. Sasaki, M. Koshioka, H. Misawa, N. Kitamura, H. Masuhara, *Appl. Phys. Lett.* 60 (1992) 807–809.
- [47] P.H. Jones, E. Stride, N. Saffari, *Appl. Phys. Lett.* 89 (2006).
- [48] D.L.J. Vossen, A. Van Der Horst, M. Dogterom, A. Van Blaaderen, *Rev. Sci. Instrum.* 75 (2004) 2960–2970.
- [49] M.T. Valentine, N.R. Gydosh, B. Gutiérrez-Medina, A.N. Fehr, J.O. Andreasson, S.M. Block, *Opt. Lett.* 33 (2008) 599.
- [50] R.K. Tyson, M. Scipioni, J. Viegas, *Appl. Opt.* 47 (2008) 6300–6306.
- [51] T. Ota, S. Kawata, T. Sugiura, M.J. Booth, M.A.A. Neil, R. Juškaitis, T. Wilson, *Opt. Lett.* 28 (2003) 465.
- [52] E. Theofanidou, L. Wilson, W.J. Hossack, J. Arlt, *Opt. Commun.* 236 (2004) 145–150.
- [53] Y. Hayasaki, M. Itoh, T. Yatagai, N. Nishida, *Opt. Rev.* 6 (1999) 24–27.
- [54] M. Reicherter, T. Haist, E.U. Wagemann, H.J. Tiziani, *Opt. Lett.* 24 (1999) 608.
- [55] J. Liesener, M. Reicherter, T. Haist, H.J. Tiziani, *Opt. Commun.* 185 (2000) 77–82.
- [56] W.J. Hossack, E. Theofanidou, J. Crain, K. Heggarty, M. Birch, *Opt. Express* 11 (2003) 2053.

## References

- [57] J.E. Curtis, B.A. Koss, D.G. Grier, *Opt. Commun.* 207 (2002) 169–175.
- [58] Y. Roichman, A. Waldron, E. Gardel, D.G. Grier, *Appl. Opt.* 45 (2006) 3425–3429.
- [59] K.D. Wulff, D.G. Cole, R.L. Clark, R. DiLeonardo, J. Leach, J. Cooper, G. Gibson, M.J. Padgett, *Opt. Express* 14 (2006) 4170.
- [60] R.W. Bowman, A.J. Wright, M.J. Padgett, *J. Opt.* 12 (2010).
- [61] E.J. Fernández, P.M. Prieto, P. Artal, *Opt. Express* 17 (2009) 11013.
- [62] A. Jesacher, A. Schwaighofer, S. Fürhapter, C. Maurer, S. Bernet, M. Ritsch-Marte, *Opt. Express* 15 (2007) 5801.
- [63] G. Sinclair, P. Jordan, J. Leach, M.J. Padgett, J. Cooper, *J. Mod. Opt.* 51 (2004) 409–414.
- [64] C. Schmitz, J. Spatz, J. Curtis, *Opt. Express* 13 (2005) 8678–8685.
- [65] S.-H. Lee, D.G. Grier, *Opt. Express* 13 (2005) 7458–7465.
- [66] E.R. Dufresne, G.C. Spalding, M.T. Dearing, S.A. Sheets, D.G. Grier, *Rev. Sci. Instrum.* 72 (2001) 1810–1816.
- [67] R.W. Gerchberg, W.O. Saxton, *Optik (Stuttg.)* 35 (1972) 237–246.
- [68] G. Sinclair, P. Jordan, J. Courtial, M. Padgett, J. Cooper, Z. Laczik, *Opt. Express* 12 (2004) 5475–5480.
- [69] R. Di Leonardo, F. Ianni, G. Ruocco, *Opt. Express* 15 (2007) 1913.

- [70] J. Leach, G. Sinclair, P. Jordan, J. Courtial, M. Padgett, J. Cooper, Z. Laczik, *Opt Express* 12 (2004) 220–226.
- [71] M. Montes-Usategui, E. Pleguezuelos, J. Andilla, E. Martín-Badosa, *Opt. Express* 14 (2006) 2101.
- [72] F. Belloni, S. Monneret, *Appl. Opt.* 46 (2007) 4587.
- [73] J.E. Curtis, C.H.J. Schmitz, J.P. Spatz, *Opt. Lett.* 30 (2005) 2086–2088.
- [74] M. Polin, K. Ladavac, S.-H. Lee, Y. Roichman, D.G. Grier, *Opt. Express* 13 (2005) 5831.
- [75] E. Schonbrun, R. Piestun, P. Jordan, J. Cooper, K. Wulff, J. Courtial, M. Padgett, *Opt. Express* 13 (2005) 3777–3786.
- [76] J. Courtial, G. Whyte, Z. Bouchal, J. Wagner, *Opt. Express* 14 (2006) 2108–2116.
- [77] P. Rodrigo, R. Eriksen, V. Daria, J. Glueckstad, *Opt. Express* 10 (2002) 1550–1556.
- [78] G. Sinclair, J. Leach, P. Jordan, G. Gibson, E. Yao, Z. Laczik, M. Padgett, J. Courtial, *Opt. Express* 12 (2004) 1665–1670.
- [79] R.W. Bowman, G.M. Gibson, A. Linnenberger, D.B. Phillips, J.A. Grieve, D.M. Carberry, S. Serati, M.J. Miles, M.J. Padgett, *Comput. Phys. Commun.* 185 (2014) 268–273.
- [80] T. Shimobaba, T. Ito, *Comput. Phys. Commun.* 138 (2001) 44–52.
- [81] M. Reicherter, S. Zwick, T. Haist, C. Kohler, H. Tiziani, W. Osten, *Appl. Opt.*

## References

- 45 (2006) 888–896.
- [82] J.A. Grieve, A. Ulcinas, S. Subramanian, G.M. Gibson, M.J. Padgett, D.M. Carberry, M.J. Miles, *Opt. Express* 17 (2009) 3595.
- [83] G. Gibson, D.M. Carberry, G. Whyte, J. Leach, J. Courtial, J.C. Jackson, D. Robert, M. Miles, M. Padgett, *J. Opt. A Pure Appl. Opt.* 10 (2008).
- [84] C. Basdogan, A. Kiraz, I. Bukusoglu, A. Varol, S. Do?anay, *Opt. Express* 15 (2007) 11616.
- [85] G. Whyte, G. Gibson, J. Leach, M. Padgett, D. Robert, M. Miles, *Opt. Express* 14 (2006) 12497.
- [86] X. Xun, R.W. Cohn, *Appl. Opt.* 43 (2004) 6400.
- [87] O. Mendoza-Yero, G. Minguez-Vega, L. Martinez-Leon, M. Carbonell-Leal, M. Fernandez-Alonso, C. Donate-Buendia, J. Perez-Vizcaino, J. Lancis, *J. Disp. Technol.* 12 (2016) 1027–1032.
- [88] J. Otón, P. Ambs, M.S. Millán, E. Pérez-Cabré, *Appl. Opt.* 46 (2007) 5667.
- [89] F.P. Ferreira, M.S. Belsley, *Opt. Express* 18 (2010) 7899–7904.
- [90] M.-L. Ll, Z. Jaroszewicz, A. Kołodziejczyk, V. Durán, E. Tajahuerce, J. Lancis, *J. Opt. A Pure Appl. Opt.* 11 (2009) 125405.
- [91] A. Bergeron, J. Gauvin, F. Gagnon, D. Gingras, H.H. Arsenault, M. Doucet, *Appl. Opt.* 34 (1995) 5133.
- [92] J. Strauß, T. Häfner, M. Dobler, J. Heberle, M. Schmidt, *Phys. Procedia* 83

- (2016) 1160–1169.
- [93] J.L.M. Fuentes, E.J. Fernández, P.M. Prieto, P. Artal, *Opt. Express* 24 (2016) 14159.
- [94] Z. Zhang, H. Yang, B. Robertson, M. Redmond, M. Pivnenko, N. Collings, W.A. Crossland, D. Chu, *Appl. Opt.* 51 (2012) 3837.
- [95] D. Engström, M. Persson, J. Bengtsson, M. Goksör, *Opt. Express* 21 (2013) 16086.
- [96] D. Engström, M. Persson, M. Goksör, in: *Biomed. Opt. 3-D Imaging*, OSA, Washington, D.C., 2012, p. DSu2C.3.
- [97] A. Ashkin, J. Dziedzic, *Science* (80-. ). 235 (1987) 1517–1520.
- [98] A. Ashkin, J.M. Dziedzic, *Berichte Der Bunsengesellschaft Für Phys. Chemie* 93 (1989) 254–260.
- [99] A. Ashkin, J.M. Dziedzic, T. Yamane, *Nature* 330 (1987) 769–771.
- [100] K.C. Neuman, E.H. Chadd, G.F. Liou, K. Bergman, S.M. Block, *Biophys. J.* 77 (1999) 2856–2863.
- [101] A. Ashkin, *ASGSB Bull.* 4 (1991) 133–46.
- [102] A. Ashkin, J.M. Dziedzic, *Proc. Natl. Acad. Sci.* 86 (1989) 7914–8.
- [103] A. Ashkin, K. Schütze, J.M. Dziedzic, U. Euteneuer, M. Schliwa, *Nature* 348 (1990) 346–8.
- [104] W. Singer, M. Frick, T. Haller, P. Dietl, S. Bernet, M. Ritsch-Marte,

## References

- Proceeding SPIE 4434 (2001) 227–232.
- [105] T. Yang, F. Bragheri, P. Minzioni, *Micromachines* 7 (2016).
- [106] J. Guck, R. Ananthakrishnan, H. Mahmood, T.J. Moon, C.C. Cunningham, J. Käs, *Biophys. J.* 81 (2001) 767–784.
- [107] J. Sleep, D. Wilson, R. Simmons, W. Gratzner, *Biophys. J.* 77 (1999) 3085–3095.
- [108] K. Svoboda, C.F. Schmidt, D. Branton, S.M. Block, *Biophys. J.* 63 (1992) 784–793.
- [109] J. Dai, M.P. Sheetz, *Biophys. J.* 77 (1999) 3363–3370.
- [110] Z. Li, B. Anvari, M. Takashima, P. Brecht, J.H. Torres, W.E. Brownell, *Biophys. J.* 82 (2002) 1386–1395.
- [111] J. Dai, M.P. Sheetz, *Biophys. J.* 68 (1995) 988–996.
- [112] S.C. Kuo, *Traffic* 2 (2001) 757–763.
- [113] G.C. Spalding, J. Courtial, R.D. Leonardo, *Holographic Optical Trapping in Structured Light and Its Applications: An Introduction to Phase-Structured Beams and Nanoscale Optical Forces*, 2008.
- [114] J.E. Molloy, M.J. Padgett, *Contemp. Phys.* 43 (2002) 241–258.
- [115] A.D. Mehta, *Science* (80-. ). 283 (1999) 1689–1695.
- [116] Y. Sako, A. Kusumi, *J. Cell Biol.* 129 (1995) 1559–1574.

- [117] K. Svoboda, S.M. Block, *Annu Rev Bioph Biom* 23 (1994) 247–285.
- [118] M.P. MacDonald, G.C. Spalding, K. Dholakia, *Nature* 426 (2003) 421–424.
- [119] P. Jordan, J. Leach, M. Padgett, P. Blackburn, N. Isaacs, M. Goksör, D. Hanstorp, A. Wright, J. Girkin, J. Cooper, *Lab Chip* 5 (2005) 1224.
- [120] T. Čižmár, V. Kollárová, X. Tsampoula, F. Gunn-Moore, W. Sibbett, Z. Bouchal, K. Dholakia, *Opt. Express* 16 (2008) 14024.
- [121] K. Svoboda, S.M. Block, *Opt. Lett.* 19 (1994) 930–932.
- [122] M. Pelton, M. Liu, H.Y. Kim, G. Smith, P. Guyot-Sionnest, N.F. Scherer, *Opt. Lett.* 31 (2006) 2075.
- [123] A.S. Zelenina, R. Quidant, M. Nieto-Vesperinas, *Opt. Lett.* 32 (2007) 1156.
- [124] G. Volpe, R. Quidant, G. Badenes, D. Petrov, *Phys. Rev. Lett.* 96 (2006).
- [125] D.L.J. Vossen, D. Fific, J. Penninkhof, T. Van Dillen, A. Polman, A. Van Blaaderen, *Nano Lett.* 5 (2005) 1175–1179.
- [126] J.P. Hoogenboom, D.L.J. Vossen, C. Faivre-Moskalenko, M. Dogterom, A. van Blaaderen, *Appl. Phys. Lett.* 80 (2002) 4828–4830.
- [127] V. Bingelyte, J. Leach, J. Courtial, M.J. Padgett, *Appl. Phys. Lett.* 82 (2003) 829–831.
- [128] Y. Roichman, D.G. Grier, *Opt. Express* 13 (2005) 5434.
- [129] S. Henderson, S. Mitchell, P. Bartlett, *Phys. Rev. Lett.* 88 (2002) 088302/1-088302/4.

## References

- [130] R. Di Leonardo, S. Keen, J. Leach, C.D. Saunter, G.D. Love, G. Ruocco, M.J. Padgett, *Phys. Rev. E - Stat. Nonlinear, Soft Matter Phys.* 76 (2007) 2–5.
- [131] N.K. Metzger, R.F. Marchington, M. Mazilu, R.L. Smith, K. Dholakia, E.M. Wright, *Phys. Rev. Lett.* 98 (2007).
- [132] S. Rao, Š. Bálint, P. Løvhaugen, M. Kreuzer, D. Petrov, *Phys. Rev. Lett.* 102 (2009) 087401.
- [133] C.J. Olson Reichhardt, C. Reichhardt, *Europhys. Lett.* 74 (2006) 792–798.
- [134] A. Libál, C. Reichhardt, B. Jankó, C.J.O. Reichhardt, *Phys. Rev. Lett.* 96 (2006) 188301.
- [135] Y. Roichman, V. Wong, D.G. Grier, *Phys. Rev. E - Stat. Nonlinear, Soft Matter Phys.* 75 (2007).
- [136] P.T. Korda, M.B. Taylor, D.G. Grier, *Phys. Rev. Lett.* 89 (2002) 128301.
- [137] M. Polin, D.G. Grier, S.R. Quake, *Phys. Rev. Lett.* 96 (2006).
- [138] S. Martin, M. Reichert, H. Stark, T. Gisler, *Phys. Rev. Lett.* 97 (2006).
- [139] P. Bartlett, S.I. Henderson, S.J. Mitchell, *Philos. Trans. R. Soc. A Math. Phys. Eng. Sci.* 359 (2001) 883–895.
- [140] J.-C. Meiners, S.R. Quake, *Phys. Rev. Lett.* 82 (1999) 2211–2214.
- [141] A.I. Bishop, T.A. Nieminen, N.R. Heckenberg, H. Rubinsztein-Dunlop, *Phys. Rev. Lett.* 92 (2004).
- [142] S. Parkin, G. Kn, T. a Nieminen, N.R. Heckenberg, *Small* 6038 (2006) 55–61.

- [143] M. Khan, a. K. Sood, *EPL (Europhysics Lett.* 92 (2010) 48001.
- [144] G. Pesce, A.C. De Luca, G. Rusciano, P.A. Netti, S. Fusco, A. Sasso, *J. Opt. A Pure Appl. Opt.* 11 (2009).
- [145] A. Yao, M. Tassieri, M. Padgett, J. Cooper, *Lab Chip* 9 (2009) 2568.
- [146] E.M. Furst, *Curr. Opin. Colloid Interface Sci.* 10 (2005) 79–86.
- [147] W. Singer, T.A. Nieminen, N.R. Heckenberg, H. Rubinsztein-Dunlop, *Phys. Rev. E - Stat. Nonlinear, Soft Matter Phys.* 75 (2007).
- [148] M. Yada, J. Yamamoto, H. Yokoyama, *Phys. Rev. Lett.* 92 (2004).
- [149] S.A. Tatarkova, D.R. Burnham, A.K. Kirby, G.D. Love, E.M. Terentjev, *Phys. Rev. Lett.* 98 (2007).
- [150] I.I. Smalyukh, A.N. Kuzmin, A. V. Kachynski, P.N. Prasad, O.D. Lavrentovich, *Appl. Phys. Lett.* 86 (2005).
- [151] C. Hertlein, L. Helden, A. Gambassi, S. Dietrich, C. Bechinger, *Nature* 451 (2008) 172–175.
- [152] S. Ahn, R.M. Kasi, S.-C. Kim, N. Sharma, Y. Zhou, *Soft Matter* 4 (2008) 1151.
- [153] P.J. Lu (陸述義), D.A. Weitz, *Annu. Rev. Condens. Matter Phys.* 4 (2013) 217–233.
- [154] P.N. Pusey, W. van Meegen, *Nature* 320 (1986) 340–342.
- [155] B.V.R. Tata, S.S. Jena, *Solid State Commun.* 139 (2006) 562–580.
- [156] P.S. Mohanty, W. Richtering, *J. Phys. Chem. B* 112 (2008) 14692–14697.

## References

- [157] R.S. CRANDALL, R. WILLIAMS, *Science*. 198 (1977) 293–295.
- [158] K.Q. Zhang, X.Y. Liu, *Nature* 429 (2004) 739–743.
- [159] P. Schall, I. Cohen, D.A. Weitz, F. Spaepen, *Nature* 440 (2006) 319–323.
- [160] A. Cacciuto, S. Auer, D. Frenkel, *Nature* 428 (2004) 404–406.
- [161] U. Gasser, *Science*. 292 (2001) 258–262.
- [162] W. van Meegen, S.M. Underwood, *Phys. Rev. E* 49 (1994) 4206–4220.
- [163] B.V.R. Tata, P.S. Mohanty, M.C. Valsakumar, *Phys. Rev. Lett.* 88 (2001) 018302.
- [164] K.H. Nagamanasa, S. Gokhale, R. Ganapathy, A.K. Sood, *Proc. Natl. Acad. Sci. U. S. A.* 108 (2011) 11323–6.
- [165] D.K. Gupta, B.V.R. Tata, J. Brijitta, R.G. Joshi, in: *AIP Conf. Proc.*, 2011, pp. 266–268.
- [166] P.L. Flaugh, S.A. Asher, S.E. O’Donnell, *Appl. Spectrosc.* Vol. 38, Issue 6, Pp. 847–850 38 (1984) 847–850.
- [167] Weissman, Sunkara, Tse, Asher, *Science* 274 (1996) 959–60.
- [168] J.H. Holtz, S.A. Asher, *Nature* 389 (1997) 829–832.
- [169] C.D. Geary, I. Zudans, A. V. Goponenko, S.A. Asher, S.G. Weber, *Anal. Chem.* 77 (2005) 185–192.
- [170] C. Reese, A. Mikhonin, M. Kamenjicki, A. Tikhonov, S. Asher, *J. Am. Chem.*

- Soc. 126 (2004) 1493–1496.
- [171] S. H. Kim, S.Y. Lee, S.-M. Yang, G.-R. Yi, *NPG Asia Mater* 3 (2011) 25–33.
- [172] L. V Woodcock, *Nature* 385 (1997) 141–143.
- [173] P.G. Bolhuis, D. Frenkel, S.-C. Mau, D.A. Huse, *Nature* 388 (1997) 235–236.
- [174] P.N. Pusey, W. van Megen, P. Bartlett, B.J. Ackerson, J.G. Rarity, S.M. Underwood, *Phys. Rev. Lett.* 63 (1989) 2753–2756.
- [175] A. Fernández-Nieves, A. Fernández-Barbero, B. Vincent, F.J. de las Nieves, *J. Chem. Phys.* 119 (2003) 10383–10388.
- [176] B.V.R. Tata, in: Shigenao Maruyama, Michio Tokuyama (Eds.), *Stat. Phys. Complex Fluids*, Tohoku University, Sendai, Japan, 2007.
- [177] M. Das, H. Zhang, E. Kumacheva, *Annu. Rev. Mater. Res.* 36 (2006) 117–142.
- [178] M. Wei, Y. Gao, X. Li, M.J. Serpe, *Polym. Chem.* 8 (2017) 127–143.
- [179] Y. Guan, Y. Zhang, *Soft Matter* 7 (2011) 6375.
- [180] B. Sierra-Martin, J.R. Retama, M. Laurenti, A. Fernández Barbero, E. López Cabarcos, *Adv. Colloid Interface Sci.* 205 (2014) 113–123.
- [181] Z. Meng, J.K. Cho, V. Breedveld, L.A. Lyon, *J. Phys. Chem. B* 113 (2009) 4590–4599.
- [182] Y. Gao, X. Li, M.J. Serpe, *RSC Adv.* 5 (2015) 44074–44087.
- [183] L.Y. Chen, C.M. Ou, W.Y. Chen, C.C. Huang, H.T. Chang, *ACS Appl. Mater. Interfaces* 5 (2013) 4383–4388.

## References

- [184] Q. Luo, Y. Guan, Y. Zhang, M. Siddiq, *J. Polym. Sci. Part A Polym. Chem.* 48 (2010) 4120–4127.
- [185] D. SCHMALJOHANN, *Adv. Drug Deliv. Rev.* 58 (2006) 1655–1670.
- [186] J. Brijitta, B.V.R. Tata, T. Kaliyappan, *J. Nanosci. Nanotechnol.* 9 (2009) 5323–8.
- [187] C.D. Jones, A. Lyon, *Macromolecules* 33 (2000) 8301–8305.
- [188] M. Ballauff, Y. Lu, *Polymer (Guildf)*. 48 (2007) 1815–1823.
- [189] J. Wu, B. Zhou, Z. Hu, *Phys. Rev. Lett.* 90 (2003) 48304.
- [190] E.C. Cho, J. Lee, K. Cho, *Macromolecules* 36 (2003) 9929–9934.
- [191] B.R. Saunders, *Langmuir* 20 (2004) 3925–3932.
- [192] M. Stieger, W. Richtering, J.S. Pedersen, P. Lindner, *J. Chem. Phys.* 120 (2004) 6197–6206.
- [193] I. Varga, T. Gilányi, R. Mészáros, G. Filipcsei, M. Zrínyi, *J. Phys. Chem. B* 105 (2001) 9071–9076.
- [194] A. Fernández-Nieves, A. Fernández-Barbero, B. Vincent, F.J. de las Nieves, *J. Chem. Phys.* 119 (2003) 10383–10388.
- [195] A. Fernández-Nieves, A. Fernández-Barbero, B. Vincent, F.J. de las Nieves, *Langmuir* 17 (2001) 1841–1846.
- [196] J. Wu, B. Zhou, Z. Hu, *Phys. Rev. Lett.* 90 (2003) 048304.

- [197] C.L.A. Berli, D. Quemada, *Langmuir* 16 (2000) 10509–10514.
- [198] H. Senff, W. Richtering, *J. Chem. Phys.* 111 (1999) 1705–1711.
- [199] R. Agrawal, D.A. Kofke, *Mol. Phys.* 85 (1995) 23–42.
- [200] D. Gottwald, C.N. Likos, G. Kahl, H. Löwen, *Phys. Rev. Lett.* 92 (2004) 068301.
- [201] D. Gottwald, C.N. Likos, G. Kahl, H. Löwen, *J. Chem. Phys.* 122 (2005) 074903.
- [202] A.R. Denton, *Phys. Rev. E* 67 (2003) 011804.
- [203] T. Hellweg, C.D. Dewhurst, E. Brückner, K. Kratz, W. Eimer, *Colloid Polym. Sci.* 278 (2000) 972–978.
- [204] J. Brijitta, B.V.R. Tata, R.G. Joshi, T. Kaliyappan, *J. Chem. Phys.* 131 (2009) 74904.
- [205] H.M. Wyss, J. Mattsson, T. Franke, A. Fernandez-Nieves, D.A. Weitz, in: *Microgel Suspens.*, Wiley-VCH Verlag GmbH & Co. KGaA, Weinheim, Germany, 2011, pp. 311–325.
- [206] D. Parasuraman, M.J. Serpe, *ACS Appl. Mater. Interfaces* 3 (2011) 2732–2737.
- [207] A.K. Bajpai, S.K. Shukla, S. Bhanu, S. Kankane, *Prog. Polym. Sci.* 33 (2008) 1088–1118.
- [208] S.M. Hashmi, E.R. Dufresne, *Soft Matter* 5 (2009) 3682.
- [209] O. Tagit, N. Tomczak, G.J. Vancso, *Small* 4 (2008) 119–126.

## References

- [210] A. Ashkin, J. Dziedzic, *Science* 210 (1980) 1081–8.
- [211] D. Engström, G. Milewski, J. Bengtsson, S. Galt, *Appl. Opt.* 45 (2006) 7195–204.
- [212] O. Mendoza-Yero, G. Mínguez-Vega, L. Martínez-León, M. Carbonell-Leal, M. Fernández-Alonso, C. Doñate-Buendía, J. Pérez-Vizcaíno, J. Lancis, *J. Disp. Technol.* 12 (2016) 1027–1032.
- [213] B.V.R. Tata, J. Brijitta, R.G. Joshi, *Int. J. Adv. Eng. Sci. Appl. Math.* 5 (2013) 240–249.
- [214] R.G. Joshi, B.V.R. Tata, J. Brijitta, *J. Chem. Phys.* 139 (2013) 124901–124907.
- [215] A.A. Polotsky, F.A. Plamper, O. V. Borisov, *Macromolecules* 46 (2013) 8702–8709.
- [216] B.J. Frisken, *Appl. Opt.* 40 (2001) 4087–4091.
- [217] S. Takata, K. Suzuki, T. Norisuye, M. Shibayama, *Polymer (Guildf)*. 43 (2002) 3101–3107.
- [218] D.K. Gupta, D. Karthickeyan, B.V.R. Tata, T.R. Ravindran, *Colloid Polym. Sci.* 294 (2016) 1901–1908.
- [219] B. Sierra-Martín, Y. Laporte, A.B. South, L.A. Lyon, A. Fernández-Nieves, *Phys. Rev. E - Stat. Nonlinear, Soft Matter Phys.* 84 (2011) 011406.
- [220] M. Allard, E.H. Sargent, in: *Conf. Lasers Electro-Optics/International Quantum Electron. Conf. Photonic Appl. Syst. Technol.*, Optical Society of America, San Francisco, California, 2004, p. CTuDD1.

- [221] M. Allard, E.H. Sargent, E. Kumacheva, O. Kalinina, *Opt. Quantum Electron.* 34 (2002) 27–36.
- [222] M. Allard, E.H. Sargent, *Appl. Phys. Lett.* 85 (2004) 5887–5889.
- [223] B.V.R. Tata, *Statistical Physics of Complex Fluids*, Tohoku University Press, Sendai Japan, 2007.
- [224] W. Song, Y. Guan, Y. Zhang, X.X. Zhu, *Soft Matter* 9 (2013) 2629.
- [225] S.A. Asher, J.H. Holtz, *Nature* 389 (1997) 829–832.
- [226] G. Pan, R. Kesavamoorthy, S.A. Asher, *Phys. Rev. Lett.* 78 (1997) 3860–3863.
- [227] G. Romeo, L. Imperiali, J.-W. Kim, A. Fernández-Nieves, D.A. Weitz, *J. Chem. Phys.* 136 (2012) 124905.
- [228] J. Museh, S. Schneider, P. Lindner, W. Richtering, *J. Phys. Chem. B* 112 (2008) 6309–6314.
- [229] A. Ashkin, J.M. Dziedzic, J.E. Bjorkholm, S. Chu, *Opt. Lett.* 11 (1986) 288.
- [230] A. Ashkin, *IEEE J. Sel. Top. Quantum Electron.* 6 (2000) 841–856.
- [231] Y. Pang, R. Gordon, *Nano Lett.* 12 (2012) 402–6.
- [232] A.R. Zakharian, P. Polynkin, M. Mansuripur, J. V Moloney, *Opt. Express* 14 (2006) 3660–3676.
- [233] F.M. Fazal, S.M. Block, *Nat Phot.* 5 (2011) 318–321.
- [234] W.H. Wright, G.J. Sonek, Y. Tadir, M.W. Berns, *IEEE J. Quantum Electron.* 26 (1990) 2148–2157.

## References

- [235] D.G. Grier, *Curr. Opin. Colloid {&} Interface Sci.* 2 (1997) 264–270.
- [236] Y. Ishii, A. Ishijima, T. Yanagida, *Trends Biotechnol.* 19 (2001) 211–216.
- [237] J.C. Crocker, D.G. Grier, *Phys. Rev. Lett.* 73 (1994) 352–355.
- [238] K. Wang, J.G. Forbes, A.J. Jin, *Prog. Biophys. Mol. Biol.* 77 (2001) 1–44.
- [239] G. Knöner, S. Parkin, T.A. Nieminen, N.R. Heckenberg, H. Rubinsztein-Dunlop, *Phys. Rev. Lett.* 97 (2006) 157402–157405.
- [240] A. Ashkin, J.M. Dziedzic, *Appl. Phys. Lett.* 19 (1971) 283–285.
- [241] K.C. Neuman, S.M. Block, *Rev. Sci. Instruments* 75 (2004) 2787.
- [242] M. KERKER, M. KERKER, in: *Scatt. Light Other Electromagn. Radiat.*, 1969, pp. 27–96.
- [243] A. Ashkin, J.M. Dziedzic, J.E. Bjorkholm, S. Chu, *Opt. Lett.* 11 (1986) 288.
- [244] M. Born, E. Wolf, *Principles of Optics : Electromagnetic Theory of Propagation, Interference and Diffraction of Light*, Pergamon Press, 1980.
- [245] D. ZAGURY, R. LEONARD, M. FOUCHARD, B. REVEIL, *Nature* 330 (1987) 1987.
- [246] A.A. Ashkin, J.M. Dziedzic, *Adv. Sci.* 235 (2011) 1517–1520.
- [247] A. Ashkin, *Biophys. J.* 61 (1992) 569–582.
- [248] C.F. Bohren, D.R. Huffman, *Absorption and Scattering of Light by Small Particles*, Wiley, 1983.

- [249] X. Han, H. Shin, Pdfs.Semanticscholar.Org (n.d.).
- [250] T. Tlusty, A. Meller, R. Bar-Ziv, *Phys. Rev. Lett.* 81 (1998) 1738–1741.
- [251] B.J. Park, E.M. Furst, *Macromol. Res.* 21 (2013) 1167–1170.
- [252] S.N.S. Reihani, L.B. Oddershede, *Opt. Lett.* 32 (2007) 1998–2000.
- [253] W.H. Wright, G.J. Sonek, M.W. Berns, *Appl. Opt.* 33 (1994) 1735–1748.
- [254] A. Schönle, S.W. Hell, *Opt. Lett.* 23 (1998) 325.
- [255] E.J.G. Peterman, F. Gittes, C.F. Schmidt, *Biophys. J.* 84 (2003) 1308–1316.
- [256] W.P. Wong, K. Halvorsen, *Opt. Express* 14 (2006) 12517–12531.
- [257] N. Osterman, *Comput. Phys. Commun.* 181 (2010) 1911–1916.
- [258] G. Volpe, G. Volpe, *Am. J. Phys.* 81 (2013) 224–230.
- [259] E.L. Florin, A. Pralle, E.H.K. Stelzer, J.K.H. Hörber, *Appl. Phys. A Mater. Sci. Process.* 66 (1998) S75–S78.
- [260] A. Haldar, S.B. Pal, B. Roy, S.D. Gupta, A. Banerjee, *Phys. Rev. A - At. Mol. Opt. Phys.* 85 (2012).
- [261] Y. Kimura, P.R. Bianco, *Analyst* 131 (2006) 868–874.
- [262] M. Reicherter, T. Haist, E.U. Wagemann, H.J. Tiziani, *Opt. Lett.* 24 (1999) 608.
- [263] E.R. Dufresne, G.C. Spalding, M.T. Dearing, S.A. Sheets, D.G. Grier, *Rev. Sci. Instrum.* 72 (2001) 1810.

## References

- [264] D.K. Gupta, B.V.R. Tata, T.R. Ravindran, in: AIP Conf. Proc., 2017, p. 060028.
- [265] B.P. Cumming, A. Jesacher, M.J. Booth, T. Wilson, M. Gu, Opt. Express 19 (2011) 9419–9425.
- [266] J. Hong, Y. Kim, H.-J. Choi, J. Hahn, J.-H. Park, H. Kim, S.-W. Min, N. Chen, B. Lee, Appl. Opt. 50 (2011) H87-115.
- [267] M.S. Millán, J. Otón, E. Pérez-Cabré, Opt. Express 14 (2006) 6226–42.
- [268] M.S. Millán, J. Otón, E. Pérez-Cabré, Opt. Express 14 (2006) 9103–12.
- [269] A. Márquez, C. Iemml, J. Campos, J.C. Escalera, M.J. Yzuel, Opt. Express 13 (2005) 1655–1663.
- [270] A.M. Weiner, D.E. Leaird, J.S. Patel, J.R. Wullert, Opt. Lett. 15 (1990) 326.
- [271] L. Lobato, A. Márquez, A. Lizana, I. Moreno, C. Iemmi, J. Campos, Proc. SPIE 7797 (2010) 77970Q–77970Q–12.
- [272] T.J. McIntyre, C. Maurer, S. Bernet, M. Ritsch-Marte, Opt. Lett. 34 (2009) 2988.
- [273] G. Lazarev, A. Hermerschmidt, S. Krüger, S. Osten, in: Opt. Imaging Metrol., Wiley-VCH Verlag GmbH & Co. KGaA, Weinheim, Germany, 2012, pp. 1–29.
- [274] W. Osten, C. Kohler, J. Liesener, Opt. Pura Apl 38 (2005) 228–233.
- [275] S. Reichelt, Appl. Opt. 52 (2013) 2610–8.

- [276] C. Lingel, T. Haist, W. Osten, *Appl. Opt.* 52 (2013) 6877.
- [277] H. Zhang, J. Zhang, L. Wu, *Meas. Sci. Technol.* 18 (2007) 1724–1728.
- [278] Z. Zhang, *Opt. Eng.* 33 (1994) 3018.
- [279] J.L. Martínez, I. Moreno, M. del Mar Sánchez-López, A. Vargas, P. García-Martínez, *Opt. Express* 22 (2014) 25866.
- [280] E. Martín-Badosa, M. Montes-Usategui, A. Carnicer, J. Andilla, E. Pleguezuelos, I. Juvells, *J. Opt. A Pure Appl. Opt.* 9 (2007) S267.
- [281] C. Poynton, (2002) 1–5.
- [282] J.E. Curtis, B.A. Koss, D.G. Grier, *Opt. Commun.* 207 (2002) 169–175.
- [283] J.E. Curtis, C.H.J. Schmitz, J.P. Spatz, *Opt. Lett.* 30 (2005) 2086.
- [284] G.C. Spalding, J. Courtial, R. Di Leonardo, *Physics (College. Park. Md.)* 11 (2011) 1196–205.
- [285] K.D. Wulff, D.G. Cole, R.L. Clark, R. DiLeonardo, J. Leach, J. Cooper, G. Gibson, M.J. Padgett, *Opt. Express* 14 (2006) 4170.
- [286] R.G. Joshi, B.V.R. Tata, J. Brijitta, *AIP Conf. Proc.* 1349 (2011) 208–209.
- [287] M. Chen, L. Zhou, Y. Guan, Y. Zhang, *Angew. Chemie - Int. Ed.* 52 (2013) 9961–9965.
- [288] D. SCHMALJOHANN, *Adv. Drug Deliv. Rev.* 58 (2006) 1655–1670.
- [289] Q. Luo, Y. Guan, Y. Zhang, M. Siddiq, *J. Polym. Sci. Part A Polym. Chem.* 48 (2010) 4120–4127.

## References

- [290] K. Lee, S.A. Asher, *J. Am. Chem. Soc.* 122 (2000) 9534–9537.
- [291] J.D. Debord, L.A. Lyon, *J. Phys. Chem. B* 104 (2000) 6327–6331.
- [292] S.A. Asher, K.W. Kimble, J.P. Walker, *Chem. Mater.* 20 (2008) 7501–7509.
- [293] J. Shin, P. V. Braun, W. Lee, *Sensors Actuators B Chem.* 150 (2010) 183–190.
- [294] C.E. Reese, A. V Mikhonin, M. Kamenjicki, A. Tikhonov, S.A. Asher, *J. Am. Chem. Soc.* 126 (2004) 1493–1496.
- [295] Y.Y. Zhang, Y.Y. Zhang, B. Li, *Opt. Express* 15 (2007) 9287.
- [296] B.J. Berne, R. Pecora, *Dynamic Light Scattering : With Applications to Chemistry, Biology, and Physics*, Dover Publications, 2000.
- [297] Y. Kimura, P.R. Bianco, *Analyst* 131 (2006) 868–74.
- [298] K. Svoboda, M. Block, (1994).
- [299] C. Bustamante, Z. Bryant, S.B. Smith, *Nature* 421 (2003) 423–427.
- [300] D.G. Grier, *Nature* 424 (2003) 810–816.
- [301] Y. Hong, J.-W. Pyo, S.H. Baek, S.W. Lee, D.S. Yoon, K. No, B.-M. Kim, *Opt. Lett.* 35 (2010) 2493–2495.
- [302] B.J. Frisken, *Appl. Opt.* 40 (2001) 4087–91.
- [303] A. Eshuis, G. Harbers, D.J. Doornink, P.F. Mijnlief, *Langmuir* 1 (1985) 289–293.
- [304] K.C. Neuman, S.M. Block, *Rev. Sci. Instrum.* 75 (2004) 2787–2809.

- [305] T.A. Nieminen, V.L.Y. Loke, A.B. Stilgoe, G. Knöner, A.M. Brańczyk, N.R. Heckenberg, H. Rubinsztein-Dunlop, *J. Opt. A Pure Appl. Opt.* 9 (2007) S196–S203.
- [306] P.A. Hiltner, Y.S. Papir, I.M. Krieger, *J. Phys. Chem.* 75 (1971) 1881–1886.
- [307] K.C. Vermeulen, G.J.L. Wuite, G.J.M. Stienen, C.F. Schmidt, *Appl. Opt.* 45 (2006) 1812.
- [308] R.S. Dutra, N.B. Viana, P.A. Maia Neto, H.M. Nussenzveig, *Phys. Rev. A* 90 (2014) 013825.
- [309] F. Borghese, P. Denti, R. Saija, M.A. Iatì, *Opt. Express* 15 (2007) 11984.
- [310] R.P.A. Dullens, A. V Petukhov, *Europhys. Lett.* 77 (2007) 58003.
- [311] A. Guinier, *X-Ray Diffraction in Crystals, Imperfect Crystals, and Amorphous Bodies*, Dover, New York, 1994.
- [312] B.V.R. Tata, S.S. Jena, *Solid State Commun.* 139 (2006) 562–580.
- [313] S. Maruyama, M. Tokuyama, *Statistical Physics of Complex Fluids*, Tohoku University Press, 2007.
- [314] I.A. Sukhoivanov, I. V. Guryev, *Springer Ser. Opt. Sci.* 152 (2010) 1–12.
- [315] E. Yablonovitch, *Phys. Rev. Lett.* 58 (1987) 2059–2062.
- [316] S. John, *Phys. Rev. Lett.* 58 (1987) 2486–2489.
- [317] T.F. Krauss, *Nat. Mater.* 2 (2003) 777–778.
- [318] Y. Akahane, T. Asano, B.-S. Song, S. Noda, *Nature* 425 (2003) 944–947.

## References

- [319] D.R. Solli, C.F. McCormick, R.Y. Chiao, J.M. Hickmann, *Appl. Phys. Lett.* 82 (2003) 1036–1038.
- [320] J.O. Brien, O. Painter, R. Lee, C.C. Cheng, A. Yariv, A. Scherer, *Electron. Lett.* 32 (1996) 2243.
- [321] T.F. Krauss, O.J. Painter, A. Scherer, J.S. Roberts, R.M.D. La Rue, *Opt. Eng.* 37 (1998) 1143.
- [322] M. Lipson, *J. Light. Technol.* Vol. 23, Issue 12, Pp. 4222- 23 (2005) 4222.
- [323] D. O'Brien, M.D. Settle, T. Karle, A. Michaeli, M. Salib, T.F. Krauss, *Opt. Express* 15 (2007) 1228.
- [324] M.C. Wanke, *Science* (80-. ). 275 (1997) 1284–1286.
- [325] S. Noda, *Science* (80-. ). 289 (2000) 604–606.
- [326] S.Y. Lin, J.G. Fleming, D.L. Hetherington, B.K. Smith, R. Biswas, K.M. Ho, M.M. Sigalas, W. Zubrzycki, S.R. Kurtz, J. Bur, *Nature* 394 (1998) 251–253.
- [327] H. Masuda, M. Ohya, H. Asoh, M. Nakao, M. Nohtomi, T. Tamamura, *Jpn. J. Appl. Phys.* 38 (1999) L1403–L1405.
- [328] A.J. Turberfield, M. Campbell, D.N. Sharp, M.T. Harrison, R.G. Denning, *Nature* 404 (2000) 53–56.
- [329] S. Shoji, S. Kawata, *Appl. Phys. Lett.* 76 (2000) 2668–2670.
- [330] C.C. Cheng, *J. Vac. Sci. Technol. B Microelectron. Nanom. Struct.* 13 (1995) 2696.

- [331] J.H. Moon, J. Ford, S. Yang, *Polym. Adv. Technol.* 17 (2006) 83–93.
- [332] Y. Zhong, L. Wu, H. Su, K.S. Wong, H. Wang, *Opt. Express* 14 (2006) 6837.
- [333] C. López, *J. Opt. A Pure Appl. Opt.* 8 (2006) R1–R14.
- [334] Y. Xia, B. Gates, Y. Yin, Y. Lu, *Adv. Mater.* 12 (2000) 693–713.
- [335] Y. Masuda, *KONA Powder Part. J.* 25 (2007) 244–254.
- [336] K. Lee, S.A. Asher, (2000).
- [337] J.D. Debord, L.A. Lyon, *J. Phys. Chem. B* 104 (2000) 6327–6331.
- [338] S.A. Asher, K.W. Kimble, J.P. Walker, *Chem. Mater.* 20 (2008) 7501–7509.
- [339] Chad E. Reese, Alexander V. Mikhonin, Marta Kamenjicki, and Alexander Tikhonov, S.A. Asher\*, (2004).
- [340] Y. Zhang, Y. Zhang, B. Li, *Opt. Express* 15 (2007) 9287.
- [341] B.V.R. Tata, J. Brijitta, R.G. Joshi, *Int. J. Adv. Eng. Sci. Appl. Math.* 5 (2013) 240–249.
- [342] M. Chen, L. Zhou, Y. Guan, Y. Zhang, *Angew. Chemie Int. Ed.* 52 (2013) 9961–9965.
- [343] R. Phillips, *Crystals, Defects and Microstructures : Modeling across Scales*, Cambridge University Press, 2001.
- [344] S. John, A. Blanco, E. Chomski, S. Grabtchak, M. Ibisate, S.W. Leonard, C. Lopez, F. Meseguer, H. Miguez, J.P. Mondia, G.A. Ozin, O. Toader, H.M. van Driel, *Nature* 405 (2000) 437–440.

## References

- [345] P.S. Mohanty, W. Richtering, *J. Phys. Chem. B* 112 (2008) 14692–14697.
- [346] R. J. Speedy, *J. Physics. Condens. Matter* 10 (1998) 4387–4391.
- [347] P.N. Pusey, W. van Megen, *Nature* 320 (1986) 340–342.
- [348] Q. Luo, Y. Guan, Y. Zhang, M. Siddiq, *J. Polym. Sci. Part A Polym. Chem.* 48 (2010) 4120–4127.
- [349] D. Karthickeyan, D.K. Gupta, B.V.R. Tata, *J. Opt.* 18 (2016) 105401.
- [350] B.V.R. Tata, R.G. Joshi, D.K. Gupta, J. Brijitta, B. Raj, *Curr. Sci.* 103 (2012).
- [351] M. Chen, L. Zhou, Y. Guan, Y. Zhang, *Angew. Chemie Int. Ed.* 52 (2013) 9961–9965.
- [352] R.G. Joshi, B.V.R. Tata, J. Brijitta, in: *AIP Conf. Proc.*, 2011, pp. 208–209.
- [353] Q. Yuan, J. Gu, Y. Zhao, L. Yao, Y. Guan, Y. Zhang, *ACS Macro Lett.* 5 (2016) 565–568.
- [354] Z. Tang, S. Jia, L. Yao, Y. Guan, Y. Zhang, *J. Colloid Interface Sci.* 526 (2018) 83–89.
- [355] B.R. Saunders, *Langmuir* 20 (2004) 3925–3932.
- [356] I. Lynch, K.A. Dawson, *J. Phys. Chem. B* 107 (2003) 9629–9637.
- [357] N. Huang, Y. Guan, X.X. Zhu, Y. Zhang, *ChemPhysChem* 15 (2014) 1785–1792.
- [358] J.Z. Xue, D.J. Pine, S.T. Milner, X.-L. Wu, P.M. Chaikin, *Phys. Rev. A* 46

- (1992).
- [359] R.G. Joshi, B.V.R. Tata, *Colloid Polym. Sci.* 295 (2017) 1671–1683.
- [360] C. Haro-Pérez, G.J. Ojeda-Mendoza, L.F. Rojas-Ochoa, *J. Chem. Phys.* 134 (2011) 244902.
- [361] F. Scheffold, P. Díaz-Leyva, M. Reufer, N. Ben Braham, I. Lynch, J.L. Harden, *Phys. Rev. Lett.* 104 (2010) 128304.
- [362] C. Urban, P. Schurtenberger, *J. Colloid Interface Sci.* 207 (1998) 150–158.
- [363] H.B. Bohidar, *Curr. Sci.* 80 (2001) 1008–1017.
- [364] R.G. Joshi, B.V.R. Tata, J. Brijitta, *J. Chem. Phys.* 139 (2013) 124901.
- [365] Y. Yan, L. Liu, Z. Cai, J. Xu, Z. Xu, D. Zhang, X. Hu, *Sci. Rep.* 6 (2016) 31328.
- [366] T.H. de Keijser, J.I. Langford, E.J. Mittemeijer, A.B.P. Vogels, *J. Appl. Crystallogr.* 15 (1982) 308–314.
- [367] S. Jia, Z. Tang, Y. Guan, Y. Zhang, *ACS Appl. Mater. Interfaces* 10 (2018) 14254–14258.